ARCHIVES OF MECHANICS **Appears since 1949**

Aims and Scope

ARCHIVES OF MECHANICS provides a forum for original research on mechanics of solids, fluids and discrete systems, including the development of mathematical methods for solving mechanical problems. The journal encompasses all aspects of the field, with the emphasis placed on:

- mechanics of materials: elasticity, plasticity, time-dependent phenomena, phase transformation, damage, fracture; physical and experimental foundations, micromechanics, thermodynamics, instabilities
- methods and problems in continuum mechanics: general theory and novel applications, thermomechanics, structural analysis, porous media, contact problems
- dynamics of material systems
- fluid flows and interactions with solids

Address of the Editorial Office:
Institute of Fundamental Technological Research
Świętokrzyska 21
PL 00-049 Warsaw, Poland

Tel.: (48-22) 826 60 22, Fax: (48-22) 826 98 15, E-mail: publikac@ippt.gov.pl

Abstracted/indexed in:

Applied Mechanics Reviews, Current Mathematical Publications, Mathematical Reviews, MathSci, Zentralblatt für Mathematic, UnCover.

Polish Academy of Sciences
Institute of Fundamental Technological Research

Archives of Mechanics

Archiwum Mechaniki Stosowanej

volume 51 issue 6

Agencja Reklamowo-Wydawnicza A. Grzegorczyk
Warszawa 1999

SUBSCRIPTIONS

Address of the Editorial Office: Archives of Mechanics
Institute of Fundamental Technological Research, Świętokrzyska 21
PL 00-049 Warsaw, Poland
Tel.: (48-22) 826 60 22, Fax: (48-22) 826 98 15, E-mail: publikac@ippt.gov.pl

Subscription orders for all journals edited by IFTR may be sent directly to the Editorial Office of the Institute of Fundamental Technological Research

Subscription rates

Annual subscription rate (1999) including postage is US $ 174.
Please transfer the subscription fee to our bank account: Payee: IPPT PAN,
Bank: PKO SA. IV O/Warszawa,
Account no. 12401053-40054492-3000-401112-001.

All journals edited by IFTR are available also through:

- Foreign Trade Enterprise ARS POLONA Krakowskie Przedmieście 7, 00-068 Warszawa, Poland fax: (48-22) 826 86 73
- RUCH S.A. ul. Towarowa 28, 00-958 Warszawa, Poland fax:(48-22) 620 17 62
- Agencja Reklamowo-Wydawnicza A. Grzegorczyk, Bitwy Warszawskiej 1920r. 3, 00-973 Warszawa, Poland tel./fax: (48-22) 822 49 36

Warunki prenumeraty

Redakcja przyjmuje prenumeratę na wszystkie czasopisma wydawane przez IPPT PAN. Bieżące numery można nabyć a także zaprenumerować roczne wydanie Archiwum Mechaniki Stosowanej bezpośrednio w Dziale Wydawnictw IPPT PAN, Świętokrzyska 21, 00-049 Warszawa, Tel.: (48-22) 826 60 22; Fax: (48-22) 826 98 15.
Cena rocznej prenumeraty z bonifikatą (na rok 1999) dla krajowego odbiorcy wynosi 80 zł

Również można je nabyć, a także zamówić (przesyłka za zaliczeniem pocztowym) we Wzorcowni Ośrodka Rozpowszechniania Wydawnictw Naukowych PAN,
00-818 Warszawa, ul. Twarda 51/55, tel. (48-22) 697 88 35.
Wpłaty na prenumeratę przyjmują także jednostki kolportażowe RUCH S.A. Oddział Krajowej Dystrybucji Prasy, 00-958 Warszawa, ul. Towarowa 28. Konto: PBK.S.A. XIII Oddział Warszawa nr 11101053-16551-2700-1-67. Dostawa odbywa się pocztą zwykłą w ramach opłaconej prenumeraty z wyjątkiem zlecenia dostawy pocztą lotniczą, której koszt w pełni pokrywa zleceniodawca. Tel.: (48-22) 620 10 39, fax: (48-22) 620 17 62

Arkuszy wydawniczych 21. Arkuszy drukarskich 22,30/A5.
Papier offset. kl III 70 g. B1.
Oddano do składania w listopadzie 1999 r. Druk ukończono w grudniu 1999 r.
Skład i łamanie: G. Wasilewska. Druk i oprawa: Drukarnia OMIKRON, Stare Babice ul. Kutrzeby 15.

Arch. Mech., **51**, 6, pp. 647–649, Warszawa 1999

Preface

The present issue of Archives of Mechanics contains the submitted and reviewed contributions to the Polish-Japanese Workshop on "B Testing and Modelling the Behaviour of Shape Memory Alloys", which was organised as an accompanying event at the 32nd Solid Mechanics Conference: SolMec '98, held in Zakopane, September 1 – 5, 1998.

History of scientific co-operation between Poland and Japan is long and close in the field of mechanics. Already in 1970s Prof. P. Perzyna and Prof. S. Murakami started together the investigations of creep phenomena, reaching finally the concept of damage mechanics. On the other hand, Prof. A. Sawczuk, Prof. B. Raniecki and Prof. T. Inoue have developed the foundation of quenching stress analysis that accounts for the effect of plastic flow and phase distortions due to martensitic and diffusive phase transformations in steels. It opened the way to a quite new field in applied thermomechanics. These pioneering co-operative works were frequently followed by many researchers in both countries, who have been developing, year by year, the closer and stronger scientific tie-up in the wider field of mechanics.

The chairmen of the present workshop have agreed in 1995 to start, together with Prof. L. Dietrich and Prof. S. Miyazaki, a Polish-Japanese co-operative research project under the theme "Testing and Modelling the Behaviour of Shape Memory Alloys", in order to verify the theory of pseudoelasticity in shape memory alloys presented by them in 1992 with French colleague Prof. C. Lexcellent. They prepared thin-walled tubular specimens in TiNi shape memory alloy for a series of tests under multiaxial stresses, covering the temperature range from the R-phase reorientation process to the martensitic transformation. Modelling the alloy behaviour, based fully on thermodynamics, was also included to the aims of their project. The informal co-operation between Prof. W.K. Nowacki and Prof. H. Tobushi initiated in 1996 in the field of mechanics of shape memory alloys should also be mentioned.

In fact such co-operative works were just an urgent request of the times; shape memory alloys were about to be used, not only as thin wires or coils but also as thin films of the order of mm in thickness, large pipes and bars of the order of scores of cm in diameter, fillers in a matrix material to form shape memory alloy composites, etc. Designers of the shape memory devices requested a sound theoretical framework to predict rationally the alloy performance, both under multiaxial stresses and in the wider temperature range. Theoretical concepts, which have been so far developed on macroscopic and microscopic ground

should be verified in the course of systematic and well designed experiments. The task is, however, quite difficult because the behaviour of shape memory alloys under thermomechanical loadings are extremely complex when compared to the performance of standard alloys.

The activity of the Polish-Japanese teams was adopted as one of the joint projects of the Polish Academy of Sciences and the Japan Society of Promotion of Sciences, who offered the teams a chance to hold the Workshop. Seven Japanese and twenty two Poles participated in the Workshop and discussed intensively, together with eight scientists from four countries, the topics reported on experimental results, mechanical and thermal, so far obtained in the project and proposals of data processing and model building. The thermomechanical behaviour in other alloy systems, such as Cu-based shape memory alloy and Fe-based shape memory alloy, was also presented.

As the chairmen of the Workshop, we sincerely wish that the present issue will become something like a forum of the researchers who have interest in the subject. The readers might hopefully find out in this forum some hints for their current and future study. And some new co-operation might be promoted in the forum.

Finally, we express our cordial thanks for the financial aid of the Polish Academy of Sciences, Polish State Committee for Sciences (project KBN No 7T07A00513) and the Japan Society of Promotion of Sciences, and also for the generous support of the office of the SolMec '98.

Bogdan Raniecki and Kikuaki Tanaka

Workshop Chairmen

Arch. Mech., **51**, 6, pp. 649–663, Warszawa 1999

Temperature evolution during tensile test of TiNi shape memory alloy

S.P. GADAJ ([1]), W.K. NOWACKI ([1]), H. TOBUSHI ([2])

([1]) *Polish Academy of Sciences*
Center of Mechanics and Information Technology
Institute of Fundamental Technological Research
Świętokrzyska 21, 00–049 Warszawa, Poland

([2]) *Department of Mechanical Engineering*
Aichi Institute of Technology,
1247 Yachigusa, Toyota 470–03, Japan

EXPERIMENTAL RESULTS containing both the mechanical characteristics and the changes of temperature obtained during tensile test of TiNi shape memory alloy strained at various strain rates have been presented. The investigations were carried out at room temperature ($\approx$ 295 K) and at chamber temperature equal to 333 K. The temperature changes were measured in a contactless way by recording the infrared radiation emitted by the surface of the sample. It was found that during loading at room temperature, the phase transformation process is homogeneous but at temperature 333 K the process seems to be heterogeneous. The martensitic transformation was accompanied by an increase in temperature. Both the stresses and the temperature changes were higher for the tests carried out at elevated temperature. Decreases in temperature during unloading were higher too. For tests carried out in the same conditions, the temperature increments in the range of the martensitic transformation plotted as a function of stress, turned out to lie on the same curve, independently of the strain rate.

1. Introduction

THE MECHANICAL PROPERTIES of shape memory alloys (SMA) during uniaxial tensile test, are strongly temperature – dependent. When SMA is tested above its transformation temperature A_f, martensite can be stress-induced and then, after unloading, the material transforms to austenite at a lower stress; the tensile specimen after crossing the hysteresis loop returns to the initial state. This effect is related to dissipation of energy and is known as pseudoelasticity (PE) [1, 2].

At temperatures below A_f, stress-strain curve is governed mainly by the martensite transformation: the strain in the specimen will not completely recover even after the stress removal. This strain can be almost completely eliminated by

heating the specimen to the temperature above A_f. This phenomenon is known as the shape memory effect (SME) [1].

The thermomechanical behaviour of SMA was modelled with one- [2] or three-dimensional models [3, 4]. The models describe mechanical behaviour of the material under arbitrary condition of loading. To integrate the constitutive laws obtained from these models, the mechanical characteristics obtained from experiments are necessary. There are many interesting experimental papers concerning the shape memory alloys deformed under various rates of strain and various temperatures (e.g. [5, 6, 7, 8]). Their goal was to investigate the influence of these factors on PE and SME characteristic behaviour.

In reality, the hysteresis loop that has been observed during PE examination and the stress-strain curve registered during SME monitoring, indicate the mechanical energy dissipation [2, 9, 10]. The strain energy dissipated in the material causes an increase in temperature which can change the phase transformation process. There are few papers in which such process has been considered. For example, in [11] the temperature changes have been considered but temperature was measured there only in the range 1% of elongation. W. HUANG [12] measured the temperature during tension tests of NiTi wire using thermocouples placed in some points of the sample. He observed differences in temperature in the points what indicates the phase transformation fronts movement. Nucleation and propagation of phase transformation fronts during loading and unloading of NiTi alloy in temperature above A_f have been also observed by J.S. SHAW [13] using the infrared camera.

During fatigue test of TiNi shape memory alloy the changes of temperature were measured by H.TOBUSHI *et al.* [14, 15]. A thermocouple was used there to determine the temperature changes. It was noticed that temperature increases both with the increasing number of cycles (especially in the first 500 cycles) and with the increasing strain amplitude. The increments of temperature averaged over a cycle are small but significant. It seems however, that the applied measuring method causes a reduction of the temperature increments.

The purpose of this paper is to present experimental results of the study of thermomechanical coupling during loading and unloading of TiNi shape memory alloy in the range of martensitic transformation. The investigations were carried out both at ambient temperature (295 K) and at chamber temperature equal to 333 K. The temperature changes were measured in a contactless way, by recording the infrared radiation emitted by the surface of the sample.

2. Experimental procedure

The investigations were performed on the sheet samples: 240 mm × 6 mm × 0.5 mm, Ni 55.3wt% and the balance Ti shape memory alloy, produced by

Furukawa Electric Co. The temperature A_f of this material was about 340 K. Before testing the samples were annealed at 180°C during 10 min. The sample was placed in a specially designed grip, fitted in the tensile testing machine. Its elongation was measured by an extensometer; the measured gauge length was 178.5 mm. The samples were first loaded to the range a little above the martensitic transformation, and then unloaded with the same rate of deformation.

The experiments were performed in room temperature (about 295 K) and in the thermal chamber at temperature 333 K. In the case of room temperature, the samples were tested at four , specially chosen strain rates: $0.47 \cdot 10^{-3}$ s^{-1}, $0.93 \cdot 10^{-3}$ s^{-1}, $1.87 \cdot 10^{-3}$ s^{-1} and $4.67 \cdot 10^{-3}$ s^{-1}. These rates should be high enough in order to provide sufficiently high temperature increments, measurable by the used thermovision set. In the case of temperature 333 K the samples were tested at three strain rates: $0.93 \cdot 10^{-3}$ s^{-1}, $1.87 \cdot 10^{-3}$ s^{-1} and $4.67 \cdot 10^{-3}$ s^{-1}. In these conditions, the specimens were observed by thermovision camera through the silicon window placed in the wall of the thermal chamber.

In the course of the straining, the load and the deformation vs. time, the stress-strain relations and the distributions of infrared radiation, emitted by the sample's surface (size 6 mm × 100 mm), were continuously registered. The distribution of infrared radiation was measured using the thermovision camera coupled to a computer system of data acquisition and conversion. The system allows us to obtain the thermovision pictures (thermograms) with various precision which are the basis for analysis of the temperature distributions of the examined surface. A thermovision camera scans the examined specimen collecting the infrared radiation from its surface. During 0.06 s the camera creates an image called frame. The frame contains few details, but the short time of its creation can be valuable in monitoring the change of temperature corresponding to the beginning of the process of elongation. Four such frames superimposed over each other create a thermal picture, obtained during 0.24 s. This thermal picture is a basis for analysis of the temperature distributions of the examined surface. Such distributions can be presented in different units depending on the chosen curve of calibration. The mean-square error of temperature evaluation was about 0.2 K. In order to secure higher and more homogeneous emissivity, the surfaces of the samples were blackened with a carbon powder. More details about the used thermovision equipment are given in [16].

The temperature was determined as the average value taken from the surface of the specimen of about 70 mm × 5 mm. An example of thermogram with marked zone of temperature measurement and the calculated value of temperature was shown in Fig. 1.

3. Changes in the field of temperature during martensite transformation

Mechanical characteristics and numerous thermograms were obtained, which show the temperature distribution on the surface of samples during their deformation. A detailed analysis of thermograms indicate, that the changes of temperature fields measured on the sample surface during its straining at room temperature (295 K) are different than those obtained for higher temperature (333 K). In order to illustrate the differences, the thermograms corresponding to some choosen points of stress-strain curves for both ambient temperatures were made.

For example, in the case of the room temperature test with the strain rate equal to $1.87 \cdot 10^{-3}$ s^{-1}, thermograms at the following values of strain were chosen: 0, 0.01, 0.02, 0.03, and the last one made at the end of unloading. The characteristic points have been marked on the stress-strain curve in Fig. 2 and the obtained thermograms are shown in Fig. 3.

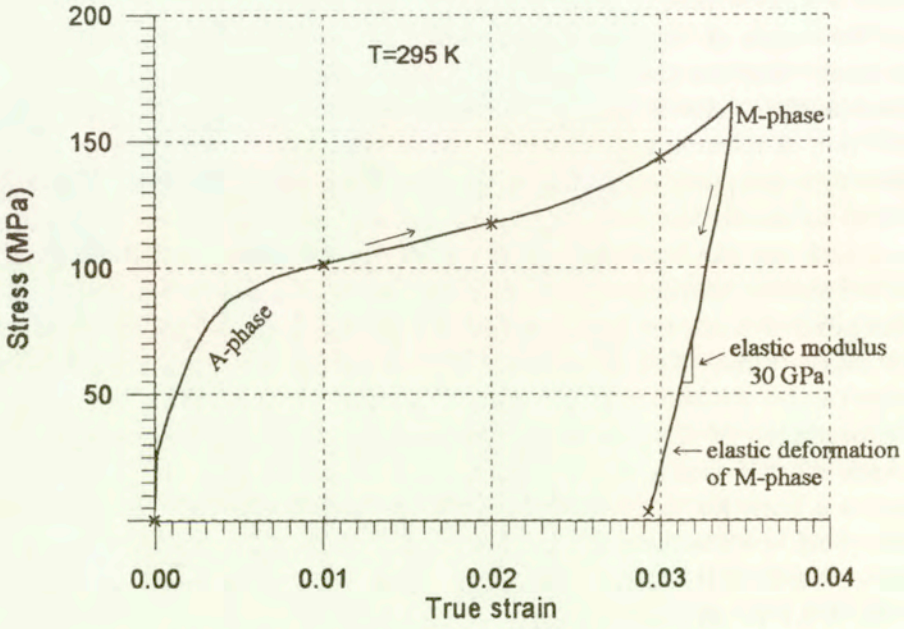

FIG. 1. Stress-strain curve with marked points chosen for analysis of the fields of temperature under room conditions, $\varepsilon = 1.87 \cdot 10^{-3}$ s^{-1}.

It is seen that temperature distribution on the surface of the specimens examined in room temperature was uniform, what indicates the homogeneity of the stress and the strain state along the specimen. In other words, the infrared measurements prove , that the process of nucleation and the growth of martensite proceed homogeneously in the whole volume of the specimen.

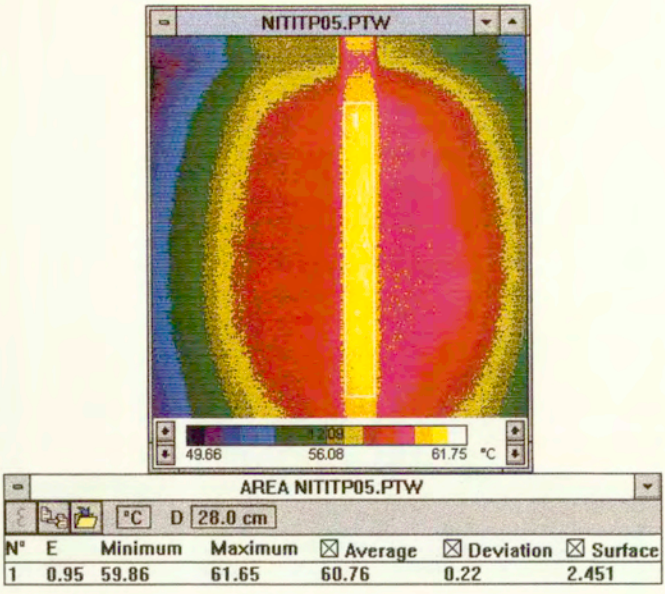

FIG. 2. Example of thermogram with the pointed area of temperature measurement.

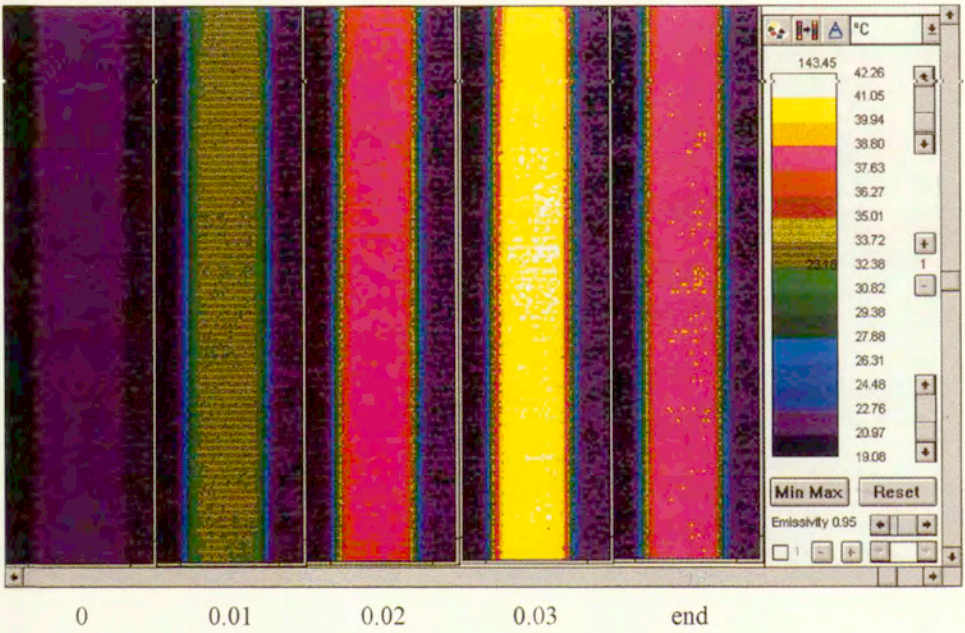

0 0.01 0.02 0.03 end

FIG. 3. Temperature distribution on the surface of TiNi specimen subjected to uniaxial loading test at room temperature with the constant strain rate $\dot{\varepsilon} = 1.87 \cdot 10^{-3}$ s^{-1}, obtained after straining: 0, 0.01, 0.02, 0.03, and at the end of unloading.

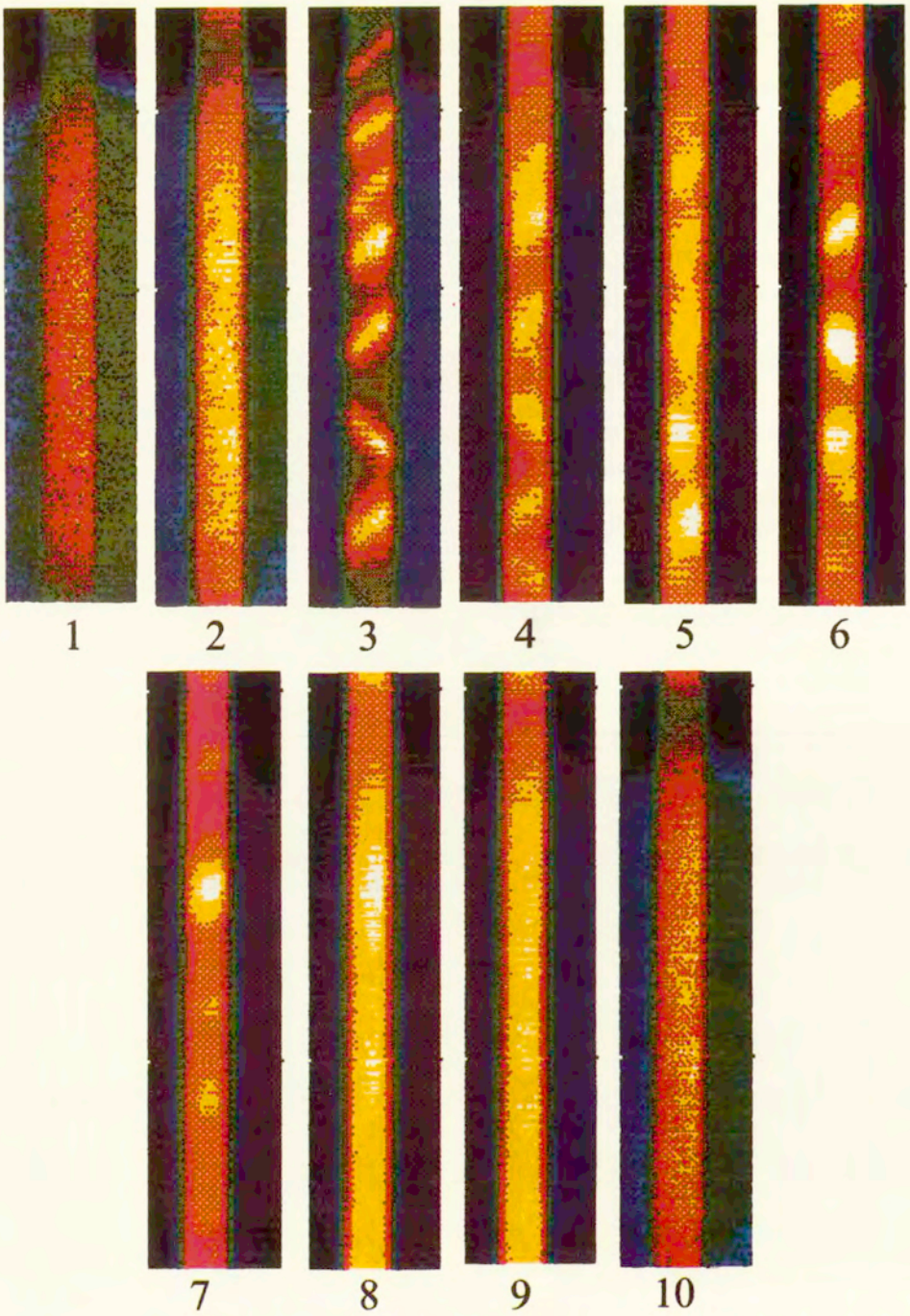

FIG. 5. Temperature distribution on the surface of TiNi specimen subjected to uniaxial loading test at temperature 333 K with the constant strain rate $\dot{\varepsilon} = 1.87 \cdot 10^{-3}$ s^{-1}. Numbers below the thermograms correspond to points at the curve in the Fig. 4.

In the case of temperature equal to 333 K different results were obtained. The example of the stress-strain curve with marked points which have been chosen for the analysed fields of temperature are shown in Fig. 4 and the corresponding thermograms are presented in Fig. 5. The strain rate was equal to $1.87 \cdot 10^{-3}$ s^{-1}, the same as in the previous example. Black colour in Fig. 5 (minimum of temperature) corresponds to 58°C and is the same in all thermograms. The temperature values of white colour for each thermogram as well as the strain values corresponding to them, are given in Table 1.

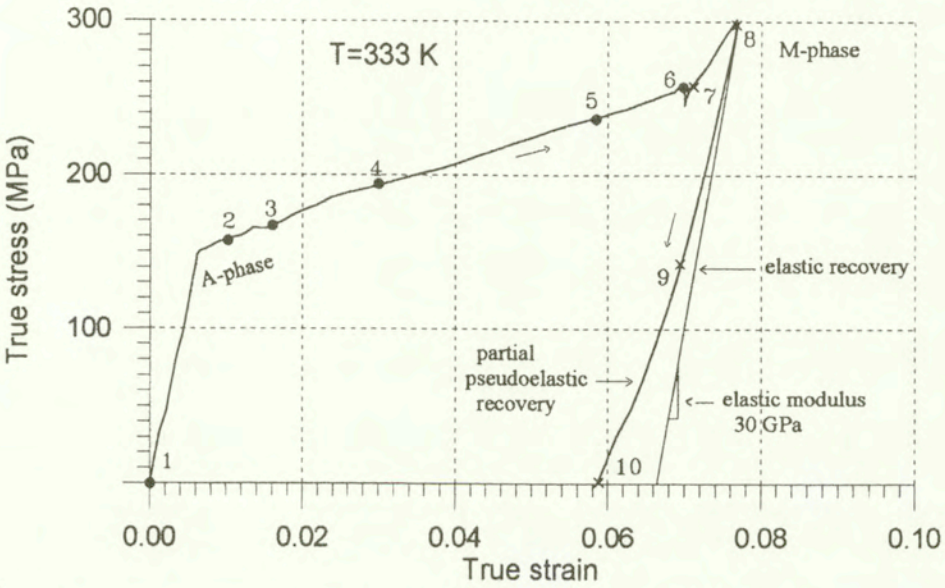

FIG. 4. Stress-strain curve with marked points chosen for analysis of the thermograms at temperature 333 K, $\dot{\varepsilon} = 1.87 \cdot 10^{-3}$ s^{-1}.

Table 1.

No. of thermograms	White colour temperature (°C)	True strain
1	61.06	0.0000
2	62.52	0.0133
3	65.68	0.0153
4	72.88	0.0305
5	79.55	0.0588
6	82.10	0.0695
7	81.70	0.0710
8	78.43	0.0765
9	70.40	0.0697
10	61.94	0.0589

At the beginning of tension (points 1, 2 in the Fig. 4, 5), the temperature of the sample surface is homogeneous. (Dimension of the silicon window was smaller than that of the used infrared camera objective, so we have taken into account only a part of the sample picture, without the end areas.) Next, at point 3, temperature in the same areas of the sample rapidly increases. These areas are probably regions of creation of the martensite phase. As the strain grows, appearance of these areas changes (points 4, 5, 6); they become not well marked, because the heat flows and the martensitic phase develops. When the martensite transformation is finished (point 7), the differences in the field of temperature decreases. During unloading (points 8, 9, 10) temperature of the sample surface becomes homogeneous again.

FIG. 6. Regions of plastic deformations created during martensite transformation caused by deformation of TiNi shape memory alloy in temperature 333 K.

Creation and next extension of the martensite phase in the same regions of the sample leads to creation of local plastic deformations in the neighbour regions. They have the form of bulges on the surface of the sample (Fig. 6). These regions are caused by the stress concentration occurring during martensite transformation and constrains following from the holding system of the sample [17]. Heating, after which the sample returns to its previous size, does not remove completely the traces of the plastic deformation but only makes them less visible.

4. Thermomechanical coupling during loading and unloading

The mechanical characteristics obtained during the uniaxial tensile test of the samples of TiNi shape memory alloy strained at four strain rates in room temperature are shown in Fig. 7.

After the elastic deformation in the short initial range of loading, yielding – caused by the martensitic transformation – occurs at the stress of $70 \div 90$ MPa. It corresponds to the strain of about 0.005. The intensity of martensitic transformation increases with the strain (caused by loading) and it is followed by a small increase of stress. At the end of martensitic transformation elastic deformation starts again.

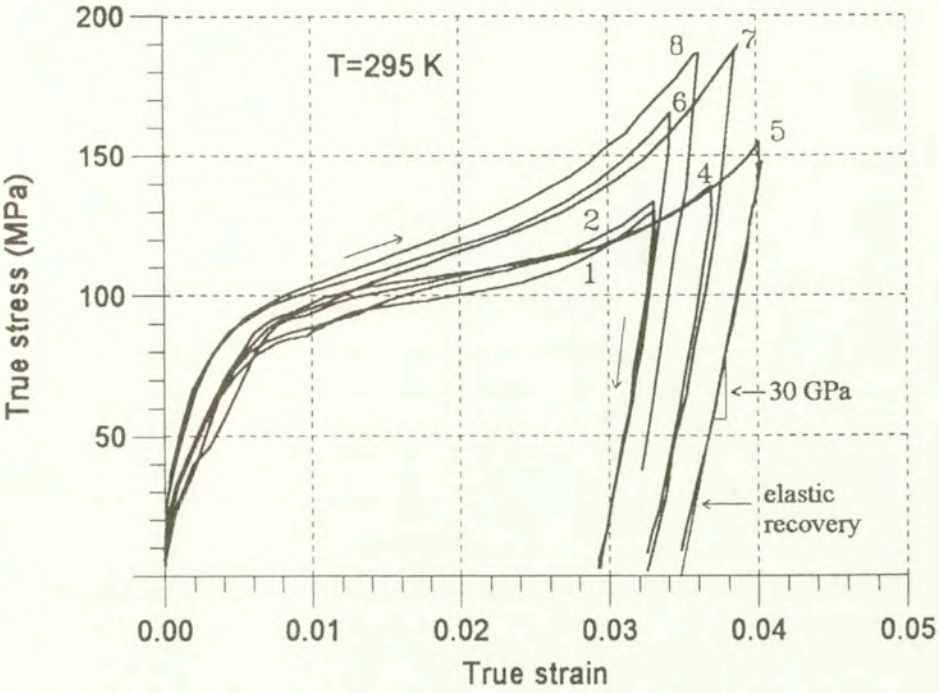

FIG. 7. The stress-strain relation of TiNi shape memory alloy strained at the temperature 295 K with various strain rates: $1, 2 - 0.47 \cdot 10^{-3}$ s^{-1}; $4, 5 - 0.93 \cdot 10^{-3}$ s^{-1}; $6, 7 - 1.87 \cdot 10^{-3}$ s^{-1} and $8 - 4.67 \cdot 10^{-3}$ s^{-1}.

After unloading started from the strain of $0.03 \div 0.04$, the recoverable residual strain of the order of $0.029 \div 0.035$ appears. The starting point of unloading was not the same in all tests. The temperature evolution of the surface of the tested specimens, obtained during their loading and unloading in room temperature at four various rates of deformation, is shown in Fig. 8. One should notice that the thermoelastic effect was not observed here.

The relations $\Delta T(\varepsilon)$ (Fig. 8) point out a visible dependence of temperature on the strain rate, when the differences between the mechanical curves are not so well-marked (Figs. 7 and 8). Changes of the mechanical characteristics obtained for the higher strain rates can be related to the increase of the temperature of the material during these processes, what follows from in the results of the investigations of TiNi shape memory alloys presented in other papers [9].

The mechanical characteristics obtained during the test performed at the temperature 333 K (Fig. 9) are located much higher, i.e. the value of stresses corresponding to martensite transformation is greater: $150 \div 180$ MPa. Range of the strain of this transformation is also higher. The starting points of unloading in each test were not the same, as in the case of room temperature.

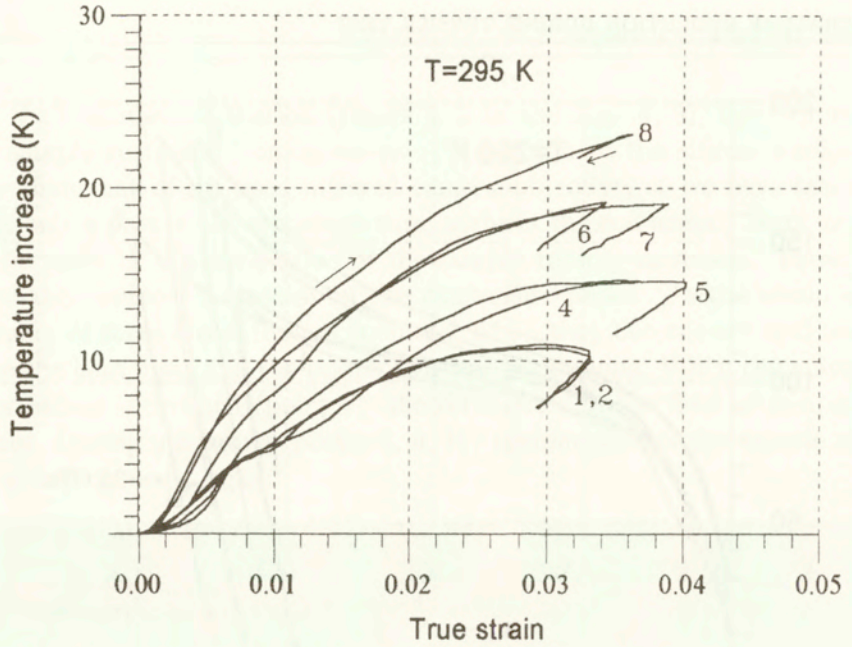

FIG. 8. Changes in temperature of TiNi shape memory alloy strained at the temperature 295 K with various strain rates: $1, 2 - 0.47 \cdot 10^{-3}$ s^{-1}; $4, 5 - 0.93 \cdot 10^{-3}$ s^{-1}; $5, 7 - 1.87 \cdot 10^{-3}$ s^{-1} and $8 - 4.67 \cdot 10^{-3}$ s^{-1}.

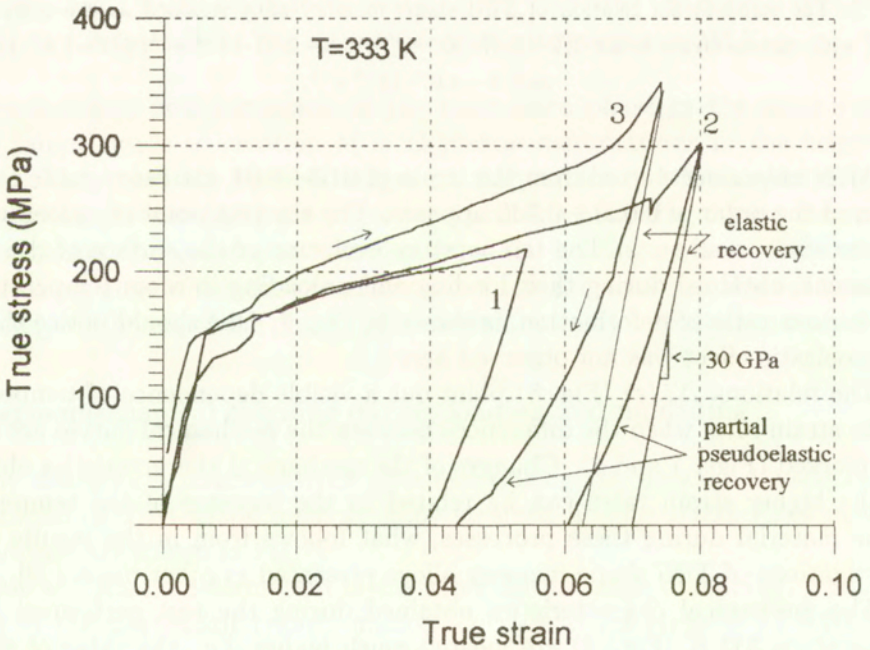

FIG. 9. The stress-strain relation of TiNi shape memory alloy strained at the temperature 333 K with various strain rates: $1 - 0.93 \cdot 10^{-3}$ s^{-1}; $2 - 1.87 \cdot 10^{-3}$ s^{-1} and $3 - 4.67 \cdot 10^{-3}$ s^{-1}.

The changes in temperature (Fig. 10) corresponding to them are not so smooth as at room temperature, because temperature on the sample surface is not homogeneous in the region of martensitic transformation. The increments of temperature are higher and the decrements measured during unloading are higher too.

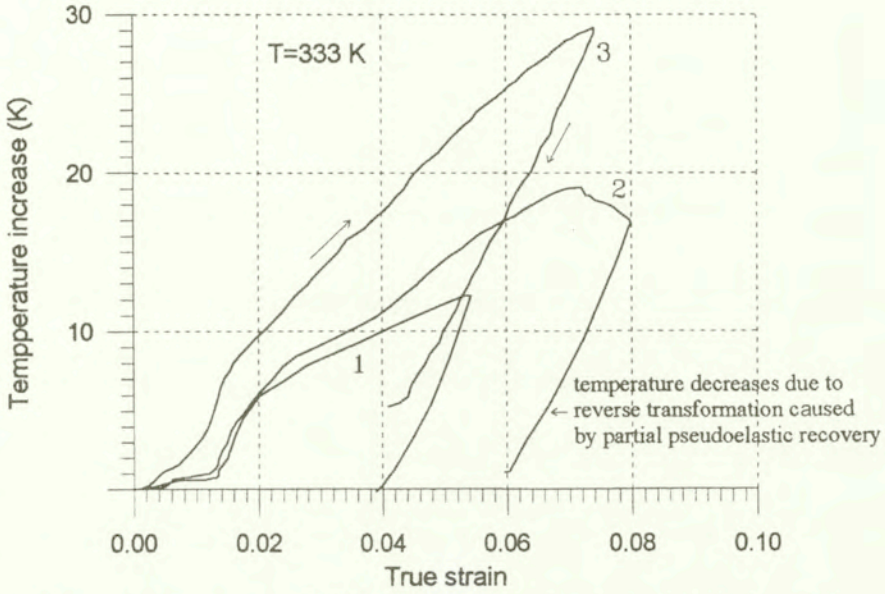

FIG. 10. Changes in temperature of TiNi shape memory alloy strained at the temperature 333 K with various strain rates: $1 - 0.93 \cdot 10^{-3}$ s^{-1}; $2 - 1.87 \cdot 10^{-3}$ s^{-1} and $3 - 4.67 \cdot 10^{-3}$ s^{-1}.

Especially interesting results of the experiments carried out are the temperature changes obtained for various strain rates and described as a function of stress. The results obtained for temperature 295 K are presented in the Fig. 11, and those for elevated temperature (333 K) in the Fig. 12.

Temperature distribution on the sample surface deformed at room temperature was homogeneous, so mean square error of the temperature was the same and equal to 0.2 K. At elevated temperature this distribution was not homogeneous. The mean square error of its measurement was different and is shown in the Fig. 12.

It was found, that the temperature changes during loading plotted as a function of stress, are similar for all of the applied strain rates. The relations between the temperature changes and the stress registered in the range of martensitic transformation are independent of the strain rate. One can conclude that the stress related to the temperature increments induces the martensitic transformation independently of the path and time of deformation. The relation $\Delta T(\sigma)$ can be regarded as the intrinsic characteristic of the tested shape memory alloy.

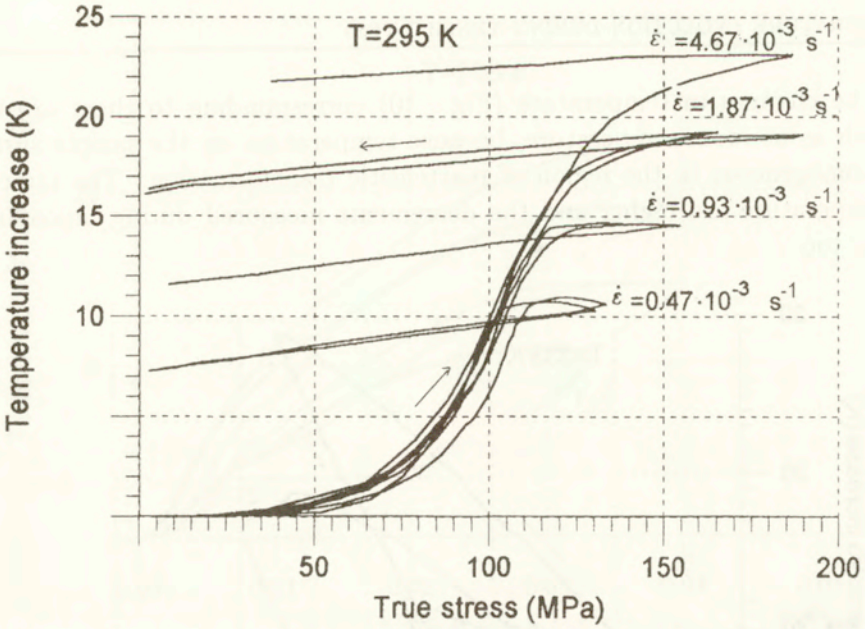

FIG. 11. Stress dependence of temperature change for various strain rates of TiNi shape memory alloy loaded at the temperature of 295 K.

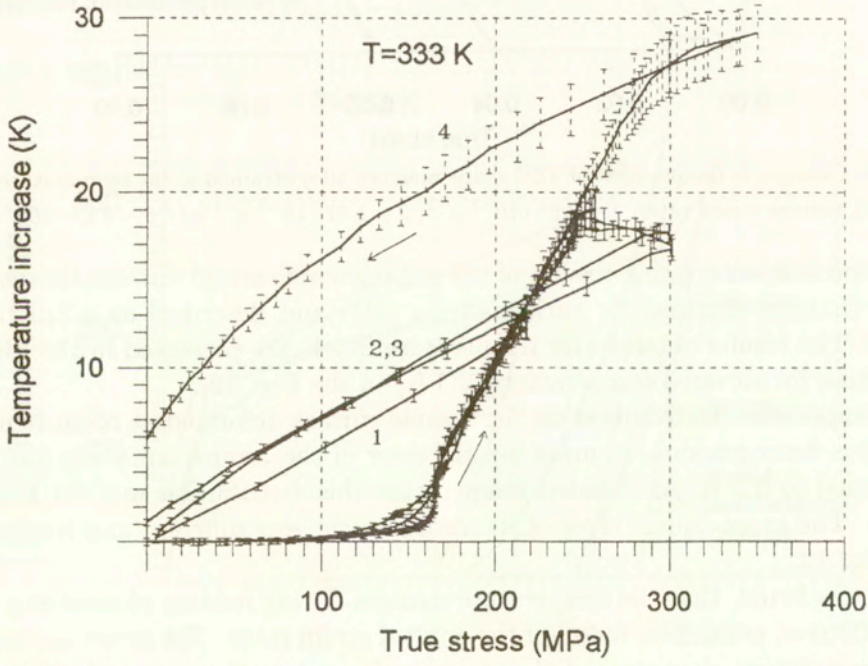

FIG. 12. The increase of temperature-strain relation of TiNi shape memory alloy loaded at the temperature of 333 K with various strain rates: $1 - 0.93 \cdot 10^{-3}$ s^{-1}; $2,3 - 1.87 \cdot 10^{-3}$ s^{-1} and $4 - 4.67 \cdot 10^{-3}$ s^{-1}.

During unloading of the specimen at room temperature, the curves $\Delta T(\sigma)$ are parallel to each other (Fig. 11). Temperature decreases by about 1 – 2 K for every test. The process of cooling was independent of the strain rate, what means that disturbances related to the differences in the heat transfer to the surrounding (for various rates of deformation) are negligible.

For tests carried out at temperature 333 K, changes of temperature obtained during unloading are much larger – reaching 20 K (Fig. 12). Such a high temperature changes are caused by the reverse transformation. As seen in Figs. 2 and 7, the unloading curves are linear and elastic modulus of the martensitic phase is 30 MPa. On the other hand, as seen in Figs. 4 and 9, the unloading curves are nonlinear and partial pseudoelastic recovery is observed. Therefore, in the case of 333 K, partial pseudoelastic deformation appears during unloading and temperature decreases due to the reverse transformation.

5. Conclusions

The temperature distribution measured on the surface of the SMA samples loaded at room temperature (295 K) was uniform, what indicates the homogeneity of the phase transformation process.

Bands of relatively higher temperature increment were observed on the surface of samples loaded at temperature equal to 333 K. The effect of nonhomogeneity was observed during pseudoelastic flow of the sample. It can be concluded that the development of the inartensitic transformation is nonhomogeneous. Before and after the martensitic transformation, the temperature distribution on samples' surface is homogeneous. Both nucleation and the following extension of the martensitic phase in the same regions are accompanied by local plastic deformation in the neighbour regions of the sample. Heating, during which the sample returns to its previous size, does not remove completely the traces of the plastic deformation but only makes them less clearly observable.

The stresses and temperature increases were much higher during the study at temperature 333 K than that at the room temperature. Mechanical characteristics of the tested samples and changes in temperature increase with the strain rate.

The temperature increments presented as a function of stress in the range of the martensitic transformation, for the test carried out in the same conditions, turned out to lie on the same curve, independently of the strain rate. It seems that the relation $\mathrm{DT}(\sigma)$ is a characteristic of the tested shape memory alloy.

The parallelism of $\Delta T(\sigma)$ characteristics during unloading of the samples tested at room temperature indicates that the decrease of temperature was caused only by heat of energy dissipation. Decrease of temperature during unloading of

the samples tested in ambient temperature of 333 K was much higher and was caused by reverse transformation accompanied by partial pseudoelastic recovery.

Acknowledgments

This work has been supported by the State Committee for Scientific Research under Grant No. 7 T07A 00513

References

1. *Shape Memory Alloys, Ed. Hiroyasu Funakubo*, Gordon and Breach Sci. Publ., New York, London 1987.
2. Y. HUO, I. MULLER, *Nonequilibrum thermodynamics of pseudoelasticity*, Cont. Mech. Thermodyn., **5**, 3, 163, 1993.
3. K. TANAKA, S. KOBAYASHI, Y. SATO, *Termomechanics of transformation pseudoelasticity and shape memory effect in alloys*, Int. Jour. Plast., **2**, 59, 1986.
4. B. RANIECKI, C. LEXCELLENT and K. TANAKA, *Thermodynamics models of pseudoelastic behaviour of shape memory alloys*, Arch. Mech., **44**, 261, 1992.
5. D.S. FORD, S.R. WHITE, *Thermomechanical behaviour of* $55Ni45Ti$ *nitinol*, Acta Mater., **44**, 6, 2295, 1996.
6. P.H. LIN, H. TOBUSHI, K. TANAKA, *et al.*, *Pseudoelastic behaviour of TiNi shape memory alloy subjected to strain variations*, J. Intell. Mat. Sys. Struc., **5**, 694, 1994.
7. K. TANAKA, F. NISHIMURA and H. TOBUSHI, *Transformation start lines in NiTi and Fe-based shape memory alloys after incomplete transformations induced by mechanical and/or thermal loads*, Mech. Mater., **19**, 271, 1995.
8. H. TOBUSHI, A. IKAI, S. YAMADA, *et al.*, *Thermomechanical properties of TiNi shape memory alloy*, Jour. Phys. IV, **6**, C1-385, 1996.
9. P.H. LIN, H. TOBUSHI, K. TANAKA, *et al.*, *Influence of strain rate on deformation properties of TiNi shape memory alloy*, JSME Inter. Jour., **A39**, 1, 117, 1996.
10. H. TOBUSHI, K. TANAKA, T. HORI, *et al.*, *Pseudoelasticity of TiNi shape memory alloy*, JSME Inter. Jour., **A36**, 3, 314, 1993.
11. C. LEXELLENT, C. ROGUEDA and G. BOURBON, *Parameter determination for thermodynamical models of the pseudoelastic behaviour of shape memory alloy by resistivity measurements and infrared thermography*, Cont. Mech. Thermodyn., **6**, 273, 1994.
12. W. HUANG, *Shape memory alloy and their application to actuators for deployable structures*, Doctor's Dissertation, Univesity of Cambrige, March 1998.
13. J.A. SHAW, S. KYRIAKIDES, *On the nucleation and propagation of phase transformation fronts in a NiTi alloy*, Acta Mater., **45**, 2, 683–700, 1997.
14. H. TOBUSHI, S. YAMADA, T. HACHISUKA, *et al.*, *Thermomechanical properties due to martensitic and R-phase transformations of NiTi shape memory alloy subjected to cyclic loading*, Smart Mater. Struct., **5**, 788, 1996.
15. H. TOBUSHI, T. HACHISUKA, S. YAMADA, P.H. LIN, *Rotating-bending fatigue of a NiTi shape memory alloy wire*, Mech. Mater., **26**, 35–42, 1997.

16. S.P. GADAJ, W.K. NOWACKI, E.A. PIECZYSKA, *Changes of temperature during the simple shear test of stainless steel*, Arch. Mech., **48**, 4, 779–788, 1996.

17. J. KACZMAREK, *A thermodynamical description of the martensitic transformation. A model with small volume of averaging*, Arch. Mech., **50**, 1, 53–81, 1998.

Received March 11, 1999; revised version May 31, 1999.

Arch. Mech., **51**, 6, pp. 665–692, Warszawa 1999

Multiaxial constitutive modelling for R-phase and M-phase transformations of TiNi shape memory alloys

M. KAWAI, H. OGAWA, V. BABURAJ, and T. KOGA

Institute of Engineering Mechanics and Systems,
University of Tsukuba, Tsukuba 305-8573, JAPAN
e-mail: mkawai@kz.tsukuba.ac.jp

A MULTIAXIAL CONSTITUTIVE MODEL for describing the pseudoelastic and shape memory behaviour of a titanium-nickel (TiNi) shape memory alloy due to the stress-induced rhombohedral and martensitic transformations has been developed from a phenomenological point of view. First, the existing constitutive models proposed for shape memory alloys are reviewed in brief. On the basis of a comparison between these models, an expression prescribing the transformation strain range is proposed which depends on the applied stress and the current phase volume fraction. Then, the uniaxial Tanaka model for the rhombohedral and martensitic transformations of TiNi shape memory alloys is extended to a multiaxial form using the framework of the Boyd-Lagoudas model and the proposed expression of the transformation strain range. Finally, the capability of the present model to predict the pseudoelastic behaviour of TiNi shape memory alloys is examined through numerical simulations of stress-strain responses under uniaxial and multiaxial proportional/nonproportional loading-unloading conditions.

1. Introduction

SHAPE MEMORY ALLOY (SMA) BASED SMART STRUCTURES are typically fabricated of composite materials embedding fibres, films or particles of SMAs [1 – 8]. For optimum designs of SMA composite laminae, laminates and structures, it is required to evaluate the fabrication conditions under which the pseudoelasticity (PE) and the shape memory effect (SME) of SMA are reflected and the thermomechanical conditions under which SMA composites appropriately work as intended. To design the performance characteristics, a suitable numerical simulation technique should be developed. To this end, it is prerequisite to establish constitutive models for describing the transformation behaviour of SMA embedded in matrix materials. The local states of stress and strain of the embedded SMA always become multiaxial and the phase transformations are believed to be very sensitive to complex combined states of stress and strain. For advanced designs of SMA smart composites, therefore, it is one of the most significant tasks

to formulate a constitutive model which accurately describes the SME and the nonlinear PE, including the changes in stiffness and energy dissipation property, of SMAs under arbitrary multiaxial thermomechanical loading conditions.

To describe the pseudoelastic and shape memory behaviour of SMA under uniaxial loading conditions, TANAKA *et al.* [9 – 12] developed rate-form constitutive relations from phenomenological points of view. A fundamental version of the Tanaka model is very useful in practice for a description of the martensitic transformation of SMA. It has a relatively simple structure and the material constants involved can be easily identified. For this reason, this model is frequently used in reporting experimental results on the stress-strain behaviour of SMAs [13 – 16]. Tanaka's pioneering works stimulated the subsequent development in the constitutive modelling of the transformation behaviour of SMAs. LIANG and ROGERS applied a finite form of the Tanaka model which was combined with a slightly different expression of the transformation kinetics [17]. An extension of the Tanaka model was also discussed by BRINSON [18]. Other different formulations were presented by MULLER and XU [19], GRAESSER and COZZARELLI [20], IVSHIN and PENCE [21, 22], ABEYARATNE *et al.* [23] and BARRETT [24].

A multiaxial phenomenological modelling of the martensitic transformation behaviour of SMAs was first discussed by LIANG and ROGERS [25]. This model was based on the classical plasticity and the uniaxial Tanaka model, and an isotropic transformation criterion of von Mises type was assumed. A change in the elastic property due to phase transformation was not considered. An improved multiaxial version which accounted for the change in stiffness due to the martensitic transformation was developed by BOYD and LAGOUDAS [26, 27], also using the von Mises equivalent stress and the framework of the Tanaka model. RANIECKI *et al.* [28] and RANIECKI and LEXCELLENT [29] developed three-dimensional pseudoelasticity models which furnished rigorous loading-unloading criteria for the forward and reverse martensitic transformations and a capability to describe the change in elastic modulus due to phase evolution. Validity of these pseudoelasticity models were evaluated by ROGUEDA *et al.* [30] through combined tension-torsion tests. GRAESSER and COZZARELLI [31] also attempted to develop a multiaxial SMA model using a different framework. BRINSON and HUANG [32] made a comparison between Tanaka, Liang-Rogers, Brinson, Ivshin-Pense and Boyd-Lagoudas models. From this comparison, it was elucidated that these SMA models exhibited many similarities, and essential differences appeared in the formulation of the transformation kinetics. Physically-based micromechanical formulations which took into account the crystallographic growth of twin variants and their movements were developed by PATOOR *et al.* [33, 34] and SUN and HWANG [35, 36]. More detailed reviews on the constitutive modelling of the pseudoelastic and shape memory behaviour can be found in the articles given by FISCHER *et al.* [37] and BIRMAN [38].

Experimental results on the multiaxial stress-strain behaviour of SMAs have not been sufficiently reported so far [30, 39, 40]. For this reason, a stress criterion of the multiaxial phase transformation of SMAs is not completely understood, and the transformation kinetics assumed in developing the SMA models is not fully justified. To remove this insufficiency, systematic experiments to elucidate the multiaxial transformation kinetics of SMAs should be programmed. In parallel with experimental efforts, additional investigations will also be required on the theoretical sophistication of existing multiaxial SMA constitutive models as well as new developments from different points of view. Recently, experimental data on the uniaxial stress-strain behaviour of SMAs under tensile and compressive loading conditions are increasingly reported in literature. This has partly eliminated some difficulties in determining the material constants involved by the phenomenological constitutive models. Therefore, we are now able to promote further basic studies for examining the applicability of existing SMA models and for developing multiaxial SMA constitutive models, irrespective of a limited amount of information on the transformation behaviour of SMAs under general thermomechanical loading conditions.

A titanium-nickel (TiNi) shape memory alloy is a promising candidate for practical applications, since its characteristic performance is presently superior to other existing SMAs [41]. It is a characteristic of TiNi SMA that the rhombohedral (R-phase) transformation occurs in a particular temperature range before the martensitic (M-phase) transformation starts, which depends on the heat treatment [42]. Since the R-phase transformation takes place at a lower stress, the pseudoelastic and shape memory behaviour due to the R-phase transformation are more stable under repeated application. The consecutive R-phase and M-phase transformations are believed to have a significant influence on the stress-strain curves for TiNi SMA. To design TiNi-SMA fibre (or particle) embedded composites and to evaluate their performance characteristics under arbitrary thermomechanical loading conditions, a multiaxial SMA constitutive model for describing the R-phase and M-phase transformations of TiNi SMAs is required. However, a three-dimensional modelling of the R-phase and M-phase transformations occurring in TiNi SMAs has not been discussed so far, and effects of the R-phase transformation on the multiaxial behaviour of SMA have not been studied through numerical simulations.

The objective of the present study is to develop a multiaxial constitutive model for describing the stress-induced R-phase and M-phase transformations in TiNi SMA from a phenomenological point of view. First, the uniaxial TANAKA model [11] and the multiaxial BOYD and LAGOUDAS model [26] are briefly discussed. On the basis of a comparison between these models, an expression of the transformation strain range is proposed. Then, the uniaxial Tanaka model for the R-phase and M-phase transformations of TiNi SMAs is extended into a

multiaxial form by applying the framework of the Boyd-Lagoudas model together with the proposed expression of the transformation strain range. To examine the capability of the present model for TiNi SMAs, the stress-induced phase transformation behaviour is numerically simulated for various uniaxial and multiaxial proportional/nonproportional loading-unloading conditions.

2. Phenomenological SMA constitutive models

2.1. Uniaxial Tanaka model for M-phase transformation

The basic rate equation of the uniaxial Tanaka model for the M-phase transformation [9 – 12] is expressed as

$$\dot{\sigma} = D\dot{\varepsilon} + \Theta\dot{T} + \Omega\dot{\xi}, \tag{2.1}$$

where σ, ε and T denote the uniaxial stress, the infinitesimal total strain and the absolute temperature, and ξ is the volume fraction of M-phase. The coefficients D, Θ and Ω are material constants that represent the average Young's modulus, the thermal expansion coefficient and the modulus for the M-phase transformation. The dot $(\cdot)$ above the symbols represents the time rate.

The rate of the transformation strain $\varepsilon^{\mathrm{tr}}$ is described as

$$\dot{\varepsilon}^{\mathrm{tr}} = -\frac{\Omega}{D}\dot{\xi}, \tag{2.2}$$

where the coefficient $-\Omega/D$ is equivalent to the maximum transformation strain (when $\xi = 1$) caused by the stress-induced M-phase transformation.

The volume fraction ξ is a single internal variable which characterizes the M-phase transformation. The evolution equation of ξ is specified separately for the forward and reverse transformations, and it is described using the exponential form of MAGEE type [43]. LIANG and ROGERS [17] have integrated Eq. (2.1) and applied it to the analyses of smart structures.

2.2. Uniaxial Tanaka model for R-phase and M-phase transformations

In TiNi SMAs, the R-phase transformation occurs before the M-phase transformation starts in a particular range of temperature [41]. To describe the thermomechanical behaviour of TiNi SMAs due to these two kinds of consecutive phase transformations, LIN *et al.* [13] extended the Tanaka model, Eq. (2.1), to the following form:

$$\dot{\sigma} = D\dot{\varepsilon} + \Theta\dot{T} + K\dot{z}, \tag{2.3}$$

where z represents the volume fractions η and ξ of R-phase and M-phase, respectively. Hence, the last term on the right-hand side of Eq. (2.3) is interpreted as

$$K\dot{z} = \begin{cases} \Psi\dot{\eta} & (\mathrm{R}-\mathrm{phase}) \\ \Omega\dot{\xi} & (\mathrm{M}-\mathrm{phase}) \end{cases}. \tag{2.4}$$

2.3. Multiaxial Boyd-Lagoudas model for M-phase transformation

The multiaxial SMA model proposed by BOYD and LAGOUDAS [26, 27] takes into account the changes in stiffness and thermal expansion coefficient during the martensitic phase transformation, and it considers the volumetric elastic strain. In this model, the rate of the deviatoric transformation strain $\dot{\varepsilon}_{ij}^{\mathrm{tr}}$ is expressed as

$$\dot{\varepsilon}_{ij}^{\mathrm{tr}} = \Lambda_{ij}\dot{\xi}, \tag{2.5}$$

where ξ is the volume fraction of M-phase, and Λ_{ij} represents the transformation tensor given by

$$\Lambda_{ij} = \begin{cases} \mathrm{HN}_{ij}^{\sigma}, & \dot{\xi} > 0, \\ \mathrm{HN}_{ij}^{\varepsilon}, & \dot{\xi} < 0 \end{cases}. \tag{2.6}$$

The flow directions N_{ij}^{σ} and N_{ij}^{ε} are specified as

$$N_{ij}^{\sigma} = \frac{3}{2}\frac{s_{ij}}{\sigma_e}, \tag{2.7}$$

$$N_{ij}^{\varepsilon} = \frac{\varepsilon_{ij}^{\mathrm{tr}}}{\varepsilon_e^{\mathrm{tr}}}, \tag{2.8}$$

for the forward and reverse transformations, respectively.

It is seen that the transformation flow takes place in the direction of the stress deviator during the forward transformation, and in the direction of the origin of the transformation strain during the reverse transformation. The coefficient H in Eq. (2.6) represents the maximum transformation strain attained when $\xi = 1$; $H = \varepsilon_{\max}^{\mathrm{tr}}$ under uniaxial tension.

The infinitesimal total strain ε_{ij} is given by the sum of the elastic, thermoelastic and phase transformation strains:

$$\varepsilon_{ij} = \varepsilon_{ij}^{e} + \varepsilon_{ij}^{T} + \varepsilon_{ij}^{\mathrm{tr}}, \tag{2.9}$$

where ε_{ij}^{e} and ε_{ij}^{T} denote the elastic and thermal expansion strain tensors. Using the Hooke's law, the constitutive relationship can be written as

$$\dot{\sigma}_{ij} = \overline{C_{ijkl}\varepsilon_{kl}^{e}} = C_{ijkl}\dot{\varepsilon}_{kl}^{e} + \dot{C}_{ijkl}\varepsilon_{kl}^{e}. \tag{2.10}$$

To take into account the changes in the elastic tensor C_{ijkl} and the thermal expansion tensor α_{ij} of SMAs due to phase transformation, the rule of mixture is assumed:

$$C_{ijkl} = C^{\mathrm{A}}_{ijkl} + \xi \left(C^{\mathrm{M}}_{ijkl} - C^{\mathrm{A}}_{ijkl} \right), \tag{2.11}$$

$$\alpha_{ij} = \alpha^{\mathrm{A}}_{ij} + \xi \left(\alpha^{\mathrm{M}}_{ij} - \alpha^{\mathrm{A}}_{ij} \right), \tag{2.12}$$

where the superscripts A and M indicate the austenite and martensite, respectively.

Then, the constitutive relationship for the M-phase transformation is expressed as

$$\dot{\sigma}_{ij} = C_{ijkl} \left(\dot{\varepsilon}_{kl} - \alpha_{kl} \dot{T} \right) + Q_{ij} \dot{\xi}, \tag{2.13}$$

where

$$Q_{ij} = \left(C^{\mathrm{M}}_{ijkl} - C^{\mathrm{A}}_{ijkl} \right) \varepsilon^{e}_{kl} - C_{ijkl} \left(\alpha^{\mathrm{M}}_{kl} - \alpha^{\mathrm{A}}_{kl} \right) \Delta T - C_{ijkl} \Lambda_{kl}. \tag{2.14}$$

In Eq. (2.14), $\Delta T = T - T_0$ and T_0 is a reference temperature.

3. Transformation strain range

A description of the transformation strain range is an important part of modelling of the thermomechanical behaviour of SMAs. By comparing the Tanaka model and the Boyd-Lagoudas one for the M-phase transformation, we find the following correspondence:

$$C^{-1}_{11kl} Q_{kl} \leftrightarrow \frac{\Omega}{D}. \tag{3.1}$$

To examine this correspondence in more detail, we can use the following relationship:

$$C^{-1}_{ijkl} Q_{kl} = \frac{\kappa^{\mathrm{M}} - \kappa^{\mathrm{A}}}{9 \left[\kappa(\xi) \right]^2} \sigma_m \delta_{ij} + \frac{\mu^{\mathrm{M}} - \mu^{\mathrm{A}}}{2 \left[\mu(\xi) \right]^2} s_{ij} - \left(\alpha^{\mathrm{M}}_{ij} - \alpha^{\mathrm{A}}_{ij} \right) \Delta T - \Lambda_{ij}, \tag{3.2}$$

where σ_m and δ_{ij} are the mean stress $\sigma_{aa}/3$ and the Kronecker delta, respectively, and $\kappa(\xi)$ and $\mu(\xi)$ represent the bulk and shear moduli described as

$$\kappa(\xi) = (1 - \xi) \kappa^{\mathrm{A}} + \xi \kappa^{\mathrm{M}}, \tag{3.3}$$

$$\mu(\xi) = (1 - \xi) \mu^{\mathrm{A}} + \xi \mu^{\mathrm{M}}, \tag{3.4}$$

for the mixture of A-phase and M-phase.

Using this general relationship for isotropic SMAs, we can describe the coefficient $H (= \Lambda_{11})$ involved by the Boyd-Lagoudas model as follows:

$$H = -\frac{\Omega}{D} + \left[\frac{\kappa^{\mathrm{M}} - \kappa^{\mathrm{A}}}{9 \left[\kappa(\xi) \right]^2} + \frac{\mu^{\mathrm{M}} - \mu^{\mathrm{A}}}{3 \left[\mu(\xi) \right]^2} \right] \sigma - \left(\alpha^{\mathrm{M}} - \alpha^{\mathrm{A}} \right) \Delta T. \tag{3.5}$$

The second and third terms on the right-hand side of Eq. (3.5) compensate for the constant stiffness and thermal expansion assumed in the uniaxial Tanaka model [9]. Experimental results for the uniaxial stress-strain behaviour of SMAs are often reported in terms of the coefficients Ω and D included by the uniaxial Tanaka model, e.g., [13]. To utilize the supplied information on the transformation strain range characterized by these coefficients in the calculations using the Boyd-Lagoudas model, the relationship given by Eq. (3.5) should be considered. In view of this requirement, the transformation strain range is newly defined as follows:

$$H^* = -\frac{\Omega^*}{E(\xi)} + \frac{E^{\mathrm{M}} - E^{\mathrm{A}}}{[E(\xi)]^2}\sigma_e - \left(\alpha^{\mathrm{M}} - \alpha^{\mathrm{A}}\right)\Delta T, \tag{3.6}$$

where a scalar quantity Ω^* is a history-dependent material parameter in general, and

$$E(\xi) = E^{\mathrm{A}} + \xi(E^{\mathrm{M}} - E^{\mathrm{A}}). \tag{3.7}$$

Note that $H^* = -\Omega/D$ when $E^{\mathrm{M}} = E^{\mathrm{A}} = D$, $\nu^{\mathrm{M}} = \nu^{\mathrm{A}}$, $\alpha^{\mathrm{M}} = \alpha^{\mathrm{A}}$ and $\Omega^* = \Omega$.

4. A description of multiaxial R-phase and M-phase transformation behaviour

A simple multiaxial SMA model for describing the R-phase and M-phase transformation behaviour of TiNi SMAs is developed on the basis of the uniaxial Tanaka model [9] and the multiaxial Boyd-Lagoudas model [26, 27]. In the following description, the superscripts (x, y) represent the pairs of (A, R), (R, M) or (A, M): A, austenitic phase; R, rhombohedral phase; M, martensitic phase. The changes in the elastic and thermoelastic properties due to the R-phase and M-phase transformations are considered through the rule of mixture, i.e.,

$$C_{ijkl}^{x\to y} = C_{ijkl}^{x} + z(C_{ijkl}^{y} - C_{ijkl}^{x}), \tag{4.1}$$

$$\alpha_{ij}^{x\to y} = \alpha_{ij}^{x} + z(\alpha_{ij}^{y} - \alpha_{ij}^{x}, \tag{4.2}$$

where the volume fraction of y-phase is expressed by a scalar variable z; $z = \eta$ for the R-phase transformation and $z = \xi$ for the M-phase transformation.

4.1. Transformation strain rate

The rate of the deviatoric transformation strain $\varepsilon_{ij}^{\mathrm{tr}(x\to y)}$ during the transformation from x-phase to y-phase is described by

$$\dot{\varepsilon}_{ij}^{\mathrm{tr}(x\to y)} = \Lambda_{ij}^{x\to y}\dot{z}, \tag{4.3}$$

where the flow direction is characterized by the transformation tensor $\Lambda_{ij}^{x\to y}$ given by

$$\Lambda_{ij}^{x\to y} = \begin{cases} H^{*(x\to y)} N_{ij}^{\sigma}, & \dot{z} > 0, \\ H^{*(x\to y)} N_{ij}^{\varepsilon}, & \dot{z} < 0. \end{cases} \tag{4.4}$$

The coefficient $H^{*(x\to y)}$, which controls the magnitude of the transformation strain, is assumed to be

$$H^{*(x\to y)} = -\frac{\Gamma^{*(x\to y)}}{E^{x\to y}(z)} + \frac{E^y - E^x}{[E^{x\to y}(z)]^2}\sigma_e - (\alpha^y - \alpha^x)\Delta T, \tag{4.5}$$

where

$$\Gamma^{*(x\to y)} = \begin{cases} \Psi^*, & z = \eta, \\ \Omega^*, & z = \xi, \end{cases} \tag{4.6}$$

$$E^{x\to y}(z) = E^x + z(E^y - E^x). \tag{4.7}$$

In general, $\Gamma^{*(x\to y)}$ is a material function which depends on temperature and other internal variables. A simple temperature dependence is assumed in the simulations presented later. The basic constitutive relationship for TiNi SMAs is finally obtained as

$$\dot{\sigma}_{ij} = C_{ijkl}^{x\to y}(\dot{\varepsilon}_{kl} - \alpha_{kl}^{x\to y}\dot{T}) + Q_{ij}^{x\to y}\dot{z}, \tag{4.8}$$

where

$$Q_{ij}^{x\to y} = \left(C_{ijkl}^{y} - C_{ijkl}^{x}\right)\varepsilon_{kl}^{e} - C_{ijkl}^{x\to y}(\alpha_{kl}^{y} - \alpha_{kl}^{x})\Delta T - C_{ijkl}^{x\to y}\Lambda_{kl}^{x\to y}. \tag{4.9}$$

4.2. Transformation criteria

The transformation kinetics for TiNi SMAs was identified by LIN *et al.* [13] through uniaxial tensile tests using wire specimens. The uniaxial evolution equations determined for the volume fractions η and ξ of R-phase and M-phase can be written in a compact form using the representative volume fraction z as follows:

$$\dot{z} = (-1)^{\ell^{x\to y}} z^{m^{x\to y}} (1-z)^{n^{x\to y}} b^{x\to y}(c^{x\to y}\dot{T} - \dot{\sigma}). \tag{4.10}$$

The coefficients involved in this equation take different values for the forward and reverse transformations, and they are classified in Table 1 for the R-phase and M-phase transformations, respectively.

Table 1. Coefficients involved in the evolution equations of phase volume fractions.

$x \to y$	z	$\ell^{x\to y}$	$m^{x\to y}$	$n^{x\to y}$	$b^{x\to y}$	$c^{x\to y}$
A→R	η	2	0	0	$b_{\mathrm{M}}^{\mathrm{R}}\dagger$	$c_{\mathrm{M}}^{\mathrm{R}}$
R→A	η	1	0	0	$b_{\mathrm{A}}^{\mathrm{R}}$	$c_{\mathrm{A}}^{\mathrm{R}}$
A→ M (R→M)	ξ	2	0	1	b_{M}	c_{M}
M→ A	ξ	1	1	0	b_{A}	c_{A}

$\dagger b_{\mathrm{M}}^{\mathrm{R}} = b_{\mathrm{M1}}^{\mathrm{R}}(T \le M_{\mathrm{S}}^{\mathrm{R}});\ b_{\mathrm{M}}^{\mathrm{R}} = b_{\mathrm{M2}}^{\mathrm{R}}(T > M_{\mathrm{S}}^{\mathrm{R}})$

The evolution equation for the phase volume fraction is assumed to be rate-independent. The rate-independent formulation of the transformation kinetics for TiNi SMA was verified by WU *et al.* [44]. They elucidated that the effect of the loading rate on the stress-strain relationships for SMAs were caused by the temperature variation due to the latent heat. Suppressing the change in temperature, the stress-strain behaviour observed for different strain rates almost agreed with each other. This reveals that the transformation mechanisms of SMAs are essentially rate-independent.

The uniaxial transformation start and finish conditions for TiNi SMA were also determined by LIN *et al.* [13]. Under uniaxial tensile loading conditions, the transformation start and finish stresses of R-phase at a low temperature are almost constant, while at a higher temperature they increase in proportion to temperature. Therefore, the transformation lines (TL) on the stress-temperature plane which characterize the transformation start/finish conditions of R-phase were described using two-segment parallel broken lines. Namely, the transformation line (TL) for the R-phase transformation on the stress-temperature plane is composed of two intersecting straight lines: a horizontal line (TL_1) and another line (TL_2) extending in the right upper direction. For the R-phase transformation, it should be noticed that the temperatures at the intersections of the segment lines do not coincide with the stress-free transformation start/finish temperatures. For the M-phase transformation, on the other hand, the relationships between the transformation start/finish stresses and temperature can be described by straight lines. Similar to Eq. (4.10), the relationships between the transformation start/finish stresses and temperature can be written as

$$\sigma^{Y} = d^{x\to y}(T - T^{x\to y}) - \sigma^{(0)}, \tag{4.11}$$

where the superscript Y represents the label of start or finish. The coefficients involved depend on the transformation conditions, and they are classified as

shown in Table 2. In Table 2, the forward and reverse transformation lines are symbolically expressed by TL(M^R) and TL(A^R) for the R-phase transformation and by TL(M) and TL(A) for the M-phase transformation, respectively.

Table 2. Transformation start and finish streses.

$x \to y$	TL	Y	z	$d^{x\to y}$	$T^{x\to y}$	$\sigma^{(0)}$
A→R	$TL_1(M^R)$	start	η	0	–	$-\sigma^R_{MO}$
		finish		0	–	$-\sigma^R_{MO} + 1/b^R_{M1}$
	$TL_2(M^R)$	start		c^R_M	M^R_S	0
		finish		c^R_M	M^R_S	$1/b^R_{M2}$
R→A	$TL_1(A^R)$	start		0	–	$-\sigma^R_{AO}$
		finish		0	–	$-\sigma^R_{AO} + 1/b^R_A$
	$TL_2(A^R)$	start		c^R_A	A^R_S	0
		finish		c^R_A	A^R_S	$1/b^R_A$
A→ M	TL(M)	start	ξ	c_M	M_S	0
		finish		c_M	M_S	$2\ln(10)/b_M$
M→ A	TL(A)	start		c_A	A_S	0
		finish		c_A	A_S	$2\ln(10/b_A$

For analyses of the transformation behaviour of TiNi SMA in the present study, simple multiaxial extensions of the uniaxial evolution equation for the phase volume fraction and of the transformation start and finish stresses are assumed; viz., the uniaxial stress and stress rate are replaced with the von Mises equivalent stress and its time rate, respectively.

4.3. Limitations

For the TiNi SMA examined by LIN *et al.* [13], the uniaxial transformation finish stresses of R-phase and M-phase are negative in the temperature range where the shape memory effect is observed. Thus, the multiaxial transformation kinetics of J_2 type discussed in the present study can be used only for analyses of the pseudoelastic behaviour. Moreover, the J_2-type extension excludes consideration for the tension-compression asymmetry of the pseudoelastic behaviour [45, 46], the volumetric change due to phase transformation [47], the pressure dependence of the transformation kinetics [48 – 50] and the rubber-like behaviour due to reorientation [51].

The pseudoelastic transformation of TiNi SMA is incrementally evaluated by integrating the rate evolution equation of the phase volume fraction: Eq. (4.10). For given rates (or increments) of stress and temperature, the current sign of the rate of volume fraction and the current stress and temperature on the phase transformation diagram characterized by the transformation start and finish lines enable us to evaluate numerically what kind of phase transformation follows. Using the incremental calculations based on the stress-temperature diagram, it is possible to know if the next incremental step corresponds to the transformation loading or unloading. For a neutral thermomechanical loading along the phase transformation line, no phase transformation proceeds in the present modelling. The validity of this assumption should be examined in future studies. It is also an interesting subject to model the consecutive R-phase and M-phase transformations of TiNi SMA on the basis of more sophisticated multiaxial criteria for the transformation loading-unloading and descriptions of the transformation potential surfaces [28 – 29].

5. Numerical simulations

5.1. Material constants

The material constants to characterize the R-phase and M-phase transformation kinetics for TiNi SMAs are listed in Table 3 and Table 4. These data were taken from the experimental study performed by LIN *et al.* [13]. Since the elastic moduli of the monolithic R-phase and M-phase were not found in literature, they were assumed as listed in Table 5.

Table 3. Material constants for the R-phase transformation of TiNi.

b^{R}_{M1} MPa^{-1}	b^{R}_{M2} MPa^{-1}	c^{R}_{M} $MPaK^{-1}$	b^{R}_{A} $MPaK^{-1}$	c^{R}_{A} $MPaK^{-1}$	M^{R}_{S} K	A^{R}_{S} K	σ^{R}_{M0} MPa	σ^{R}_{A0} MPa
−0.094	−0.028	15.2	0.025	17.4	317.0	318.0	25	5

Table 4. Material constants for the M-phase transformation of TiNi.

b^{M} MPa^{-1}	c^{M} $MPaK^{-1}$	b^{A} MPa^{-1}	c^{A} $MPaK^{-1}$	M_S K	A_S K
−0.132	6.125	0.132	8.8	272.5	318

Table 5. Mechanical properties of TiNi.

α^{M} K^{-1}	α^{R} K^{-1}	α^{A} K^{-1}	ν	E^{A} MPa	E^{M} MPa	E^{R} MPa
6.6E-06	6.6E-06	11.0E-06	0.33	80.0E+03	30.0E+03	80.0E+03

The parameter $\Gamma^{*(x\to y)}$ controlling the transformation strain range was assumed to be a function of only temperature in the range (300 $\sim$ 360 K) examined by LIN *et al.* [13]. On the basis of the stress-strain relationships for TiNi SMAs [13], the material function was determined as

$$\Psi^* = 6.49T - 2286, \tag{5.1}$$

for the R-phase transformation, and

$$\Omega^* = -6.0T - 700, \tag{5.2}$$

for the M-phase transformation. The unit of Ψ^* and Ω^* is MPa/K.

5.2. Results of uniaxial simulations

First of all, we have performed the numerical simulations which correspond to the experimental results reported by LIN *et al.* [13].

Figure 1(a) shows the predicted stress-strain behaviour of TiNi SMAs at 303 K for a single loading-unloading cycle in tension ($\sigma_{\max}$ = 200 MPa). We can clearly observe two phenomena: 1) at 303 K both the R-phase and M-phase transformations occur, and 2) the strain is not entirely recovered by complete unloading. Fig. 1(b) shows the similar result at 303 K when loaded up to a larger stress $\sigma_{\max}$ = 700 MPa. In this case, the initial loading was given until the M-phase transformation was completely finished. It is important to read from the first observation that the R-phase transformation varies the appearance of the overall stress-strain behaviour. The second phenomenon indicates that the shape memory effect appears at 303 K and the residual strain is recovered by heating.

Figures 2(a) through 2(c) show the predicted stress-strain curves at 333 K for loading up to different maximum tensile stresses ($\sigma_{\max}$ = 370, 372 and 700 MPa). The total strain completely recovers with unloading, irrespective of the value of the prior maximum tensile stress. Hence, the TiNi SMA at 333 K exhibits the pseudoelastic behaviour. More detailed observations are made as follows. A small pseudoelastic hysteresis loop shown in Fig. 2(a) is caused by the R-phase transformation. In Fig. 2(b), we can see that the R-phase and M-phase transformations take place. Note that the TiNi SMA is unloaded before the M-phase transformation is completely finished. During unloading, therefore, the residual R-phase first transforms back to A-phase, and then the M-phase induced by the prior loading changes to A-phase. In the numerical simulation shown in Fig. 2(c), the M-phase transformation is completed during the prior tensile loading. Thus, the subsequent unloading behaviour is characterized by the elastic unloading and the reverse transformation of M-phase.

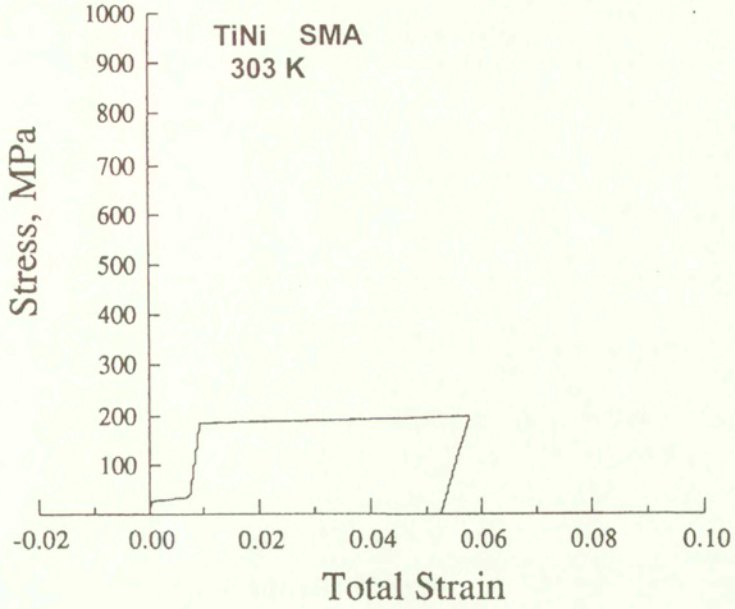

(a) $\sigma_{max} = 200$ MPa

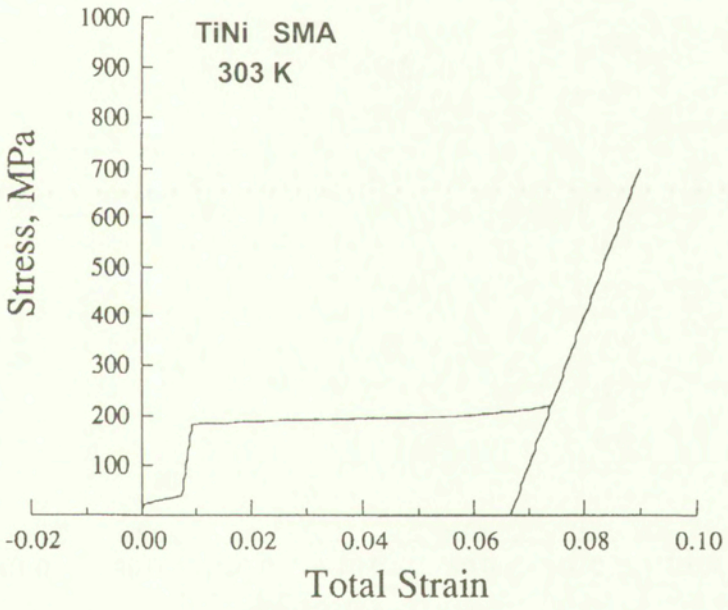

(b) $\sigma_{max} = 700$ MPa

FIG. 1. Predicted uniaxial stress-strain curve for TiNi-SMA at 303 K. (a) $\sigma_{max} = 200$ MPa; (b) $\sigma_{max} = 700$ MPa.

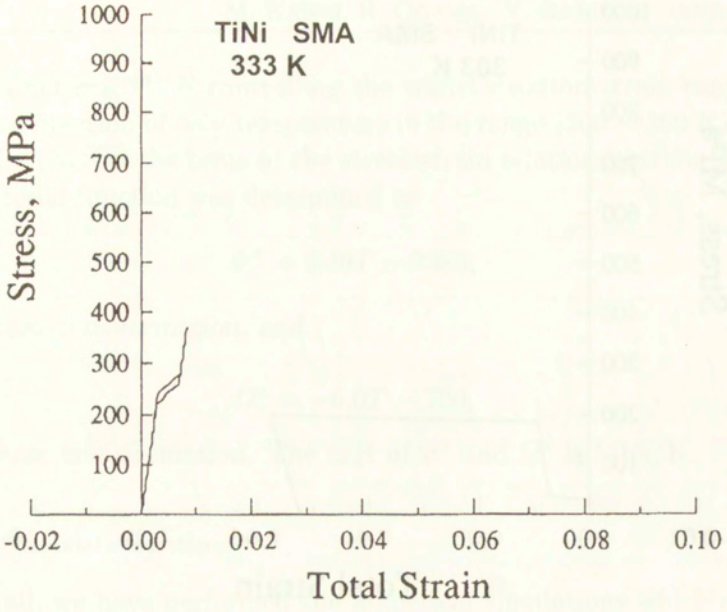

(a) $\sigma_{max} = 370$ MPa

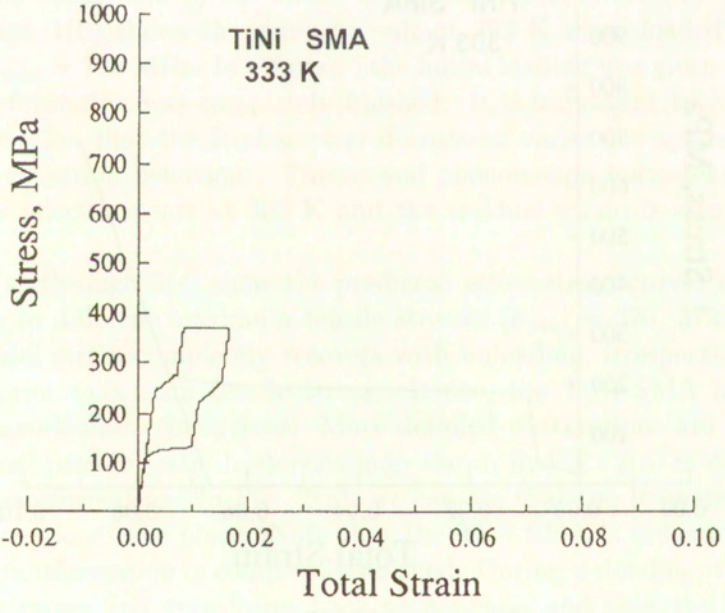

(b) $\sigma_{max} = 372$ MPa

[FIG. 2(a),(b)]

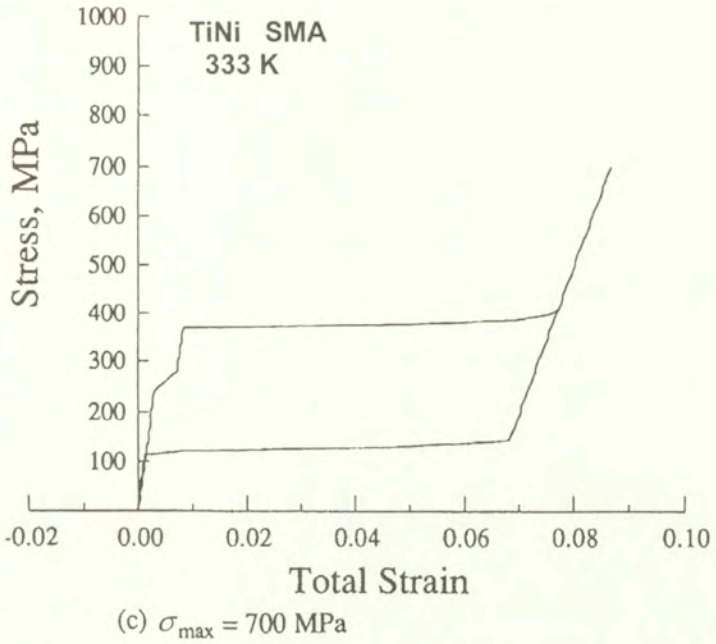

FIG. 2. Predicted uniaxial stress-strain curve for TiNi-SMA at 333 K. (a) σ_{max} = 370 MPa; (b) σ_{max} = 372 MPa; (c) σ_{max} = 700 MPa.

Figures 3(a) through 3(c) show the predicted stress-strain relationships for loading-unloading cycles at 353 K (σ_{max} = 495, 500 and 700 MPa). Also at 353 K, the transformation strain completely recovers with unloading. Hence, the predicted behaviour is pseudoelastic. Unlike the previous simulations shown in Figs. 2(a) through 2(c), the R-phase transformation does not appear at 353 K and the pseudoelastic behaviour is caused only by the M-phase transformation.

The predictions using the present constitutive model obviously differ from those using the SMA models which describe only the M-phase transformation. Namely, as observed in Figs. 1 and 2, the stress-strain behaviour of TiNi SMAs is significantly influenced by the R-phase transformation. To evaluate the PE and SME of TiNi SMAs in such a low stress regime, a capability to predict the R-phase transformation is required in the SMA model assumed. This partly proves the significance of the proposed constitutive model for TiNi SMA.

The SMA constitutive model used for these simulations takes into account the change in stiffness due to phase transformation. Therefore, the slopes of the stress-strain relationships during elastic unloading vary depending on the extent of the forward transformation. For example, a difference between the Young's moduli of A-phase and M-phase can be observed in Fig. 3(c). In the Tanaka model, a constant average stiffness is assumed for the whole process of the phase transformation, and the effect of stiffness change caused by the phase transfor-

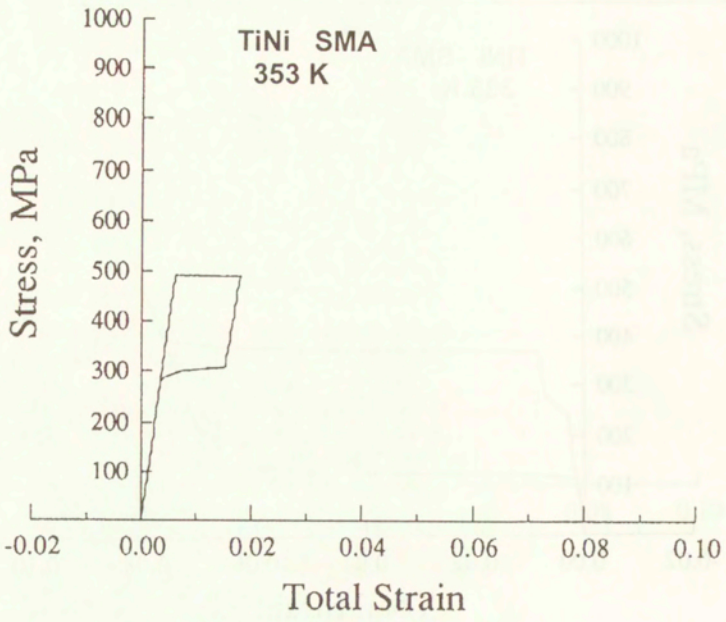

(a) $\sigma_{max} = 495$ MPa

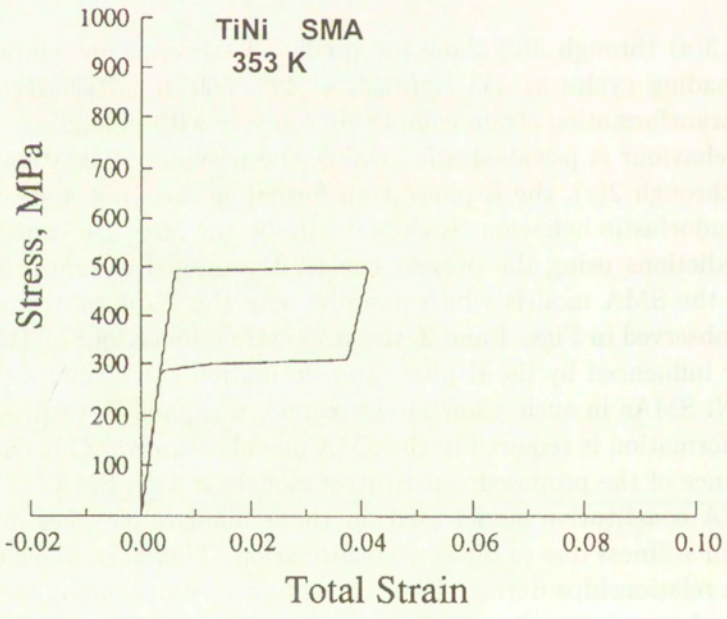

(b) $\sigma_{max} = 500$ MPa

[FIG. 3(a), (b)]

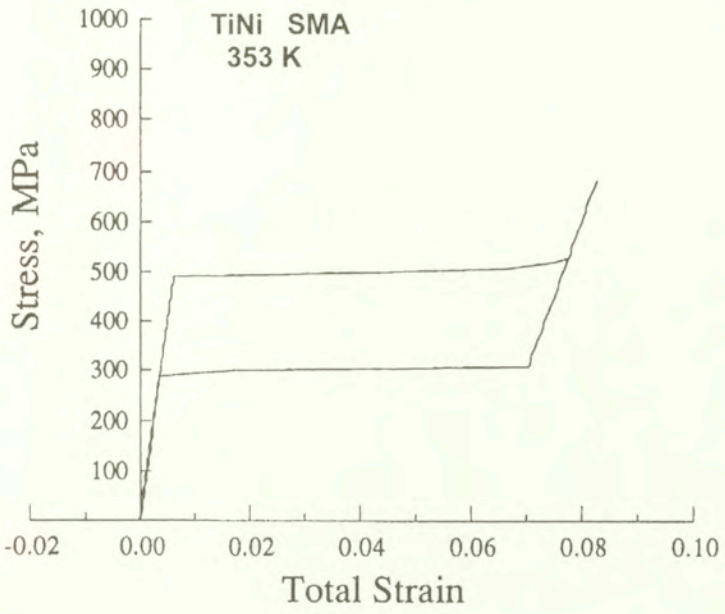

FIG. 3. Predicted uniaxial stress-strain curve for TiNi-SMA at 353 K. (a) σ_{max} = 495 MPa; (b) σ_{max} = 500 MPa; (c) σ_{max} = 700 MPa.

mation is not described. However, the uniaxial simulations presented above do not differ much from those predicted by using the uniaxial Tanaka model. This means that these simulation results are in good agreement with the experimental results reported by LIN *et al.* [13]. As far as the present simple loading conditions are concerned, therefore, a consideration of the transformation-induced stiffness change does not drastically alter the appearance of the pseudoelastic stress-strain behaviour.

5.3. Results of multiaxial simulations

To observe the multiaxial transformation behaviour of TiNi SMAs predicted by the present SMA model, the pseudoelastic behaviour under combined tension and torsion and biaxial tension was simulated at a constant temperature of 333 K.

Figures 4 and 5 show the predicted axial and torsional stress-strain curves for multiaxial proportional loading-unloading cycles under combined tension and torsion. On the plane $(\sigma_{11}, \sqrt{3}\sigma_{12})$, the stress is applied along the line paths with slopes of $\theta = \text{arctg}(\sqrt{3}\sigma_{12}/\sigma_{11}) = 30°$ and 45°, respectively. Since the present SMA model assumes the transformation plasticity based on the von Mises equivalent stress, the tensile and torsional phase transformations simultaneously

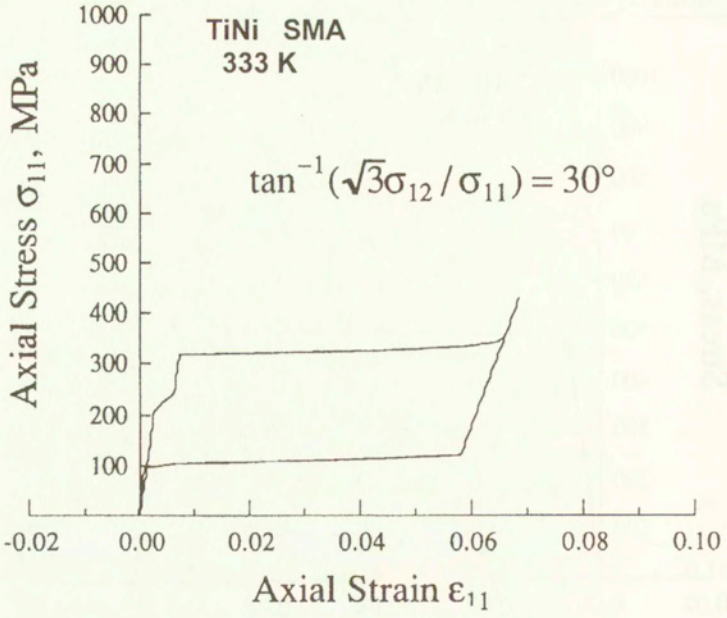

(a) Axial stress-strain curve

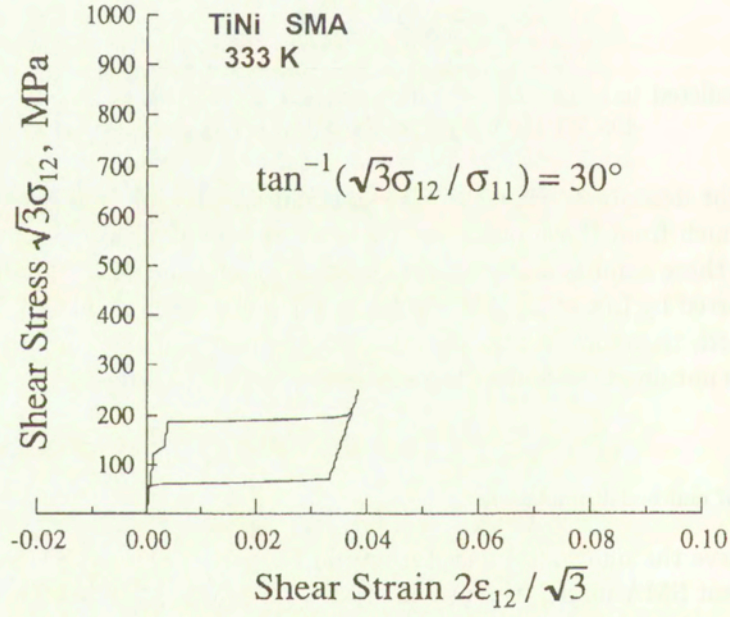

(b) Torsional stress-strain curve

FIG. 4. Predicted stress-strain curves for TiNi-SMA at 333 K under tension-torsion proportional loading (arc $\mathrm{tg}(\sqrt{3}\sigma_{12}/\sigma_{11}) = 30°$). (a) Axial stress-strain curve; (b) Torsional stress-strain curve.

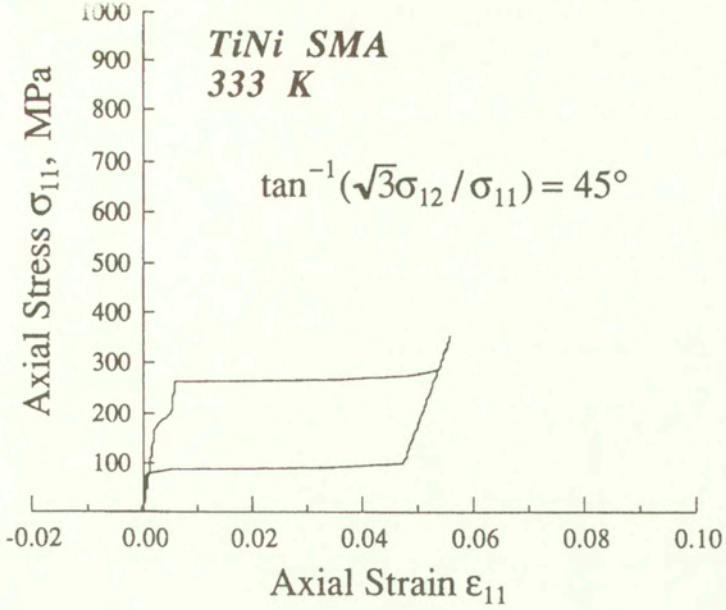

(a) Axial stress-strain curve

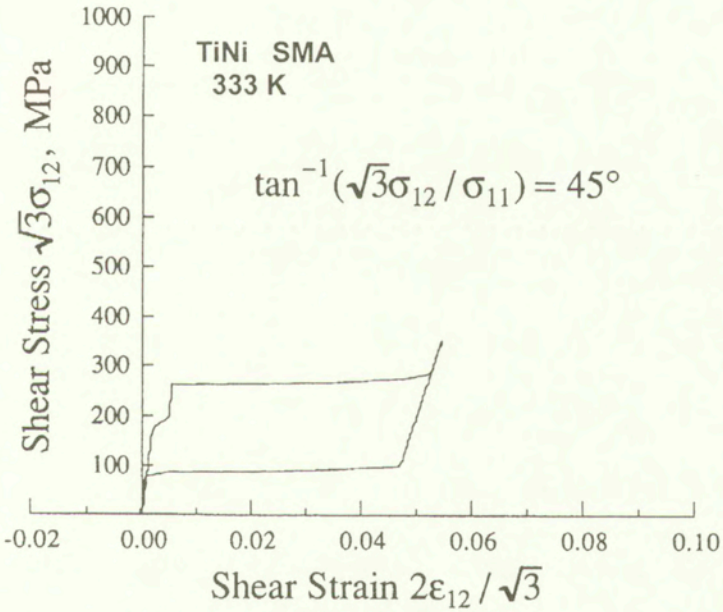

(b) Torsional stress-strain curve

FIG. 5. Predicted stress-strain curves for TiNi-SMA at 333 K under tension-torsion proportional loading (arc $\mathrm{tg}(\sqrt{3}\sigma_{12}/\sigma_{11}) = 45°$). (a) Axial stress-strain curve; (b) Torsional stress-strain curve.

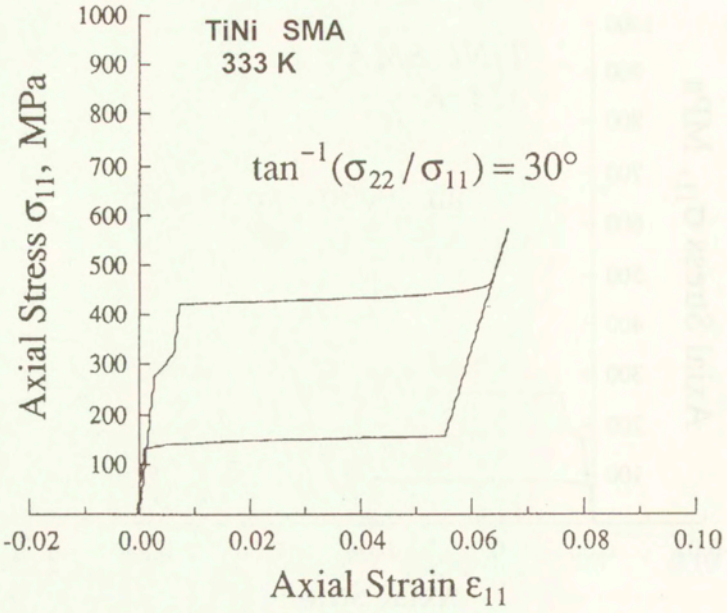

(a) σ_{11} v.s. ε_{11}

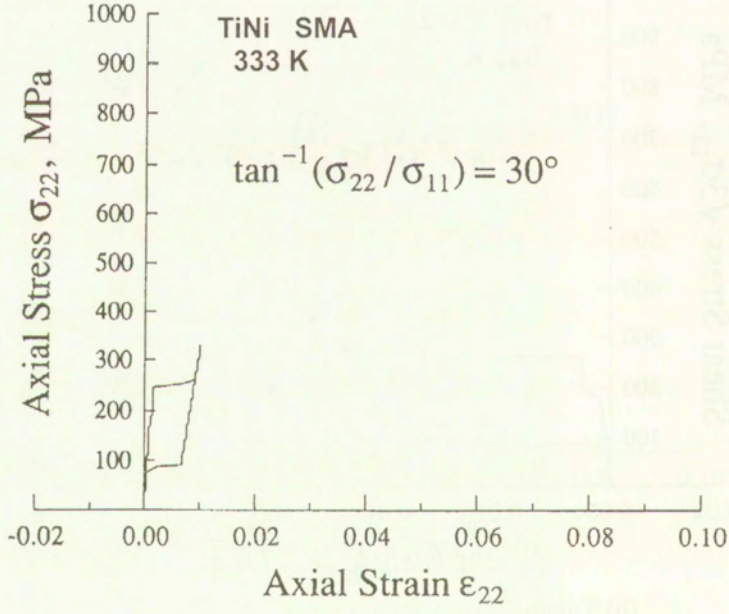

(b) σ_{22} v s. ε_{22}

FIG. 6. Predicted stress-strain curves for TiNi-SMA at 333 K under biaxial proportional loading (arc $\mathrm{tg}(\sigma_{22}/\sigma_{11}) = 30°$). (a) σ_{11} vs. ε_{11}; (b) σ_{22} vs. ε_{22}.

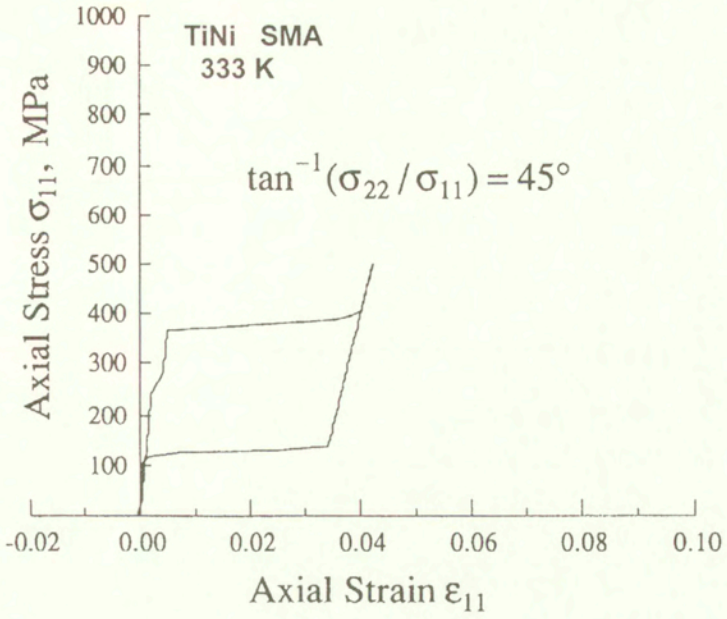

(a) σ_{11} v.s. ε_{11}

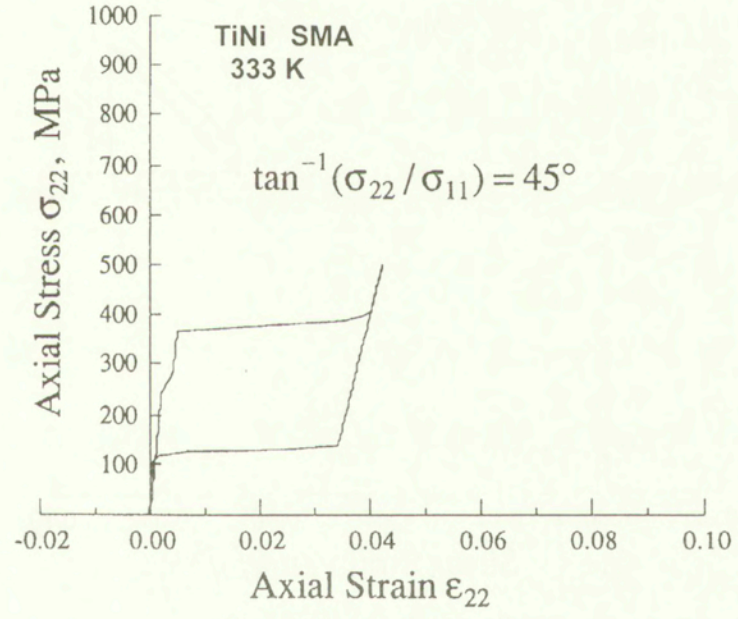

(b) σ_{22} v s. ε_{22}

FIG. 7. Predicted stress-strain curves for TiNi-SMA at 333 K under biaxial proportional loading (arc $\mathrm{tg}(\sigma_{22}/\sigma_{11}) = 45°$). (a) σ_{11} vs. ε_{11}; (b) σ_{22} vs. ε_{22}.

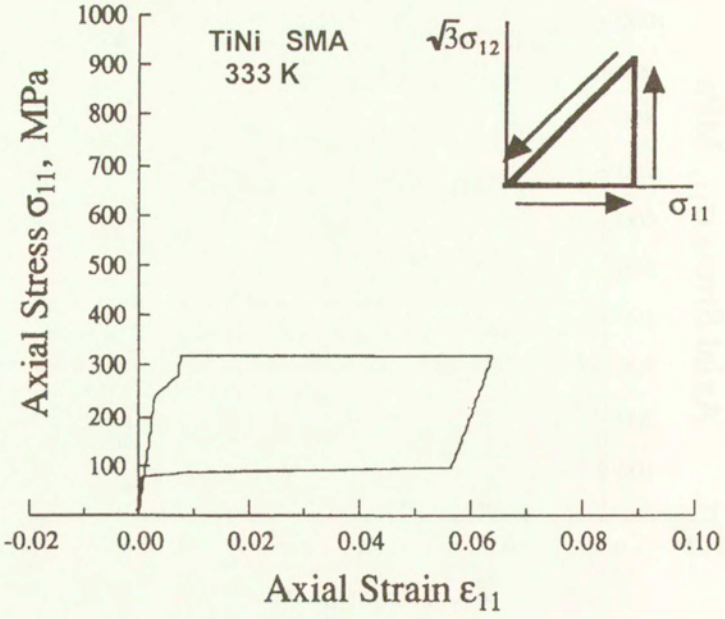

(a) Axial stress-strain curve

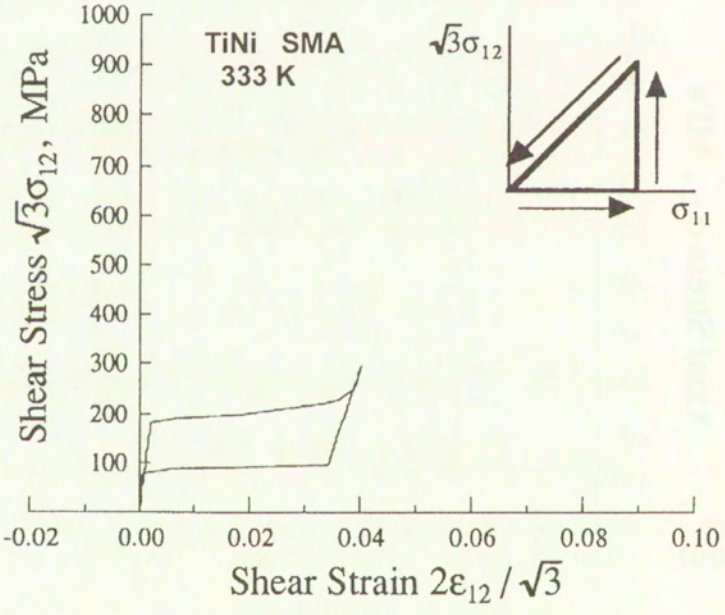

(b) Torsional stress-strain curve

FIG. 8. Predicted stress-strain curves for TiNi-SMA at 333 K under tension-torsion nonproportional loading; (a) Axial stress-strain curve; (b) Torsional stress-strain curve.

continue, once the transformation condition is satisfied. It is important to note that the transformation strain ranges in the component stress-strain relationships differ, depending on the magnitude of the component stresses. Namely, an identical stress-strain curve is predicted in tensile and torsional directions for the case of $\theta = 45°$, while for $\theta = 30°$ the stress-strain curve and the maximum transformation strain in the torsion component become smaller than those in the tensile component.

Figures 6 and 7 present the predicted stress-strain behaviour under biaxial tension for $\theta = \text{arctg}(\sigma_{22}/\sigma_{11}) = 30°$ and 45°, respectively. These results are similar to those for combined tension and torsion.

The SMA behaviour predicted for a multiaxial nonproportional loading and unloading path under combined tension and torsion is shown in Fig. 8. Unlike the simulations discussed above for proportional loading paths, the torsional stress-strain relationship does not exhibit the R-phase transformation. This is because the R-phase transformation is entirely finished during the prior tensile loading. If the nonproportional stress path is changed so that the torsion comes first, the results become opposite and the R-phase transformation in turn appears only in the torsional stress-strain relationship. Under the multiaxial nonproportional loading conditions, therefore, the phase transformation behaviour of TiNi SMAs becomes much more complicated due to such a path-dependence.

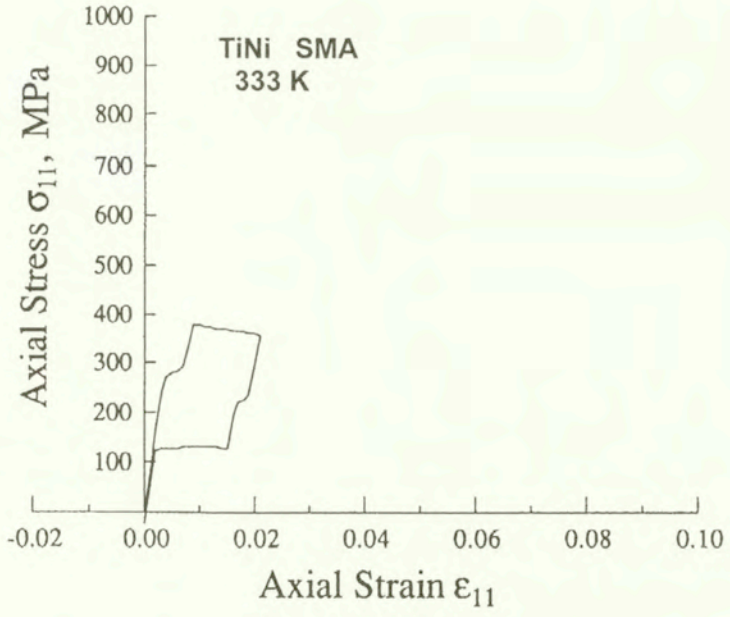

(a) $\varepsilon_{11max} = 0.02$

[FIG. 9(a)]

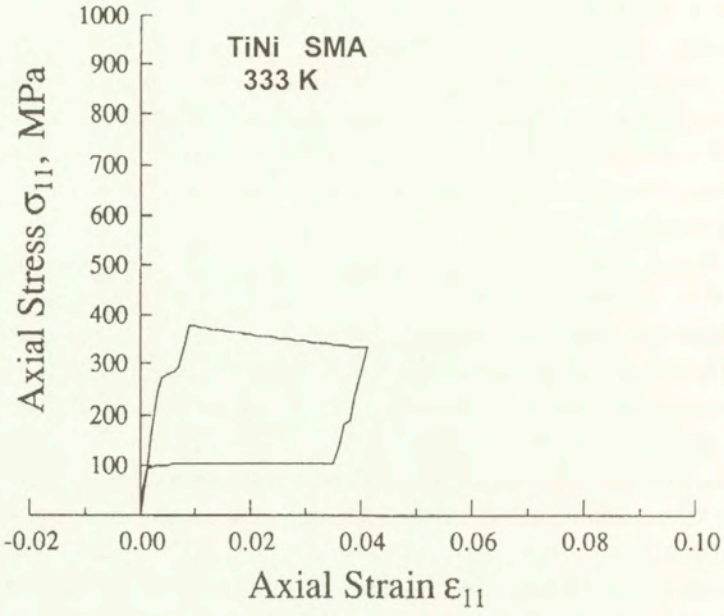

FIG. 9. Predicted stress-strain curves for TiNi-SMA at 333 K under tensile straining (arc tg$(2\varepsilon_{12}/\sqrt{3}/\varepsilon_{11}) = 0°$). (a) $\varepsilon_{11\,max} = 0.02$; (b) $\varepsilon_{11\,max} = 0.04$.

Finally, the predicted stress-strain relationships in the loading direction for a strain-controlled uniaxial tension are presented in Figs. 9(a) and 9(b). Since the lateral contraction is constrained, TiNi SMA is simultaneously subjected to tensile stresses in the lateral directions. Therefore, these results also demonstrate the multiaxial transformation behaviour of TiNi SMAs.

6. Conclusion

A three-dimensional phenomenological constitutive model for describing the transformation behaviour of TiNi shape memory alloys was developed with a particular emphasis on an incorporation of the R-phase and M-phase transformations into a multiaxial formulation. An expression of the transformation strain range was proposed which was influenced by the applied stress and the current phase volume fraction. The three-dimensional model presented may be classified as an extension of the uniaxial Tanaka model and the multiaxial Boyd-Lagoudas model. The proposed model can reproduce fairly well the observed stress-strain behaviour of TiNi SMAs under uniaxial loading conditions. The capability of the

proposed model to describe the pseudoelastic behaviour under several isothermal multiaxial proportional and nonproportional loading conditions, is also elucidated through numerical simulations. From these numerical simulations, it is verified that the proposed expression of the transformation strain range is effective to predict the closed hysteresis loops under various pseudoelastic loading conditions.

It was thus demonstrated that the multiaxial constitutive model developed to describe the R-phase and M-phase transformations of TiNi SMAs could be used as a tool for analysis-based designs of SMA composites and structures. However, some important phenomena, e.g., the volumetric change due to phase transformation, the pressure dependence of the transformation kinetics and the rubber-like behaviour caused by a reorientation, were disregarded in the present study. Therefore, an appropriate incorporation of capabilities to describe these phenomena into modelling, together with a verification based on multiaxial experiments, should be made in the future research.

References

1. M.V. GANDHI and B.S. THOMPSON, *Smart materials and structures*, 192–215, Chapman and Hall, 1992.
2. B. CULSHAW, *Smart structures and materials*, 122–126, Artech House, 1996.
3. T. TAKAGI, *Recent research on intelligent materials*, [in:] Proc. Int. Symp. on Microsystems, Intelligent Materials and Robots, 3–10, 1995.
4. C.A. ROGERS and Z. CHAUDHRY, *Smart structures: on-line monitoring concepts and challenges*, Proc. [in:] Int. Symp. on Microsystems, Intelligent Materials and Robots, 407–410, 1995.
5. A. BAZ, S. POH, J. RO, M. MUTUA and J. GILHEANY, *Active control of nitinol-reinforced composite beam*, [in:] Intelligent Structural Systems, H.S. Tzou and G.L. Anderson [Eds.], 169–212, 1992.
6. K. OTSUKA, *Fundamentals of shape memory alloys – in view of intelligent materials*, [in:] Proc. Int. Symp. on Microsystems, Intelligent Materials and Robots, 225–230, 1995.
7. C. LIANG and C.A. ROGERS, *Design of shape memory alloy springs with applications in vibration control*, ASME Journal of Vibration and Acoustics, **115**, 129–135, 1993.
8. P.F. GOBIN, G. GUENIN, M. MORIN and J. TATIBOUET, *Smart materials: a future for composites*, [in:] Proc. Int. Symp. on Microsystems, Intelligent Materials and Robots, 239–242, 1995.
9. K. TANAKA, *A thermomechanical sketch of shape memory effect: one-dimensional tensile behavior*, Res Mechanica, **18**, 251–263, 1986.
10. K. TANAKA, S. KOBAYASHI and Y. SATO, *Thermomechanics of transformation pseudoelasticity and shape memory effect in alloys*, International J. Plasticity, **2**, 59–72, 1986.
11. K. TANAKA, *A phenomenological description on thermomechanical behavior of shape memory alloys*, [in:] Elastic-Plastic Failure Modelling of Structures With Applications, D. Hui and T.J. Kozik [Eds.], PVP **141**, 163–170, 1988.

12. K. TANAKA and Y. SATO, *Phenomenological description on mechanical behavior of shape memory alloys*, Trans. JSME, **53**, 491, 1368–1373, 1992.

13. P. LIN, H. TOBUSHI, K. TANAKA, T. HATTORI and K. UCHINO, *Deformation properties associated with martensitic and R-phase transformation in TiNi shape memory alloy*, Trans. JSME, **60**, 569, A, 126–133, 1994.

14. H. TOBUSHI, K. TANAKA, T. HORI, T. SAWADA and T. HATTORI, *Pseudoelasticity of TiNi shape memory alloy (Dependence on maximum strain and temperature)*, Trans. JSME, **58**, 549, A, 694–699, 1992.

15. H. TOBUSHI, H. IWANAGA, A. INABA and M. KAWAGUCHI, *A study on mechanical properties of TiNi shape memory alloy (Experiments on cyclic characteristics of shape memory effect)*, Trans. JSME, **55**, 515, A, 1663–1668, 1989.

16. A. INABA, K. KIMURA, H. IWANAGA and H. TOBUSHI, *A study on mechanical properties of TiNi shape memory alloy (Experiments on cyclic characteristics of pseudo-elasticity)*, Trans. JSME, **55**, 511, A, 628–633, 1989.

17. C. LIANG and C.A. ROGERS, *One-dimensional thermomechanical constitutive relations for shape memory materials*, Journal of Intelligent Material Systems and Structures, **1**, 2, 207–234, 1990.

18. L.C. BRINSON, *One-dimensional constitutive behavior of shape memory alloys: thermomechanical derivation with non-constant material functions*, Journal Intelligent Material Systems and Structures, **4**, 2, 229–242, 1993.

19. I. MÜLLER and H. XU, *On the pseudo-elastic hysteresis*, Acta Metall. Mater., **39**, 3, 263–271, 1991.

20. E.J. GRAESSER and F.A. COZZARELLI, *Shape-memory alloys as new materials for aseismic isolation*, ASCE, Journal of Engineering Mechanics, **117**, 11, 2590–2608, 1991.

21. Y. IVSHIN and T.J. PENCE, *A constitutive model for hysteretic phase transition behavior*, Int. J. Eng. Sci., **32**, 681–704, 1994.

22. Y. IVSHIN and T.J. PENCE, *A thermodynamical model for a one-variant shape memory material*, Journal of Intelligent Material Systems and Structures, **5**, 455–473, 1994.

23. R. ABEYARATNE, S.J. KIM and J.K. KNOWLES, *A one-dimensional continuum model for shape-memory alloys*, Int. J. Solids and Structures, **31**, 16, 2229–2249, 1994.

24. D.J. BARRETT, *A one-dimensional constitutive model for shape memory alloys*, Journal of Intelligent Material Systems and Structures, **6**, 329–337, 1995.

25. C. LIANG and C.A. ROGERS, *The multi-dimensional constitutive relations of shape memory alloys*, [in:] Proceedings of the AIAA 32nd Structures, Conf. Structural Dynamics and Materials Conference, 178–185, 1991.

26. J.G. BOYD and D.C. LAGOUDAS, *Thermomechanical response of shape memory composites*, Journal of Intelligent Material Systems and Structures, **5**, 333–346, 1994.

27. D.C. LAGOUDAS, J.G. BOYD and Z. BO, *Micromechanics of active composites with SMA fibers*, Journal of Engineering Materials and Technology, **116**, 337–347, 1994.

28. B. RANIECKI, CH. LEXCELLENT and K. TANAKA, *Thermodynamic models of pseudoelastic behaviour of shape memory alloys*, Arch. Mech., **44**, 3, 261–288, 1992.

29. B. RANIECKI and C. LEXCELLENT, *R_L-models of pseudoelasticity and their specification for some shape memory solids*, Eur. J. Mech., A/Solids, **13**, 1, 21–50, 1994.

30. C. ROGUEDA, C. LEXCELLENT and L. BOCHER, *Experimental study of pseudoelastic behaviour of a CuZnAl polycrystalline shape memory alloy under tension-torsion proportional and non-proportional loading tests*, Arch. Mech., **48**, 6, 1025–1045, 1996.

31. E.J. GRAESSER and F.A. COZZARELLI, *A proposed three-dimensional constitutive model for shape memory alloys*, Journal of Intelligent Material Systems and Structures, **5**, 78–89, 1994.

32. L.C. BRINSON and S. HWANG, *Simplifications and comparisons of shape memory alloy constitutive models*, Journal of Intelligent Material Systems and Structures, **7**, 97–107, 1996.

33. E. PATOOR, A. EBERHARDT and M. BERVEILLER, *Thermodynamic behaviour of shape memory alloys*, Arch. Mech., **40**, 5–6, 775–794, 1988.

34. E. PATOOR, A. EBERHARDT and M. BERVEILLER, *Micromechanical modelling of superelasticity in shape memory alloy*, J. de Physique IV, C1, **6**, 277–292, 1996.

35. Q.P. SUN and K.C. HWANG, *Micromechanics modelling for the constitutive behavior of polycrystalline shape memory alloy -I. Derivation of general relations*, Journal of the Mechanics and Physics of Solids, **41**, 1, 1–17, 1993.

36. Q.P. SUN and K.C. HWANG, *Micromechanics modelling for the constitutive behavior of polycrystalline shape memory alloy -II. Study of the individual phenomena*, Journal of the Mechanics and Physics of Solids, **41**, 1, 19–33, 1993.

37. F.D. FISCHER, Q.P. SUN and K. TANAKA, *Transformation-induced plasticity (TRIP)*, Applied Mechanics Reviews, **49**, 6, 317–364, 1996.

38. V. BIRMAN, *Review of mechanics of shape memory alloy structures*, Applied Mechanics Reviews, **50**, 11, 629–645, 1997.

39. M. TOKUDA and P. SITTNER, *Polycrystalline shape memory alloy under multi-axial loading conditions*, J. Soc. Mat. Sci., **45**, 5, 527–536, 1996.

40. P. SITTNER, M. TAKAKURA, Y. HARA and M. TOKUDA, *On transformation pathways of general stress controlled thermoelastic martensitic transformation in shape memory alloys*, J. de Physique IV, C1, **6**, 357–366, 1996.

41. H. FUNAKUBO [Ed.], *Shape memory alloys*, New York, Gordon and Breach Science Publishers, 1987.

42. K. TANAKA, H. TOBUSHI and S. MIYAZAKI, *Mechanical properties of shape memory alloys* (in Japanese), Yokendo, 1993.

43. L.C. MAGEE, *Phase transformation*, H. I. Aaronson [Ed.], 115, AMS, 1969.

44. K. WU, F. YANG, Z. PU and J. SHI, *The effect of strain rate on detwinning and superelastic behavior of NiTi shape memory alloys*, Journal of Intelligent Material Systems and Structures, **7**, 138–144, 1996.

45. P. SITTNER, V. NOVAK and N. ZARUBOVA, *Martensitic transformations in [001] CuAlZnMn single crystals*, Acta Mater., **46**, 4, 1265–1281, 1998.

46. Y. LIU, Z. XIE, J.V. HUMBEECK and L. DELAEY, *asymmetry of stress-strain curves under tension and compression for NiTi shape memory alloys*, Acta mater., **46**, 12, 4325–4338, 1998.

47. K. JACOBUS, H. SEHITOGLU and M. BALZER, *Effect of stress state on the stress-induced martensitic transformation in polycrystalline Ni-Ti alloy*, Metallurgical and Material Transactions, **27A**, 3066–3073, 1996.

48. Y. GEFEN, A. HALWANY and M. ROSEN, *Effect of hydrostatic pressure on the cubic-orthorhombic phase transformation in Au-47.5 at % Cd alloy*, Philosophical Magazine, **28**, 1–9, 1973.

49. N. NAKANISHI, T. MORI, S. MIURA, Y. MURAKAMI and S. KACHI, *Pseudoelasticity in Au-Cd thermoelastic martensite*, Philosophical Magazine, **28**, 277–292, 1973.

50. T. KAKESHITA, Y. YOSHIMURA, K. SHIMUZU, S. ENDO, Y. AKAHAMA and F.E. FUJITA, *Effect of hydrostatic pressure on martensitic transformations in Cu-Al-Ni shape memory alloys*, Transactions of Japan Institute of Metals, **29**, 10, 781–789, 1988.

51. K. TSUCHIYA and K. MARUKAWA, *The mechanism of Rubber-like behavior in Cu-Zn-Al martensite*, J. de Physique IV, C8, **5**, 901–905, 1995.

Received January 13, 1999.

Arch. Mech., **51**, 6, pp. 693–715, Warszawa 1999

Modelling of hysteresis in two-phase systems

M.S. KUCZMA ([1]), A. MIELKE ([2]), and E. STEIN ([3])

([1]) *Institute of Structural Engineering,*
Poznań University of Technology, Poznań, Poland

([2]) *Institute for Applied Mathematics,*
University of Hannover, Hannover, Germany

([3]) *Institute for Structural and Computational Mechanics,*
University of Hannover, Hannover, Germany

A MATHEMATICAL FORMULATION for the hysteretic behaviour of a two-phase thermoelastic material undergoing stress-induced coherent martensitic phase transformations is proposed. The hysteresis effects are taken into account by making use of the second principle of thermomechanics and the postulate of realizability. The effective free energy density of the two-phase system is a result of homogenization of the piecewise quadratic potential adopted. The deformation process is formulated as an evolution variational inequality, which is finally solved as a sequence of linear complementarity problems. The answer to the question of existence and uniqueness of a solution to the problem is established. Results of numerical simulations for the shape-memory strips tested under uniaxial tension are included. The strips are initially in an austenitic phase which under prescribed elongation transforms in a martensitic phase and subsequently, after releasing, returns to the initial state. The phase transformation occurs provided its driving force reaches some threshold value, and is accompanied by the energy dissipation and inhomogeneous deformation. The results show the influence of the phase transformation, strain and boundary conditions on the propagation of the transformation front and the deformation mode of the specimen.

1. Introduction

HYSTERESIS IS OBSERVED in many phenomena of physics, engineering mechanics and biology, including ferromagnetism, ferroelectricity and plasticity [20]. In particular, hysteresis effects are induced by the reverse martensitic transformation which is a first-order solid-to-solid phase change occurring in various crystalline solids, e.g. in the pseudoelastic *shape memory alloys*. This special phenomenon is attributed to discontinuous changes in the crystal lattice of the high temperature phase, *austenite*, which possesses a higher symmetry and that of the low

temperature phase, *martensite*, which may exist in many variants. The changes in the crystal lattice can be described by homogeneous deformation. The resulting microstructure of shape memory alloys is usually reversible even if they are subject to comparatively large strains.

It is well understood that a phase transformation in crystalline solids is a complex process which takes place in grains at a microscale, [9, 15, 18]. To get an understanding of the process and to tailor the special properties and microstructure of the material, laboratory tests and crystallographic calculations related to this scale are necessary. On the other hand, in order to be able to solve boundary value problems encountered in engineering practice we need possibly simple models which should, however, properly reflect the characteristic features of material behaviour. These are usually phenomenological, macroscopic models of continuum mechanics which are obtained by an averaging procedure. Yet, the fundamental question here is how to find the proper parameters necessary in describing the response of a mixture of phases. On the mathematical side, some averaging procedures corresponding to the relaxation or homogenization of the microscale relations have been studied, in which the notion of a weak solution and the mathematical concepts of Young-measures and H-measures are employed, e.g. [2, 3, 19, 31]. In the field of continuum mechanics, the phenomenological models of phase transformation have been devised in which the microstructural rearrangements are taken into account by means of a set of internal variables with their evolution laws; here we shall cite [40, 13, 30, 11, 12]. The martensitic phase transformation may be induced by temperature or stress. The local self-heating and self-cooling of the material, respectively due to the exothermic character of the austenite-martensite phase transformation and the endothermic character of the reverse one, is the experimentally observed phenomenon [41]. Inclusion of the temperature effects makes the deformation process rate-dependent and highly nonlinear. This is because the stress (more generally, the driving force) of phase transformation depends upon temperature and additionally, the location of the moving heat source (phase front) is not known *a priori*. In this paper we consider the isothermal problem, some numerical results for a nonisothermal one-dimensional case are presented in [10, 8, 43, 23]. So, due to the isothermal assumption our considerations here are related to slow deformation processes in which there is "enough" time for the temperature in the specimen to reach a homogeneous distribution with the value very close to that of the bath.

We propose a mathematically useful description of the hysteretic behaviour which is typically shown by shape memory alloys, extending the approach [24] to a three-dimensional case. It is generally agreed that the appearance of hysteresis in solids undergoing martensitic phase transformations is connected with existence of a nonconvex energy function and some microscopic energetic barriers. The model we use is capable of reproducing the hysteresis, which is mainly

induced by frictional effects, through an additional term in the free energy expression, the so-called mixing energy and an extra discrete memory variable. The thermomechanical model applied here was developed by many researchers who contributed to its different aspects and generalizations, MÜLLER *et al.* [16, 33], RANIECKI *et al.* [38, 36, 39, 35, 37], LEVITAS *et al.* [27, 29]. The model is based on quadratic free energies for the parent phase, W_1, and the product phase, W_2. The free energy of the mixture $\widetilde{W}$ (per unit volume) is a weighted sum of the component energies and the "mixing" energy

$$\widetilde{W} = (1-c)\,W_1 + c\,W_2 + W_{\mathrm{mix}}\,, \tag{1.1}$$

wherein $c \in [0,1]$ is the volume fraction of the martensitic phase. The final form of (1.1) as given in (2.2) resembles the expression rigorously derived in a mathematical way by KOHN [19] who uses a relaxation procedure at fixed volume fractions, see also PIPKIN [34].

In this paper our aim is to formulate in a unifying manner the corresponding rate boundary value problem for the experimentally observed hysteretic behaviour discussed in [16, 38, 27]. The proposed formulation takes the form of a variational inequality of the first kind, cf. (3.8), which is defined on the product set $U \times K$ where U is the space of kinematically admissible displacements, $\mathbf{u} \in U$, and K is the convex set of admissible volume fractions, $c \in K$. The variational inequality assures the satisfaction in a weak form of both the equilibrium conditions and the phase transformation rules. Furthermore, the domain (in a special case: boundary) between the region where the material is the pure austenite phase and that where it is in the pure martensite state, which is the additional unknown of the problem, is determined automatically as a sort of "by-product" by solving the variational inequality. The rate boundary value problem is integrated in time by an implicit scheme and for its space discretization the finite element method is applied. Finally, the governing variational inequality is solved as a sequence of linear complementarity problems.

2. Free energy and thermomechanical relations

The type of hysteretic behaviour we wish to describe is schematically illustrated in Fig. 1 which corresponds to the experimental results presented in [16], for example. In fact, the stress-strain relations shown were obtained for a one-dimensional bar made of a single crystal CuZnAl alloy, in which the ideal pseudoelastic flow without hardening is a conventional assumption. Our recent results indicate that this hysteretic behaviour is very sensitive to any inhomogeneities, what finally leads to differences between the local response at a material point and the system behaviour [25].

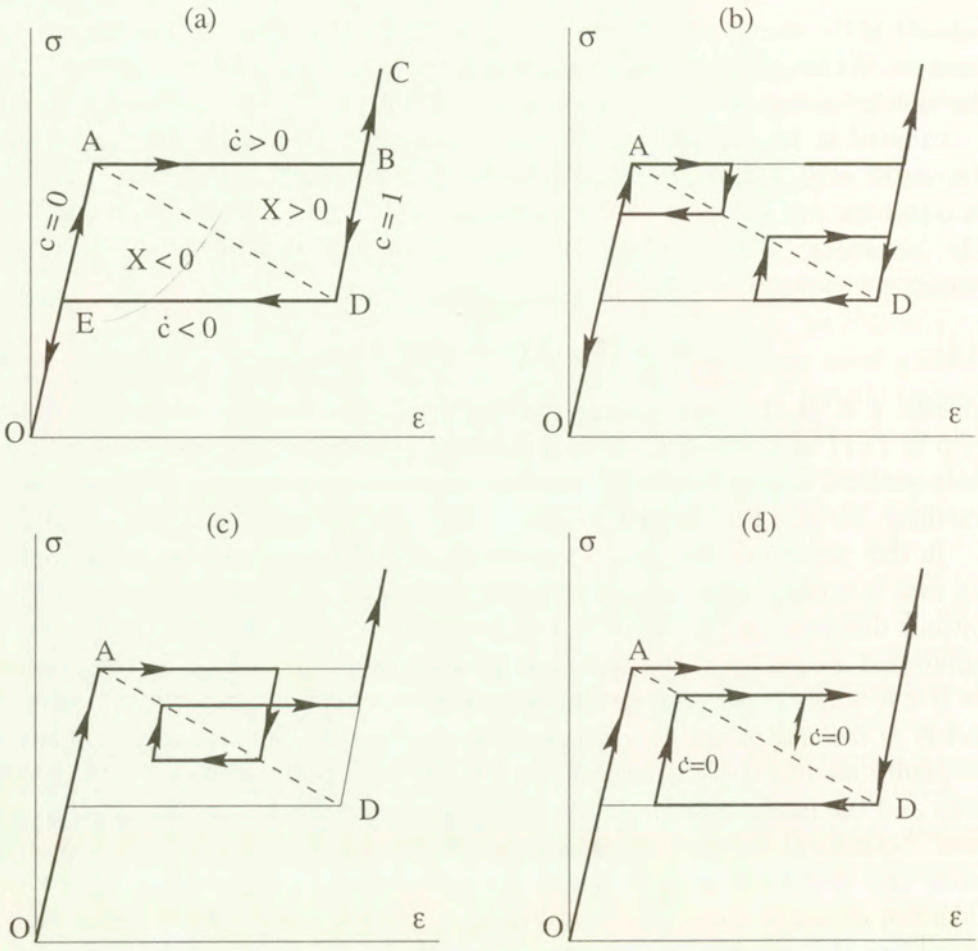

FIG. 1. Stress vs strain diagram of ideal pseudoelastic behaviour. Phase transformation starts at the diagonal AD: (a) Yield and recovery; outer loop. (b) Internal yield and internal recovery. (c) Internal loop. (d) Internal elasticity and history-dependence.

We consider the quasi-static evolution of a two-phase thermoelastic solid which undergoes a martensitic transformation. The problem is treated in the context of small deformations, under the assumption that the material prefers two strain states: the parent phase (austenite), and the product phase (martensite). It may be noted that a two-phase model for martensitic phase transformations is a conceptual simplification as the martensite phase may, in general, appear in many variants, e.g. six variants of martensite in a cubic to orthorombic transformation [4, 5]. We consider the multi-phase problem in [21, 32]. In its natural state at a temperature θ_0 ($\theta_0 > A_f^0$), the body occupies an open region $\Omega \subset \mathbb{R}^d$ with $d = 1, 2, 3$. In a material point (particle) $\mathbf{x} \in \Omega$ we postulate the

Helmholtz free energy W_i, $i = 1, 2$ in the form

$$W_i(\boldsymbol{\epsilon}, \theta) = \frac{1}{2}(\boldsymbol{\epsilon} - \mathbf{d}_i) \cdot \mathbf{E}_i(\boldsymbol{\epsilon} - \mathbf{d}_i) + \varpi_i(\theta),$$

where, for simplicity, the same elasticity tensor $\mathbf{E}_1 = \mathbf{E}_2 = \mathbf{E}$ for each phase is taken. By $\boldsymbol{\epsilon} = \boldsymbol{\epsilon}(\mathbf{u}) = \frac{1}{2}(\nabla\mathbf{u} + (\nabla\mathbf{u})^{\mathrm{T}})$ we denote the strain tensor, whereas $\mathbf{d}_i$ is the transformation strain (domain) of ith phase, and a dot $\cdot$ designates the scalar product of tensors. Taking the austenite lattice as the reference state, we may set $\mathbf{d}_1 = \mathbf{0}$ and the transformation strain $\mathbf{d}_2 \equiv \mathbf{d}$. The function $\varpi_i(\theta)$ depends on temperature θ, treated here as a parameter, and we assumed $\varpi_i(\theta) = C_v(\theta - \theta_0) - C_v\theta\ln(\theta/\theta_0) + e_i^0 - \theta s_i^0$ where e_i^0, s_i^0 are the energy and entropy constants of ith phase, C_v the common specific heat. So, the free energy function is a two-well functional which is piecewise quadratic

$$W(\boldsymbol{\epsilon}) = \min\{W_1(\boldsymbol{\epsilon}), W_2(\boldsymbol{\epsilon})\}. \tag{2.1}$$

But, it is known that if the free energy function of the elastic material is not quasiconvex [2, 3, 31], it is possible to find a boundary value problem for which the energy functional has no minimizer. This mathematical property of the phase transformation problem is connected with the "proclivity" of the material to form a finer and finer microstructure, when minimizing the elastic energy. Quasiconvexification of the phase transformation problem is a remedy used for its regularization which leads to an energetically equivalent solution, that is still of great importance. Denoting by c the volume fraction of martensite we can define the free energy of the mixture by

$$\widetilde{W}(\boldsymbol{\epsilon}, c) = \frac{1}{2}(\boldsymbol{\epsilon} - c\mathbf{d}) \cdot \mathbf{E}(\boldsymbol{\epsilon} - c\mathbf{d}) + [(1-c)\varpi_1 + c\varpi_2] + \frac{1}{2}Bc(1-c). \tag{2.2}$$

Observe that the function $\widetilde{W}$ defined in (2.2) corresponds to the relaxation at fixed volume fractions $Q_cW(\boldsymbol{\epsilon})$ derived by KOHN, see Eq. (3.11) in [19]. We recall that for the function W specified in (2.1), its relaxation $Q_cW(\boldsymbol{\epsilon})$ at fixed $c \in [0, 1]$ is defined as, cf. [19],

$$Q_cW(\boldsymbol{\epsilon}) = \inf_{\chi} \inf_{\boldsymbol{\varphi}|_{\partial U}=\mathbf{0}} \frac{1}{|U|}\int_U [(1-\chi)W_1(\boldsymbol{\epsilon} + \mathbf{e}(\boldsymbol{\varphi})) + \chi W_2(\boldsymbol{\epsilon} + \mathbf{e}(\boldsymbol{\varphi}))] \tag{2.3}$$

where $\mathbf{e}(\boldsymbol{\varphi}) = \frac{1}{2}(\nabla\boldsymbol{\varphi} + (\nabla\boldsymbol{\varphi})^{\mathrm{T}})$ and χ, being the characteristic function equal to 0 or 1, describes a partition of U into two phases, with the constraint that the volume fraction of the second phase equals c,

$$\frac{1}{|U|}\int_U \chi = c.$$

By $\boldsymbol{\varphi}$ we denote the test displacements with vanishing values at the boundary ∂U of U. The minimization in (2.3) is carried out over the physical domain $U \subset \mathbb{R}^d$, with respect to the displacements $\boldsymbol{\varphi}$ and the partitions of U into distinct phases described by distributions of χ. The set U may be related to the "representative volume element" in the theory of composites. Notice, however, that the austenite-martensite mixture is a special kind of composites in which the volume fractions of constituent phases (variants) are not given *a priori*, but constitute the additional unknowns of the problem. It is not our purpose here to address this aspect in more detail, we only remark that the minimization in (2.3) does not depend upon the domain U. This is a more general result that comes from the theory on quasiconvexification, see [19] for further discussion and references to original sources. In deriving the expression for $Q_c W(\boldsymbol{\epsilon})$, KOHN [19] has used the relaxation via Fourier analysis with $\boldsymbol{\varphi}$ being periodic functions. The relaxation of W, denoted by QW, can finally be determined by the minimization of $Q_c W(\boldsymbol{\epsilon})$ with respect to c over the interval [0, 1]; for a one-dimensional case it is shown schematically in Fig. 2. The most useful property of QW is that it has a minimizer with the corresponding minimal value equal to that of W as defined in (2.1). In this work our point of departure is the function $\widetilde{W}$ by (2.2) which corresponds to Kohn's relaxed energy at fixed volume fractions, $Q_c W(\boldsymbol{\epsilon})$. We wish to stress the fundamental role which is played here by the term W_{mix}. In the case of the free energy $\widetilde{W}$ of (2.2), W_{mix} depends on the material parameter B, but more general expressions are known in the literature, see [30, 36, 35]. According to [16], the value of B may be related to the area of hysteresis in the elongation-force diagram, another expression for B is given in [19]. In the case $B = 0$, the phase transformation proceeds at a constant stress (the Maxwell line) determined by the "double tangent construction", what in mathematical terms amounts to the convexification of the energy W assigned in (2.1) and is illustrated by the dotted bold line in Fig. 2.

In order to take into account the dissipation and hysteresis which are characteristics of the phase transformation behaviour illustrated in Fig. 1, we minimize the free energy $\widetilde{W}$, defined in (2.2), with respect to c under the requirements imposed by the second principle of thermodynamics, supplemented with the postulate of realizability [28].

From the second law of thermodynamics it follows that the (mechanical) dissipation must be non-negative,

$$\mathcal{D} = \boldsymbol{\sigma} \cdot \dot{\boldsymbol{\epsilon}} - (\dot{\widetilde{W}} + s\dot{\theta}) \geq 0. \tag{2.4}$$

Furthermore, by the standard argument of constrained equilibrium [17, 40], we arrive at the constitutive laws for entropy $s = -\partial \widetilde{W} / \partial \theta$ and stresses $\boldsymbol{\sigma}$,

$$\sigma = \partial \widetilde{W} / \partial \boldsymbol{\epsilon} = \mathbf{E}(\boldsymbol{\epsilon} - c\mathbf{d}), \tag{2.5}$$

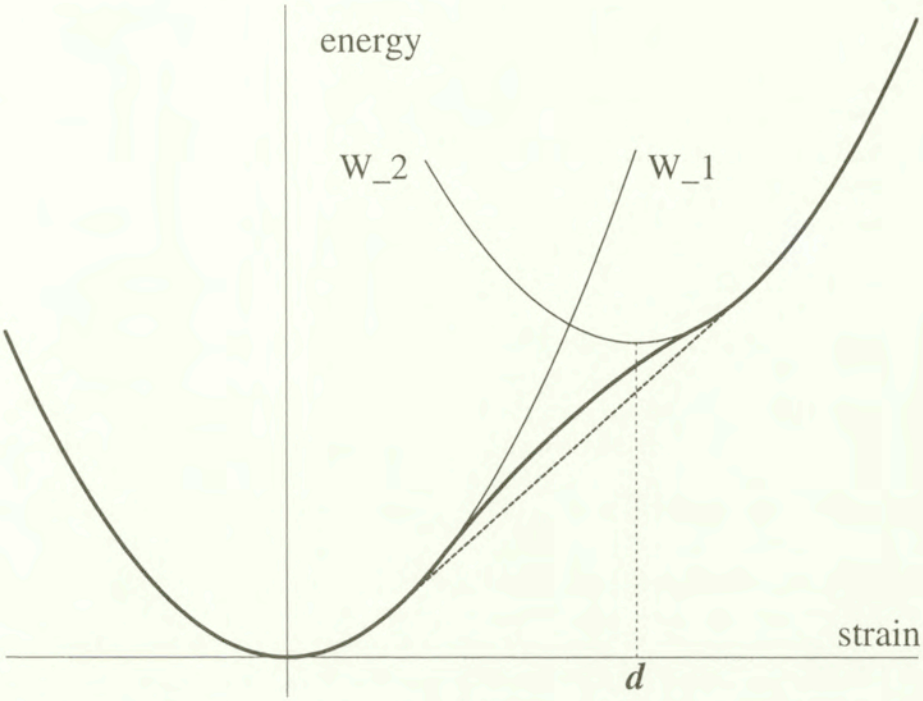

FIG. 2. Quasiconvexified energy function QW for a two-phase system with parabolic energies W_1 and W_2, and transformation strains $\mathbf{d}_1 = \mathbf{0}$, $\mathbf{d}_2 \equiv \mathbf{d}$. The dotted bold line corresponds to the convexification of W.

so that expression (2.4) reduces finally to the inequality

$$\mathcal{D} = X\,\dot{c} \geq 0 \tag{2.6}$$

wherein X is the driving force of phase transformation,

$$X \equiv -\partial \widetilde{W}/\partial c = \boldsymbol{\sigma}\cdot\mathbf{d} - (\varpi_2 - \varpi_1) - \frac{1}{2}B(1-2c). \tag{2.7}$$

The condition $X = 0$ defines a plane in the space of stresses $\boldsymbol{\sigma}$, parameterized by the volume fraction c. In the one-dimensional case, $X = 0$ and $c \in [0, 1]$ describe the diagonal AD in Fig. 1. When related to the one-dimensional situation, the driving force $X = X(\boldsymbol{\sigma}, c)$ is positive in the triangle ADB and negative in the triangle ADE of Fig. 1. At this point the following observations can be made.

1. The equilibrium states on the diagonal AD are unstable. Condition (2.6) shows that for $X = 0$ there is no dissipation.

2. As evidenced in Fig. 1, the phase transformation can proceed only if X equals some threshold value and this process possesses some directive tendency which can be controlled by the forward and reverse evolution of c.

Thus, accounting for the dissipation and consequently for hysteresis effects, we assume that phase transformation may take place only if its driving force X reaches some threshold values $\kappa_{1\to 2} = \kappa_{1\to 2}(c, c^0) > 0$ or $\kappa_{2\to 1} = \kappa_{2\to 1}(c, c^0) < 0$. The thresholds $\kappa_{1\to 2}$ and $\kappa_{2\to 1}$ depend upon the current value of volume fraction c and the additional internal variable c^0, which plays the role of a discrete memory. In connection with the type of hysteretic loops shown in Fig. 1, it is reasonable to adopt the following evolution law of the discrete memory c^0 at point $\mathbf{x} \in \bar{\Omega}$,

$$
\begin{aligned}
&\dot{c}^0(\mathbf{x}, t) = 0, && \text{if} \quad X(\mathbf{x}, t) \neq 0,\\
&c^0(\mathbf{x}, t^0) = c(\mathbf{x}, t^0), && \text{if} \quad X(\mathbf{x}, t^0) = 0,
\end{aligned}
\tag{2.8}
$$

where t^0 is the time during the process at which the state reaches the diagonal AD in Fig. 1. For the thresholds we have adopted the simple linear expressions

$$
\kappa_{1\to 2} = \max\{L(c - c^0), 0\}, \qquad \kappa_{2\to 1} = \min\{L(c - c^0), 0\}, \tag{2.9}
$$

in which L is an additional material parameter.

Notice that the functions $\kappa_{1\to 2}$ and $\kappa_{2\to 1}$ are a measure of the dissipated energy in the course of the forward and the reverse phase transformation, respectively. In fact, relations (2.9) can be derived from the dissipation potential Φ of the form

$$
\Phi(c, c^0) = \frac{1}{2} L(c - c^0)^2, \tag{2.10}
$$

which is a homogeneous quadratic function of the difference $c - c^0$. Expression (2.10) shows that the physical meaning of material parameter $L > 0$ is that of the energy which is dissipated while transforming a unit volume of one phase into the other. We assume that $L \geq B$, whereas the case $L = B > 0$ corresponds to the ideal pseudoelastic flow shown in Fig. 1.

With these understandings, we have the following phase transformation conditions:

$$
\begin{aligned}
&\text{if} \quad X = \kappa_{1\to 2}(c, c^0) && \text{then} \quad \dot{c} \geq 0,\\
&\text{if} \quad X = \kappa_{2\to 1}(c, c^0) && \text{then} \quad \dot{c} \leq 0,\\
&\text{if} \quad \kappa_{2\to 1}(c, c^0) < X < \kappa_{1\to 2}(c, c^0) && \text{then} \quad \dot{c} = 0.
\end{aligned}
\tag{2.11}
$$

It is, perhaps, important to indicate some differences of the hysteretic response pictured in Fig. 1 and a usual phase transformation problem [6]. These are because of the condition $(2.11)_3$, which says that there is no phase transformation for some range of the driving force X, and due to the characteristic

internal loops which we model by means of the discrete memory c^0. Clearly, our modelling of the very complex hysteresis loops by means of c^0 should be understood as a first approximation of accounting for internal loops, which is based rather on macroscopic observations. How a memory variable evolves in shape memory alloys under cyclic loading is, however, a difficult and subtle question which requires further research, for related discussions see [42, 1, 7]. In fact, there is no general consensus on the issue what kind of process may proceed from a given state in the upper triangle ABD of Fig. 1d under reloading after unloading: for instance, MÜLLER and his co-workers assert that the reloading is a passive (elastic) process till the previous flow stress, cf. Fig. 5d of [16], but RANIECKI and his co-workers claim that this process is from its beginning an active phase transformation flow, cf. the path ABEH in Fig. 4a of [38]. In this paper we have adopted the simplifying assumption that c^0 is equal to the value of c at the latest state defined by the condition $X = 0$ (the diagonal AD in Fig. 1, for the one-dimensional case). Our discrete memory c^0 may be treated simply as an extra variable which is helpful to follow the internal loops in the diagrams of Fig. 1. However, the use of c^0 is not essential to the approach we develop in this paper. In the particular case we may stipulate that the phase transformation flow will take place only along the interval AB (austenite-martensite phase transformation with $c^0 = 0$) and the interval DE (martensite-austenite phase transformation with $c^0 = 1$). In that case the thresholds assigned in (2.9) become

$$\kappa_{1\to 2} = \kappa_{1\to 2}(c) = Lc, \qquad \kappa_{2\to 1} = \kappa_{2\to 1}(c) = L(c-1). \tag{2.12}$$

Finally we recall the equilibrium equations, which for the stresses defined in (2.5) take the form

$$\operatorname{div}[\mathbf{E}(\boldsymbol{\epsilon}(\mathbf{u}) - c\mathbf{d})] + \mathbf{f} = \mathbf{0}, \tag{2.13}$$

where $\mathbf{f}$ is a body force per unit volume. For the rate boundary value problem considered later on, Eq. (2.13) should be supplemented by appropriate initial and boundary conditions. We assume that the latter are regular, i.e. they satisfy all the relations defining the problem.

3. Mathematical formulation

3.1. Variational inequality

Referring to (2.11) we define the phase transformation functions

$$F_{1\to 2}(\boldsymbol{\sigma}, c, c^0) \equiv \kappa_{1\to 2} - X \geq 0, \qquad F_{2\to 1}(\boldsymbol{\sigma}, c, c^0) \equiv X - \kappa_{2\to 1} \geq 0, \tag{3.1}$$

which correspond to the forward and the reverse phase transformation, and by $\dot{c}^+$ and $\dot{c}^-$ we denote the positive and the negative part of the rate of volume

fraction,

$$\dot{c}^+ \equiv \max\{\dot{c}, 0\}, \qquad \dot{c}^- \equiv \max\{-\dot{c}, 0\}, \tag{3.2}$$

so that

$$\dot{c} = \dot{c}^+ - \dot{c}^- .$$

Under these definitions we have the following result, cf. the equivalence lemma in [26].

LEMMA 3.1. *The phase transformation rules (2.11) are equivalent to the rate variational inequality*

$$c \in [0, 1] \qquad F_{1\to 2}(c) \cdot (y_+ - \dot{c}^+) + F_{2\to 1}(c) \cdot (y_- - \dot{c}^-) \geq 0 \tag{3.3}$$

for all $y_+, y_- \geq 0$.

P r o o f. We prove the assertion in the special case that $c \in (0, 1)$, for the sake of simplicity [1]. First, assume the "if" part of $(2.11)_3$ so that $F_{1\to 2} > 0$ and $F_{2\to 1} > 0$, then (3.3) implies that $\dot{c}^+ = \dot{c}^- = 0$, because the existence of a $\dot{c}^+ = p > 0$ would lead to the contradiction: $F_{1\to 2}(c) \cdot (y_+ - p) < 0$ for all $y_+ < p$. Further, if one of the phase transformation functions is equal to zero, say, $F_{1\to 2} = 0$, i.e. the "if" part of $(2.11)_1$, then $\dot{c}^+ > 0$ satisfies (3.3) (a degenerated case $\dot{c}^+ = 0$ is also covered). Note that by (3.1), $F_{1\to 2} = F_{2\to 1} = 0$ is possible only for the states on the diagonal AD in Fig. 1 and if the thresholds are defined as in (2.9); such a coincidence is not possible for thresholds assigned by (2.12). Finally, by satisfying inequality (3.3) on the positive cone $\mathbb{R}_+$, with $\dot{c}^+, \dot{c}^- \in \mathbb{R}_+$, we enforce the conditions (3.1). This completes the proof.

Inequality (3.3) implicitly defines the evolution law of c, thereby the kinetics of the strain induced by the phase transformation. Usually, the evolution law for the volume fraction variable is written in the form of an equation for the active phase transformation process which is the pivotal concern in the metallurgical literature. However, from the standpoint of computational mechanics one of the main difficulties lies in the determination of the domain in a body where the forward and reverse phase transformations do take place, i.e. where the evolution law(s) of c with $\dot{c} \neq 0$ is in force, and the domain where the response is elastic and a different constitutive law with $\dot{c} = 0$ holds. The variational inequality encompasses both the "active" and the "passive" evolution of c, playing the role of a switch. It may be remarked that the above formulation of the phase transformation criteria is similar to that of the loading/unloading conditions in the flow theory of plasticity [26]. Yet, one of the main differences is due to the

[1] The case $c = 0$ or $c = 1$ leads to the expression for X, cf. [24], which includes the subdifferential of the indicator function, $\partial I_{[0,1]}(c)$, so that (3.1) will hold for any $c \in [0, 1]$.

constraint $c \in [0,1]$ and that imposed on the plastic multiplier λ which is bounded only from below and whose rate must be non-negative, i.e. $\lambda \geq 0$, with $\dot{\lambda} \geq 0$.

From the computational reasons, it is natural to express the functions (3.1) in terms of displacements through the strain tensor. This leads to the new phase transformation functions

$$
\begin{aligned}
G_{1\to 2}(\boldsymbol{\epsilon}, c, c^0) \equiv\ & -\mathbf{d}\cdot\mathbf{E}\boldsymbol{\epsilon} + (\mathbf{d}\cdot\mathbf{E}\mathbf{d} - B)\, c + \kappa_{1\to 2}(c, c^0) \\
& + (\varpi_2 - \varpi_1) + B/2, \\
G_{2\to 1}(\boldsymbol{\epsilon}, c, c^0) \equiv\ & \mathbf{d}\cdot\mathbf{E}\boldsymbol{\epsilon} - (\mathbf{d}\cdot\mathbf{E}\mathbf{d} - B)\, c - \kappa_{2\to 1}(c, c^0) \\
& - (\varpi_2 - \varpi_1) - B/2.
\end{aligned}
\tag{3.4}
$$

The formulation discussed above constitutes a natural advantageous basis for the numerical treatment of the problem. Toward this end, the finite-dimensional counterpart of the variational inequality (3.3) in terms of the phase transformation functions (3.4) is obtained by the finite element method, and its evolution in time is solved as a sequence of linear complementarity problems.

3.2. Incremental problem

For boundary value problems of practical significance it is necessary to solve the evolution problem (3.3) in a weak form with respect to the space variable, and incrementally in time. To this end, the relations (3.4) will be expressed in displacements through the strain tensor and imposed to be valid for the body Ω as a whole. Doing this, from (2.6) we arrive at a reduced form of the global Clausius-Duhem inequality [14]. Problem (3.3) is a free boundary problem in which the boundary between the pure phase region in which $c = 0$ or $c = 1$ and the phase transformation region in which $c \in (0,1)$ is not known in advance. Furthermore, the hysteresis loops depend also on the discrete memory variable c^0. Due to this kind of history dependence, we treat the stress-strain path as a piecewise monotone one, making use of the monotone path rule [25]. We apply an implicit time integration scheme, imposing the phase transformation conditions (3.4) and the elastic equilibrium Eq. (2.13) at selected (process) times $t_n \in [0,T]$, with $n = 1,2,\ldots$, and $T < \infty$.

Using the notations $\mathbf{u}_n \equiv \mathbf{u}(\cdot, t_n)$, $c_n \equiv c(\cdot, t_n)$ for the displacement vector and the volume fraction at time $t = t_n$ and the symbol Δ for finite increments, we define

$$\Delta\mathbf{u}_n \equiv \mathbf{u}_n - \mathbf{u}_{n-1},$$

$$\Delta c_n \equiv c_n - c_{n-1}.$$

Further, we split the function Δc_n into its positive and negative part, cf. (3.2), obtaining the decomposition

$$\Delta c_n = \Delta c_n^+ - \Delta c_n^- .$$

Let $U(t_n)$ designate the set of kinematically admissible displacements of the body Ω at time $t = t_n$,

$$U(t_n) = \left\{ \mathbf{v} \in H^1(\Omega, \mathbb{R}^d) |\ \mathbf{v}(\mathbf{x}) = \mathbf{w}(\mathbf{x}, t_n) \ \text{ for a.e. } \ \mathbf{x} \in \partial\Omega_u \right\}$$

where $H^1(\Omega, \mathbb{R}^d)$ is a usual Hilbert space of vector-valued functions defined on Ω, i.e. the set of functions which, together with their first derivatives, are square-integrable. By $\partial\Omega_u$ we denote a part of the boundary $\partial\Omega$ where displacements $\mathbf{w}$ are prescribed (at time t_n), and let V stand for the space of test functions, defined by $V = U(t_n)$. The sets $K_+(c_{n-1})$ and $K_-(c_{n-1})$ that impose constraints on the finite, positive Δc_n^+ and negative Δc_n^- parts of increments of volume fraction take the form

$$\begin{aligned} K(z) &= \left\{ w \in L^2(\Omega) :\ 0 \le z + w \le 1,\ z \in Z \right\}, \\ K_+(z) &= \left\{ w \in L^2(\Omega) :\ w \ge 0,\ z + w \le 1,\ z \in Z \right\}, \\ K_-(z) &= \left\{ w \in L^2(\Omega) :\ w \ge 0,\ z - w \ge 0,\ z \in Z \right\}, \\ Z &= \left\{ z \in L^2(\Omega) :\ 0 \le z \le 1 \right\}, \end{aligned} \tag{3.5}$$

where $L^2(\Omega)$ is the space of square-integrable functions.

Before giving a weak formulation of the boundary value problem, we define the following bilinear and linear forms which correspond to relations (3.4) and (2.13),

$$\begin{aligned} a(\mathbf{w}, \mathbf{v}) &= \int_\Omega \mathbf{E}\nabla\mathbf{w}\cdot\nabla\mathbf{v}\, d\mathbf{x}, \\ g(w, \mathbf{v}) &= \int_\Omega w\mathbf{E}\mathbf{d}\cdot\nabla\mathbf{v}\, d\mathbf{x}, \\ h(w, v) &= \int_\Omega (\mathbf{d}\cdot\mathbf{E}\mathbf{d} + L - B) wv\, d\mathbf{x}, \end{aligned} \tag{3.6}$$

$$l_{n,n-1}(\mathbf{v}) = \int_\Omega \Delta\mathbf{f}_n\cdot\mathbf{v}\, d\mathbf{x} + (\text{terms on } \partial\Omega)_{n,n-1},$$

$$b_{n-1}^{\pm}(c_{n-1}, w) = \int_\Omega [B/2 + (\varpi_2 - \varpi_1) + L(c_{n-1} - c_{n-1}^0)^{\pm}] w\, d\mathbf{x} \tag{3.7}$$

$$\mp g(w, \mathbf{u}_{n-1}) \pm h(c_{n-1}, w).$$

With these notation we can define a typical time step $t_{n-1} \Longrightarrow t_n$ of the incremental boundary value problem for the phase transformation process under consideration as the variational inequality.

Find $(\Delta \mathbf{u}_n, \Delta c_n) \in U(t_n) \times K(c_{n-1})$ such that

$$a(\Delta \mathbf{u}_n, \mathbf{v}) - g(\Delta c_n, \mathbf{v}) = l_{n,n-1}(\mathbf{v}) \qquad \forall\, \mathbf{v} \in V$$

$$\mp g(z_\pm - \Delta c_n^\pm, \Delta \mathbf{u}_n) \pm h(\Delta c_n, z_\pm - \Delta c_n^\pm) \geq \mp b_{n-1}^\pm(c_{n-1}, z_\pm - \Delta c_n^\pm) \qquad \forall\, z_\pm \in K_\pm(c_{n-1}) \tag{3.8}$$

Having solved (3.8) for increments $\Delta \mathbf{u}_n$ and Δc_n, we can easily update the discrete memory c_{n-1}^0 to c_n^0 at the current time $t = t_n$, details are given in [25].

Under the usual assumptions including those of symmetry and pointwise stability of the elasticity tensor $\mathbf{E}$, and provided that the set $\partial\Omega_u$ has a positive measure and excludes rigid motions of the body Ω, the following result can be proved, [21].

THEOREM 3.2. *Let the material parameters $L, B \geq 0$ satisfy the inequality $L \geq B$. Then the problem (3.8) possesses a solution. The solution is unique, provided $L > B$.*

The first equation of the system (3.8) is a weak form of the equilibrium conditions (2.13), whilst $(3.8)_2$ represents two variational inequalities which are a weak form of the phase transformation rules (2.11) in virtue of the equivalence lemma (3.1) and expressions (3.4). The system (3.8) can conveniently be discretized in space by the finite element method and is solved finally as a standard form of the linear complementarity problem, after some rearrangements due to the restricted variations of the variables Δc_n^+, Δc_n^- and the fact that changes $\Delta \mathbf{u}_n$ of the displacement vector are not restricted in sign.

3.3. Linear complementarity problem

Let $\varphi_i(x)\,(1 \leq i \leq N)$ and $\psi_j(x)\,(1 \leq j \leq M)$ be the finite element bases we use for the displacement $\mathbf{u}$ and phase fraction c in $H^1(\Omega)$ and $L^2(\Omega)$. In particular, the field of displacement $\mathbf{u}$ can be approximated by a piecewise quadratic polynomial, whereas for the function of phase fraction c (and c^0) a piecewise linear approximation can be utilized. We remark that using of piecewise linear basis functions ψ_j leads to the internal approximation of the sets $K_\pm$ in (3.5).

The finite-dimensional counterpart of the weak formulation (3.8) may be expressed as the following linear complementarity problem:

(3.9)
$$\boxed{\begin{aligned} &\mathbf{D}\mathbf{x}_n + \mathbf{y}_n = \mathbf{b}_{n,n-1} \\ &\mathbf{x}'_n \geq \mathbf{0},\ \mathbf{y}^1_n = \mathbf{0},\ \mathbf{y}_n \geq \mathbf{0},\ \mathbf{x}_n \cdot \mathbf{y}_n = 0 \end{aligned}}$$

in which $\mathbf{D}$ is a square matrix, $\mathbf{x}_n$ is a vector of unknowns (nodal values of the finite element approximations), $\mathbf{y}_n$ denotes a vector of slack variables, and the vector $\mathbf{b}_{n,n-1}$ is known at time t_n. By $\mathbf{x}'_n$ we denote the elements of the vector $\mathbf{x}_n$, excluding the subvector $\mathbf{x}^1_n \equiv \Delta\mathbf{u}_n$ which is sign-unrestricted. The above matrix and vectors have the following structure:

$$\mathbf{D} = \begin{bmatrix} -\mathbf{K} & \mathbf{G}^{\mathrm{T}} & -\mathbf{G}^{\mathrm{T}} & \mathbf{0} & \mathbf{0} \\ \mathbf{G} & -\mathbf{H} & \mathbf{H} & -\mathbf{I} & \mathbf{0} \\ -\mathbf{G} & \mathbf{H} & -\mathbf{H} & \mathbf{0} & -\mathbf{I} \\ \mathbf{0} & \mathbf{I} & \mathbf{0} & \mathbf{0} & \mathbf{0} \\ \mathbf{0} & \mathbf{0} & \mathbf{I} & \mathbf{0} & \mathbf{0} \end{bmatrix}, \quad \mathbf{x}_n = \begin{Bmatrix} \Delta\mathbf{u}_n \\ \Delta\mathbf{c}^+_n \\ \Delta\mathbf{c}^-_n \\ \mathbf{r}^1_n \\ \mathbf{r}^0_n \end{Bmatrix},$$

$$\mathbf{b}_{n,n-1} = \begin{Bmatrix} \mathbf{b}^u_{n,n-1} \\ \mathbf{b}^{c^+}_{n-1} \\ \mathbf{b}^{c^-}_{n-1} \\ \mathbf{1} - \mathbf{c}_{n-1} \\ \mathbf{c}_{n-1} \end{Bmatrix}.$$

Matrices $\mathbf{K}, \mathbf{G}$ and $\mathbf{H}$ are generated by the bilinear forms (3.6),

$$\begin{aligned} \mathbf{K} &= [K_{ij}] = [a(\varphi_i, \varphi_j)], \quad \dim\mathbf{K} = N \times N, \\ \mathbf{G} &= [G_{ij}] = [g(\psi_i, \varphi_j)], \quad \dim\mathbf{G} = M \times N, \\ \mathbf{H} &= [H_{ij}] = [h(\psi_i, \psi_j)], \quad \dim\mathbf{H} = M \times M, \end{aligned}$$

and $\mathbf{I}$ is the $M \times M$ identity matrix corresponding to the vectors $\Delta\mathbf{c}^+_n$, $\Delta\mathbf{c}^-_n$ and their conjugates $\mathbf{r}^1_n$, $\mathbf{r}^0_n$. The latter are Lagrange's multipliers which are induced by the constraint imposed on the volume fraction that $c \in [0, 1]$, cf. footnote 1 in LEMMA 3.1. Vectors $\mathbf{b}^u_{n,n-1}$, $\mathbf{b}^{c^+}_{n-1}$ and $\mathbf{b}^{c^-}_{n-1}$ are generated by the linear forms (3.7). The matrices $\mathbf{K}$ (stiffness matrix) and $\mathbf{H}$ are symmetric

and positive definite. For the solution of problem (3.9) we developed our own computer program based on the algorithm presented in [22].

4. Numerical results

Our goal here is to check numerically the presented formulation and to see the consequences of the assumptions taken. We have simulated the basic, uniaxial tension test on a strip made from a two-phase material, as a plane stress displacement-driven problem. The strip and the imposed boundary conditions (4.1) are schematically displayed in Fig. 3. In the coordinate axis xy, let the displacement vector $\mathbf{u} = (u, v)$ have the components u and v, and let the length and width of the strip be a and b, respectively. We assumed the following boundary conditions:

$$
\begin{aligned}
&\text{on the left-hand side of the strip} \quad \begin{cases} u(0,y) = 0 & 0 \le y \le b, \\ v(0, b/2) = 0, \end{cases} \\
&\text{on the right-hand side of the strip} \quad \begin{cases} u(a,y) = w(t) & 0 \le y \le b, \\ v(a, b/2) = 0. \end{cases}
\end{aligned} \tag{4.1}
$$

The loading program $w(t)$ is a bilinear hat function, increasing from zero to the scaled maximum value of $w(t')/a = 0.050833$ at a time $t = t'$, and then decreasing to zero.

For the field of displacements $\mathbf{u}(\cdot, t) \equiv (u(\cdot, t), v(\cdot, t))$ we have used a 6-node triangle finite element with quadratic shape functions (linear strain triangle), whilst for the volume fraction $c(\cdot, t)$ a 3-node linear triangle. The uniform mesh of $(6 \times 18) \times 4$ finite elements we employed is shown in Fig. 3. Due to the difficulty

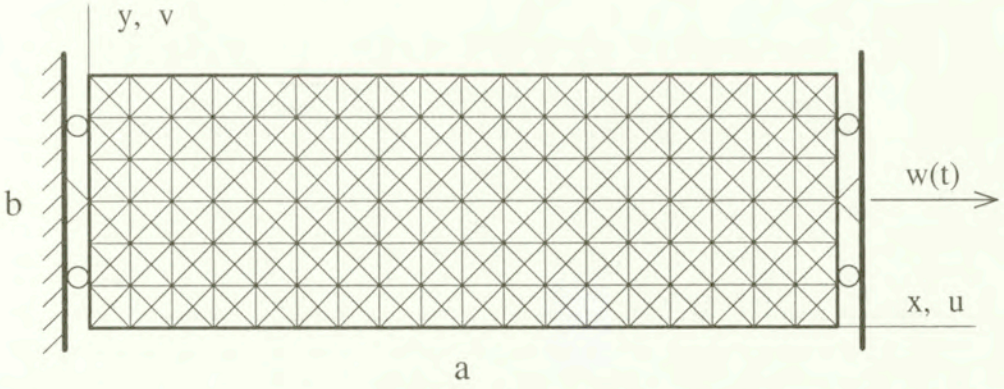

FIG. 3. The strip made of a material with two preferred states, of length a and width b with $a : b = 12 : 4$, under uniaxial tension $w(t)$.

in finding all the needed parameters for a specific material, we have assumed the following material parameters corresponding to a CuZnAl single crystal [16]: $E = 10000.00$ MPa, $B = 1.20$ J/m^3, $L = 1.01B$, $\nu = 0.30$, $\varpi_2 - \varpi_1 = 3.756$ J/m^3, the thresholds $\kappa_{1\to 2}$ and $\kappa_{2\to 1}$ by (2.9), and the transformation strain corresponding to one variant of a CuAlNi alloy [5],

$$\mathbf{d} = \begin{bmatrix} 0.045 & 0.020 \\ 0.020 & 0.045 \end{bmatrix}.$$

Using the same material data, we have calculated the strip for two proportions of its length to width: case 1 with $a : b = 12$ mm : 4 mm, and case 2 with $a : b = 24$ mm : 4 mm, and the same thickness of 0.4 mm. In its initial state the strip was in the austenite phase, and $c(\mathbf{x}, t_0) = c^0(\mathbf{x}, t_0) = 0$, $\mathbf{x} \in \Omega = [0, a] \times [0, b]$. The characteristic major hysteresis loop is shown in Fig. 4a. Displayed is the relation between the force F at the side ($x = a, 0 \le y \le b$), divided by the initial cross-sectional area A_0 of the strip, versus the scaled elongation $w(t)/a$. On the graph two pairs (A,A') and (B,B') of states corresponding to the same scaled elongation but with different histories are marked. Figs. 4b and c, and Fig. 6

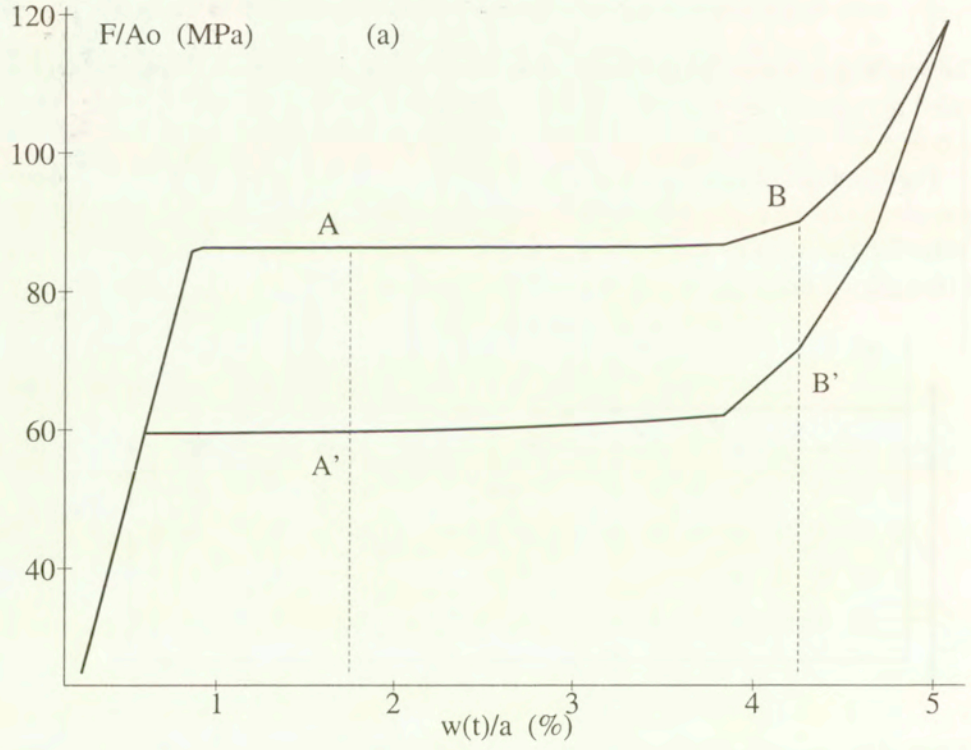

Fig. 4a

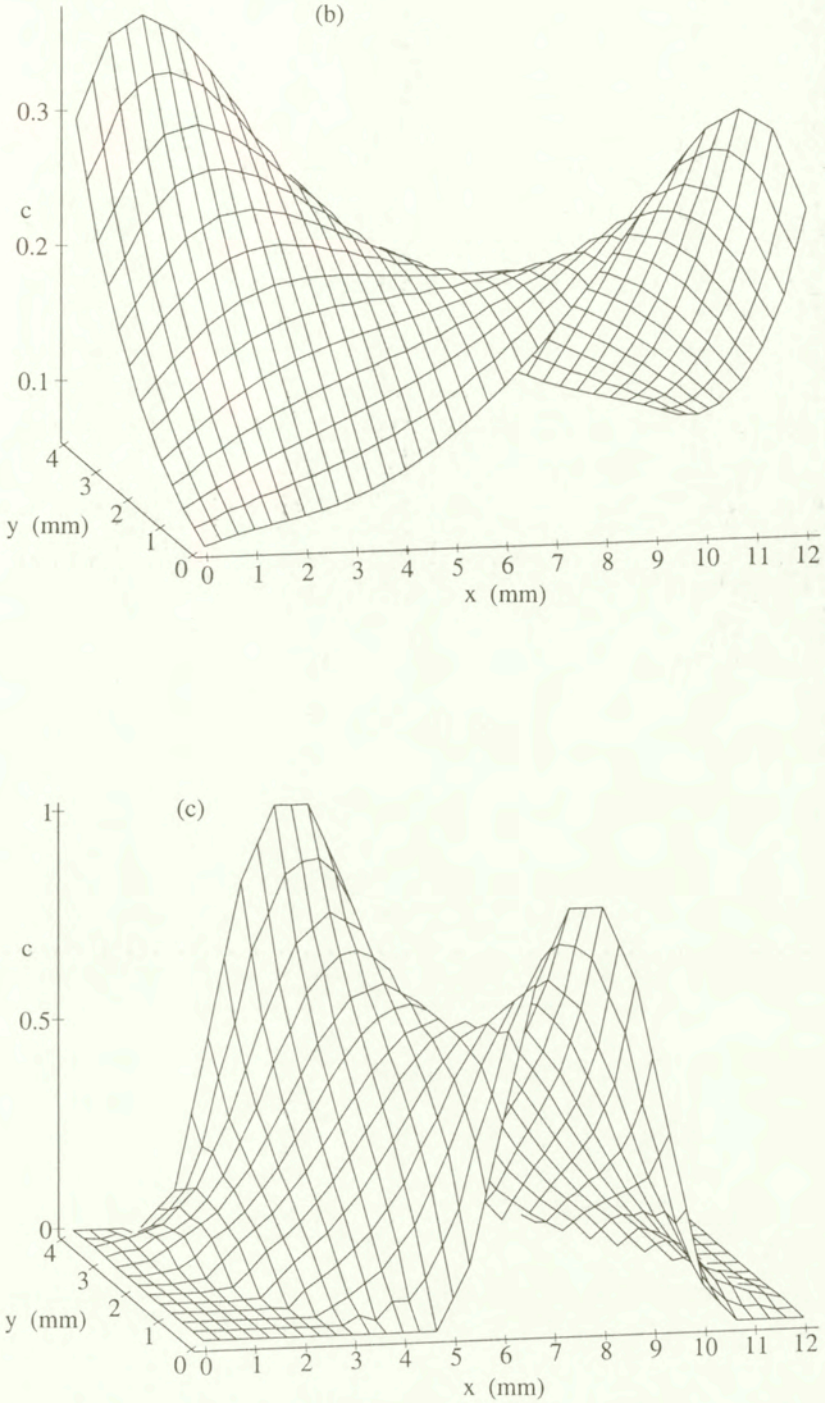

FIG. 4. Case 1. The 12×4 strip under uniaxial extension program $w(t)$. (a) Major hysteresis loop in the scaled force—elongation space (F/A_0) — $(w(t)/a)$, (b) and (c) Distribution of c at the corresponding states A and A′.

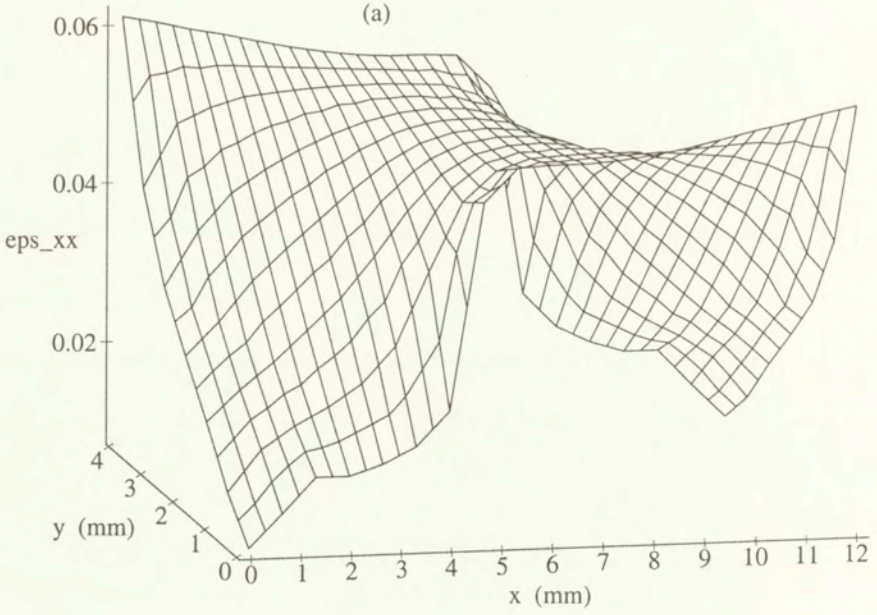

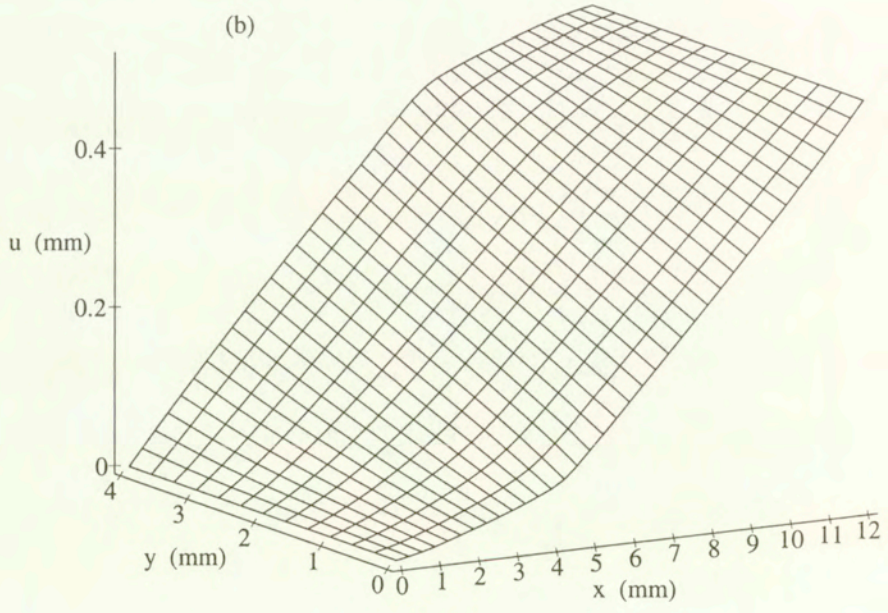

[FIG. 5a, b]

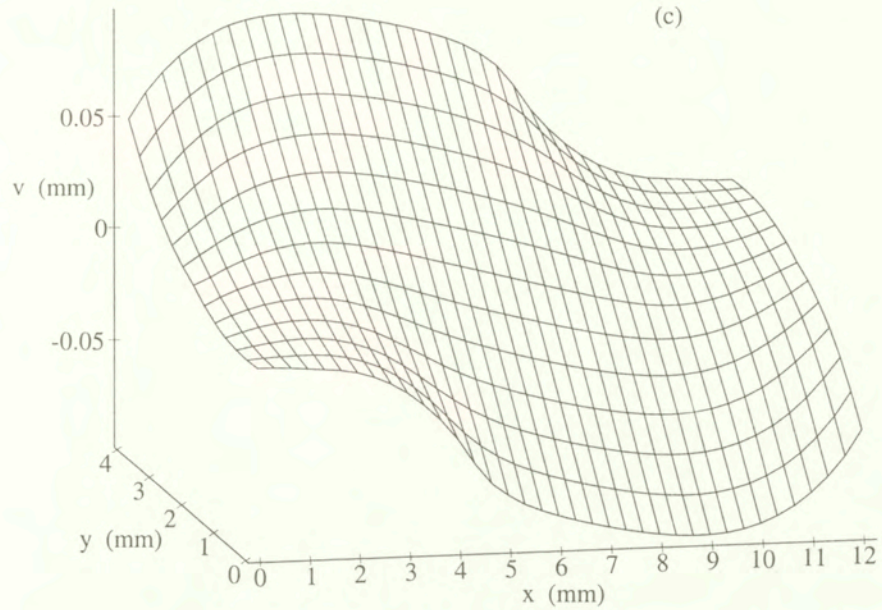

FIG. 5. Case 1. Distributions of strain ϵ_{xx}, (a), and the corresponding displacement u along the elongation, (b), and perpendicular displacement v, (c), at the state B in Fig. 4.

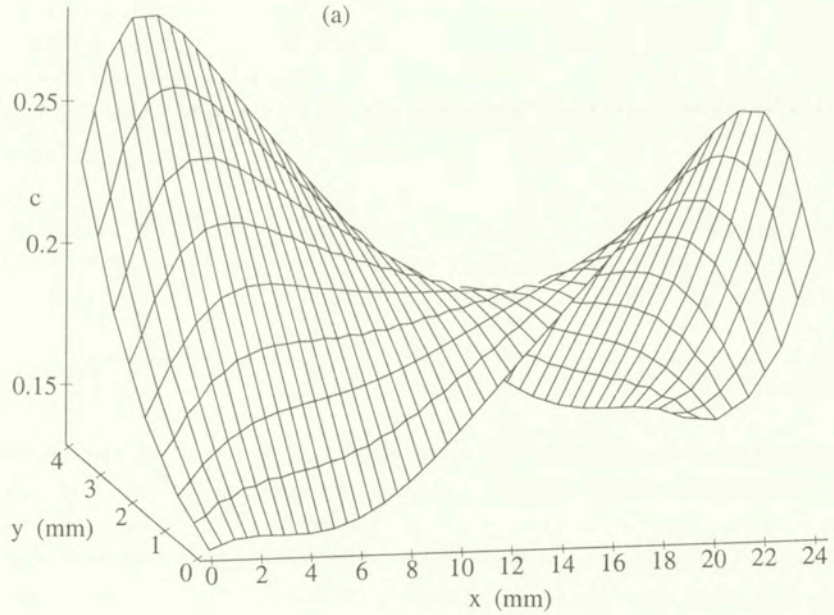

FIG. 6a]

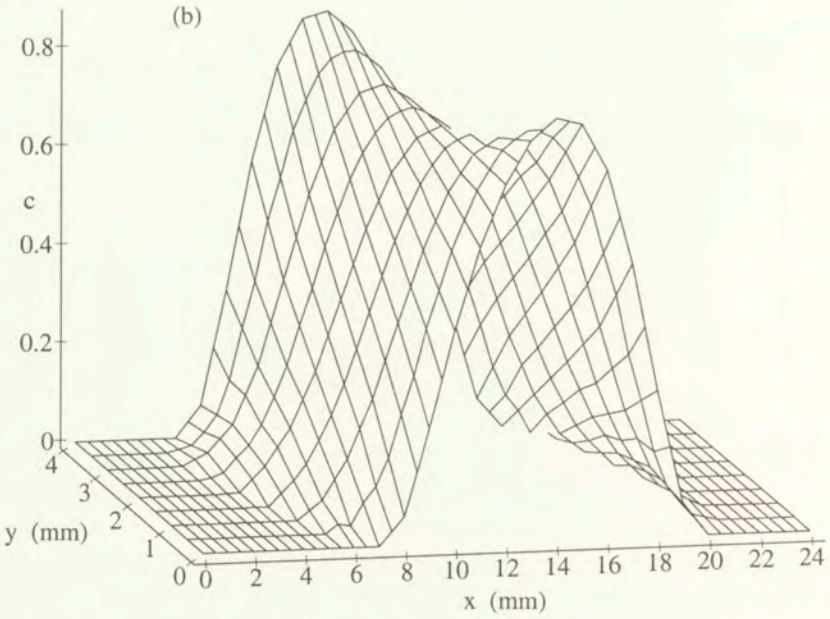

FIG. 6. Case 2. The 24 × 4 strip under uniaxial extension program $w(t)$. (a) and (b) Distribution of c at the states corresponding to A and A′ in Fig. 4.

reveal that the extension of the two-phase strip induces inhomogeneous fields whose paths of evolution do not coincide during the loading and unloading stages, even for this simple uniaxial loading program. Observe also that the initially straight axis $(0 \leq x \leq a, y = b/2)$ of the strip does not remain straight in the xy-plane in the course of the process, see Fig. 5c for the component v of the displacement vector $\mathbf{u}$. Finally, it is worthy to mention that the proposed formulation allows us to determine the solution of this initially homogeneous problem without introducing any disturbance to the system in order to initiate the phase transformation.

5. Closing remarks

In the paper, a variational inequality approach to the hysteresis behaviour of a two-phase system undergoing thermoelastic martensitic transformations is developed. The starting point is a homogenized free energy for the mixture of two phases, in the setting of linearized theory of elasticity with a parabolic energy function for each phase. The mathematical model proposed is a weak expression of the equilibrium conditions and the phase transformation rules. The latter take into account the characteristic dissipative effects of friction type and comply with the second principle of thermodynamics; they constitute an implicit

form of the equation of kinetics of the phase transformation. To solve the rate variational inequality, a computational algorithm is devised which comprises an implicit time integration scheme and a mathematical programming procedure (linear complementarity problem). The existence of a unique solution to the problem considered is assured. The numerical results obtained for the tension test on austenite-martensite strips show that, even in the two-phase system, two corresponding states on the force-elongation diagram are connected with different inhomogeneous states in the bulk of the sample. In future work we will concentrate on the case of multi-phase systems. Also, accounting for the effects of plasticity and temperature is desirable.

Acknowledgements

The support of the Volkswagen Foundation through Grant I/70284 is gratefully acknowledged. One of the authors (M.S.K.) would sincerely like to thank Professor B. Raniecki for the valuable and inspiring discussions. Part of the calculations were performed at the Poznań Supercomputing and Networking Centre (PCSS).

References

1. J.M. BALL, C. CHU and R.D. JAMES, *Hysteresis during stress-induced variant rearrangement*, J de Physique IV, Coll. C8, suppl. J. de Physique III, 5: (**C8–245**)–(**C8–251**), 1995.
2. J.M. BALL and R.D. JAMES, *Fine phase mixtures as minimizers of energy*, Arch. Rational Mech. Anal., **100**(1):13–52, 1987.
3. J.M. BALL and R.D. JAMES, *Proposed experimental tests of a theory of fine microstructure and two-well problem*, Phil. Trans. R. Soc. Lond., **338A**, 389–450, 1992.
4. K. BHATTACHARYA, *Wedge-like, microstructure in martensites*, Acta Metall. Mater., **39**(10):2431–2444, 1991.
5. K. BHATTACHARYA, *Comparison of the geometrically nonlinear and linear theories of martensitic transformation*, Continuum Mech. and Thermodyn., **5**:205–242, 1993.
6. D. BLANCHARD, M. FREMOND and A. VISINTIN, *Phase change with dissipation*, [In:] H.D. Bui and Q.S. Nguyen [Eds.], Thermomechanical Couplings in Solids, 411–418, IUTAM, North-Holland, Amsterdam 1987.
7. Z. BO and D.C. LAGOUDAS, *Thermomechanical modelling of polycrystalline SMAs under cyclic loading, Part IV. Modelling of minor hysteresis loops*, Int. J. Engng. Sci., 1997. (submitted).
8. M. BROKATE and J. THEEL, *Some numerical simulations of pseudoelastic hysteresis in shape memory alloys*, Continuum Mech. Thermodyn., **5**, 265–280, 1993.
9. J.W. CHRISTIAN, *The theory of transformations in metals and alloys* volume I, 2nd edition. Pergamon Press, Oxford, New York 1975.

10. B. FEDELICH and G. ZANZOTTO, *One-dimensional quasistatic nonisothermal evolution of shape-memory material inside the hysteresis loop*, Continuum Mech. Thermodyn., **3**:251–276, 1991.

11. F.D. FISCHER, M. BERVEILLER, K. TANAKA and E.R. OBERAIGNER, *Continuum mechanical aspects of phase transformations in solids*, Arch. Appl. Mech., **64**:54–85, 1994.

12. M. FREMOND, *Shape memory alloy. A thermomechanical macroscopic study*, CISM, **351** Chapter 1, 1–67. Springer, Wien, New York 1996.

13. P. GERMAIN, Q.S. NGUYEN and P. SUQUET, *Continuum thermodynamics*, Transactions of the ASME J. Appl. Mechanics, **50**:1010–1020, 1983.

14. A.E. GREEN and N. LAWS, *On a global entropy production inequality*, Quart. J. Mech. Appl. Math., **25**, 1–11, 1972.

15. E. HORNBOGEN, *Werkstoffe*, 6th edition, Springer-Verlag, Berlin 1994.

16. Y. HUO and I. MÜLLER, *Nonequlibrium thermodynamics of pseudoelasticity*, Continuum Mech. and Thermodyn., **5**, 163–204, 1993.

17. J. KESTIN and J.R. RICE, *Paradoxes in the application of thermodynamics to strained solids* [In:] B. Gal-Or E.B. Stuart and A.J. Brainard [Eds.], A Critical Review of Thermodynamics, 275–298, Mono book Corp., Baltimore 1970.

18. A.G. KHACHATURYAN, *Theory of structural transformations in solids*, John Wiley and Sons, New York 1983.

19. R.V. KOHN, *The relaxation of a double-well energy*, Continuum Mech. Thermodyn., **3**, 193–236, 1991.

20. M.A. KRASNOSIELSKI and A.V. POKROWSKI, *Systems with hysteresis*, Springer-Verlag, Berlin 1989.

21. M.S. KUCZMA, *Application of variational inequalities in the mechanics of plastic flow and martensitic phase transformations*, Transactions of the Poznań University of Technology, **352**, PUT Press, Poznań 1999.

22. M.S. KUCZMA, *A viscoelastic-plastic model for skeletal structural systems with clearances*, Comp. Assist. Mech. Engng. Sci., **6**(1), 83–106, 1999.

23. M.S. KUCZMA, V.I. LEVITAS, A. MIELKE and E. STEIN, *Nonisothermal hysteresis loops in pseudoelasticity* [In:] Proceedings of the XIII Conference on Computer Methods in Mechanics, 711–718, Poznań, 5-8 May 1997.

24. M.S. KUCZMA and A. MIELKE, *Variational approach to pseudoelastic behaviour*, ZAMM, **77**, Suppl. 1, S175 – S176, 1997.

25. M.S. KUCZMA and A. MIELKE, *Influence of hardening and inhomogeneity on internal loops in pseudoelasticity*, IfAM-preprint A7, University of Hannover, Institute for Applied Mathematics, July 1998. (Zeits. Angew. Math. Mech., accepted, 1999).

26. M.S. KUCZMA and E. STEIN, *On nonconvex problems in the theory of plasticity*, Arch. Mech., **46**(4), 505–529, 1994.

27. V.I. LEVITAS, *Thermomechanical description of pseudoelasticity – the threshold-type dissipative force with discrete memory*, Mech. Res. Comm., **21**, 273–280, 1994.

28. V.I. LEVITAS, *The postulate of realizability: Formulation and applications to postbifurcation behavior and phase transitions in elastoplastic materials.* Part I and II, Int. J. Engng. Sci., **33**, 921–971, 1995.

29. V.I. LEVITAS, E. STEIN and M. LENGNICK, *On a unified approach to the description of phase transition and strain localization*, Arch. Appl. Mech., **66**, 242–254, 1996.

30. V.I. LEVITAS, *Thermomechanics of phase transitions and inelastic deformations of microinhomogeneous materials* (in Russian), Naukova Dumka, Kiev 1992.

31. A. MIELKE, *Flow properties for Young-measure solutions of semilinear hyperbolic problems*, IfAM-preprint A4, University of Hannover, Institute for Applied Mathematics, September 1997.

32. A. MIELKE, F. THEIL and V.I. LEVITAS, *Mathematical formulation of quasistatic phase transformations with friction using and extremum principle*, IfAM-preprint A8, University of Hannover, Institute for Applied Mathematics, September 1998.

33. I. MÜLLER and S. SEELECKE, *Thermodynamical aspects of shape memory*, Trans. Tech. Publications (submitted), 1996.

34. A.C. PIPKIN, *Elastic materials with two preferred states*, Quart. J. Mech. Appl. Math., **44**, 1–15, 1991.

35. B. RANIECKI, *Thermomechanics of pseudoelasticity of shape memory materials* (in Polish), volume 1 of Current Trends in the Mechanics of Materials (ed. W.K. Nowacki), Chapter 2, 55–140, IPPT PAN, Warsaw 1996.

36. B. RANIECKI and CH. LEXCELLENT, *R_L models of pseudoelasticity and their specification for some shape memory alloys*, Eur. J. Mech., A/Solids, **13**(1), 21–50, 1994.

37. B. RANIECKI and CH. LEXCELLENT, *Thermodynamics of isotropic pseudoelasticity in shape memory alloys*, Eur. J. Mech., A/Solids, **17**(2), 185–205, 1998.

38. B. RANIECKI and CH. LEXCELLENT and K. TANAKA, *Thermodynamic models of pseudoelastic behaviour of shape memory alloys*, Arch. Mech., **44**(3), 261–284, 1992.

39. B. RANIECKI and K. TANAKA *On the thermodynamic driving force for coherent phase transformations*, Int. J. Engng. Sci., **32**(12), 1845–1858, 1994.

40. J.R. RICE, *Inelastic constitutive relations for solids: An internal-variable theory and its application to metal plasticity*, J. Mech. Phys. Solids, **19**, 433–455, 1971.

41. J.A. SHAW and S KIRIAKIDES, *On the nucleation and propagation of phase transformation fronts in a NiTi alloy*, Acta Mater., **45**(2), 683–700, 1997.

42. K. WILMANSKI, *On pattern formation in stress-induced martensitic transformation* [In:] G. Maugin and W. Muschik [Eds.], Nonlinear thermodynamical processes in continua, 88–105, TU Berlin 1992.

43. A. ZIÓŁKOWSKI, *Pseudoelasticity problems of materials with shape-memory* (in Polish), PhD thesis, IPPT PAN, Warsaw 1995.

Received March 29, 1999; revised version August 30, 1999.

Arch. Mech., **51**, 6, pp. 717–726, Warszawa, 1999

Experimental investigations of thermomechanical couplings in TiNi shape memory alloy during a torsion-tension (compression) test

W. OLIFERUK

Polish Academy of Sciences
Institute of Fundamental Technological Research,
Świętokrzyska 21, 00–049 Warsaw, Poland
e-mail: wolif@ippt.gov.pl

EXPERIMENTAL INVESTIGATIONS of thermomechanical coupling in TiNi alloy during uniaxial and biaxial loading at the temperature higher than the room temperature is presented. The applied method is based on contactless temperature measurements. The results of the investigations are reported. They are interpreted in terms of the phase transitions.

1. Introduction

THE SHAPE-MEMORY EFFECT (SME) in the TiNi alloy appears as a result of phase transitions. The kind of phase transitions depends on the range of mechanical and thermal loading of the material tested. During phase transitions, the thermomechanical couplings take place. Some part of the expended mechanical energy is dissipated in the form of heat (exoenergic process). Because of this, temperature of the tested sample increases. When the phase transitions process is endoenergic, the temperature of the sample decreases.

The measurements of temperature changes of the sample due to thermomechanical coupling are important for understanding the overall deformation behaviour of shape-memory alloys (SMA) and they give a basis for verification of the constitutive thermomechanical models describing this behaviour. Such statement results first of all from high temperature sensitivity of most of the SMA.

The present work is devoted to experimental investigations of the thermomechanical coupling in TiNi sample during the uniaxial and biaxial loading at a low level of stress range, where the B2 $\leftrightarrow$ R transition proceeds.

The temperature measurements of the sample of TiNi alloy were carried out during: (1) – *torsion*, (2) – *tension*, (3) – *compression*, (4) – *simultaneous torsion*

(shear stress τ) and *tension* (axial stress σ) ($m = \tau/\sigma = 1$) and (5) – *torsion-compression* ($m = -1$) tests, at different temperature ranges. The tests were performed on a tubular sample. It was strained (to a limited extent) on an Instron testing machine with constant stress rate equal to 1 MPa/s. The details of the test program and the conditions of experiments are given in the papers [1, 3]. First part of this program includes the investigations of five various loading paths at a low temperature range: 200 K, 280 K, 300 K and the maximum effective stress equal to 100 MPa, when reorientation of the pre-existing R-phase occurs; in other words, when the strain is the result of a twinning process. If the ambient temperature is different than the room temperature, the use of a temperature chamber is required. The temperature was measured on the basis of detection of IR radiation of the sample under test. It has been found that the change of sample temperature during the twinning process is negligible (is not higher than 1K). At the chamber temperature lower than the room temperature, higher accuracy was impossible because of the temperature instability of the chamber used.

There exist many works on contactless sample temperature measurements during deformation tests of metals carried out at the room temperature, without the use of a temperature chamber. However, as far as the author is aware, there exists no work on contactless monitoring of the temperature sample during multiaxial loading tests carried out in a temperature chamber.

Detection of IR radiation was applied to determine the heat of the Austenite-Martensite (A $\leftrightarrow$ M) phase transition in Cu Zn Al SMA in [2].

In the present paper, the results of the instantaneous temperature measurements of the TiNi alloy sample during uni- and multiaxial loading at 310 K and in the range of stresses, where B2 $\leftrightarrow$ R phase transitions take place, are given. The maximum of effective stress was equal to 290 MPa. In such conditions, the temperature stability of the chamber used was better than at the temperature lower than the room temperature.

2. Temperature measurements based on infrared radiation detection

The contactless temperature measurements are based on the Stefan Boltzmann formula stating that the total power M_{bb} of infrared radiation (IR) emitted by a black body is a single-valued function of its temperature T.

$$M_{bb} = \xi \cdot T^4, \tag{2.1}$$

where ξ is the Stefan Boltzmann constant, $\xi = 5.7 \cdot 10^{-8} \mathrm{Wm^{-2}K^{-4}}$. Thus, by measuring the IR radiation power emitted by the tested object, it is possible to determine its temperature. Such a measurement does not disturb the temperature field of the object.

However, the real object behaviour never complies with the Eq. (2.1).

The factor required to describe the IR radiation produced by a real object is called emissivity. The spectral emissivity ε_λ is defined as the ratio of spectral radiant emittance from an object to that emitted from a black body at the same temperature and wavelength.

The Stefan Boltzmann formula for real objects takes the form:

$$M = \varepsilon \cdot \xi \cdot T^4, \tag{2.2}$$

where ε is the average emissivity within the range from $\lambda = 0$ to $\lambda = \infty$.

According to Kirchhoff's law, for any material, the spectral emissivity is equal to the spectral absorbance of an object at any specified temperature and wavelength. When the object is non-transparent, the formula for the complex IR detector response signal S can be written as:

$$S = \varepsilon \cdot f(T_0) + (1 - \varepsilon) \cdot f(T_i), \tag{2.3}$$

where T is the object temperature, T_i is the ambient temperature, $\varepsilon f(T_0)$ – signal as a function of the object temperature, $(1-\varepsilon)f(T_i)$ – signal as a function of the ambient temperature.

In order to determine the non-transparent object temperature, the emissivity of this object, the ambient temperature and function $f(T)$ which is the calibration curve of an IR detector or the whole measurement instrument must be known.

In the experiments described hereafter, the temperature of the sample surface was determined using the Infrared Camera of the 680 type, manufactured by the AGA Company. It is equipped with the indium antimonide (InSb) IR detector. The response time of this detector is shorter than one microsecond. Its response sets in (2.5 – 5.5) μm range of wavelength.

The Infrared Camera principle of operation is as follows: an optical-mechanical scanner scans the tested surface and focuses the IR radiation on the InSb detector, which converts the IR signal into an electrical video one. The scanner gives the thermal image of the tested surface.

Operation of the Infrared Camera is modified by application of the PTR WIN System manufactured by the CEDIP Company. The PTR WIN consists of the digitiser and the PTR software. It allows to digitise the video signal into 12 bits digital one with sampling frequency of 1 MHz.

The thermal image is displayed on a computer screen. The PTR WIN System allows for digitising and then continuous storing of the film of IR images in the hard disc(16 frames per second). The PTR 9020 software allows for the digital processing of thermal images, for example: the temperature measurement along an arbitrarily selected line of the tested surface.

3. Experiments

The investigations of the thermomechanical couplings in the TiNi alloy during loading at temperature 310 K require the use of the temperature chamber. The contactless measurement of the sample temperature requires a window in the chamber, which is transparent for IR radiation in the (2.5 – 5) μm spectral range. The single crystal of silicon has got such a property.

The old chamber-equipment of the testing machine was adopted. There the glass window was replaced by a silicon one. The IR transmission of the silicon window in the (3 – 5) μm spectral range reaches 85%. Owing to this window, the IR radiation power emitted by the sample could be measured as a function of the deformation process parameters. The surface area, where the IR radiation power was measured, was blackened to ensure a homogeneous and known emissivity of the surface.

The calibration curve for Infrared Camera with silicon chamber window was obtained.

The experiment was performed on the thin-walled tube made of TiNi alloy (Fig. 1).

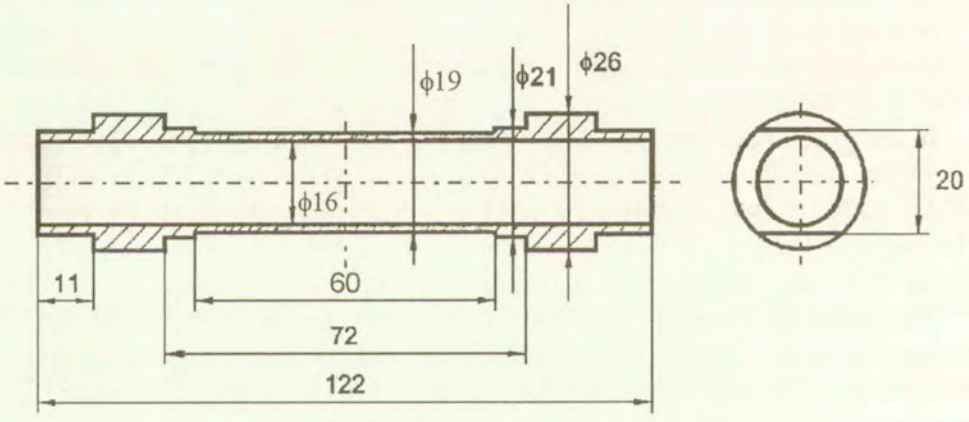

FIG. 1. The shape of the tested sample.

The temperature of the sample as function of effective stress during (1) – *torsion*, (2) – *tension*, (3) – *compression*, (4) – *simultaneous torsion* (shear stress) and *tension* (axial stress σ) ($m = \tau/\sigma = 1$) and (5) – *torsion* – *compression* ($m-1$) test at the chamber temperature 310 K was measured.

All tests have been carried out on the multiaxial Instron testing machine equipped with the MTS Test Star fully digital controller connected to the computer [3]. The sample was heated up to 343 K after each loading in order to recover the initial state of microstructure.

4. Results

Because of the cylindrical shape of the sample, only the temperature distribution along a generating line of the tested sample has been determined. Figure 2 shows the examples of the temperature distribution on the blackened area of the sample surface at $\sigma_0 = 0$ (Fig. 2a) and during the tension at $\sigma_2 = 198$ MPa (Fig. 2b), $\sigma_3 = 281$ MPa, at which the temperature increase was the highest (Fig. 2c). Fig. 3 shows the increase of the temperature as the difference between the temperature along the generating line at $\sigma = 198$ and $\sigma = 0$ MPa.

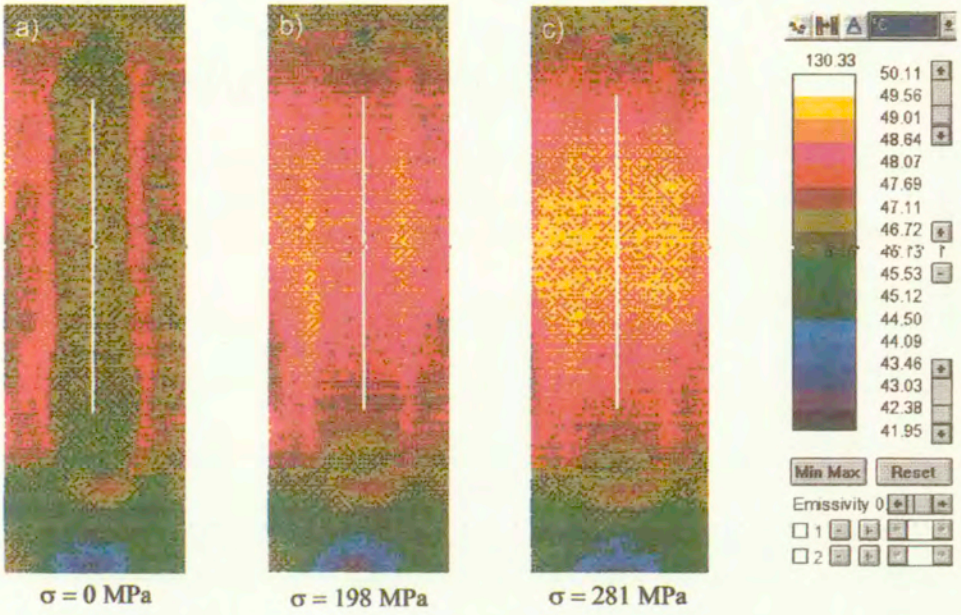

FIG. 2. Examples of thermal images of the sample during the tensile test of the TiNi shape memory alloy under constant stress rate = 1MPa/s.

It was observed that the temperature distribution along the generating line of the sample was approximately uniform. The temperature distributions along the generating line of the sample during other tested deformation paths were also uniform. It indicates that phase transition processes in the tested sample were almost homogeneous.

With the aid of Infrared Camera, the monitoring of the chamber temperature during loading and unloading was possible. The results of such monitoring are presented in Fig. 4. The chamber temperature variation (ΔT_{ch}) was about 0.2 K.

The strain-stress curves of TiNi shape memory alloy for five proportional stress-controlled loading paths are shown in Fig. 5. They exhibit clearly the pseudoelastic effect associated with the B2 $\leftrightarrow$ R transition. The area limited by

the strain-stress curve is close to the expended energy in the loading-unloading cycle. Figure 5 shows that this energy depends on the loading path. It is the highest during tension (Fig. 5, curve 2) and the lowest one during compression (curve 3). This fact can not be explained by the tested alloy anisotropy alone, because the third invariant of stresses in an individual loading path is not the same.

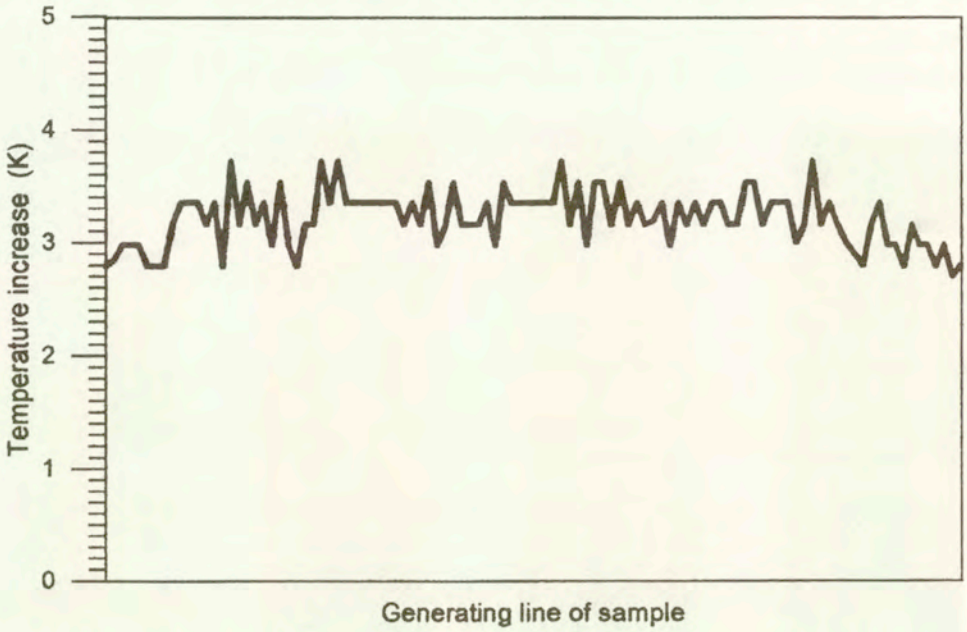

FIG. 3. The temperature increase distribution along the generating line of the sample of TiNi alloy at $\sigma = 198$ MPa during the tensile test at the chamber temperature of 310 K.

The expended energy is equal to the heat dissipated by the tested sample, provided that the state of the sample after unloading is recovered. However, the area limited by the strain-stress curve may, in general, be not equal to the total work done in the cycle [4].

The dissipated energy and the heat of phase transition generate variations of the sample temperature. It can be expected that when the hysteresis loop (shown in Fig. 5) is thicker, the maximal increase of sample temperature in the cycle is higher.

Thus, on the basis of the results presented in Fig 5 it can be expected that the temperature increase should be the greatest one in tension and the smallest one in compression.

The changes of average temperature along the generating line as the function of the effective stress are presented in Fig. 6 ($\sigma_{ef} = \sqrt{\sigma^2 + 3\tau^2}$, see reference [4]). The maximum of effective stress was equal to 290 MPa. In such a case only the

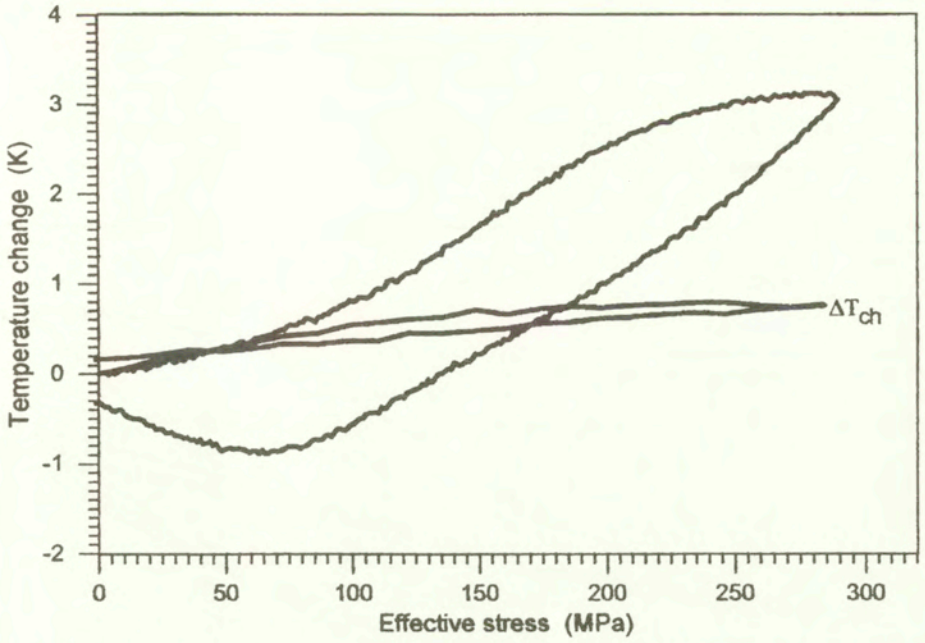

FIG. 4. The temperature change of the TiNi sample during tension and the chamber temperature variation (ΔT_{ch}) due to the temperature instability of the chamber used.

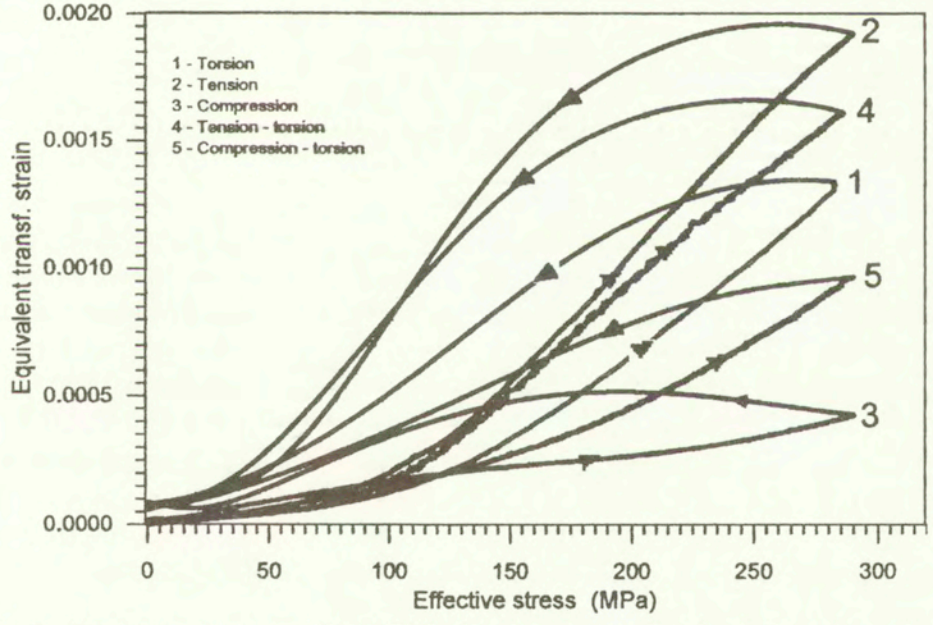

FIG. 5. Strain-stress curves of the TiNi shape memory alloy loaded at the constant stress rate = 1 MPa/s at 310 K.

B2 ↔ R phase transition is possible. The expectation has been confirmed by all the tested loading paths except the compression (Fig. 6, curve 3), where the increase of sample temperature is not the smallest one.

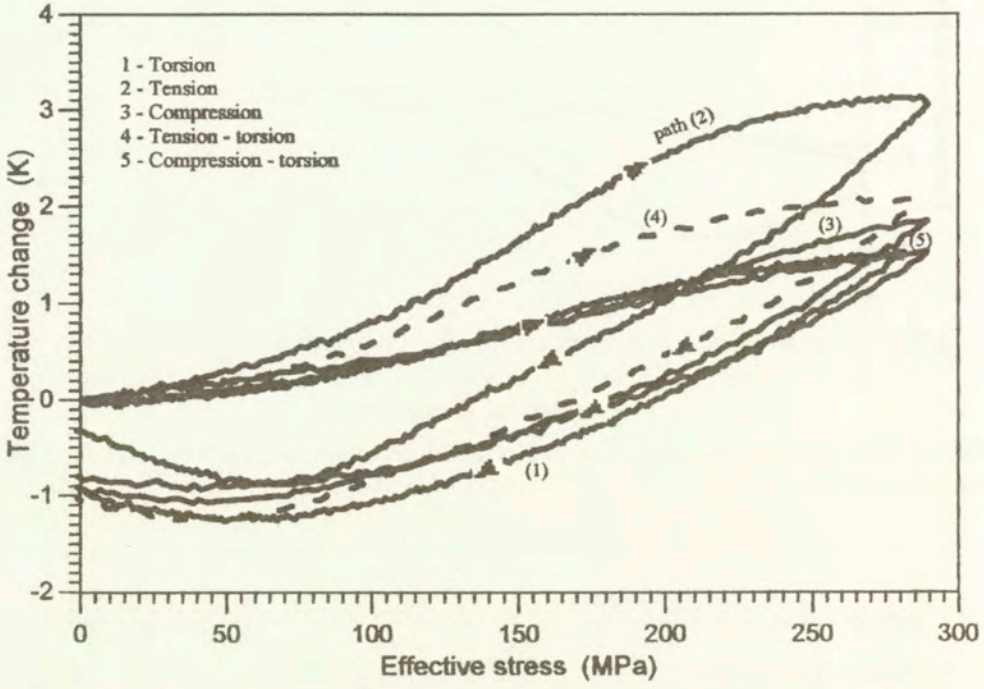

FIG. 6. The change of sample temperature vs. the effective stress during loading at constant stress rate = 1 MPa/s at 310 K.

It is known that the B2 ↔ R phase transition is exoenergic. The existence of the hysteresis loops proves that the process of deformation is dissipative. These effects cause the observed increase of the sample temperature in the course of loading. During unloading, the reverse transition R ↔ B2 takes place and the temperature of the sample decreases. It attains the value below the temperature of the chamber. Some energy was taken by the sample. We can observe that in the last stadium of unloading, the temperature of the sample started to rise (Fig. 6, curves 1, 2). This is related to the pure elastic behaviour of the investigated alloy. The sample is warmed by the environment.

The observed temperature variations suggest that progress of the B2 ↔ R phase transitions was most advanced in the tension test while the least advanced progress was observed during a pure shear (*torsion*) test.

The temperature changes of the tested sample during loading are shown in Fig. 7. It is observed that the reverse R ↔ B2 phase transitions in all of the tested loading paths proceed more rapidly than the B2 ↔ R phase transitions.

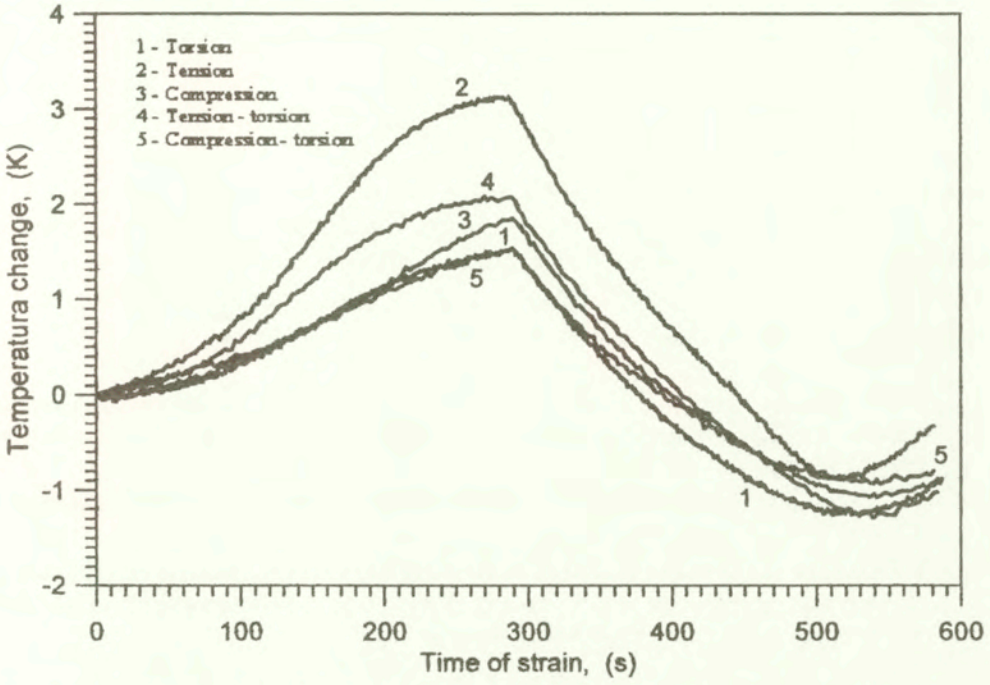

FIG. 7. The temperature change of the tested sample during the loading cycles for five proportional loading paths.

5. Some remarks concerning the results

The detection of IR radiation has been successfully applied to investigate the thermocouplings in the TiNi alloy during loading at temperatures higher than the room temperature.

It has been observed that the temperature distribution along the generating line of the sample during five different loading tests performed at constant rates is approximately uniform. It indicates that phase transition processes in the tested sample are homogeneous.

The energy expended during the loading-unloading cycle depends on the deformation path.

The temperature change of the sample under test ($\sigma_{ef\,\max} = 290$ MPa) shows that kinetics of the B2 $\leftrightarrow$ R phase transitions and the reverse ones are different; the R $\leftrightarrow$ B2 phase transitions proceeds more rapidly. It concerns all the tested deformation paths.

It has been found that progress of the B2 $\leftrightarrow$ R phase transitions was most advanced in tension while the least advanced progress is observed during the pure shear (*torsion*) and during the *compression-torsion* test ($\sigma_{ef\,\max} = 290$ MPa).

The effect of the deformation path on the expended energy is in accordance with the temperature change of the sample during the particular loading path, except the case of compression.

Acknowledgements

This work has been supported by State Committee for Scientific Research (Poland) under Grants No. 7T 07A 00513 and 7T 08A 025 11.

References

1. B. RANIECKI, S. MIYAZAKI, L. DIETRICH, K. TANAKA and CH. LEXCELLENT, *Deformation behaviour of TiNi SMA undergoing phase transition in torsion – tension (compression) tests*, Arch. Mech, (in print) 1999.
2. CH. LEXCELLENT, G. ROGUEDA, C. BOURBON, *Continuum Mech. and Thermodynamics*, **6**, 4, 1994.
3. B. RANIECKI, L. DIETRICH, Z. KOWALEWSKI, G. SOCHA, S. MIYAZAKI and A. ZIÓŁKOWSKI, *On experimental techniques used to investigate deformation behaviour of TiNi under complex stress state*, Arch. Mech, (in print) 1999.
4. B. RANIECKI, CH. LEXCELLENT, Eur. J. Mech., A/Solids, **13**, 1, 21–50, 1994.

Received April 28, 1999; revised version November 11, 1999.

Arch. Mech., **51**, 6, pp. 727–744, Warszawa 1999

Experimental methodology for TiNi shape memory alloy testing under complex stress state

B. RANIECKI ([1]), L. DIETRICH ([1]), Z.L. KOWALEWSKI ([1]), G. SOCHA ([1]), S. MIYAZAKI ([2]), K. TANAKA ([3]), A. ZIÓŁKOWSKI ([1])

([1]) *Polish Academy of Sciences*
Institute of Fundamental Technological Research,
Świętokrzyska 21, 00–049 Warsaw, Poland

([2]) *Institute of Material Science, University of Tsukuba*

([3]) *Tokyo Metropolitan Institute of Technology*

THE EXPERIMENTAL METHOD and preliminary results of multiaxial proportional loadings at a range of different temperatures are discussed for the TiNi shape memory alloy. The results are limited to the R-phase reorientation and transformation pseudoelasticity of the material tested at the selected constant temperatures. The main objective of the paper is to develop experimental knowledge of the shape memory alloy properties under complex stress states which would allow better understanding of the material behaviour and create a basis for theoretical modelling.

1. Introduction

THE PAPER DEALS with a research method of the TiNi shape memory alloy deformation behaviour under complex stress states at different temperatures. Experimental details concerning the test equipment, new gripping system, strain measurement system, test procedure and programme are presented. The raw experimental results in the concise graphical form are also given.

A detailed analysis and discussion of the obtained results are presented in the accompanying paper [1]. Although the paper [1] presents the state of affairs concerning shape memory alloys, and in particular with respect to their thermomechanical properties, engineering applications, testing and modelling, a short literature survey concerning the main idea of the planned experimental programme and investigation of the shape memory alloys under complex stress states is also given in this paper.

Increasing progress of the shape memory alloys (SMA) applications requires reliable theoretical descriptions of their thermomechanical behaviour. A number of authors have attempted to develop constitutive equations for a solid-solid phase transformation under applied stresses [2, 3, 4, 5, 6 and 7]. These theories are based mostly on the experimental results obtained under uniaxial loading conditions. Only a few experimental papers [8, 9, 10 and 11] deal with the phase transformation phenomenon under multiaxial loading of such shape memory materials as Cu-based, Fe-based and TiNi alloys.

In the TiNi alloys, the shape memory effect and transformation pseudoelasticity appear due to the martensitic transformation and the rhombohedral phase reorientation [12]. The knowledge of the thermomechanical behaviour of the TiNi shape memory alloys associated with such effects as the reorientation of the R-phase and the stress-induced martensitic transformation becomes to be a crucial point in all engineering applications of that type alloys and creates a basis for their theoretical modelling. Such knowledge can be achieved from experiments performed under complex stress states.

Mechanical testing of materials under combined stress states is usually realised on a thin-walled tubular specimen subjected to axial force, torque and/or internal pressure. This kind of specimen reflects well the current state-of-the-art for biaxial testing. The thin-walled tubular specimen allows the known biaxial stress states to be generated to satisfy the basic testing conditions as closely as possible. Since for this kind of testing technique a region of homogeneous stress can be known directly from the measured external loads applied to the specimen, the strain state may be independently measured in the homogeneously stressed region.

Majority of the reported results of mechanical testing of SMA were carried out using rather small specimens in comparison to the specimen size usually applied in the testing of standard structure materials. It follows from certain limitations of the manufacturing procedure used to produce the SMA specimen which is often trained in order to attain a stable performance. For this reasons, an outer diameter of the thin-walled specimen used in experimental study of SMA under multiaxial loading conditions usually does not exceed 8 mm [8, 11].

In this paper the experimental method and the preliminary results of multiaxial proportional loadings at a range of different temperatures are discussed for the TiNi shape memory alloy. It exhibits stable and isotropic thermomechanical properties at room temperature. It has to be mentioned however, that these properties are strongly dependent on the temperature and the stress level, since the material exhibits a thermal and stress-induced phase transformations. The material and specimen used in the project were prepared by the Japanese partner of the Japanese-Polish co-operative study on Testing and Modelling the Behaviour of Shape Memory Alloys. A procedure to obtain the material and a process of the specimen preparation are reported elsewhere [13].

The known biaxial stress method [14, 15, 16] is adopted to investigate the TiNi shape memory alloy. A description of the experimental setup and testing procedure applied as well as the raw experimental data from multiaxial tests are presented.

The main objective of the study is to fill the gap between theory and experiment by reporting recent experimental results obtained on the TiNi shape memory alloy, which was subjected to the phase transformations under complex stress states. The results reported here are limited to the reorientation of the R-phase and the transformation pseudoelasticity at the selected constant test temperatures.

2. Experimental details

2.1 Material and specimen

The tests were performed on the thin-walled tubular specimen manufactured from 28 mm rod of the Ti-51.0at%Ni polycrystalline alloy prepared by the Institute of Materials Science at University of Tsukuba [13]. The alloy was designed by careful adjusting the composition and selecting an appropriate heat treatment to realise a very stable response to the thermomechanical loading. The thermomechanical training was not necessary for the alloy before testing, and this fact distinguishes it from the majority of the other shape memory alloys tested so far. Although the thermomechanical training was not applied, the thermomechanical properties of the material enabled multiple application of the same specimen without any fear of accumulation of some irreversible structural variations. Such a response can be achieved if some precautions are undertaken during the thermomechanical loading. The specimen should not be overloaded. Moreover, after each cycle of the loading/unloading process, the specimen have to be heated up to the desired temperature in order to remove any residual strain.

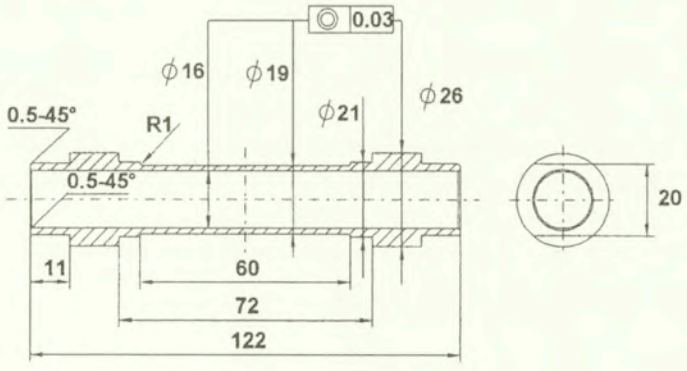

FIG. 1. Geometry of the specimen.

The engineering drawing of the specimen is shown in Fig. 1. It was etched by acid solution after machining and was left in the unstressed state at room temperature for one month before testing. The specimen was designed in the form of the thin-walled tube in order to avoid buckling during compression and to ensure the ratio of a thickness to outer diameter to be as small as possible, and moreover, to enable its fit into the mechanical gripping system prepared specially for the project. The specimen dimensions were adapted to the maximum axial and torsion loading capacities of the testing machine used, assuming that the tested material would be able to carry the stress level up to 1000 MPa.

Two small marks were punched on the 20 mm diameter cylindrical surfaces located on the specimen close to its gauge length. The distance between the marks and their mutual rotation were measured before testing and these values have been subsequently used to control whether the specimen was not accidentally overloaded and whether all the remaining strains were removed. The entire programme of tests consisting of 46 thermomechanical loading and unloading cycles was performed on the single specimen. After the entire history of loading, the distance between two marks was changed only by 0.02 mm with respect to the initial one, and in the perpendicular direction the mutual position of these marks was changed by the angle equal to $0°6'$ only.

Since full description of the material, the specimen preparation procedure, and selected preliminary alloy properties are reported in detail elsewhere [13], in Table 1 are given only these basic transformation temperatures determined by the differential scanning calorimetric tests [12] which were useful for planning an experimental programme.

Table 1.

Parameters for the R-phase transformation		Parameters for the martensitic transformation	
$R_s = 306$ K,	$R_f = 293$ K,	$M_s = 253$ K,	$M_f = 208$ K,
$RA_s = 305$ K,	$RA_f = 316$ K,	$A_s = 268$ K,	$A_f = 306$ K.

Notations in the Table: R_s – R-phase transformation start, R_f – R-phase transformation finish, M_s – martensitic transformation start, M_f – martensitic transformation finish, A_s – austenitic transformation start, A_f – austenitic transformation finish, RA_s – start of the R-phase to austenitic transformation, RA_f – finish of the R-phase to austenitic transformation.

2.2 Experimental setup

The combined tension/compression – torsion experiments were performed using the Instron 1343 servohydraulic biaxial loading frame, with 100 kN and

1000 Nm loading capacities. A control of the axial load and torque were achieved using two independent control loops of the fully digital controller (MTS TestStar II) coupled with the actuator servovalves of the loading frame. It was connected to the PC computer, thus enabling on-line control of the system.

The axial stress/strain and the torsional stress/strain signals could be controlled either independently or simultaneously using the controller. The selected signals measured during the test provided a feedback to the machine control loops. The software enabled the maintenance of constant effective stress or strain rates during loading in the whole range of deformation including stress-induced phase transformation. All tests were performed in the stress control mode under proportional and isothermal conditions. The stress rate was kept constant and equal to 1 MPa/sec during conducting each of the tests under consideration.

The axial force and the torque applied to the specimen were measured using loading cells incorporated in the machine. The uniform stress state had two nonzero components, namely the axial stress (σ_z) and the shear stress (τ). They were on-line calculated during a test using the following expressions:

$$\sigma_z = \frac{4F}{\pi(D^2 - d^2)}, \qquad \tau = \frac{16MD}{\pi(D^4 - d^4)},$$

where F denotes axial load, M – torque, D and d – outer and inner diameter of the specimen, respectively.

An average uniform strain (ε_{ij}) can be determined if the axial strain (ε_z), shear strain ($\varepsilon_{z\Theta}$), hoop strain (ε_Θ), and the radial strain (ε_r) are known. Three components of strain, i.e. the axial, shear and hoop strains were independently measured by the electrical resistance strain gauges bonded to the middle part of the specimen gauge length. The strain measurement nominal range of the strain gauges applied was equal to 10%. The radial component of strain was determined on the basis of incompressibility assumption.

The measured stress and strain signals delivered to the controller via a multiple analogue-to-digital converter provided the controlled quantities of the axial and shear stresses. In this way three strain components could be achieved. These components represented the response of the specimen to the loading programme applied. In order to enable a numerical elaboration of the experimental results, all the data, i.e. an axial displacement, rotation of the lower grip, two stress components (σ_z, τ), and three strain components (σ_z, $\sigma_{z\Theta}$, σ_Θ) were recorded as a function of time by the PC computer.

The loading train including the specimen was placed in the temperature chamber with the objective to obtain a homogeneous temperature field in the whole specimen. The chamber enables both a heating of the specimen up to 573 K by an electrical heater and its cooling down to 200 K using compressed CO_2. The required testing temperature inside the chamber was controlled within

±0.5 K using the 3110 type Instron controller. An additional temperature measurement system was also applied. It enabled the temperature measurements at the upper and lower part of the specimen gauge length by means of two K-type (chromel-alumel) thermocouples connected to a microprocessor-based thermometer. Temperature readings at both points of the outer surface in the specimen gauge length enabled us to maintain a temperature uniformity within a range of 1 K at the loading - unloading cycle.

2.3 Specimen fixing system

A new gripping system was designed to carry out the experimental programme devoted to the investigation of the TiNi shape memory alloy. It enabled high axiality of the specimen during loading by means of the simultaneous backlash elimination in the axial and torsional directions. The advantage of this system relies on its universality, i.e. it may be successfully used not only to perform tests under static loading, but also to carry out investigations realised under reverse cyclic loading tests at a wide range of temperatures.

2.4 Strain measurement system

During each test three strain components were measured using three independently operated electrical strain gauge circuits. The system consisted of two strain gauge rosettes and two uniaxial strain gauges cemented to the outer surface in the middle part of specimen. It also comprised four additional separate strain gauges located on a special compensator designed in the form of a semi-ring, which was used for temperature compensation in the axial and hoop directions. The rosettes were located on opposite sides of the specimen gauge length with respect to the symmetry axis of the specimen in order to remove the influence of bending on the strain measurements. Two uniaxial strain gauges responsible for strain measurements in the circumferential direction were located in the similar manner, however, their positions were angularly shifted up to 90° with respect to the set of rosettes.

A scheme of the mutual position of strain gauges on the gauge length of the specimen and the semi-ring is illustrated in Fig. 2. As it is seen in this figure, the three strain gauges in both of the 45° rosettes were arranged in such a manner that one strain gauge was aligned with the longitudinal axis of the specimen, while the other two gauges made a 45° angle symmetric with respect to the longitudinal gauge. Thus, such a strain measurement system enabled independent monitoring of axial, shear and hoop strains by means of three full bridge circuits. The shear strain measurement system consisted of four strain gauges which made a 45° angle with respect to the symmetry axis of the specimen. The axial strain measurement

system also consisted of four strain gauges. In this case however, the circuit was created using those strain gauges of each rosette which were aligned with the longitudinal axis of the specimen and two additional strain gauges bonded to the surface of the semi-ring. Similar system was used to measure the strain in the hoop direction.

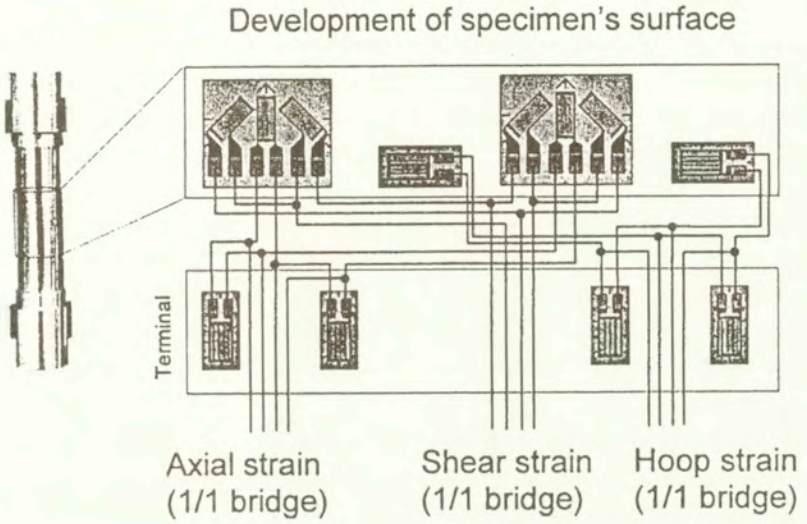

FIG. 2. Strain measurement system.

All strain measurement systems were completely temperature compensated provided that the specimen and the semi-ring have the same temperature and the same thermal properties.

Before running the tests, all strain measurement circuits were calibrated using a shunt calibration technique. Shunting resistors were selected to simulate 80% of the measuring range that was 2% for the axial and shear strains, and 1% for the hoop strain. All the signals were shunted to simulate the positive and negative signals. The output signals of the circuits were amplified to give in the controller the values equal to 10 V which represented the full range of the transducers.

3. Experimental procedure

Main programme of the single thermomechanical cycle of loading comprised the following steps:

1. Fixing the specimen in the testing machine and connecting the temperature and strain gauge measuring systems.

2. Cooling or heating the temperature chamber to the required temperature

under constant rate equal to 5 K per minute. The control system held constant values of the axial and shear stresses at zero level during cooling or heating.

3. Holding a constant value of the temperature for at least 30 minutes until the desired temperature was achieved at two measuring points of the specimen.

4. Loading the specimen along the selected proportional path of the two-dimensional stress space (σ_z, τ) at the desired constant temperature until the required value of the equivalent stress is attained.

5. Unloading the specimen up to the zero level of the axial and shear stresses for the same constant temperature as that during the loading step.

6. Heating the specimen up to 343 K while the control system holds the axial and shear stresses at zero level. The heating removes any remaining strain produced by the former loading process.

7. Cooling the specimen together with the chamber down to the room temperature.

In order to investigate the thermomechanical properties of the TiNi shape memory alloy in the range of reorientation of the R-phase, the experiments were carried out for five loading paths at three different temperatures equal to 260 K, 280 K and 300 K.

Experimental programme also included investigations of the thermomechanical properties of the TiNi shape memory alloy in the range of the transformation pseudoelasticity. In this case the tests were carried out for five loading paths at temperatures equal to 310 K, 311.5 K, 315 K and 322.5 K. Since the results for the temperature equal to 311.5 K do not differ from those for the 310 K achieved, their presentation will be omitted in this paper.

Tests for five different loading paths in the two-dimensional stress space (σ_z, τ) were carried out for each of the testing temperatures under consideration, i.e. path No. 1 – pure torsion with axial stress equal to zero, path No. 2 – uniaxial tension with shear stress equal to zero, path No. 3 – uniaxial compression with shear stress equal to zero, path No. 4 – proportional loading under combination of tension and torsion with constant ratio of shear and axial stress components equal to 1, path No. 5 – proportional loading under combination of compression and torsion with constant ratio of shear and axial stress components equal to -1, Fig. 3.

The equivalent stress and equivalent strain based on the definitions of the second invariant of stress and strain tensors, respectively, were calculated in order to control the loading process during all the tests. These quantities enabled on-line observation of the stress-strain curve course. For each proportional path, the loading process of the specimen was stopped when an increase of the specimen rigidity was observed on the monitored equivalent stress-equivalent strain diagram. This procedure allowed the characteristic stage of the material deformation depending on the stress state type to be achieved. Thanks to this procedure,

it was not necessary to define in advance a final loading point at different paths taken into account. The programme started automatically an unloading process when the operator decided to stop the loading process. Duration times of the unloading and loading periods were the same.

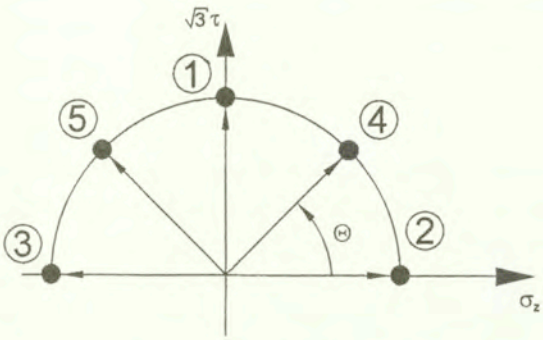

FIG. 3. Scheme of the loading programme.

4. Experimental results

An attempt was made to reflect well the principal characteristics of the deformation behaviour of the TiNi shape memory alloy at the range of the reorientation of the R-phase and transformation pseudoelasticity under complex stress states, and to present the results in the unconverted form. In the paper only raw data are presented in the concise graphical form, and no theoretical assumption has been made in the applied data processing. The expressions given above for the equivalent stress and equivalent strain were applied to qualitative evaluation of a stress-strain curve. The only assumption which is taken into account in the paper and it is usually assumed in all reported experiments of this kind, deals with the uniformity of stress and strain distributions in the measuring part of the specimen. More complete analysis of the reported observations and their data processing at the range of the reorientation of the R-phase are presented in the accompanying paper [1]. Analysis of the obtained results at the range of transformation pseudoelasticity is in progress and will be presented in a further paper.

The main goal of the paper is to evaluate the influence of the type of stress state and temperature on the mechanical properties of the TiNi shape memory alloy. Two ranges of testing temperature were taken into account. In the first one (260 K to 300 K), the reorientation of the R-phase is observed while in the second range (310 K to 322.5 K) the transformation pseudoelasticity appears. Since five various stress states were investigated for both temperature ranges, an influence of the stress state on the mechanical properties of the TiNi alloy could be well

evaluated. The results of these tests are shown in Figs. 4, 5, 6, 7. In order to keep the comparison of the results clear, only the absolute stress and strain magnitudes are exposed. Figures 4 and 5 present the results obtained at the temperatures equal to 260 K, 280 K and 300 K whereas in Figs. 6 and 7 the experimental data from tests carried out at 310 K, 315 K and 322.5 K are shown. Figures 4 and 6 present the loading paths in the stress and strain spaces. The data shown in both these figures are again presented in Figs. 5 and 7, respectively, however in this case both figures show the components of stress versus components of strain. The upper left diagram in Fig. 4 presents five proportional loading paths in the two-dimensional stress space (σ_z, τ). The upper right diagram in this figure represents the strain responses in to the stress-controlled loading processes shown in the just mentioned diagram. The strain responses are given in the form of plots of the shear and hoop strains versus axial strain (heavy and thin lines, respectively). Numbers in Fig. 4 denote loading paths realised in the programme of the tests previously shown in Fig. 3. Firstly, the loading paths at stress and strain spaces are presented, and secondly both components of stress are shown as a functions of the respective strain components.

Except for several tests conducted at the beginning of the project realisation, (e.g. the results of tests for the paths No. 1, 4, 5 at the temperature equal to 260 K), reproducibility of the loading paths programmed in the stress space was almost satisfactory. The reasons of some deviations from the straight line, and differences observed between the loading and unloading processes, were connected with the selection of too low system parameters for machine control. Such a configuration of the control parameters was initially proposed for the safety reasons in order to avoid an accidental excitation of the machine, and in consequence, a damage of the specimen. Tuning procedure of the PID regulator was repeated and improved after each cycle of loading until the optimal values of the control parameters were achieved. Reproducibility of the loading paths programmed in the stress space was improved in this way after each cycle of loading. After a few successive cycles it became quite satisfactory. It can be observed for tests conducted at the temperature equal to 300 K (Fig. 4). It is worth to mention that such improvement was obtained despite the fact that the maximum stress did not exceed 80 MPa, which corresponds to a rather small value of the load equal to 6.6 kN. This makes only 6.6% of the total loading capacity of the testing machine used.

An influence of the type of stress state on the deformation behaviour of the TiNi shape memory alloy in the range of the reorientation of the R-phase is well reflected in both types of diagrams presented. The strain response of the material on the programme of proportional loadings is more complex than that observed for the standard structure materials. Even pure torsion or uniaxial tension and compression produces complex strain state with a cross-effect. Strain paths are

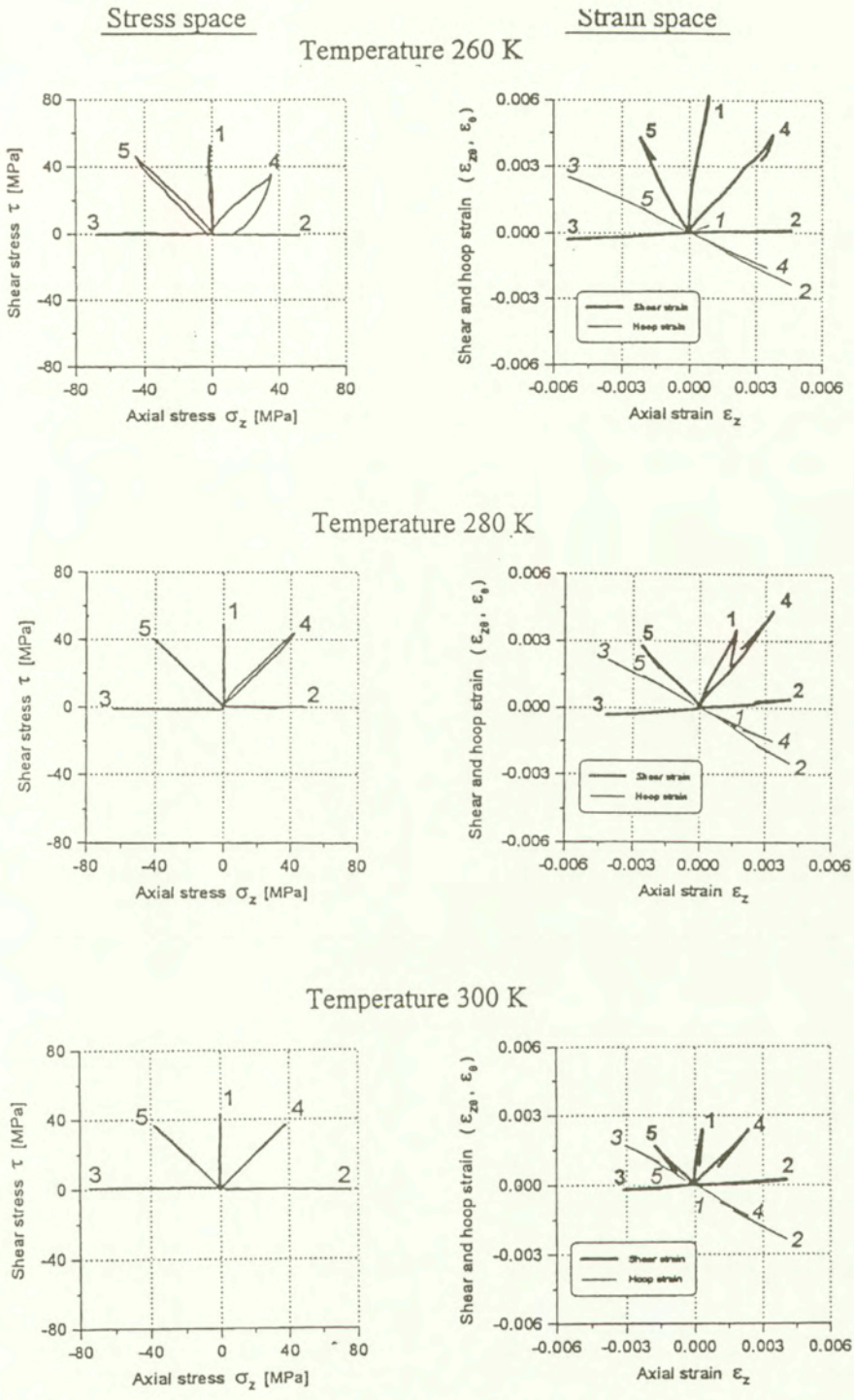

FIG. 4. The results for the TiNi alloy tested in the range of the R-phase reorientation for temperatures equal to 260 K, 280 K, 300 K.

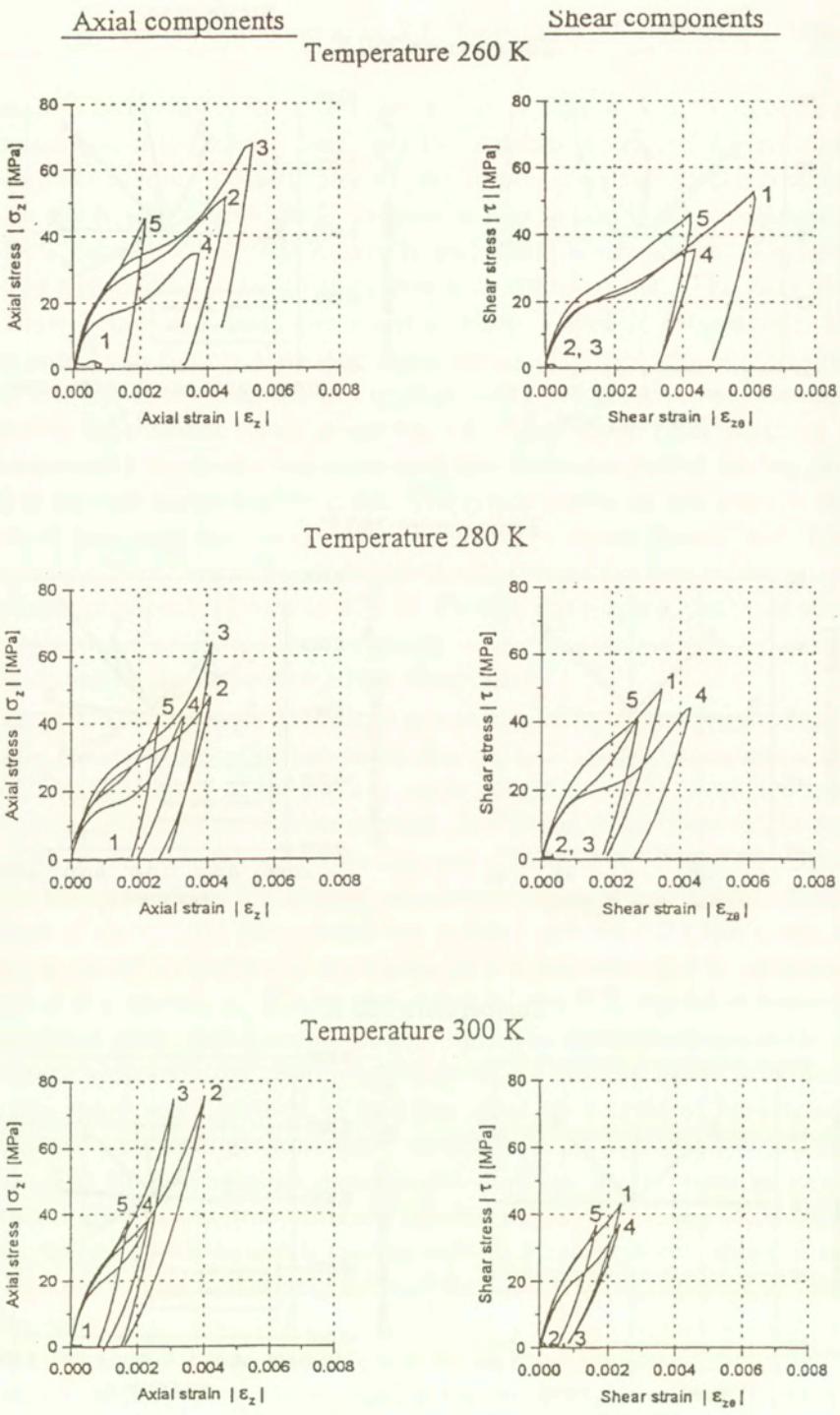

FIG. 5. Stress-strain curves for the TiNi alloy tested in the range of the R-phase reorientation for temperatures equal to 260 K, 280 K, 300 K.

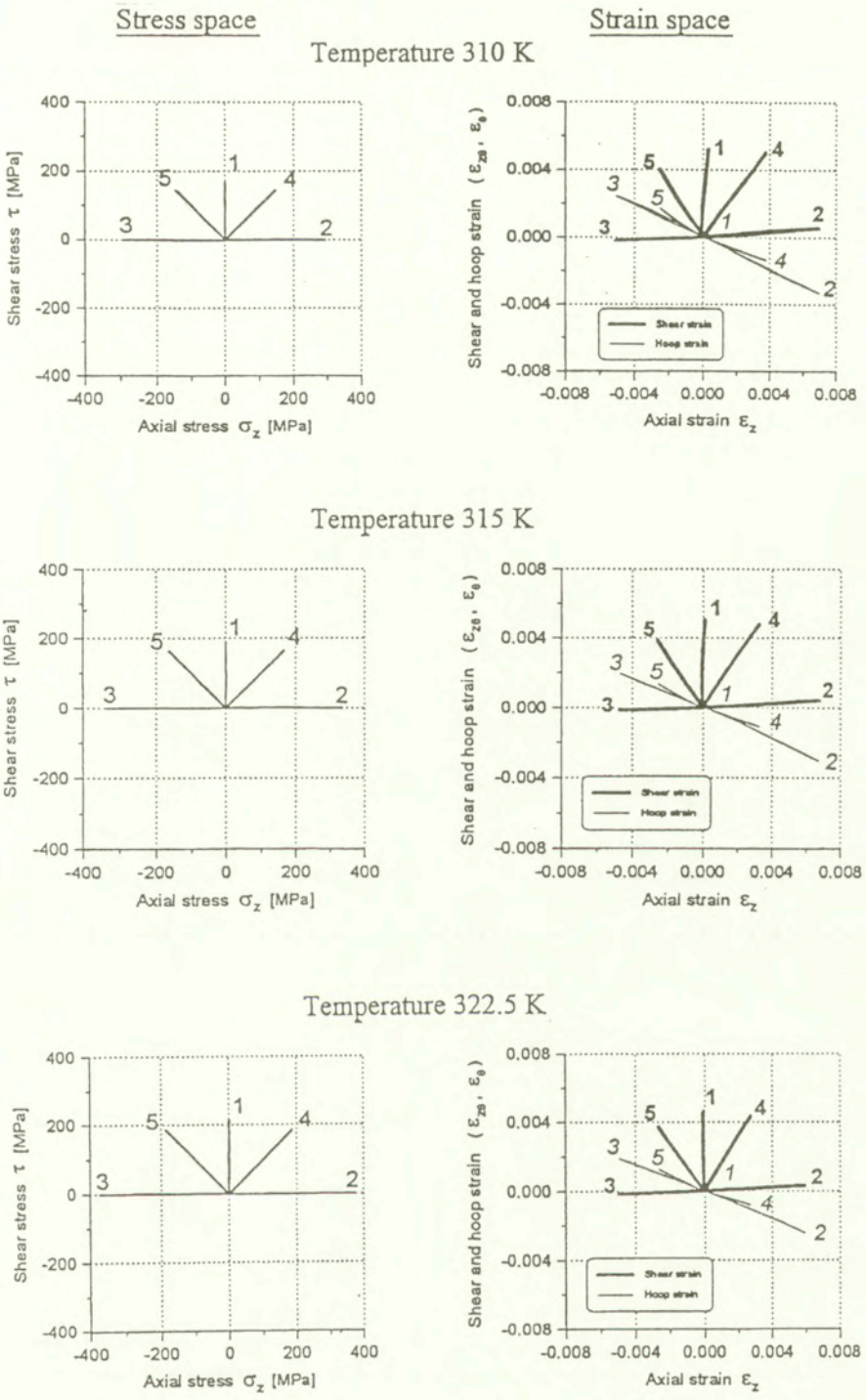

FIG. 6. The results for the TiNi alloy tested in the range of the transformation pseudoelasticity for temperatures equal to 310 K, 315 K, 322.5 K.

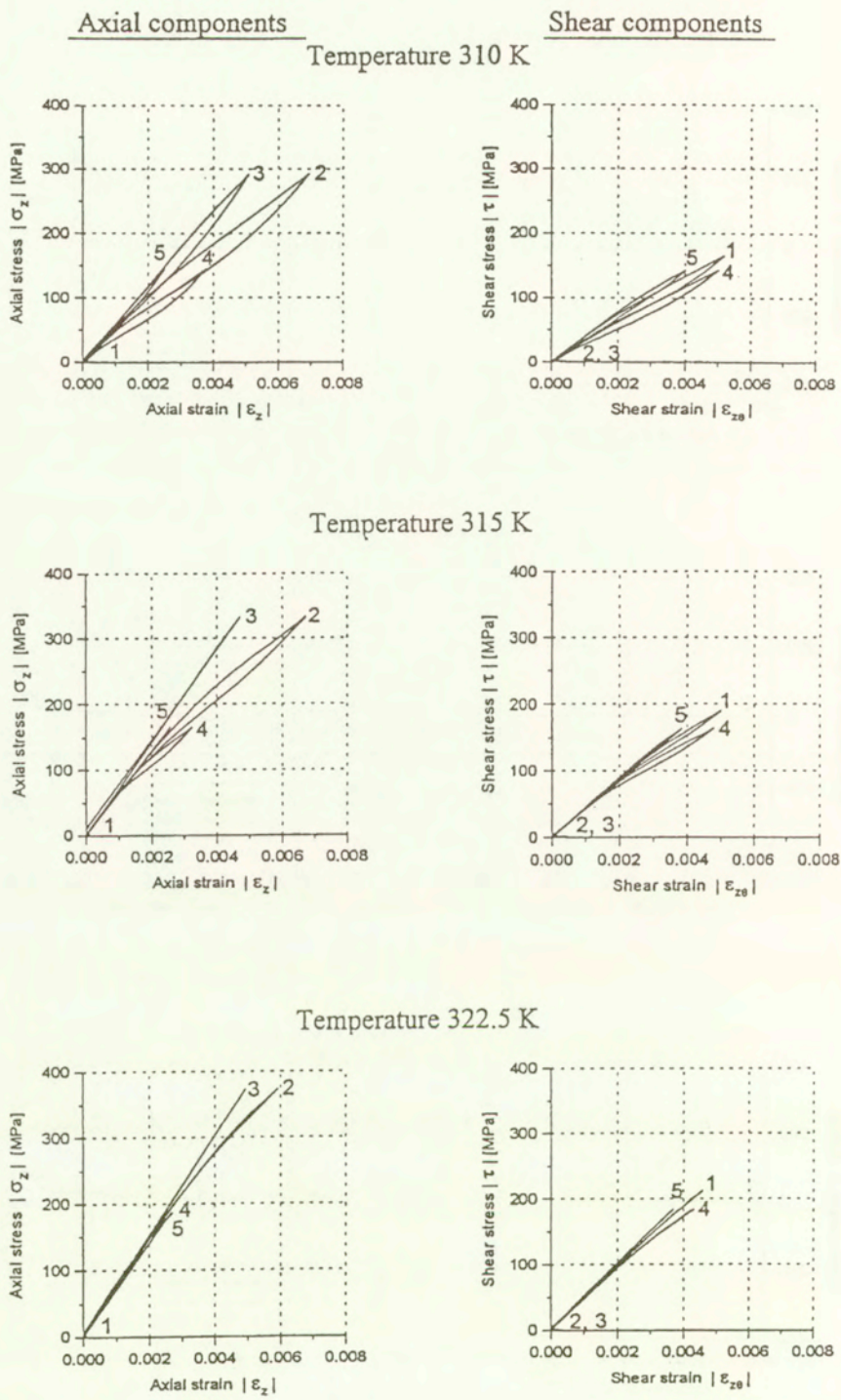

FIG. 7. Stress-strain curves for the TiNi alloy tested in the range of the transformation pseudoelasticity for temperatures equal to 310 K, 315 K, 322.5 K.

deviated from the straight lines and axial and hoop strains are produced at pure torsion while in the case of uniaxial tension or compression the shear strain appears. This indicates a directional feature of the R-phase reorientation, which may be attributed to the influence of the third invariant of the stress tensor. However, it may be also responsible for development of anisotropic properties of the TiNi shape memory alloy.

The effect of the stress state type on the deformation process of the TiNi alloy is also pronounced in the stress-strain diagrams obtained for different stress states, Fig. 5. The axial and shear stresses as functions of the respective strain components are presented for all five loading paths and three temperatures. The results clearly show an asymmetrical effect observed in comparison of the tension and compression tests. In all cases the stress-strain curve representing the uniaxial compression (curve 3) is located above the curve representing the uniaxial tension (curve 2). Moreover, the stress-strain curves for both components of the 5th path are located above the respective stress-strain curves of the 4th path, despite the fact that the 4th path is symmetrical to the 5th path with respect to shear stress axis, Fig. 3. Studying diagrams shown in Fig. 5 it is easy to note the cross-effects, that is during the pure torsion tests (path No 1) besides the shear strain component, also the axial strain component appears. Such a phenomenon for the standard structure materials is usually called the second order effect. It can be also observed in the case of uniaxial tension (path No 2) and uniaxial compression (path No 3). For these loading paths it is expressed in the form of some small twist of the specimen. As it is clearly shown in Fig. 5, the cross-effects are dependent on the temperature. It is also visible that a permanent strain remains after full unloading for the temperatures equal to 260 K, 280 K and 300 K. Besides the temperature, the magnitude of this strain strongly depends on the type of the stress state. According to the results obtained in the experimental programme, the permanent strain in the case of the compression loading path is smaller than that for the uniaxial tension test achieved under the same stress level. An influence of the type of stress state on the deformation process of the TiNi alloy was also evaluated in the range of the transformation pseudoelasticity. The results are summarised in Figs. 6 and 7. The loading paths in the two-dimensional stress space and the material response in to these loading conditions in the strain space are presented in Fig. 6 for three different testing temperatures equal to 310 K, 315 K and 322.5 K. The shear and hoop strains versus axial strain are plotted by heavy and thin lines, respectively. As it is seen in Fig. 6, a reproducibility of the loading paths programmed in the stress space is much better than that obtained for the experiments carried out to investigate the TiNi alloy in the range of the R-phase reorientation. It has to be emphasised however, that the tests in the range of the transformation pseudoelasticity were carried out under much higher stress levels than the experiments concerning the

range of the R-phase reorientation. The maximum tension stress level was close to 400 MPa. It corresponds to the magnitude of axial loading equal to 33 kN and means that 33% of the total loading capacity was used.

The strain paths presented in Fig. 6 deviate slightly from the straight lines. The cross-effects are not so clear as those observed for the material tested in the range of the R-phase reorientation. It means that during pure torsion, only very small axial and hoop strains can be observed, and also at uniaxial tension or uniaxial compression the values of shear strains were negligibly small.

In Fig. 7 the same stress-strain results are presented, however, in a different form than in Fig. 6. Namely, there are shown diagrams of axial and shear components for all the loading paths considered. Looking at the diagrams presented in Fig. 7 it has to be noted that the TiNi alloy does not exhibit any permanent strain after the total unloading. This effect differs from that obtained for the material tested in the range of reorientation of the R-phase. Similarly to the tests carried out at the temperatures equal to 260 K, 280 K and 300 K, the material behaviour in the range of the transformation pseudoelasticity strongly depends on the type of the stress state. The stress-strain curves and the width of the hysteresis loops shown in Fig. 7 are dependent on the stress state. The effect is sensitive to the temperature variations.

5. Conclusions

1. The results of the experimental tests carried out under complex stress states proved a significant influence of the stress state type on the mechanical properties of the TiNi shape memory alloy at both temperature ranges considered. In the first one, the stress-induced reorientation of the R-phase takes place whereas in the second one the transformation pseudoelasticity is observed.

2. The type of stress state plays an essential role during the testing of TiNi alloy. It has been experimentally proved that the stress state have an influence on the

- stress-strain curve,
- value of the axial and torsional threshold stresses which correspond to the beginning of the phase transformations,
- type of strain response to the proportional loading,
- magnitude of permanent strains remaining after unloading in the case of testing the material in the range where the reorientation of the R-phase occurs,
- width of the stress-strain hysteresis loop in the range of the transformation pseudoelasticity.

3. The material shows the tension-compression asymmetry.

4. The multiaxial strain response to the proportional loading under uniaxial

tension and pure torsion identifies a directional feature of a deformation induced by means of the R-phase reorientation.

5. Because of the directional character of the phase transformation during deformation, the mechanical properties of the TiNi alloy should be investigated under complex stress states. Even under uniaxial loading conditions all strain components have to be measured.

6. Application of five loading paths in the two-dimensional stress space to test the TiNi alloy provides an excellent opportunity to determine a part of a threshold transformation stress surface. Such a surface would be determined in the same way as the yield surface for the standard structure materials.

7. The experimentally justified effects for the TiNi alloy may be useful during a future development of new constitutive models attempting to predict a true material behaviour of the shape memory alloys. The constitutive equations for the stress-induced martensitic transformation elaborated so far are not able to predict the observed influence of the stress state on the deformation process of this kind of materials.

Acknowledgements

This work was financially supported by the Polish State Committee for Scientific Research through the research project KBN Nr 7T07A00513.

References

1. B. RANIECKI, S. MIYAZAKI, K. TANAKA, L. DIETRICH and CH. LEXCELLENT, *Deformation behaviour of TiNi shape memory alloy undergoing R-phase reorientation in torsion-tension (compression) tests*, see this issue of Arch. Mech., **51**, 6, 745–773, 1999.
2. F. FALK, *Model free energy, mechanics, and thermomechanics of shape memory alloys*, Acta Metall., **28**, 1773–1780, 1980.
3. K. TANAKA, S. KOBAYASHI and Y. SATO, *Thermomechanics of transformation pseudoelasticity and shape memory effect in alloys*, Int. J. Plasticity, **2**, 59–72, 1986.
4. I. MÜLLER, *On the size of the hysteresis in pseudoelasticity*, Continuum Mech. Thermodyn., **1**, 125–142, 1989.
5. C. LIANG and C.A. ROGERS, *One-dimensional thermomechanical constitutive relations for shape memory materials*, J. Intell. Mater. Syst. Struct., **1**, 207–234, 1990.
6. B. RANIECKI, CH. LEXCELLENT and K. TANAKA, *Thermodynamical model of pseudoelastic behavior of shape memory alloys*, Arch. Mech., **44**, 261–268, 1992.
7. B. RANIECKI and CH. LEXCELLENT, *RL-models of pseudoelasticity and their specification for some shape memory solids*, Euro. J. Mech., A/Solids, **13**, 21–50, 1994.
8. M. TOKUDA, P. SITTNER, M. TAKAKURA and YE MEN, *Experimental study on performances in Cu-based shape memory alloy under multiaxial loading conditions*, Materials Sci. Research Int., **1**, 260–265, 1995.

9. C. ROGUEDA, CH. LEXCELLENT and L. BOCHER, *Experimental study of pseudoelastic of a CuZnAl polycrystalline shape memory alloy under tension-torsion proportional and non-proportional loading tests*, Arch. Mech., **48**, 1025–1045, 1996.

10. F. NASHIMURA, N. WATANABE, T. WATANABE and K. TANAKA, *Transformation conditions in an Fe-based shape memory alloy under tensile-torsional loads: Martensite start surface and austenite start/finish planes*, Materials Sci. Engng A, **264**, 232–244, 1999.

11. K. JACOBUS, H. SEHITOGLU and M. BLAZER, *Effect of stress state on the stress-induced martensitic transformations in polycrystalline Ni-Ti alloy*, Metall. Mater. Trans. A, **27A**, 1–8, 1996.

12. S. MIYAZAKI and K. OTSUKA, *Deformation and transition behavior associated with the R-phase in Ti-Ni alloys*, Metall. Trans. A, **17A**, 53–63, 1986.

13. K. TANAKA, K. KITAMURA and S. MIYAZAKI, *Shape Memory Alloy Preparation for Multiaxial Tests and Identification of Fundamental Alloy Performance*, see this issue of Arch. Mech., **51**, 6, 745–784, 1999.

14. L. DIETRICH, Z.L. KOWALEWSKI, *Experimental investigation of an anisotropy in copper subjected to predeformation due to constant and monotonic loadings*, Int. J. Plast., **13**, 1–2, 87–109, 1997.

15. Z.L. KOWALEWSKI, M. ŚLIWOWSKI, *Effect of cyclic loading on the yield surface evolution of 18G2A low-alloy steel*, Int. J. Mech. Sci., **39**, 51–68, 1997.

16. Z.L. KOWALEWSKI, *Assessment of cyclic properties of 18G2A low-alloy steel at biaxial stress state*, Acta Mechanica, **120**, 71–89, 1997.

Received August 8, 1999; revised version October 26, 1999.

Arch. Mech., **51**, 6, pp. 745–784, Warszawa 1999

Deformation behaviour of TiNi shape memory alloy undergoing R-phase reorientation in torsion-tension (compression) tests

B. RANIECKI ([1]), S. MIYAZAKI ([2]), K. TANAKA ([3]),
L. DIETRICH ([1]) and C. LEXCELLENT ([4]),

([1]) *Polish Academy of Sciences*
Institute of Fundamental Technological Research,
Świętokrzyska 21, 00–049 Warsaw, Poland
E-mail: braniec@ippt.gov.pl

([2]) *University of Tsukuba, Japan*

([3]) *Tokyo Metropolitan Institute of Technology, Hino/Tokyo, Japan*

([4]) *LMARC-UMR CNRS 6604 UFR Sciences, Besançon, France*

THE DEFORMATION BEHAVIOUR associated with the R-phase reorientation is investigated in a Ti-51.0 at%Ni polycrystalline shape memory alloy under the torsion-tension (compression) stress state, and special theoretical framework is developed to describe the observed alloy performance. The limit condition to start the reorientation process, represented as a surface on the axial stress-shear stress plane, is determined for the proportional loading path. The result is well described, not by the Huber-Mises condition (the J_2-theory) but by the model (the J_3-theory), by taking into account the third invariant of stress deviator through the concept of the shape function. The values of the shape function are determined experimentally. The basic experimental features of the deformation in the R-phase, such as the flow rule, the ratios of the reorientation strain rates and the dimensionless ratio of the reorientation work, are compared with the predictions of theories that neglect the effects of pressure, compressibility of reorientation strains and effects of induced anisotropy. The J_3-theory turns out to be more realistic than the J_2-theory.

Keywords: TiNi shape memory alloy, Multiaxial stress state, Torsion-tension (compression) test, Reorientation of R-phase, Stress-induced R-phase, Limit surface to start reorientation.

1. Introduction

CURRENT APPLICATIONS of shape memory alloys (SMAs) look to progress simultaneously and rapidly along the different directions of "downsizing", "upsizing" and "compositization". Thin films of the order of μm in thickness, which exhibit

almost perfect shape memory effect have been developed, and are regarded as a potential candidate material to drive micromachines [1 – 3]. Development of thin films showing stable shape memory effect associated with both the R-phase and martensitic transformations are still an urgent task in current metallurgy. On the other hand, larger SMA devices, of the order of 10 cm or larger in size, are increasingly required, being expected to carry mechanical loads while exhibiting shape memory effect. Fasteners of the pipes are a successful example realized by advanced Fe-based SMAs [4]. SMAs are favorably employed as a component material to form a composite with a matrix material [5 – 7]. The composites are expected to perform, as a smart material, a special function, which is impossible to be performed by any single material. Among such competitors as the piezoelectric materials, the electrorheological fluids and the electrostrictive/magnetostrictive materials, SMAs dominate in producing larger driving force and stroke. The way of cooling is, however, always the point of special consideration, especially when a high speed response is expected of the composite.

In all these applications, SMAs are in action under not a simple uniaxial stress state but a complicated multiaxial stress state, and in addition, the non-isothermal state in both space and time is the usual case. Alloy performance under such complicated thermomechanical situation should, therefore, be fully clarified both experimentally and theoretically, from the point of view of both metallurgy and thermomechanics. On the theoretical side, starting from FALK [8, 9] and TANAKA [10, 11], many attempts have been made to establish unified frameworks governing the transformation and deformation phenomena in SMAs [12 – 28]. The work by RANIECKI *et al.* should especially be mentioned for its sound base on thermodynamics and subsequent wide applicability [29 – 32]. The transformation driving force was rationally formulated in close relation to the second law of thermodynamics, and the transformation kinetics was introduced consistently. The micromechanical study by PATOOR *et al.* [33] and the thermomechanical FEM modelling by FISCHER [34] should also be worth remarking since they have established each methodology in transformation thermomechanics in SMAs.

Huge amount of experiments have been carried out in many SMAs under uniaxial stress state, accumulating data on the stress-strain-temperature hysteresis, the propagation of phase interface, the transformation conditions, and so on, both static and cyclic conditions [2, 35 – 36]. These results helped a lot to establish and refine the theories, and to identify the material parameters. For example, the knowledge on the transformation zones in the stress-temperature space, only in which the transformations progress, has presented a clear picture about the thermomechanical behaviour of SMAs, and driven the establishment of the theories based on it [11, 37 – 40]. The concept of the transformation zone finally leads to the transformation start/finish conditions represented by the surfaces

in the general stress-temperature space, which is similar to the yield surface in plasticity [41]. The observation of asymmetry of stress-strain curves has stimulated the study of the transformation work dissipated during transformation; its path-independence is the point of discussion [42, 43].

Under the multiaxial stress state, however, few experimental results have been reported in the martensitic transformation range by SITTNER and TOKUDA [44 – 46] and ROGUEDA *et al.* [47] in Cu-based SMA, NISHIMURA *et al.* [48, 49] in Fe-based SMA and SEHITOGLU *et al.* [50, 51] in TiNi and Cu-based SMAs. Some points to remark: Asymmetry of the martensitic transformation start surface in the stress-temperature space was clearly observed in all SMAs, thus approving the theory with the third invariant of stress tensor [16], which has been suggested in the micromechanical investigation by PATOOR *et al.* [52]. The normality rule was shown to be acceptable, though a full conclusion should be made after further accumulation of data.

Usually a series of thermomechanical loads is applied to the specimen prior to the tests in order to acquire a stable response of the specimen. The process is called the training [53]. This means that the test results might not be the intrinsic response of the alloy, but be an apparent behaviour strongly influenced by the type of training employed. In order to study precisely the intrinsic property of the alloy, one has to carefully prepare the alloy specimen so that it exhibits, without any type of training, enough stable response in the whole course of tests.

In TiNi SMAs the R-phase transformation occurs in a certain temperature range just prior to the martensitic transformation [1, 54 – 56]. The rhombohedral phase is produced from the parent B2 phase during the transformation. The stress-strain curve changes its form from apparent plasticity to pseudoelasticity depending on the test temperature; the former is the shape memory effect exhibiting the recoverable deformation, whereas in the latter, the stress-induced pseudoelasticity is associated with the stress-induced forward and reverse transformations. In almost all cases, the pseudoelasticity is observed in a relatively narrow temperature range without showing any large hysteresis. This is the reason why the R-phase transformation is preferably used in shape memory devices requiring a sensitive response to the input.

Metallurgy tells us that the R-phase transformation starts during thermomechanical loading when a transformation start condition is satisfied, and finishes when a transformation-finish condition is fulfilled, forming the twin related R-phase variants. The twinned structure is self-accommodated under the stress-free state and is preferred by the applied stress, as in the case of the martensitic transformation. The lattice distortion in the R-phase and/or the variants reorientation of the twinned variants then follow in the subsequent thermomechanical loading. At higher stress and higher temperature range, after the preceding R-phase transformation, the usual martensitic transformation follows [35].

In this paper, as in the first report by the same authors on the comprehensive behavior of TiNi SMA under multiaxial stress state, the experimental results in the R-phase transformation is presented under torsion-tension (compression) stress state. A Ti-50.1%at.Ni SMA was specially prepared for the tests; details of the alloy preparation is reported elsewhere [57]. Special attention is focused on the limit surface to start the reorientation process and the hysteresis loops. A continuum mechanical approach is proposed to model the behaviour of R-phase.

After the experimental and theoretical preliminaries are explained in Sec. 2, Section 3 is devoted to the reorientation (detwinning) plasticity of the pre-existing R-phase, and in the forthcoming paper by the same authors the R-phase pseudoelasticity associated with the stress-induced R-phase transformation will be investigated.

2. Preliminaries

2.1. Alloy, experimental apparatus and experimental procedures

The alloy tested is a Ti-51.0at%Ni polycrystalline SMA, which was annealed at 673 K for 3.6 ks after solution treatment. Transformation temperatures, determined by means of DSC (differential scanning calorimetry) tests, are as follows:

R-phase transformation

$$Rs = 306\ K, \quad Rf = 293\ K,$$
$$RAs = 305\ K, \quad RAf = 316\ K.$$

Martensitic transformation

$$Ms = 253\ K, \quad Mf = 208\ K,$$
$$As = 268\ K, \quad Af = 306\ K.$$

Fundamental thermomechanical properties are presented in Ref. [57] together with some preliminary data of the alloy performance.

It is, nevertheless, necessary to emphasize here that the alloy was designed, by both adjusting the composition and selecting an appropriate heat treatment, to realize a very stable response to thermomechanical loading. The specimen can, as a result, be used repeatedly without any fear of accumulating some irreversible structural change on the microscopic scale. The thermomechanical training is not necessary at all. It should be stressed that all tests reported here were carried out with a single specimen. Actually the initial distance between two marks on the surface of the specimen, 65.815 mm, and the initial rotation of the line connecting the marks with respect to the specimen axis, $-0°18'$, were changed

only by 0.02 mm and 0°06′ respectively, after 46 times of thermomechanical loading/unloading to get all data shown in this paper.

The thin-walled tubular specimen, 19 mm in outer diameter, 16 mm in inner diameter and 122 mm in length, is illustrated in Fig. 1. After machining, the specimen was etched by acid solution. The design considerations on the wall-thickness were dictated by avoiding buckling in compression and a small enough thickness/outside-diameter ratio so that the wall may be considered as thin.

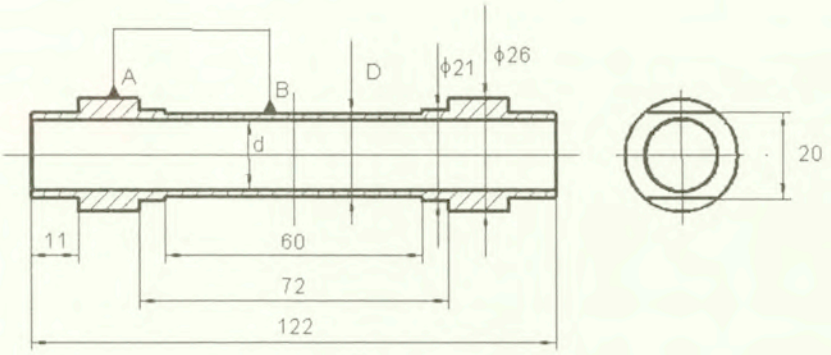

FIG. 1. Test specimen.

A servohydraulic Instron 1343 axial-torsion load frame, together with an MTS TestStar^{TM} II fully digital controller, was used for the computerized testing and data acquisition. The maximum axial and torsion load capacities are rated at ±100 kN and ±1000 Nm, respectively. Two separate servo-control channels of the TestStar^{TM} II controller connected to a PC computer of the system can independently apply controlled axial load and torque. The axial stress (σ_z) and the shear stress (τ) were determined from the output of the axial and torsion loadcells, and were controlled proportionally under isothermal conditions (for details, see Sec. 2.2). The stress rate was kept constant to 1 MPa/sec during the whole tests.

The testing machine recorded, on a hard disk of the PC computer, 8 channels of data. The axial stress (σ_z) and the shear stress (τ) are the controlled quantities, whereas the axial strain (ε_z), the shear strain ($\varepsilon_{z\theta}$) and the hoop strain (ε_θ) represent the response of the specimen. The radial component ε_r was undetermined.

Tests were carried out at constant temperatures in the range 260 K to 315 K. The temperature of the specimen was increased/decreased using an Instron chamber. Temperature inside the chamber was controlled within ±0.5 K at demanded level using Instron controller type 3110. Temperature at upper and lower part of the specimen gauge length was also measured during the test by two K-type (chromel-alumel) thermocouples connected to microprocessor based thermometer

model 502. Temperature differences at the measuring points were less than 1 K during the whole loading-unloading process for a given path of loading.

Axial, hoop and shear strains were measured by uniaxial and rosette-type strain gages cemented in the middle part of a specimen. Two 45° rosettes EP-08-125RA-120 by Micro-Measurements, bonded to the outer surface of the specimen and located diametrically opposed to each other, were wired in full bridge circuit with four active gauges for shear strain measurement. The third strain gauge of each rosette, aligned with longitudinal axis of the specimen, and two additional separate strain gauges for temperature compensation, located on a specially designed semi-ring, were wired in full bridge circuit with two active gauges for axial strain measurements. The hoop strain was measured by means of the additional two strain gauges, bonded to the specimen and located also diametrically opposed to each other. Two strain gauges (all Micro-Measurements type EP-08-125DQ-120) were bonded on the surface of the semi-ring for the temperature compensation. The gauges were wired in half bridge circuit and consist of two active and two passive elements.

Load and torque transmission is affected by specially designed grips assuring load axiality and backlash elimination, thus enabling us to perform cyclic, reverse loading of the specimen.

More details concerning the experimental procedure are given in Ref. [58].

For the tests in reorientation (detwinning) plasticity of the pre-existing R-phase, the test temperature was kept constant during tests at $T = 260$ K, 280 K, 300 K, whereas the following temperature ranges in the pseudoelasticity associated with B2 (Austenite) $\rightarrow$ R phase transformation will be selected in the forthcoming paper: $T = 310$ K, 311.5 K, 315 K, 322.5 K.

Prior to a series of test, composed of isothermal proportional loading up to a maximum stress state and subsequent unloading, the specimen is heated up to 340 K and cooled down to the test temperature. This process fully erased the macroscopic permanent strain induced in the preceding test, and assured that the temperature-induced R-phase is the only phase to exist when the test starts at the reorientation temperature range, and that only the parent B2 phase exists when the tests start at higher pseudoelastic temperature range.

2.2. Controlled quantities

Suppose $\sigma_{ij}(t)$ represents a time history of the stress tensor. The loading path is generally identified as follows:

$$\sigma_{ij}(t) = \sigma_{ij}^{\max} \frac{t}{t_{\max}},$$

where $\sigma_{ij}^{\max}$ represents the maximum value of the stress tensor σ_{ij} at the last moment of loading $t_{\max}$. Both parameters are constant in the proportional loading

tests. If the deviatoric stress tensor

$$S_{ij}(t) = \sigma_{ij}(t) - \frac{1}{3}\delta_{ij}\sigma_{mm}$$

is introduced, the proportional loading path can be rewritten by

$$S_{ij}(t) = S_{ij}^{\max}\frac{t}{t_{\max}}; \qquad \mathbf{S}^{\max} \equiv \operatorname{dev}(\sigma^{\max}) = \text{const.}$$

or in the equivalent form by

$$\sigma_{ef} \equiv \left(\frac{3}{2}S_{ij}S_{ij}\right)^{1/2} = \overline{\sigma}_{\max}\frac{t}{t_{\max}},$$

$$(\overline{\sigma}_{\max})^2 = \frac{3}{2}S_{ij}^{\max}S_{ij}^{\max} = \text{const.}$$

The effective stress σ_{ef} defined above is used in the whole course of this study to measure the extent of load state under multiaxial stresses. The stress rate $\overline{\sigma}_{\max}/t_{\max}$ was kept constant 1 MPa/sec during the whole tests.

In this study, Torsion + Tension (Compression) tests of thin-walled tubular specimen are often investigated from the theoretical point of view, and are actually carried out in TiNi alloy specimen. The class of the tests is simply called the "A-experiments" in the following discussion.

In A-experiments, the above formulae are reduced to as follows: Defining non-zero components of stress tensor by

$$\sigma_z \Leftrightarrow \sigma_{11} \quad \text{(axial stress)} \quad \text{and} \quad \tau \Leftrightarrow \sigma_{12} = \sigma_{21} \quad \text{(shear stress)},$$

one obtains

$$\sigma_{ef} = \overline{\sigma} = \sqrt{\sigma_z^2 + 3\tau^2} = (\operatorname{sign}\sigma_z)\sigma_z\sqrt{1+3m^2}, \tag{2.1}$$

where the path parameter m is defined by

$$m = \frac{\tau}{\sigma_z}. \tag{2.2}$$

Tests along five proportional paths, illustrated in Fig. 2, were performed at each temperature. These paths are identified by means of the parameter y (cf. Sec. 2.3) or m as follows:

Path #1	Simple shear	$i = 1$,	$m = \infty$,	$y = 0$,
Path #2	Simple tension	$i = 2$,	$m = 0$,	$y = 1$,
Path #3	Simple compression	$i = 3$,	$m = 0$,	$y = -1$,
Path #4	Proportional tension and shear ($\tau = \sigma_z$)	$i = 4$,	$m = +1$,	$y = 11/16$,
Path #5	Proportional compression and shear ($\tau = -\sigma_z$)	$i = 5$,	$m = -1$,	$y = -11/16$,

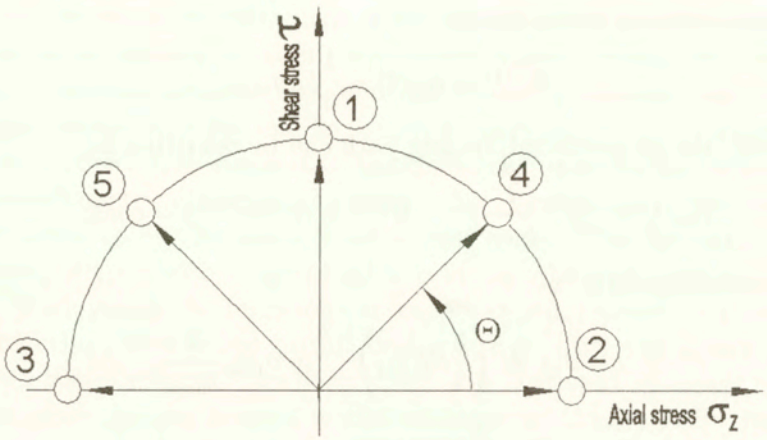

FIG. 2. Loading paths.

2.3. Path characteristics

In order to take rationally into account the path-dependence of the alloy behaviour, the y-function or y-parameter is introduced by

$$y(\sigma_{ij}) \equiv 3\sqrt{6}\frac{J_3'}{(J_2')^{3/2}} \tag{2.3}$$

$$J_2' \equiv \frac{2}{3}\sigma_{ef}^2 = S_{ij}S_{ij}, \qquad J_3' \equiv \det S_{ij} = \frac{1}{3}\mathrm{tr}(\mathbf{S})^3$$

where J_2' and J_3' denote the second and the third invariants of the stress deviator, respectively. Note that the y-parameter is homogenous of order zero in the stress tensor $\mathbf{S}$, and $-1 \leq y \leq 1$. Moreover, $y = \text{const.}$ during proportional loading.

It should be remarked that J_3' was favorably employed when elaborating the effect of loading path on the plastic behaviour in isotropic materials. PATOOR *et al.* have shown, through the micromechanical investigation, that the case is also true in thermomechanical behaviour of Cu-based SMA [52]. Raniecki and Lexcellent have recently introduced the y-function in the transformation thermomechanics to explain the limit surface of martensitic transformation in Cu-based SMA [16].

In the case of A-experiments, the parameter y reads as

$$y = \frac{\sigma_z(2\sigma_z^2 + 9\tau^2)}{2(\sigma_z^2 + 3\tau^2)^{3/2}} = (\mathrm{sign}\sigma_z)\frac{2 + 9m^2}{2(1 + 3m^2)^{3/2}} \tag{2.4}$$

the value of which is listed for each loading path in the table above.

It is worth noting the relation between the Lode-parameter μ_L and y introduced here

$$y = \frac{\mu_L(3-\mu_L)(3+\mu_L)}{(3+\mu_L^2)^{3/2}}\text{sign}(\sigma_2-\sigma_1) \tag{2.5}$$

or alternatively

$$\mu_L = -\sqrt{3}\text{tg}\theta; \qquad y = -\sin 3\theta$$

where θ stands for the angle of vector-radius on octahedral plane. In the course of proportional A-experiments the parameter y and the angle θ remains constant. Moreover, the principal axis does not rotate. There is a simple relation between the angle θ and the angle α that determines the orientation of the principal axis with respect to the z-axis,

$$\sqrt{3}\text{tg}\theta = \text{sign}(\sigma_z)|\cos(2\alpha)|, \qquad |\cos(2\alpha)| = \frac{1}{\sqrt{1+4m^2}}$$

2.4. Remarks

i) Recall that the stress paths $\sigma'(t)$ and $\sigma(t)$ connected by

$$\boldsymbol{\sigma}'(t) = \mathbf{R}^T\boldsymbol{\sigma}(t)\mathbf{R}, \quad \text{where } \mathbf{R}^T\mathbf{R} = \mathbf{1}, \quad \mathbf{R} \neq \mathbf{1} \text{ and } \det\mathbf{R} = 1,$$

are equivalent in the sense that if a physical property $\varphi(\boldsymbol{\sigma})$ is such that $\varphi(\boldsymbol{\sigma}) = \varphi(\boldsymbol{\sigma}')$ for arbitrary $\mathbf{R}$, then the specimen is isotropic with respect to the property φ. It can be shown that in the class of A-experiments there exists no two distinct proportional and equivalent paths. This makes certain problem as regards direct verification of an isotropy postulate. The anisotropy effects can be estimated only in indirect way, e.g., by confronting the conclusions following from the most general representations of the isotropic functions with the experimental facts.

ii) Likewise, the effect of hydrostatic stresses cannot be estimated directly in the A-experiments.

iii) In the A-experiments one can produce neither "tensile" ($\sigma_1 > 0$, $\sigma_2 > 0$) nor "compressive" ($\sigma_1 < 0$, $\sigma_2 < 0$) stress states, where σ_1 and σ_2 are the principal stresses ($\sigma_3 = 0$).

3. Reorientation Plasticity of R-phase

The reorientation processes of the pre-existing R-phase progress, not only in the present SMA but also in almost all TiNi SMAs, under low applied stresses at specific temperature range [54 – 56]. The detwinning of the R-phase variants is the mechanism of deformation under the applied stress, meaning the processes are highly dependent on the stress path. The low total strains of the order of

10^{-3} , at most $\varepsilon < 10^{-2}$, are induced, and the permanent strains amount to the order of $10\times$(typical elastic strain).

Experimental results are presented below, together with the way of data processing. A model of reorientation plasticity of R-phase is also discussed.

3.1. Actual loading paths

In the tests the maximum stresses

$$\sigma_{ef}(A,i) = \max_t \sigma_{ef}(t,i); \qquad (i = 1,2,3,4,5),$$

a)

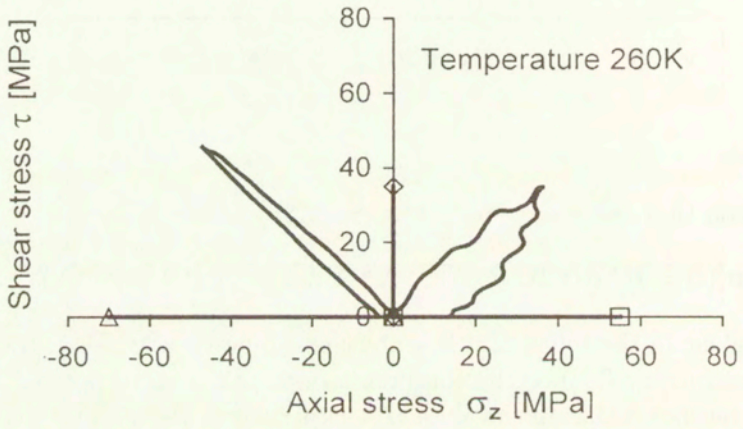

b)

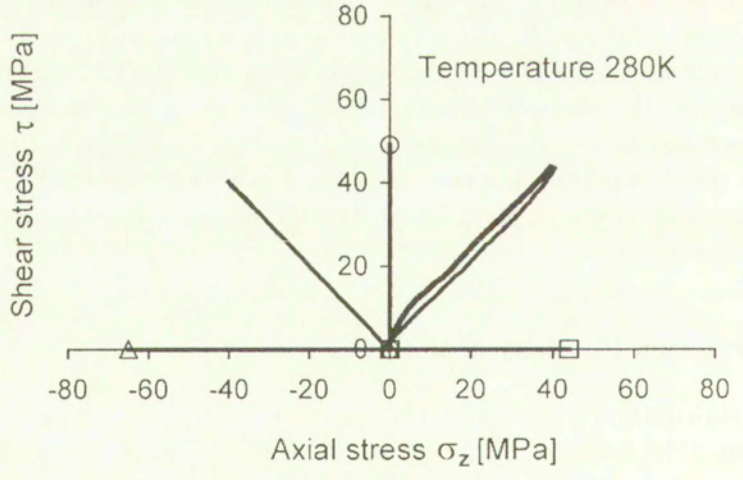

[FIG. 3 a, b]

c)

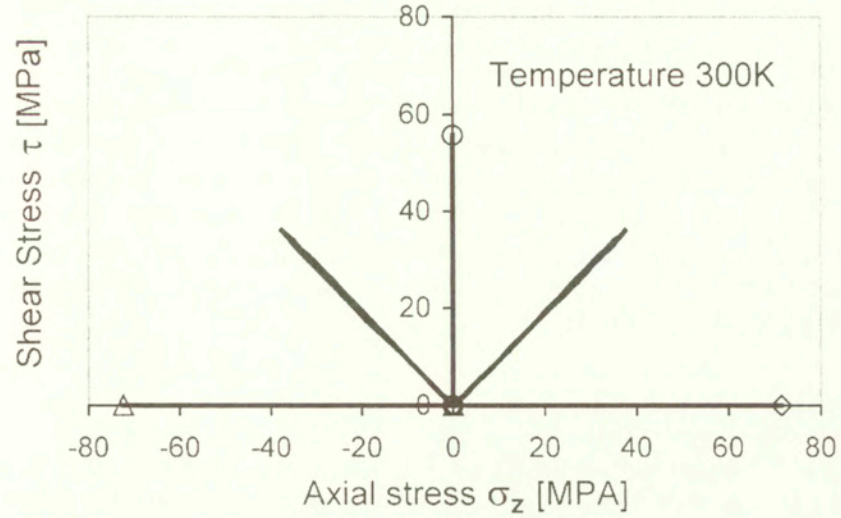

FIG. 3. Actual loading paths at; a) 260 K, b) 280 K and c) 300 K.

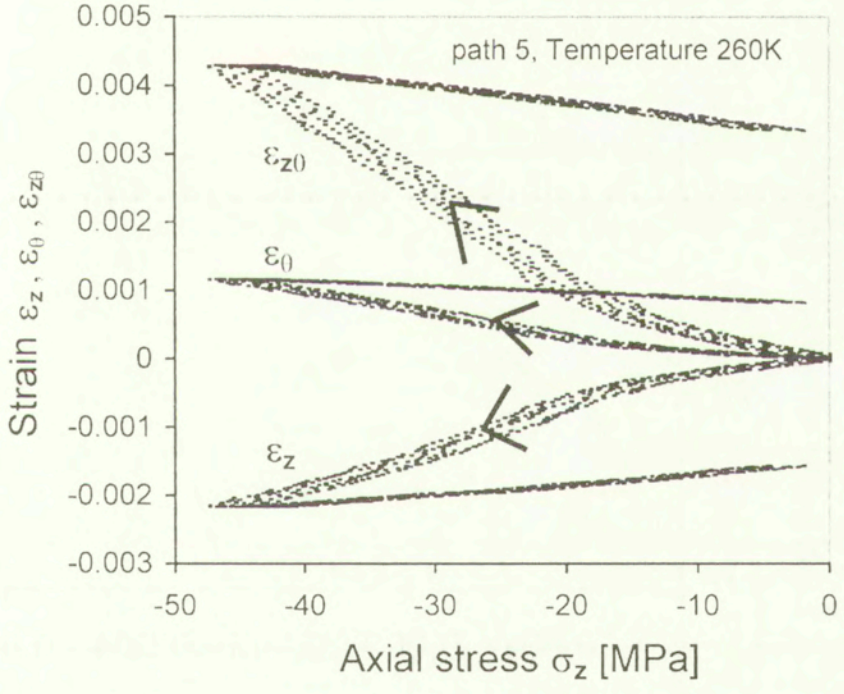

FIG. 4. An example of "on-line" stress-strain response for Path #5 at 260 K.

were different for the different path i and the test temperature T, and moreover the actual paths were not exactly proportional in some cases, as shown in Fig. 3 at different temperatures. The maximum stress was set as low as possible so that no irreversible microstructural change was accumulated in the specimen, but at the same time as high as possible so that the critical stress to start the reorientation process and the elastic modulus can be determined accurately enough (cf. Fig. 6 later). Loading is not exactly controlled by either a common stress amplitude or a common strain amplitude.

3.2. Illustration of recorded data

The typical "on-line" data for Path #5 at 260 K are shown in Fig. 4. After the initial response, characteristic behaviour in the reorientation (detwinning) process, in which the temperature-induced, self-accommodated, R-phase variants are reoriented to a favorable one during mechanical loading. The obtained on-line data were smoothed by means of two methods; the "average mean" and the "polynomial fit". The deviation of the raw data from the smoothed stress-strain curves were small enough; $|\Delta\sigma_{ij}| \leq 2$ MPa, $|\Delta\varepsilon_{ij}| \leq 5 \cdot 10^{-5}$, as can be seen from Fig. 5a,b.

a)

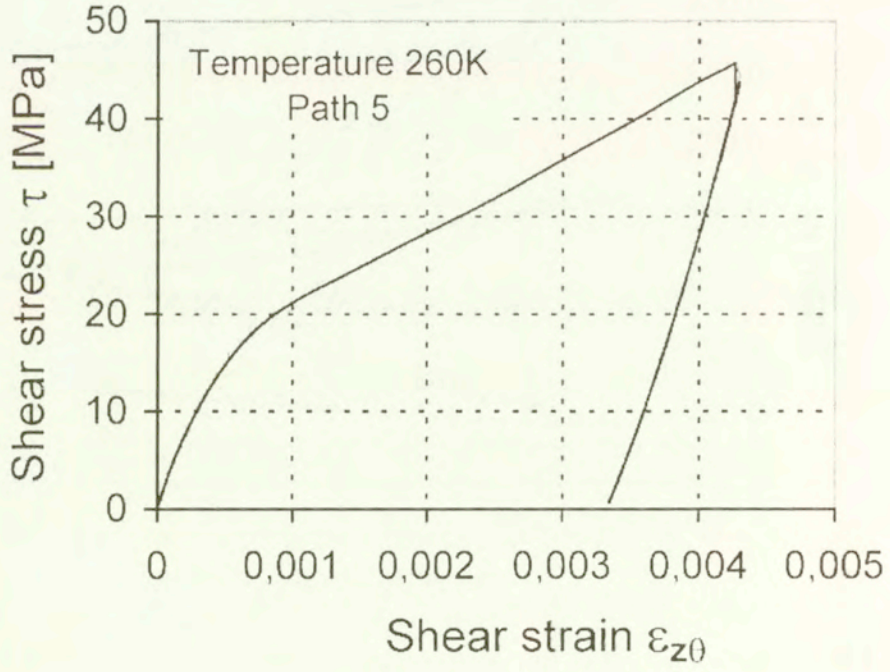

[FIG. 5 a)]

b)

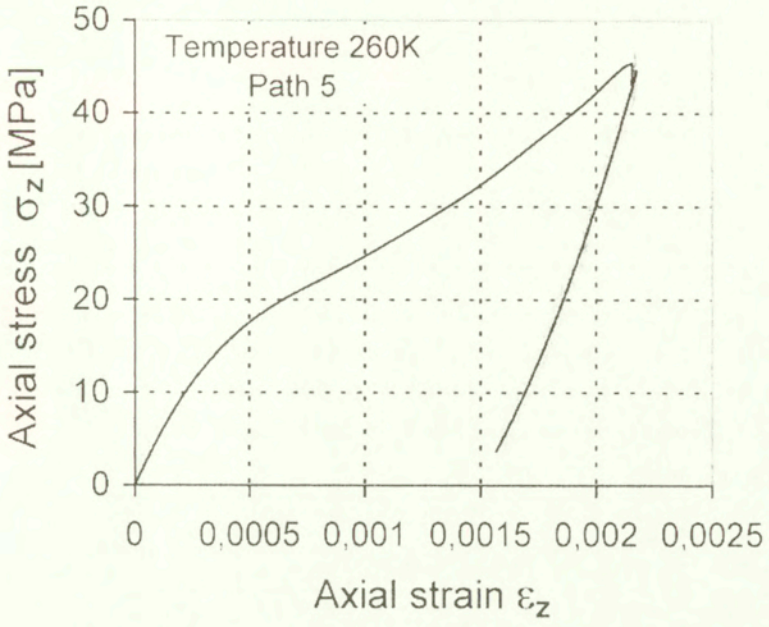

FIG. 5. "On-line data" and "smoothed data" for Path #5 at 260 K; a) $\tau - \varepsilon_{z\theta}$ curve, b) $-\sigma_z - \varepsilon_z$ curve.

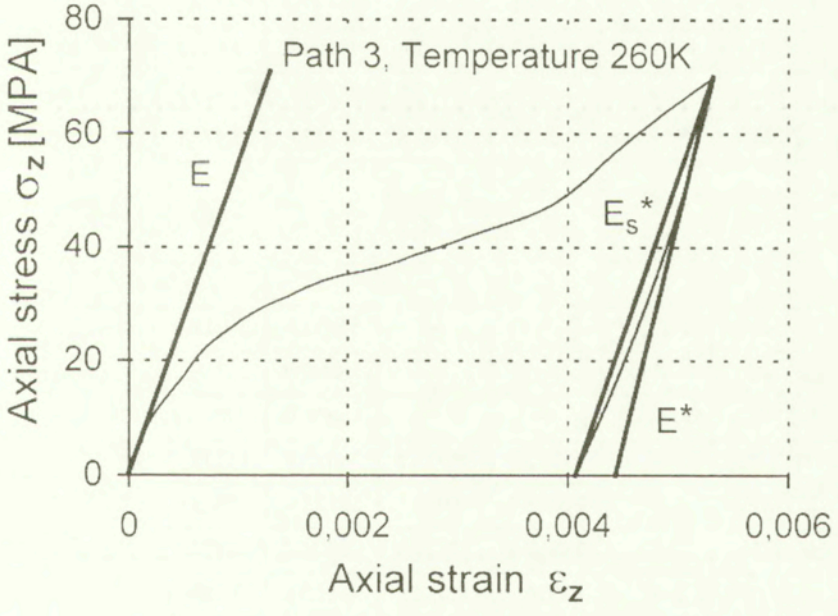

FIG. 6. Definition of elastic contants.

3.3. Determination of elastic constants

Elastic moduli E and 2μ were determined at a total strain offset equal to 10^{-4}. On the other hand, the elastic moduli during unloading, having quite different values from E and 2μ, were defined as both the secant moduli E_s^*, $2\mu_s^*$ and the tangential moduli E^*, $2\mu^*$ (cf. Fig. 6 illustrating the data for Path #3 at 260 K).

For Paths #2 and #3, Poisson's ratio was calculated by means of the isotropic relation $\nu = E/2\mu - 1$ with the shear modulus identified for Path #1. All these elastic moduli exhibit strong temperature-dependence, as tabulated in Table 1.

Table 1. Elastic constants at; a) 260 K, b) 280 K and c) 300 K.

a) Elastic constants; $T = 260$ K

	PATH Number				
	1	2	3	4	5
2μ MPa	43186.5	–	–	41976.4	44079.4
$2\mu^*$ MPa	43449.4	–	–	44454.8	60019.1
$2\mu_s^*$ MPa	30765.3	–	–	31864.3	46253.7
E MPa	–	51683.1	54489.8	48869.1	50426.2
E* MPa	–	61726.8	78903.3	58771.5	92154.8
$\mathbf{E}_s^*$ MPa	–	38300.5	55493.5	35449.0	68400.9
ν MPa	–	0.1967	0.2617	0.1642	0.1440
ν^* MPa	–	0.4207	0.8160	0.3221	0.5354
ν_s^* MPa	–	0.2449	0.8038	0.1125	0.4788

b) Elastic constants; $T = 280$ K

	PATH Number				
	1	2	3	4	5
2μ MPa	38519.3	–	–	34635.9	33711.3
$2\mu^*$ MPa	48601.8	–	–	43392.9	56736.0
$2\mu_s^*$ MPa	30565.0	–	–	26816.6	39270.8
E MPa	–	47248.3	58338.2	38525.9	41133.3
E* MPa	–	52074.9	78034.8	56423.2	77866.6
$\mathbf{E}_s^*$ MPa	–	31369.3	47724.9	31621.0	52177.7
ν MPa	–	0.2266	0.5145	0.1120	0.2200
ν^* MPa	–	0.0710	0.6060	0.3000	0.3720
ν_s^* MPa	–	0.0260	0.5610	0.1790	0.3280

c) Elastic constants; $T = 300$ K

	PATH Number				
	1	2	3	4	5
2μ MPa	31979.5	–	–	32413.2	39823.4
$2\mu^*$ MPa	44659.5	–	–	38503.4	48291.5
$2\mu_s^*$ MPa	29388.8	–	–	24275.3	32711.5
E MPa	–	33465.9	40935.2	41763.8	43538.9
E* MPa	–	55909.4	74457.0	50545.0	65466.1
$\mathbf{E}_s^*$ MPa	–	32243.8	48178.0	30057.8	43093.0
ν MPa	–	0.0460	0.2800	0.2880	0.0930
ν^* MPa	–	0.2520	0.6670	0.3130	0.3560
ν_s^* MPa	–	0.0970	0.6390	0.2380	0.3170

3.4. Reorientation (detwinning) strain

The reorientation strain is defined by subtracting the elastic component from the total strain;

$$\varepsilon_{ij} \equiv \varepsilon_{ij} - M_{ijkl}\sigma_{kl} = \varepsilon_{ij} - \varepsilon_{ij}^e,$$

where M_{ijkl} denotes the elastic compliance tensor. Under the reasonable assumptions of the isotropic elastic behaviour and the incompressibility of the reorientation strain, the following strain components have to be considered in the tests:

$$\begin{aligned} \varepsilon_r^T &= -(\varepsilon_\theta^T + \varepsilon_z^T), \\ \varepsilon_z^T &= \varepsilon_z - \sigma_z/E; \qquad \varepsilon_{z\theta}^T = \varepsilon_{z\theta} - \tau/2\mu, \\ \varepsilon_\theta^T &\equiv \varepsilon_\theta + \left(\frac{1}{2\mu} - \frac{1}{E}\right)\sigma_z. \end{aligned} \tag{3.1}$$

The equivalent total strain and the equivalent reorientation strain, defined by

$$\varepsilon_{eq} = \sqrt{\frac{2}{3}\varepsilon_{ij}\varepsilon_{ij}} \qquad \text{and} \qquad \varepsilon_{eq}^T = \sqrt{\frac{2}{3}\varepsilon_{ij}^T\varepsilon_{ij}^T},$$

respectively, can be expressed in the case of A-experiments by

$$\varepsilon_{eq}^T = \frac{2\sqrt{3}}{3}\sqrt{(\varepsilon_z^T - \varepsilon_\theta^T)^2 + 3\varepsilon_z^T\varepsilon_\theta^T + (\varepsilon_{z\theta}^T)^2}. \tag{3.2}$$

Similar definition is employed for the equivalent reorientation strain rate;

$$\dot{\varepsilon}^T \equiv \sqrt{\frac{2}{3}\dot{\varepsilon}_{ij}^T\dot{\varepsilon}_{ij}^T} = \frac{2\sqrt{3}}{3}\sqrt{\left(\dot{\varepsilon}_z^T - \dot{\varepsilon}_\theta^T\right)^2 + 3\dot{\varepsilon}_z^T\dot{\varepsilon}_\theta^T + \left(\dot{\varepsilon}_{z\theta}^T\right)^2}. \tag{3.3}$$

In Fig. 7 the reorientation strain tensor components ε_z^T, ε_θ^T and $\varepsilon_{z\theta}^T$ are plotted versus the axial component of stress tensor σ_z for the data given in Fig. 5 (Path #5, 260 K), showing clearly that the elastic components are subtracted.

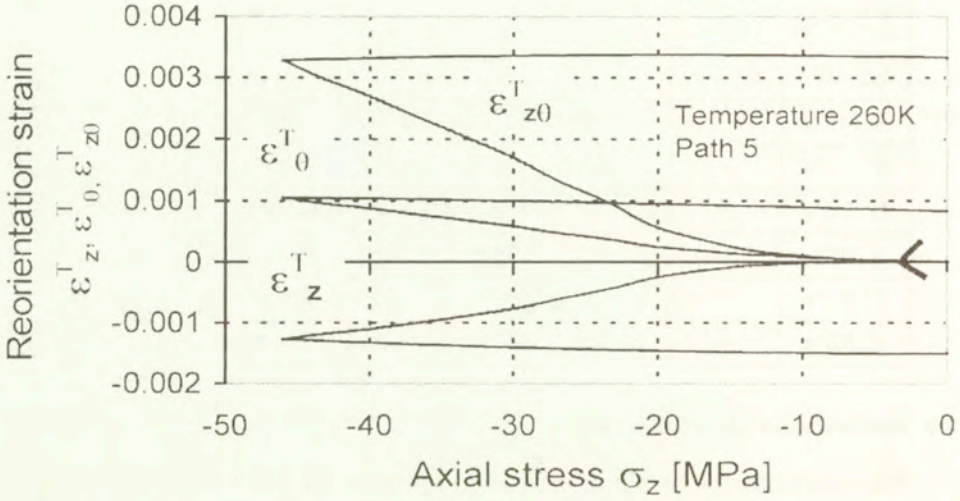

FIG. 7. Stress-reorientation strain curves for Path #5 at 260 K.

3.5. Effective stress - equivalent reorientation strain curves

The isothermal alloy response under torsion-tension (compression) loads can now be plotted on the effective stress-equivalent reorientation strain plane; Figure 8 represents the path-dependence of the curve at each test temperature, whereas in Fig. 9 its temperature-dependence is displayed for each loading path. As was explained in Sec. 3.1, loading is not exactly controlled by either a common stress amplitude or a common strain amplitude.

Figures reveal the strong path-dependence of the response of the specimen to the imposed loading. The effective stress-equivalent reorientation strain curves actually do not converge to a master curve as in von Mises plasticity (J_2-theory). Certain characteristic features of the behaviour can be distinguished:

a) At fixed temperature and fixed effective stress, the induced reorientation equivalent strains in pure shear (Path #1) or combined compression and shear (Path #5) are smaller than in simple tension (Path #2) or in combined tension and shear (Path #4).

b) Under fixed equivalent reorientation strain (geometrical constraint) the recovery effective stress, which could be produced after subsequent heating, are expected to be the highest in simple shear (or combined shear and compression) and the smallest in simple tension.

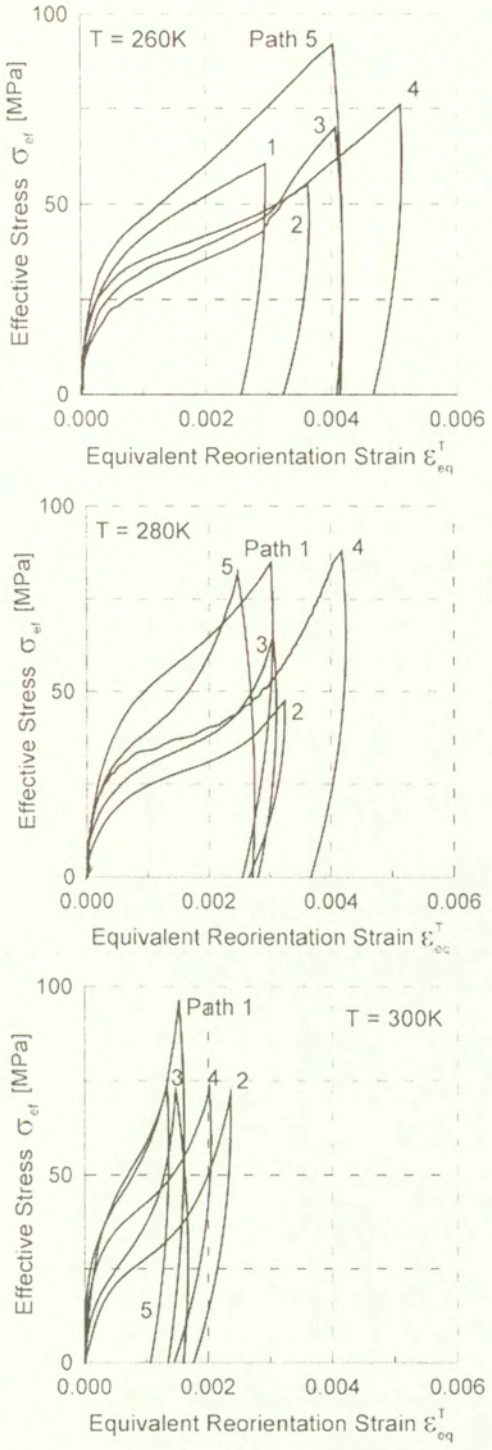

FIG. 8. Effect of loading path on effective stress-equivalent strain curves at: a) 260 K, b) 280 K and c) 300 K.

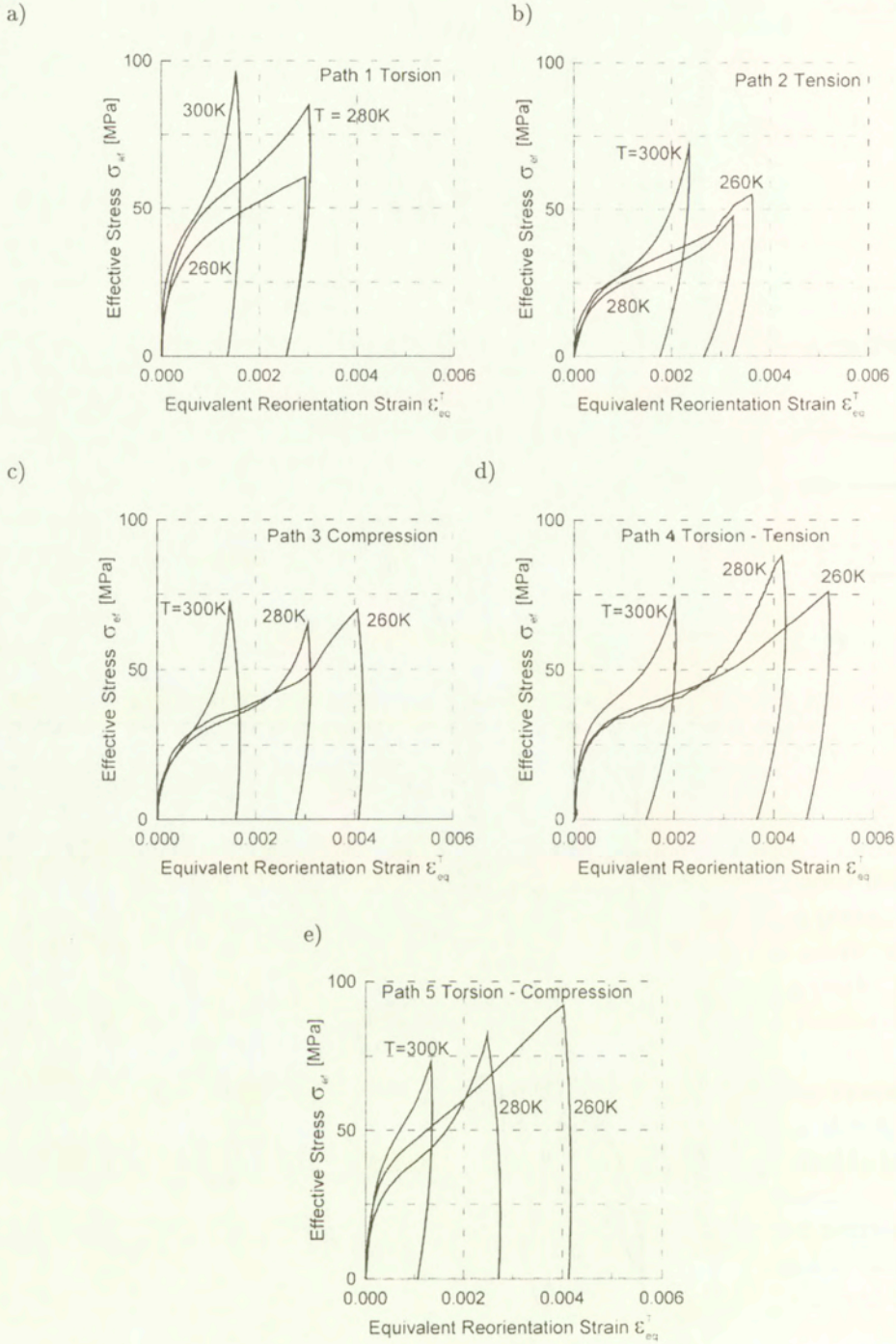

FIG. 9. Effect of temperature on effective stress-equivalent strain curves for: a) Path #1 (torsion), b) Path #2 (tension), c) Path #3 (compression), d) Path #4 (torsion-tension) and e) Path #5 (torsion-compression).

c) In accordance with the properties a) and b) above, the rate of reorientation hardening is the highest during torsion or combined torsion and compression.

d) As a rule, the rate of the reorientation hardening is increasing function of the temperature for all paths.

3.6. Limits of initial reorientation - Limit surface of reorientation

The stress-strain curves in Figs. 8 and 9 clearly show that the reorientation process starts at a critical stress, which depends on both the temperature and the loading path. By having always in mind the analogy to the yield stress and the yield surface in plasticity, the critical stress to start the reorientation process is discussed in this section.

3.6.1. Definition of critical stress. Let us denote the critical value of effective stress for path i by σ^T, and different operational definitions are introduced here (Fig. 10) illustrates them for data of Path #5 at 260 K.);

σ_1^T – Critical stress determined by means of the strain offset 10^{-4},

σ_2^T – Critical stress determined by means of the strain offset 2×10^{-4},

σ_3^T – Critical stress determined as an intersection of tangent line with the σ_{ef}-axis.

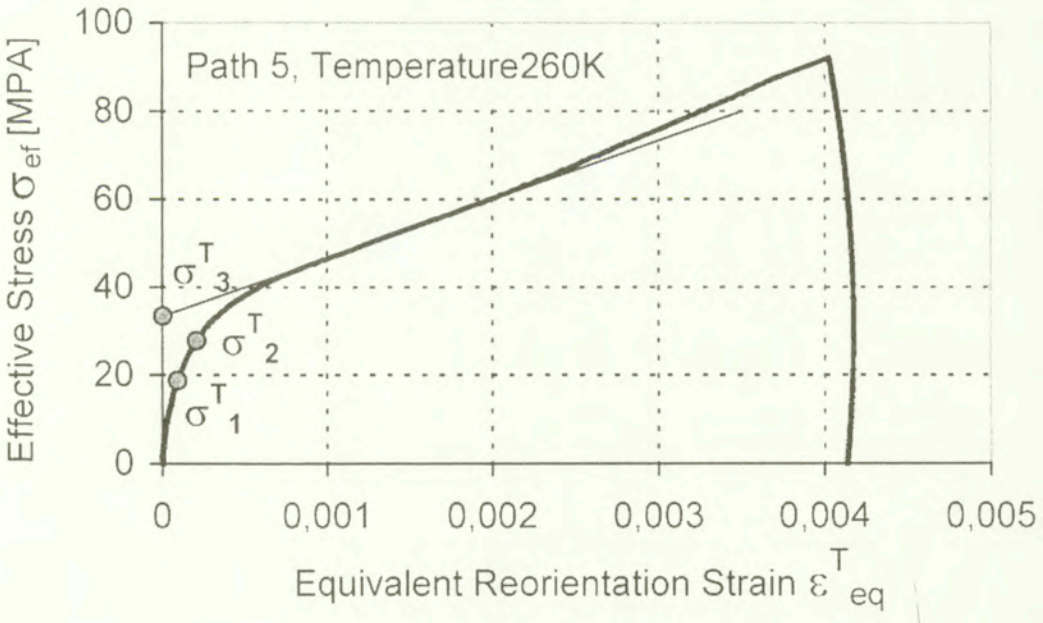

FIG. 10. Definition of critical stress.

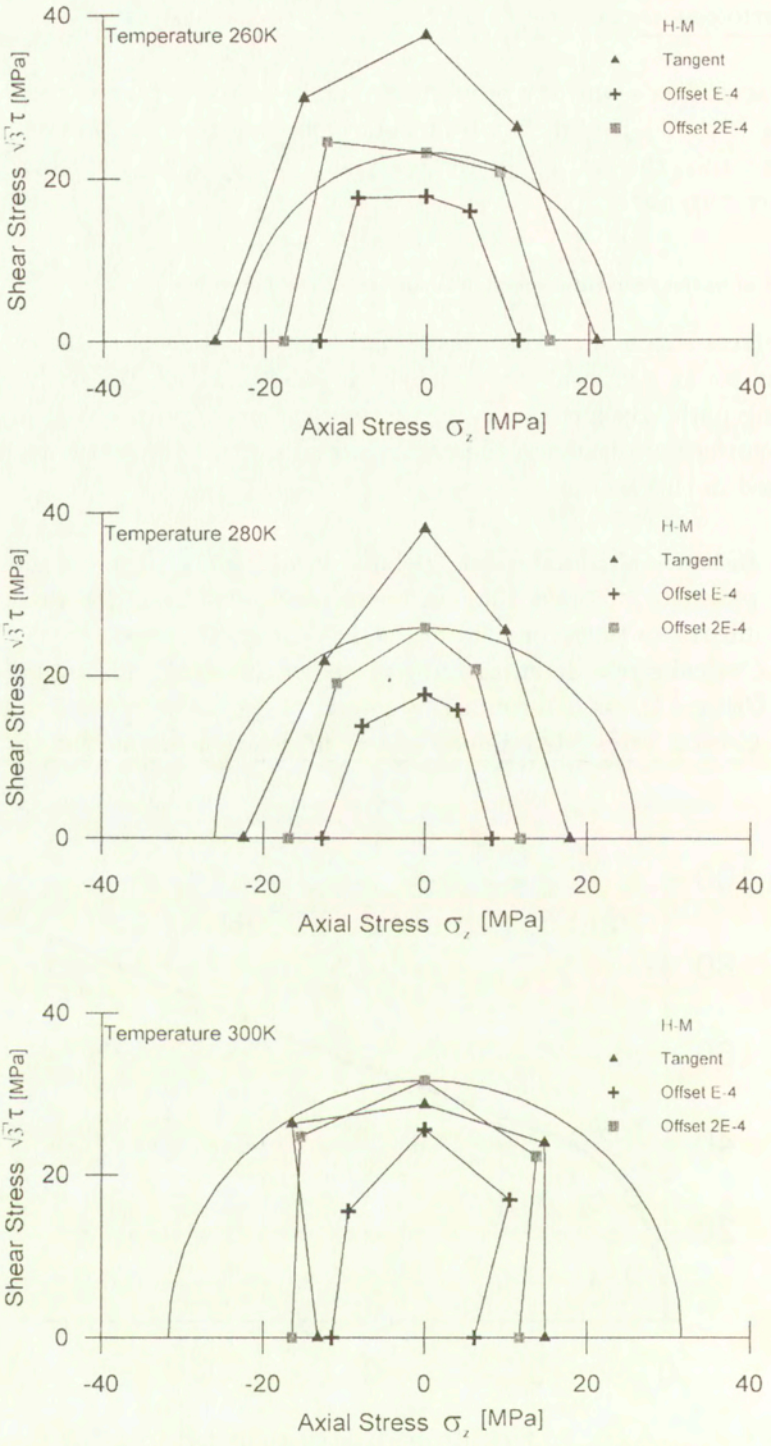

FIG. 11. Limit curve of reorientation exhibiting dependence of definition at: a) 260 K, b) 280 K and c) 300 K.

3.6.2. Obtained results. Critical reorientation effective stresses are plotted in Fig. 11 at each test temperature. The normalized Huber-Mises curve is also drawn in the figure.

The result reveals firstly the strong dependence on the definition of critical stress, as is so for the yield surface in plasticity [41]. In the case of martensitic transformation in SMAs, according to the data in TiNi SMA [50], Cu-based SMA [44 – 47] and Fe-based SMA [48, 49], the transformation start stress in compression is larger than the one in tension. This asymmetry of the limit curve with respect to the shear stress-axis is also observed in the present result, though not so clearly. More experimental data should be accumulated to conclude whether or not this is an intrinsic property of SMAs in the reorientation processes of R-phase. However, it can be noticed that the shear critical stress (effective stress) is always higher than the axial critical stresses (tension, compression) on the $\sigma_z - \sqrt{3}\tau$ plane. This tendency is observed for all definitions of the critical stress intensities.

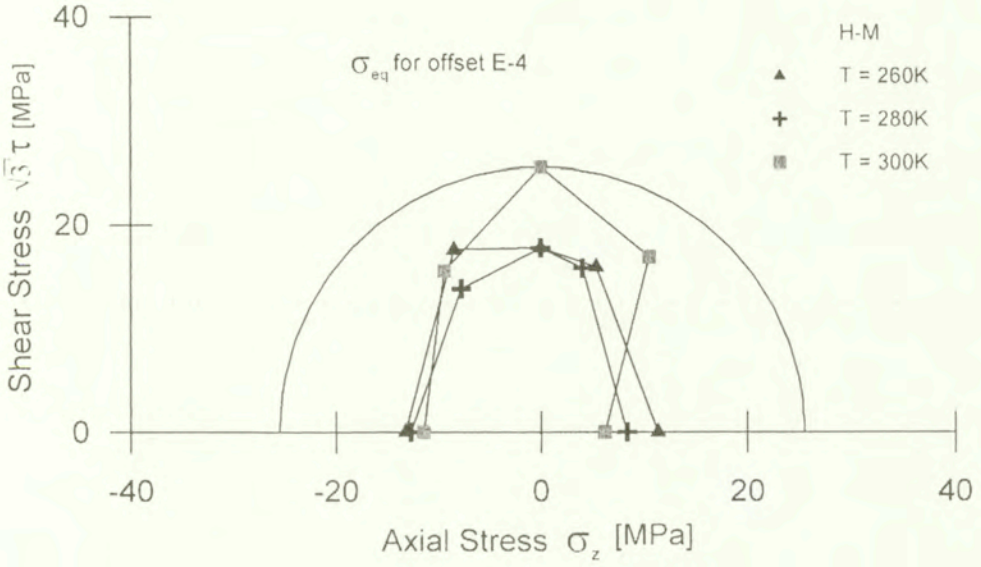

FIG. 12. Temperature-dependence of limit curve (offset 10^{-4}).

Figure 12 illustrates the temperature-dependence of the limit curve determined by the offset strain 10^{-4}. The data are replotted in Fig. 13 to compare the temperature sensitivity of the effective critical reorientation stress for each loading path. The lines represent the start line of the reorientation process of R-Phase [38 – 340, 59 – 60], about which MIYAZAKI *et al.* have discussed in detail under tension in TiNi alloys [54 – 56]. Linear relation with a negative slope and relatively high value of the critical stress in the present alloy, being similar

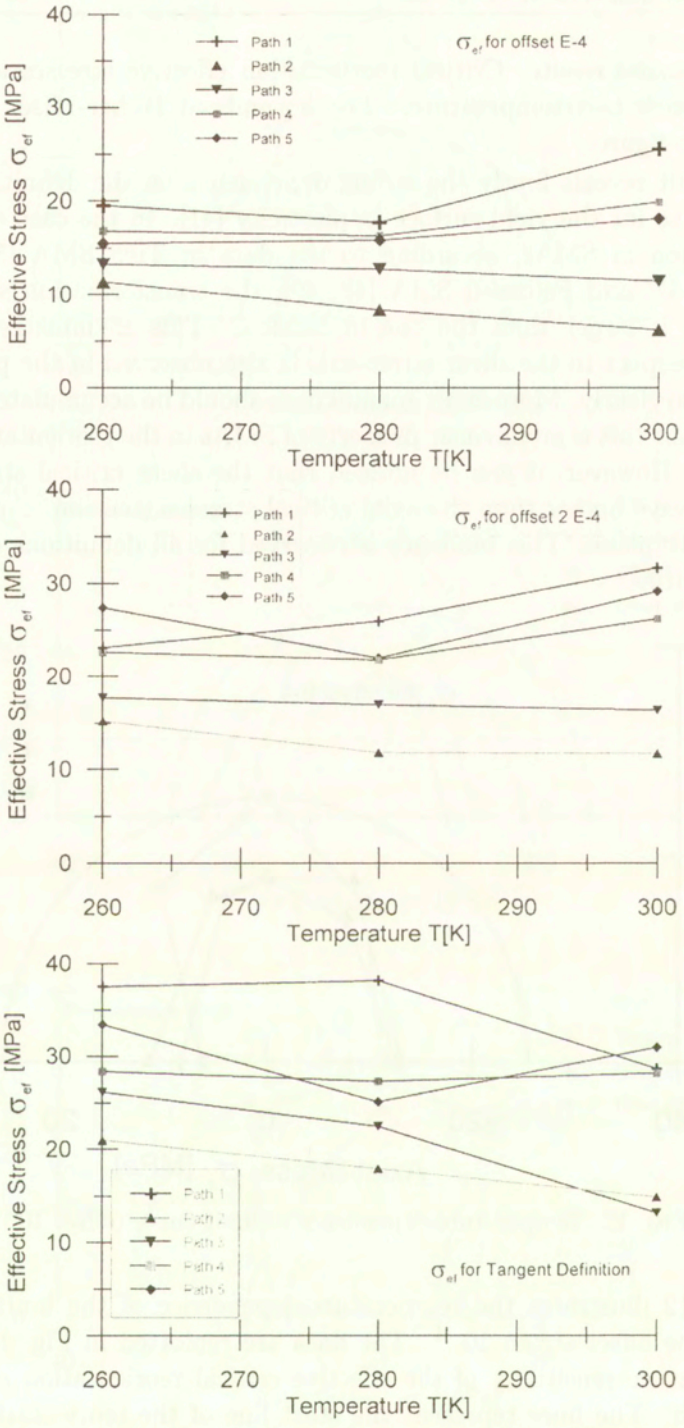

FIG. 13. Temperature sensitivity of critical reorientation stress determined by: a) offset strain 10^{-4}, b) offset strain $2 \cdot 10^{-4}$ and c) tangent.

to Miyazaki's data, can be explained by the presence of the precipitates, which have actually been introduced by alloy-designing the present alloy [57]. At all temperature range, the shear stress contributes to such alloy performance as the positive temperature-dependence of critical stress and the higher critical stress level.

3.6.3. Description of limit surface - shape function. The obtained experimental data concerning the limit surface will now be employed in the convenient theoretical framework. It is assumed that the effects of hydrostatic stress are negligible. To verify this assumption, further multiaxial tests with the additional internal pressure should be carried out. Under this assumption the parametric form of the equation of the limit surface is given in vector representation of the deviatoric stress by

$$\mathbf{S} = \sqrt{\frac{2}{3}}\sigma^T(\mathbf{N},T)\mathbf{N}; \qquad \mathbf{N} = \frac{S}{|\mathbf{S}|} = \frac{\mathbf{S}}{\sigma_{ef}}\sqrt{\frac{2}{3}},$$

(3.4)

$$\mathrm{tr}\mathbf{N} = 0, \qquad \mathrm{tr}\mathbf{N}^2 = 1,$$

where $\mathbf{N}$ stands for the unit vector along $\mathbf{S}$, and four independent components of $\mathbf{N}$ play the role of parameters. Equivalently, the limit surface (3.4) can be described by

(3.5) $$\sigma_{ef} - \sigma^T(\mathbf{N},T) = 0.$$

Assume that σ^T is an isotropic function of $\mathbf{N}$. Its most general representation is $\sigma^T = \sigma^T(y,T)$, where $y = \sqrt{6}\mathrm{tr}(\mathbf{N}^3)$. It can be shown that the quantity y coincides with the one discussed and specified for A-experiments in Sec. 2.3. It is expedient to express the function $\sigma^T(y,T)$ in the form

(3.6) $$\sigma^T = \frac{\sqrt{3}k(T)}{f(y,T)}, \qquad F = \sigma_{ef} - \sigma^T(y,T) = 0,$$

where the shape function $f(y,T)$ of the limit surface $F = 0$ is normalized such that $f(0,T) = 1$, meaning that $k(T)$ stands for the critical shear stress. The values of the shape function can now be found from

(3.7) $$f(y,T) = \frac{\sigma^T(0,T)}{\sigma^T(y,T)},$$

The actual values of y for Paths #4 and #5 at each test temperature are given in Table 2, where $y_{0.1}$, $y_{0.2}$ and y_M denote the y values at the instant of the offset strains 10^{-4} and 2×10^{-4} and at the end of loading, respectively. The corresponding values of the shape function are collected on the plots shown in Fig. 14, for the case of the offsets 10^{-4} and 2×10^{-4}, at each test temperature.

Table 2. Values of y-parameter.

Path Nr. (i)	Temp	260	280	300
	$y_{0.1}$	0.464	0.367	0.718
4	$y_{0.2}$	0.572	0.423	0.716
	y_M	0.6875	0.6568	0.6875
	$y_{0.1}$	−0.611	−0.677	−0.709
5	$y_{0.2}$	−0.629	−0.675	−0.719
	y_M	−0.6875	−0.6875	−0.6875

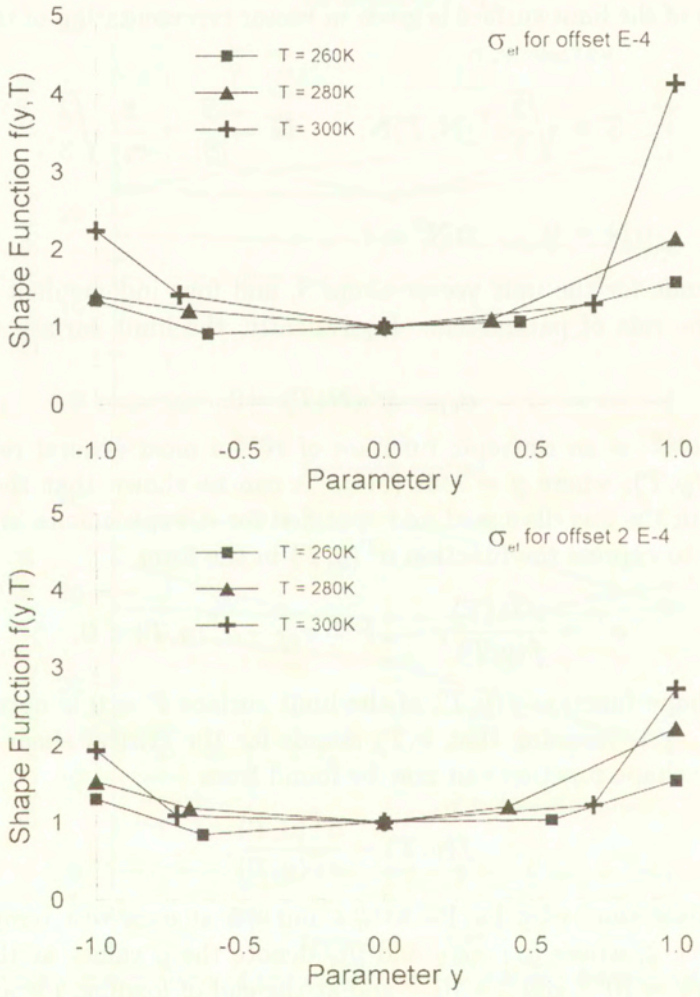

FIG. 14. Effect of temperature on shape function $f(y,T)$ determined by: a) offset strain 10^{-4} and b) offset strain 2×10^{-4}.

It should be noted that $f(y,T) = 1$ corresponds to the J_2-theory in plasticity. It can easily be seen that the behaviour of the investigated alloy is described more accurately by the J_3-theory. Figure 14 also shows the definite temperature sensitivity of the shape function for the present alloy. In the case of martensitic transformation in Fe-based SMA, TANAKA *et al.* presented the data described by an almost temperature-independent shape function [61].

3.7. Some general properties of the plastic flow associated with the reorientation of R-phase

The experimental digital data have been further processed to display some general features of the deformation behaviour associated with the reorientation of the R-phase. On the theoretical ground they are most frequently grasped by the incremental permanent strain-stress relations (flow rule). The results are discussed in the subsequent subsections.

3.7.1. Homogeneity of flow rule.

i) We take it for granted that the reorientation process is rate-independent. Thus, the flow rule is supposed to be invariant under the change of the time scale. The fairly general and simplest flow rule that satisfies this requirement in the course of monotonic loading is

$$\dot{\varepsilon}^T_{ij} = \dot{\Lambda} G_{ij}(\sigma_{mn}, T), \qquad \dot{\Lambda} > 0, \tag{3.8}$$

where $\dot{\Lambda}$ is, in general, a positive scalar function of stress rate, temperature rate, parameters representing the history of $\boldsymbol{\sigma}, T$, and details of the reorientation process. During monotonic loading it represents the extent of the reorientation. The function $\mathbf{G}$ is assumed to be scaled so that it is a homogeneous function of the order zero with respect to σ,

$$G_{ij}(\tau\sigma^0_{mn}, T) = G_{ij}(\sigma^0_{mn}, T), \qquad \tau > 0. \tag{3.9}$$

Equations (3.8) – (3.9) incorporate all isotropic-hardening models of the usual mechanics of plastic flow. Moreover, many postulated constitutive equations for transformation strain in mechanics of phase transformation have the analytical form similar to Eqs. (3.8) – (3.9) [14, 20, 62 – 63].

The general character of the variation of $\dot{\Lambda}$ in the course of reorientation of R-phase can be deduced from Fig. 15, which shows the observed typical variation of the equivalent reorientation strain rate under increase of the applied effective stress. The presented curve clearly reveals that the reorientation process is governed by the "nucleation and growth" mechanism. The data in Fig. 15 and other similar results will be used in future research of evolution equation for Λ.

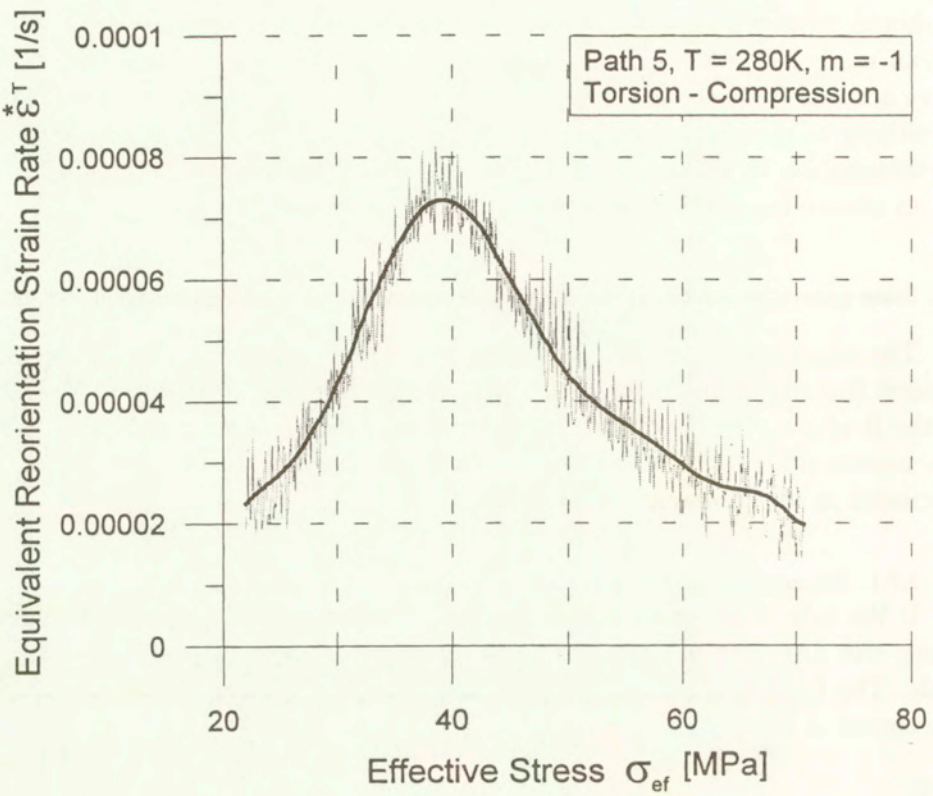

FIG. 15. Evolution of equivalent reorientation strain rate.

ii) The mathematical property (3.9) suggests that the reaction to the proportional loading is the proportional reorientation straining. Equivalently, it implies that the ratios of induced reorientation strain rates remains constant during reorientation,

$$\dot{\varepsilon}^{T}_{KL} = C\dot{\varepsilon}^{T}_{MN}; \qquad (K,L) \neq (M,N); \qquad C = \text{const}, \tag{3.10}$$

or, after integration over time,

$$\varepsilon^{T}_{KL} - \varepsilon^{offset}_{KL} = C(\varepsilon^{T}_{MN} - \varepsilon^{offset}_{MN}). \tag{3.11}$$

Thus the following formulas holds:

$$\frac{\dot{\varepsilon}^{T}_{KL}}{\dot{\varepsilon}^{T}_{MN}} = \frac{\varepsilon^{T}_{KL} - \varepsilon^{offset}_{KL}}{\varepsilon^{T}_{MN} - \varepsilon^{offset}_{MN}}. \tag{3.12}$$

The variation of ratios of reorientation strain rates at $T = 280$ K are shown in Fig. 16 for Path #5, and at $T = 260$ K in Fig. 17 for Path #4. It is seen that

a)

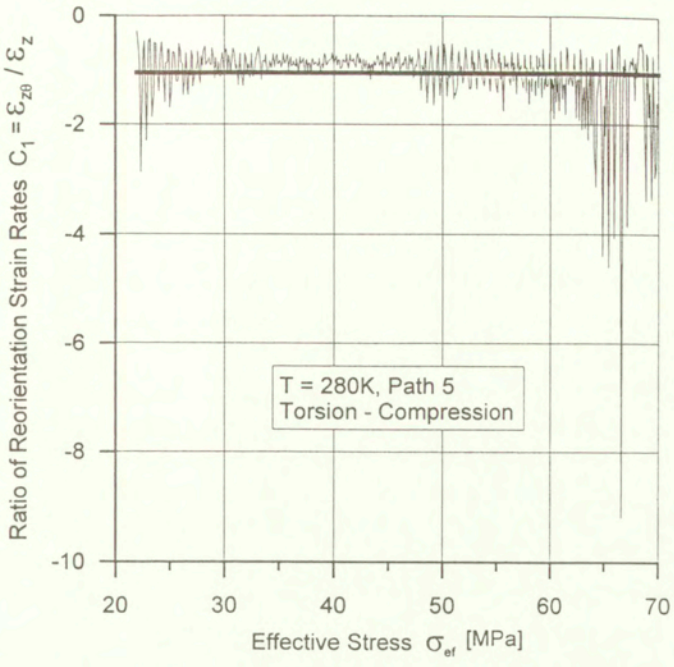

b)

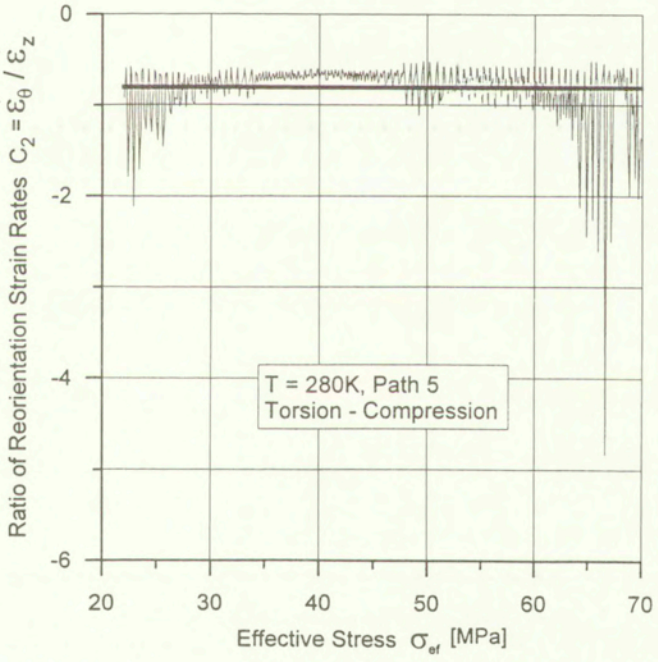

FIG. 16. Ratio of reorientation strain rates; a) and b).

a)

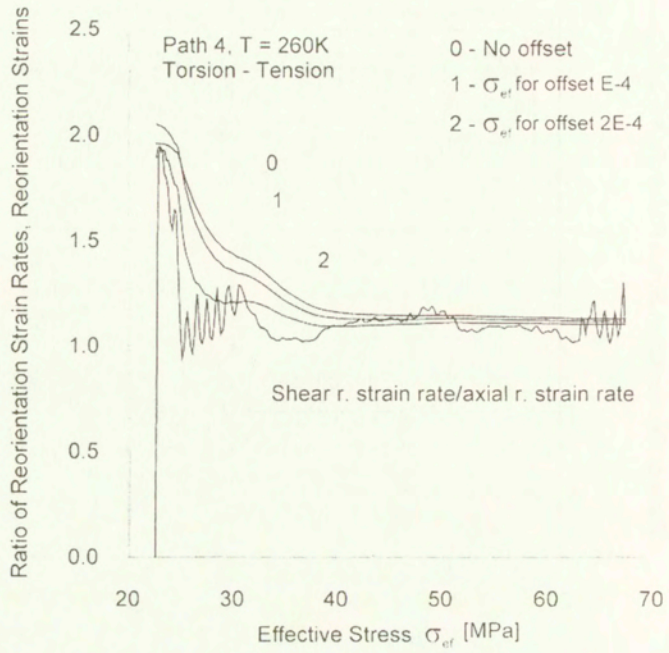

b)

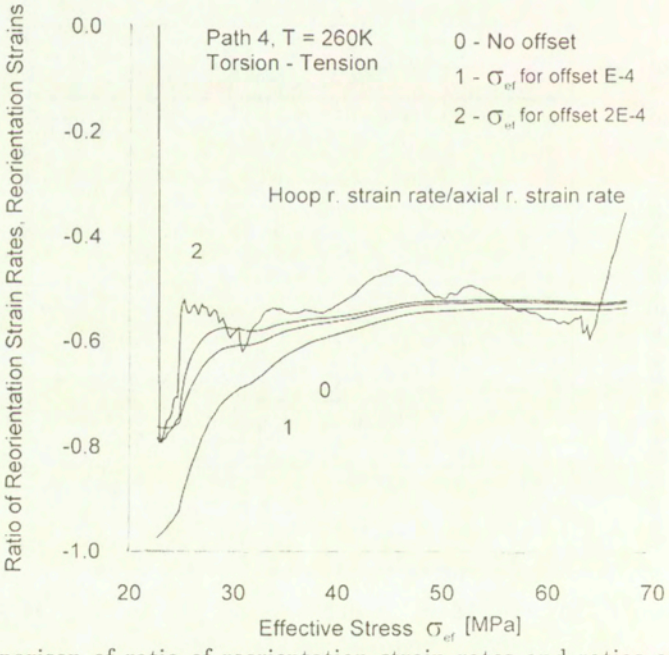

FIG. 17. Comparison of ratio of reorientation strain rates and ratios of reorientation strains for Path #4, $T = 260$ K; a) and b).

the numerical data oscillate along a constant level. The mean values determine the constants $C_1 = \dot{\varepsilon}^T_{z\theta}/\dot{\varepsilon}^T_z$ and $C_2 = \dot{\varepsilon}^T_\theta/\dot{\varepsilon}^T_z$. In Fig. 17, the measured ratios of reorientation strains are plotted in addition, for different values of strain offset. The observed discrepancies between the curves in the initial stage of loading (that show disagreement with Eq. (3.12)) cannot be easily interpreted. The numerically calculated values of ratios are uncertain in the situation when numerators and denominators are close to zero. However, the curves quickly converge to the common constant value showing the trend of the behavior, which is in accord with Eq. (3.12). Interesting is the observed fading memory effect of the strain offsets.

3.7.2. Verification of the special isotropic flow rule.

i) Rewrite the equation of the limit surface $F = 0$ (cf. Eq. (3.6)) in the form

$$g_0^* = f(y,T)\sigma_{ef} - \sqrt{3}k(T) = 0,$$

and regard the function g_0^* as a potential for $\dot{\varepsilon}^T$;

$$\dot{\boldsymbol{\varepsilon}}^T = \dot{\Lambda}\frac{\partial g_0^*}{\partial \mathbf{S}} = \dot{\Lambda}_0\left[\frac{\mathbf{S}}{\sigma_{ef}} + 3x\left(3\frac{\mathbf{S}^2}{\sigma_{ef}^2} - \frac{2}{3}\mathbf{1} - y\frac{\mathbf{S}}{\sigma_{ef}}\right)\right], \tag{3.13}$$

where x and $\dot{\Lambda}_0$ are

$$x \equiv \frac{1}{f}\frac{\partial f}{\partial y} \quad \text{and} \quad \dot{\Lambda}_0 = \frac{3}{2}f\dot{\Lambda},$$

and $\mathbf{1}$ is the unit tensor.

It is seen that the flow rule written in the form (3.13) is the homogeneous function of order 0 in $\mathbf{S}$. Under the adopted simplifications (effects of hydrostatic stress are negligible, and $\mathrm{tr}(\dot{\boldsymbol{\varepsilon}}^T) = 0$), the term occurring in the bracket on the right-hand side of Eq. (3.13) is the most general representation of the isotropic tensor function $\mathbf{G}$, provided that x and y are independent scalar functions of the second and third invariant of $\mathbf{S}$. The adopted potentiality of the flow rule imposes merely the definite relationship between x and y presented above. The case $x = 0$ implies $f = \text{const.}$ and corresponds to the J_2-theory. The situation when x is not equal to zero will be referred to as the J_3-theory.

ii) Simple inspection of the mathematical structure of Eq. (3.13) shows that five components of $\dot{\boldsymbol{\varepsilon}}^T$ are expressed in terms of 3 scalars $\dot{\Lambda}$, x and y. This suggests that there may exists, in general, two constraint relations linking components of $\dot{\boldsymbol{\varepsilon}}^T$ and stress components, which are independent of the aforementioned 3 scalars. In the case of A-experiments discussed here, one constraint relation can be derived. Combine Eqs. (3.13) and (2.4) and get for the discussed specific case of stress and strain states

$$\dot{\varepsilon}^T_{z\theta}/\dot{\varepsilon}^T_z = \frac{3}{2}\left[1 - \frac{3\tau^2 x}{M}\right]\frac{\tau}{\sigma_z},$$

(3.14)

$$\dot{\varepsilon}^T_{\theta}/\dot{\varepsilon}^T_z = -\frac{1}{2}\left[1 - \frac{9\tau^2 x}{M}\right],$$

where M is defined as

$$M = x\left(2\sigma_z^2 + 3\tau^2 - 2y\sigma_z\sigma_{ef}\right) + \frac{2}{3}\sigma_z\sigma_{ef}.$$

Elimination of x/M from Eq. (3.14) gives the final form of the constraint relation

$$\sigma_z\dot{\varepsilon}^T_{z\theta} + \tau\left(\dot{\varepsilon}^T_{\theta} - \dot{\varepsilon}^T_z\right) = 0,$$

which can be rewritten as follows:

$$Y = m = \frac{\tau}{\sigma_z}, \qquad Y = \frac{\dot{\varepsilon}^T_{z\theta}/\dot{\varepsilon}^T_z}{1 - \left(\dot{\varepsilon}^T_{\theta}/\dot{\varepsilon}^T_z\right)}. \tag{3.15}$$

Thus, in the course of A-experiments the measurable quantity Y should be equal to the stress ratio m, provided that the sample is isotropic and has the flow rule of the type (3.13). This theoretical prediction seems to be not exploited in the experimental mechanics so far. The measured and calculated values of Y are compared in Fig. 18. The result markedly verifies the theoretical prediction $Y = m$. In addition, in Table 3, we have collected the means of the strain rate ratios measured over the reorientation plateau. They are compared with the theoretical predictions of J_2- and J_3-theories. In the case of J_3-theory the theoretical values of x were chosen such that the theoretical ratios $\dot{\varepsilon}^T_{z\theta}/\dot{\varepsilon}^T_z$ are possibly closest to the measured values of the corresponding ratios for Paths #4 and #5. The measured data presented in Table 3 for Path #2 (tension), #3 (compression) and Path #1 (torsion) show substantial cross effects. Noticeably shear strain is induced during tension (compression), and large extension accompanies torsion. The former effect cannot be described by the J_3-theory at all (cf. Eq. $(3.14)_1$), and it certainly reveals the existing anisotropy. The cross effects are also present in the course of Paths #4 and #5. The disturbances they cause explain the deviations of the measured data from the straight line present in Fig. 18. However, one can conclude that the J_3-theory discussed here is more realistic than the J_2-theory.

iii) The qualitative agreement between experimental trends and theoretical predictions implied by Eq. (3.13) is also found when comparing the mean rate of reorientation work $W^* = S_{ij}\dot{\varepsilon}^T_{ij}$. The typical processed experimental data for dimensionless quantity $W^*/\sigma_{ef}\dot{\varepsilon}^T$ are plotted versus effective stress in Fig. 19

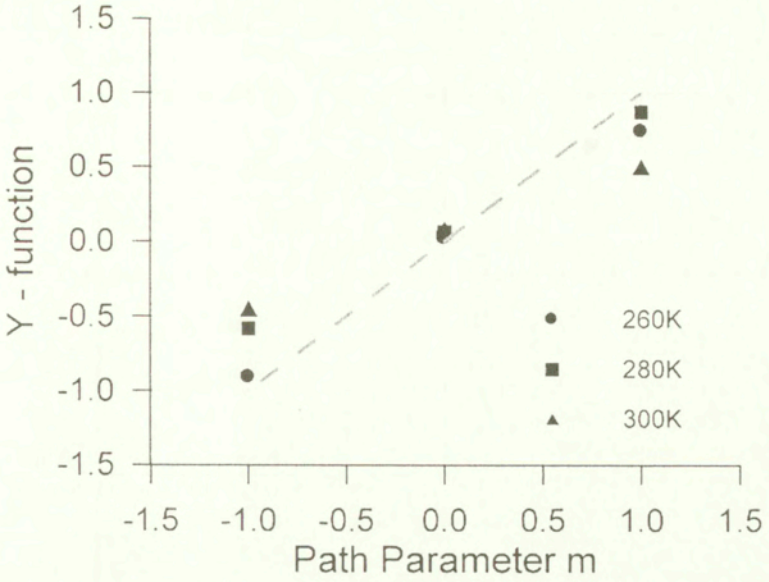

FIG. 18. Validation of constraint relation; Path-dependence of Y-function.

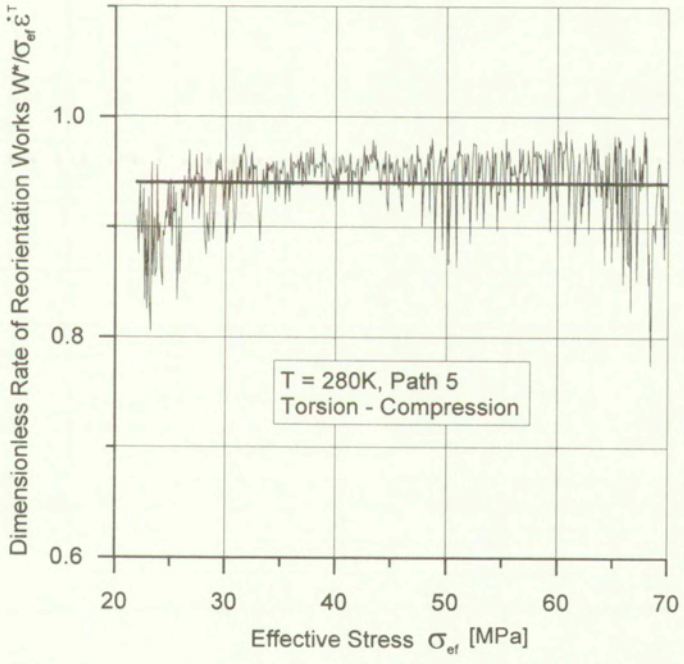

FIG. 19. Evolution in ratio of rate of reorientation works.

Table 3. Comparison of measured and theoretical ratios of strain rates at: a) 260 K, b) 280 K and c) 300 K.

T = 260K

Paths			2	3	4	5	1	
Ratios			Tension	Compression	Tension + Torsion	Compression + Torsion	Torsion	Ratios of $\dot{\underline{\varepsilon}}$ for Torsion
$\dot{\varepsilon}^T_{z\theta} / \dot{\varepsilon}^T_z$	Exp.		0.03	0.06	1.14	-1.67	0.024	$\dot{\varepsilon}^T_z / \dot{\varepsilon}^T_{z\theta}$
	Theo.	J_3	0	0	1.14	-1.67	0.044	
		J_2	0	0	1.5	-1.5	0	
$\dot{\varepsilon}^T_\theta / \dot{\varepsilon}^T_z$	Exp.		-0.63	-0.52	-0.54	-0.84	0.064	$\dot{\varepsilon}^T_\theta / \dot{\varepsilon}^T_{z\theta}$
	Theo.	J_3	-0.5	-0.5	-0.14	-0.67	0.044	
		J_2	-0.5	-0.5	-0.5	-0.5	0	
$x = f'/f$			-	-	0.13	0.046	0.025	
Y			1	-1	11/16	-11/16	0	

T = 280K

Paths			2	3	4	5	1	
Ratios			Tension	Compression	Tension + Torsion	Compression + Torsion	Torsion	Ratios of $\dot{\underline{\varepsilon}}$ for Torsion
$\dot{\varepsilon}^T_{z\theta} / \dot{\varepsilon}^T_z$	Exp.		0.098	0.03	1.43	-1.05	0.73?	$\dot{\varepsilon}^T_z / \dot{\varepsilon}^T_{z\theta}$
	Theo.	J_3	0	0	1.43	-1.05	0	
		J_2	0	0	1.5	-1.5	0	
$\dot{\varepsilon}^T_\theta / \dot{\varepsilon}^T_z$	Exp.		-0.73	-0.53	-0.64	-0.8	-0.38	$\dot{\varepsilon}^T_\theta / \dot{\varepsilon}^T_{z\theta}$
	Theo.	J_3	-0.5	-0.5	-0.43	-0.05	0	
		J_2	-0.5	-0.5	-0.5	-0.5	0	
$x = f'/f$			-	-	0.02	-0.17	0	
Y			1	-1	11/16	-11/16	0	

T = 300K

Paths			2	3	4	5	1	
Ratios			Tension	Compression	Tension + Torsion	Compression + Torsion	Torsion	Ratios of $\dot{\underline{\varepsilon}}$ for Torsion
$\dot{\varepsilon}^T_{z\theta} / \dot{\varepsilon}^T_z$	Exp.		0.02	0.17	0.86	-0.87	0.33	$\dot{\varepsilon}^T_z / \dot{\varepsilon}^T_{z\theta}$
	Theo.	J_3	0	0	1.01	-1.01	0	
		J_2	0	0	1.5	-1.5	0	
$\dot{\varepsilon}^T_\theta / \dot{\varepsilon}^T_z$	Exp.		-1.45	-1.14	-0.72	-0.94	0	$\dot{\varepsilon}^T_\theta / \dot{\varepsilon}^T_{z\theta}$
	Theo.	J_3	-0.5	-0.5	0	0	0	
		J_2	-0.5	-0.5	-0.5	-0.5	0	
$x = f'/f$			-	-	0.19	-0.19	0.025	
Y			1	-1	11/16	-11/16	0	

for Path #5 and $T = 280$ K. They oscillate around a constant level that can be identified with a mean value. This experimental trend is in agreement with the property discussed in Sec. 3.7.1. The mean values of the experimental dimensionless rate of reorientation work are presented for different paths and temperatures on a single diagram shown in Fig. 20. They are all lesser than unity – the common value, which predicts the J_2-theory. In the case of J_3-theory, for considered A-experiments, the effective reorientation strain rate and dimensionless rate of reorientation work can be calculated by means of Eqs. (3.3) and (2.2). The result is

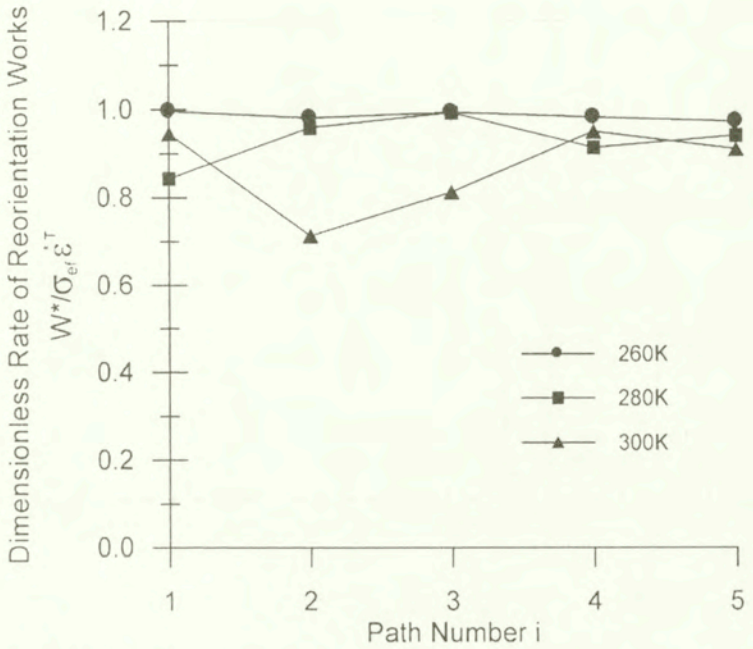

FIG. 20. Path-dependence of dimensionless rate of reorientation work.

$$\dot{\varepsilon}^T = f\dot{\Lambda}\left[1 + 9x^2(1-y^2)\right]^{1/2}, \tag{3.16}$$

$$\frac{W^*}{\sigma_{ef}\dot{\varepsilon}^T} = \frac{1}{\left[1 + 9x^2(1-y^2)\right]^{1/2}} \tag{3.17}$$

The calculated (with use of Eq. (3.17)) theoretical results are given in Table 4 for x values given in Table 3. It is interesting that the calculated values for Paths #4 and #5 are smaller than 1. This shows that account for the third invariant in a theoretical model slightly improves the quality of predictions.

Table 4. Theoretical values of dimensionless rate of reorientation work.

Temp	Path	1	2	3	4	5
	y	0	1	-1	11/16	$-11/16$
260	$W^*/\sigma_{ef}\varepsilon^{*T}$	0.997	1	1	0.962	0.995
280		1	1	1	0.999	0.938
300		1	1	1	0.924	-0.924

The observed discrepancies are again due to existence of the cross-effects. Certain influence stems also from the fact that actual paths deviate from the proportional one as shown in Fig. 3 and remarked in Sec. 3.1.

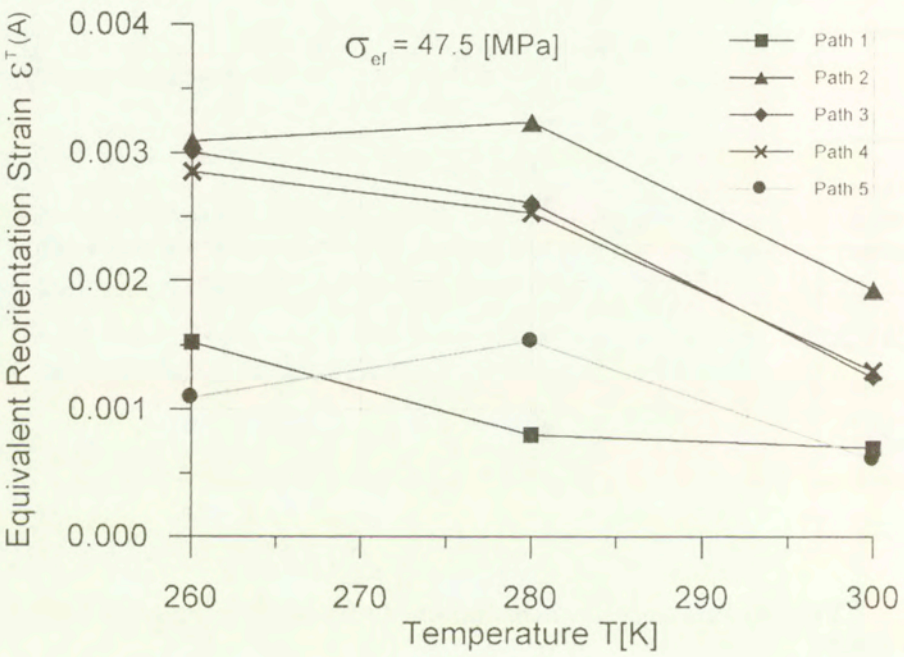

FIG. 21. Equivalent reorientation strain crresponding to $\sigma_{ef} = 47.4$ MPa.

3.8. The range of straining

As already remarked in Sec. 3.1, the maximum stresses were different for different paths and T. The minimum value equal to 47.5 MPa of the effective stress was achieved for Path #2 and $T = 280$ K. This value of the effective stress produces different equivalent reorientation strains along different paths. They are denoted by $\varepsilon^T(A)$ and collectively presented in Fig. 21. The corresponding permanent equivalent reorientation strains (that could be obtained after unload-

ing) are denoted by $\varepsilon^T(B)$. Their approximate values are obtained by "parallel" transition of the measured unloading curves that start from the maximum value of the applied effective stress for given path and temperature. They are given in Fig. 22. The presented data leads to the conclusion, which have already been drawn in Sec 3.5 that (for fixed equivalent stress) the equivalent strains in pure shear or combined shear and compression are the smallest.

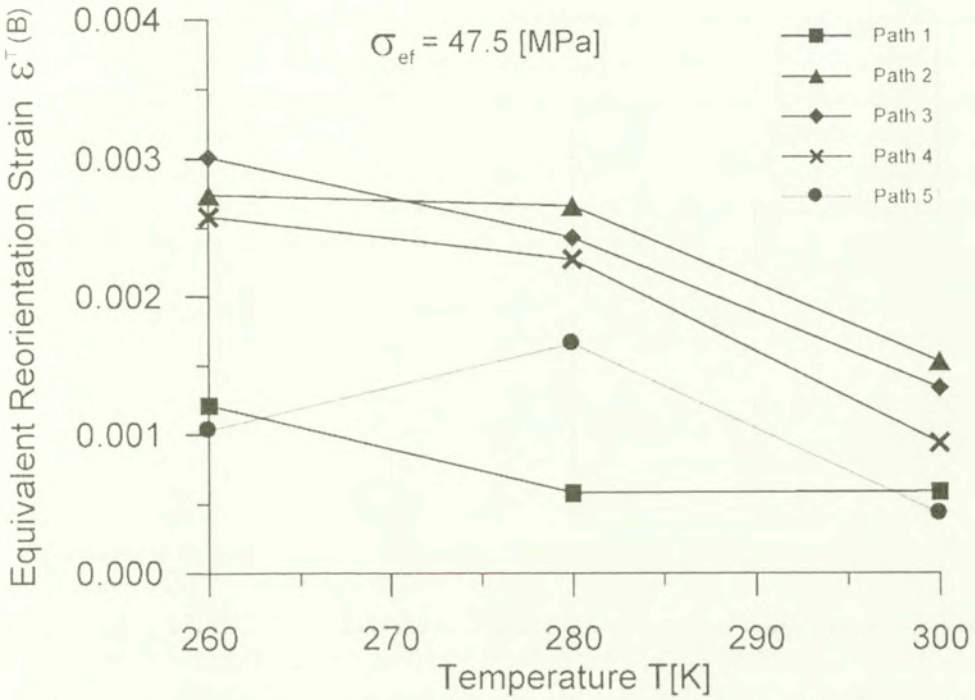

FIG. 22. Permanent equivalent reorientation strain obtained after unloading from $\sigma_{ef} = 47.4$ MPa.

4. Concluding remarks

The deformation behaviour associated with the R-phase reorientation was investigated in a Ti-51.0at%Ni polycrystalline shape memory alloy under the torsion-tension (compression) stress state, and a continuum mechanical approach was proposed to describe the alloy performance.

The limit condition to start the reorientation process, represented as a surface on the axial stress-shear stress plane, was determined for the proportional loading path, and was shown to be not described by the Huber-Mises condition (the J_2-theory). A theoretical framework was presented to model the actual limit surface by taking into account the third invariant of stress deviator through the concept of the shape function. The values of the shape function were experimentally

determined, revealing clearly its path- and temperature-dependence.

The basic experimental features of the plastic flow in the R-phase, such as the flow rule, the ratios of the reorientation strain rates and the dimensionless ratio of the reorientation work, were compared with the predictions of theories that neglect the effects of pressure, compressibility of reorientation strains and effects of induced anisotropy.

The experimental trends qualitatively confirm the predictions of both the J_2-theory and the J_3-theory. The introduction of the third invariant of stress deviator into the theoretical framework improves quantitative discrepancies. However, the macroscopic (overall) deformations accompanying the internal reorientation must be strongly influenced by the second order internal stresses generated in the processes. Therefore, better description should use an extra tensorial parameter representing the internal stresses. The kinematical hardening models, with the back stress as an additional variable, are expected to be more adequate for the description of the flow associated with detwinning. Such models would enable us to describe the experimental trends caused by the induced anisotropy observed here.

Acknowledgments

The authors are grateful for the alloy supply by Mr. T.Ueki and for preparation of the specimens by Messrs. M. Taira, M. Kadowaki and H. Kikuchi.

This work was financially supported by the Polish State Committee for Scientific Research through the research program KBN Nr.7T07A00513. The financial aid by the Japan Society of Promotion of Sciences through the Japan-Europe Research Cooperative Program is also acknowledged.

References

1. S. Miyazaki, K. Nonura and A. Ishida, *Shape memory effects associated with the martensitic and R-phase transformations in sputtered-deposited TiNi thin films*, J. Phys. IV, coll.**5**-8, 677–682, 1995.
2. M. Fremond and S. Miyazaki [Eds.], *Shape memory alloys*, Springer-Verlag, Wien-New York 1996.
3. K.D. Skrobanek, M. Kohl and S. Miyazaki, *Stress-optimised shape memory microactuator*, Proc. 3rd ICIM/ECSSM '96, Lyon 1996.
4. Y. Moriya, H. Kimura, S.Ishizaki, S. Hashizume, S. Suzuki, H. Suzuki and T. Sampei, *Properties of Fe-Cr-Ni-Mn-Si (-Co) shape memory alloys*, J. Phys. IV, coll.**1**-4, 433–438, 1991.
5. V. Birman, *Review of mechanics of shape memory alloy structures*, Appl. Mech. Rev., **50**, 629–645, 1997.

6. E.P. GEORGE, R. GOTTHARDT, K. OTSUKA, S. TROLIER-MOKINSTRY and M. WUN-FOGLE [Eds.], *Materials for smart systems* II, Materials Research Society, Pittsburg 1997.

7. Z.G. WEI, R. SANDSTRÖM and S. MIYAZAKI, *Shape-memory materials and hybrid composites for smart systems*, Part I and II, J. Materials Sci., **33**, 3743–3762, 3763–3783, 1998.

8. F. FALK, *Model free energy, mechanics, and thermodynamics of shape memory alloys*, Acta Metall., **28**, 1773–1780, 1980.

9. F. FALK, *One-dimensional model of shape memory alloys*, Arch. Mech., **35**, 63–84, 1983.

10. K. TANAKA, *A thermomechanical sketch of shape memory effect: One-dimensional tensile behavior*, Res. Mech., **18**, 251–263, 1986.

11. K. TANAKA, S. KOBAYASHI and Y. SATO, *Thermomechanics of transformation pseudoelasticity and shape memory effect in alloys*, Int. J. Plasticity, **2**, 59–72, 1986.

12. I. MÜLLER, *On the size of the hysteresis in pseudoelasticity*, Continuum Mech. Thermodyn., **1**, 125–142, 1989.

13. I. MÜLLER and HUIBIN XU, *On the pseudo-elastic hysteresis*, Acta Metall. Mater., **39**, 263–271, 1991.

14. B. RANIECKI, CH. LEXCELLENT and K. TANAKA, *Thermodynamic model of pseudoelastic behaviour of shape memory alloys*, Arch. Mech., **44**, 261–248, 1992.

15. B. RANIECKI and CH. LEXCELLENT, *R-models of pseudoelasticity and their specification for some shape memory solids*, Euro. J. Mech., A/Solids, **13**, 21–50, 1994.

16. B. RANIECKI and CH. LEXCELLENT, *Thermodynamics of isotropic pseudoelasticity in shape memory alloys*, Euro. J. Mech. A/Solids, **17**, 185–205, 1998.

17. C. LIANG and C.A. ROGERS, *One-dimensional thermomechanical constitutive relations for shape memory materials*, J. Intell. Mater. Syst. Struct., **1**, 207–234, 1990.

18. X.D. ZHANG, C.A. ROGERS and C. LIANG, *Modelling of the two-way shape memory effect*, Phil. Mag. A, **65**, 1199–1215, 1992.

19. L.C. BRINSON and R. LAMMERING, *Finite element analysis of the behavior of shape memory alloys and their applications*, Int. J. Solids Struct., **30**, 3261–3280, 1993.

20. Q.P. SUN and K.C. HWANG, *Micromechanics modelling for the constitutive behavior of polycrystalline shape memory alloys* – I. II, J. Mech. Phys. Solids, **41**, 1–17, 19–33, 1993.

21. V. KAFKA, *Shape memory: A new concept of implementation and of mathematical modelling*. Part I and II, J. Intell. Mater. Syst. Struct., **5**, 809–814, 815–824, 1994.

22. Y. IVSHIN and T.J. PENCE, *A constitutive model for hysteretic phase transition behavior*, Int. J. Engng Sci., **32**, 681–704, 1994.

23. R.D. SPIES, *Results on a mathematical model of thermomechanical phase transitions in shape memory materials*, Smart Mater. Sturct., **3**, 459–469, 1994.

24. E.J. GRAESSER and F.A. COZZARELLI, *A proposed three-dimensional constitutive model for shape memory alloys*, J. Intell. Mater. Syst. Struct., **5**, 78–89, 1994.

25. V.I. LEVITAS, *The postulate of realizability: Formulation and applications to the post-bifurcation behaviour and phase transitions in elastoplastic materials* – I, II, Int. J. Engng Sci., **33**, 921–945, 947–971, 1995.

26. E.N. MAMIYA and J.C. SIMO, *Stress-induced phase transformations in elastic solids under anti-plane deformations: dissipative constitutive models and numerical simulation*, Computer Methods Appl. Mech. Engng, **133**, 47–77, 1996.

27. F. AURICCHIO, R.L. TAYLOR and J. LUBLINER, *Shape-memory alloys: macromodelling and numerical simulations of the superelastic behavior*, Computer Methods Appl. Mech. Engng, **146**, 281–321, 1997.

28. F.D. FISCHER, E.R. OBERAIGNER, K. TANAKA and F. NISHIMURA, *Transformation induced plasticity revised: An update formulation*, Int. J. Solids Struct., **35**, 2209–2227, 1998.

29. S. LECLERCQ, C. LEXCELLENT and J.C. GELIN, *A finite element calculation of devices made of shape memory alloys*, J. Physique IV, Coll. C1, suppl. J. Physique III, **6**, 225–234, 1996.

30. A. ZIÓŁKOWSKI and B. RANIECKI, *FEM-based formulation of the coupled thermomechanical problems of shape memory alloys*, [in:] M. AAKIYAMA and M. KLEIBER [Eds.], Proceedings of the Japan-Central Europe Joint Workshop on Advanced Computing in Engineering, Pułtusk, September 26-29, 207–212, IPPT PAN, Warsaw 1994.

31. A. ZIÓŁKOWSKI and B. RANIECKI, *FEM-analysis of the one-dimensional coupled thermomechanical problem of TiNi SMA*, Suppl. J. Physique III, No. 1, c1, 395, 1996.

32. A. ZIÓŁKOWSKI, *On the layered medium with elastic and shape memory alloy plies under various loading rates*, [in:] O.T. BRUHNS and E. STEIN [Eds.], IUTAM-Symposium on Micro- and Macrostructural Aspects of Thermoplasticity, 427–436, Kluwer Academic Publishers, Dordrecht 1999.

33. E. PATOOR, A. EBERHARDT and M. BERVEILLER, *Thermomechanical behaviour of shape memory alloys*, Arch. Mech., **40**, 775–794, 1988.

34. F.D. FISCHER, *Modelling and simulation of transformation induced plasticity in elastoplastic materials*, [in:] M. BERVEILLER and F.D. FISCHER [Eds.], Mechanics of Solids with Phase Changes, Springer-Verlag, Wien-New York 1997.

35. H. FUNAKUBO, [Ed.], *Shape memory alloys*, Gordon and Breach Science Publishers, New York 1987.

36. T.W. DUERIG, K.M. MELTON, D. STÖCKEL and C.M. WAYMAN, *Engineering aspects of shape memory alloys*, Butterworth-Heinemann, London 1990.

37. F. NISHIMURA, N. WATANABE and K. TANAKA, *Analysis of uniaxial stress-strain-temperature hysteresis in an Fe-based shape memory alloy under thermomechanical loading*, Computational Mater. Sci., **8**, 349–362, 1997.

38. A. BEKKER and L.C. BRINSON, *Temperature-induced phase transformation in a shape memory alloy: Phase diagram based kinetics approach*, J. Mech. Phys. Solids, **45**, 949–988, 1997.

39. A. BEKKER and L.C. BRINSON, *Phase diagram based description of the hysteresis behavior of shape memory alloys*, Acta Mater. **46**, 3649–3665, 1998.

40. K. TANAKA, F. NISHIMURA, H. KATO and S. MIYAZAKI, *Transformation thermomechanics of R-phase in TiNi shape memory alloys*, Arch. Mech., **49**, 547–572, 1997.

41. J. LAMAITRE and J.-L. CHABOCHE, *Mechanics of solids materials*, Cambridge University Press, Cambridge 1990.

42. L. ORGEAS and D. FAVIER, *Non-symmetric tension-compression behaviour of NiTi alloy*, J. Phys., coll.**8**-5, 605–610, 1995.

43. L. ORGEAS and D. FAVIER, *Stress-induced martensitic transformation of a NiTi alloy in isothermal shear, tension and compression*, Acta Mater., **46**, 5579–5591, 1998.

44. M. TOKUDA, P. SITTNER, M. TAKAKURA and YE MEN, *Experimental study on performances in Cu-based shape memory alloy under multiaxial loading conditions*, Materials Sci. Research Int., **1**, 260–265, 1995.

45. P. SITTNER and M. TOKUDA, *Reorientation in combined stress induced martensite?*, J. Phys., coll.**8**-5, 1003–1008, 1995.

46. P. SITTNER, Y. HARA and M. TOKUDA, *Experimental study on the thermoelastic martensitic transformation in shape memory alloy polycrystal induced by combined external forces*, Metall. Mater. Trans. A, **26A**, 2923–2935, 1995.

47. C. ROGUEDA, C. LEXCELLENT and L. BOCHER, *Experimental study of psudoelastic behaviour of a CuZnAl polycrystalline shape memory alloy under tension-torsion proportional and non-proportional loading tests*, Arch. Mech., **48**, 10250–1045, 1996.

48. F. NISHIMURA, N. WATANABE, T. WATANABE and K. TANAKA, *Transformation conditions in an Fe-based shape memory alloy under tensile-torsional loads: Martensite start surface and austenite start/finish planes*, Materials Sci. Engng A, **264**, 232–244 1999.

49. F. NISHIMURA, N. WATANABE and K. TANAKA, *Evolution of martensite start condition in general thermomechanical loads of an Fe-based shape memory alloy*, Int. J. Mech. Sci., 1999, in press.

50. K. JACOBUS, H. SEHITOGLU and M. BLAZER, *Effect of stress state on the stress-induced martensitic transformation in polycrystalline Ni-Ti alloy*, Metall. Mater. Trans. A, **27A**, 1–8, 1996.

51. K. GALL, H. SEHITOGLU, H.J. MAIER and K. JACOBUS, *Stress-induced martensitic phase transformations in polycrystalline CuZnAl shape memory alloys under different stress states*, Metall. Mater. Trans. A, **29A**, 763–773, 1998.

52. E. PATOOR, A. EBERHARDT and M. BERVEILLER, *Micromechanical modelling of the shape memory behavior*, [in:] L.C. BRINSON and B. MORAN [Eds.], Mechanics of phase transformations and shape memory alloys, AMD **189**/PVP **292**, ASME, 23–37, 1994.

53. K. OTSUKA and C.M. WAYMAN [Eds.], *Shape memory materials*, Cambridge University Press, Cambridge 1998.

54. S. MIAYZAKI and K. OTSUKA, *Deformation and transition behavior associated with the R-phase in Ti-Ni alloys*, Metall. Trans., A, **17A**, 53–63, 1986.

55. S. MIYAZAKI and C.M. WAYMAN, *The R-phase transition and associated shape memory mechanism in TiNi single crystals*, Acta Metall., **36**, 181–192, 1988.

56. S. MIYAZAKI, S. KIMURA and K. OTSUKA, *Shape-memory effect and pseudoelasticity associated with the R-phase transition in Ti-50.5 at.%Ni single crystals*, Phil. Mag. A, **57**, 467–478, 1988.

57. K. TANAKA, K. KITAMURA and S. MIYAZAKI, *Shape memory alloy preparation for multiaxial tests and identification of fundamental alloy performance*, see this issue of Arch. Mech. **51**, 6, 727–744, 1999.

58. B. RANIECKI, L. DIETRICH, Z.L. KOWALEWSKI, G. SOCHA, S. MIYAZAKI, K. TANAKA, *Experimental methodology fot TiNi shape memory alloy testing under complex stress state*, see this issue of Arch. Mech., **51**, 6, 727–744, 1999.

59. D.J. BARRETT, *A three-dimensional phase transformation model for shape memory alloys*, J. Intelligent Material Syst. Structures, **6**, 831–839, 1995.

60. H. TOBUSHI, S. YAMADA, T. HACHISUKA, A. IKAI and K. TANAKA, *Thermomechanical properties due to martensitic and R-Phase transformations of TiNi shape memory alloy subjected to cyclic loadings*, Smart Mater. Struct., **5**, 788–795, 1996.

61. K. TANAKA and T. WATANABE, *Transformation conditions in a Fe-based shape memory alloy: An experimental study*, Arch. Mech., to be submitted.

62. J.B. LEBLOND, G. MOTTET and J.C. DEVAUX, *A theoretical and numerical approach to the plastic behaviour of steels during phase transformation* – I, II, J. Mech. Phys. Solids, **34**, 395–409, 411–432, 1986.

63. J.G. BOYD and D.C. LAGOUDAS, *A thermodynamical constitutive model for shape memory materials*, I, **12**, 805–842, 1996.

Received March 24, 1999.

Arch. Mech., **51**, 6, pp. 785–803, Warszawa, 1999

Shape memory alloy preparation for multiaxial tests and identification of fundamental alloy performance

K. TANAKA ([1]), K. KITAMURA ([2]) and S. MIYAZAKI ([2])

([1]) *Department of Aerospace Engineering*
Tokyo Metropolitan Institute of Technology
J-191-0065 Hino/Tokyo, Japan
e-mail: kikitana@astan1.tmit.ac.jp

([2]) *Institute of Materials Science*
University of Tsukuba
J-305-8573 Tsukuba, Japan
e-mail: miyazaki@mat.ims.tsukuba.ac.jp

TiNi SHAPE MEMORY alloy preparation for the multiaxial tests was explained. Stable response of the alloy was realized, not by training but by an effective combination of the alloying technique and the heat treatment: Ti-51.0at%Ni polycrystalline shape memory alloy heat-treated by annealing at 673 K for 3.6 ks followed by cooling in a furnace. Some preliminary tests were performed to identify the fundamental alloy characteristics: the transformation temperatures, the stress-strain curves at several temperatures and the strain-temperature curves under constant hold stresses.

Keywords: TiNi shape memory alloy, Multiaxial tests, Alloying and heat treatment, Ni-rich shape memory alloy, Training.

1. Introduction

IN RECENT APPLICATIONS of shape memory alloys (SMAs), SMA devices often work under the complex multiaxial stress states. The SMA components inside the SMA composites, for example, are actually subjected to such conditions, although the composites themselves might be operated under a simple load when performing their special function associated with the shape memory effect [1, 2]. Of course, larger size SMA devices, such as pipe fasteners, have to carry the complex mechanical loads, in addition to thermal load [3, 4].

In order to design effectively such SMA devices, one has to know as exactly as possible the thermomechanical response of SMA under multiaxial stress states. Only a few studies have been carried out so far on the thermomechanical behavior of SMAs under the multiaxial stress states; SITTNER and TOKUDA [5 – 7] and ROGUEDA *et al.* [8] in Cu-based SMA, NISHIMURA *et al.* [9 – 11] in Fe-based

SMA and SEHITOGLU *et al.* [12, 13] in TiNi and Cu-based SMAs. Torsion-tension (compression) tests were preferably carried out with thin-walled tubular specimens. The martensitic and reverse transformation start/finish conditions and the stress-strain-temperature curve hysteresis were intensively investigated. Asymmetry of the stress-strain in tension and compression [14, 15], and of the martensitic transformation start condition in the stress-temperature space were clearly observed in all SMAs, thus approving the theory with the third invariant of the stress tensor [16, 17]. The normality law was also investigated with a strong expectation that the transformation condition, represented by a surface in the stress-temperature space, could play a role of a potential, just like in plasticity, leading to the evolution equations for the internal variables, such as the transformation strain and the volume fraction of martensite [18]. The accumulation of the data is, however, still necessary to establish a rational theoretical framework in transformation thermomechanics of SMAs.

The SMA sample for the multiaxial tests has to exhibit always a stable response to repeated thermomechanical loads, since a single specimen is usually used repeatedly in the test. In order to realize a stable performance, SMAs are often "trained" prior to actual operations [19, 20]. This kind of stabilization of the alloy properties should not be employed when investigating the intrinsic alloy characteristics, since the subsequent alloy performance is strongly influenced by the directional training. Alloying technique and the heat treatment, studied intensively by MIYAZAKI *et al.* [19, 20], should be the strategy to achieve the requirement.

In 1996 the Japanese-Polish cooperative study "Testing and Modelling the Behavior of Shape Memory Alloys" has started through the Japan-Europe Research Cooperative Program promoted by both the Japan Society of Promotion of Sciences and the Polish Academy of Sciences. The torsion-tension (compression) tests with the thin-walled tubular specimen in TiNi shape memory alloy were performed to investigate the thermomechanical behavior associated with the reorientation of the R-phase or the martensite variants, and with the stress-induced R-phase or martensitic transformation [21 – 24]. In this paper, the method of alloy preparation for the Project is explained, and some preliminary alloy properties are determined.

2. Alloy strategy for multiaxial tests

2.1. Requirements for multiaxial tests

Following points should be carefully taken into account when preparing the alloy for the multiaxial tests in SMAs: First of all, as in the case of plasticity, the size of the specimen should be large enough to realize a uniform stress and

strain state inside the specimen. The experimental system, used in the present Japanese-Polish cooperative project, actually requires the dimensions of the thin-walled tubular specimen to be the following: 20 mm in outer diameter, 1.5 mm in wall thickness, 50 mm in parallel part, 120 mm in total length and 26 mm in the maximum diameter for the grip ends [25] (cf. Fig. 1). One should note that the size is extremely large compared to the specimens employed in the usual tests in SMAs. Needless to say, the alloy properties should be isotropic.

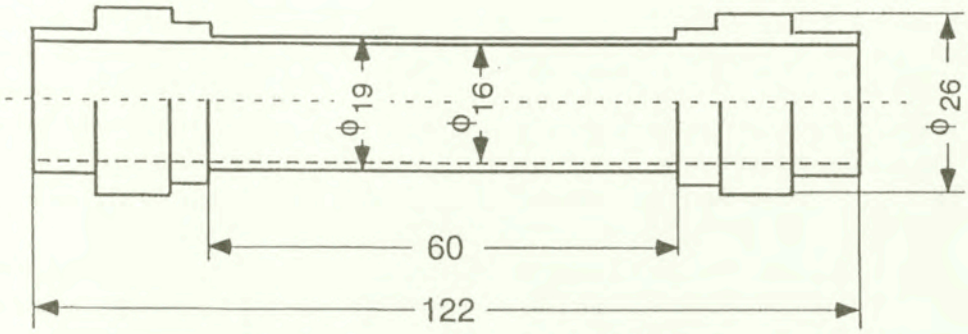

FIG. 1. Test specimen for multiaxial tests.

Secondly, almost perfect stability of the thermomechanical alloy properties is required since the specimen must be used repeatedly in the tests. The irreversible change of internal structure on the microscopic level should appear in the specimen during the tests. This requirement strongly limits the method of stabilizing the alloy response. The strain-temperature or the stress-strain hysteresis loop usually changes cycle by cycle during thermal or mechanical cyclic loading, and the loop gradually tends to a limit loop, after some 50 to 100 cycles of loading [19, 20]. The dislocations and other lattice defects are introduced during cycling, which increase the critical stress for slip, resulting in a stable response of the alloy. This way of stabilizing the alloy performance, the training, cannot be employed in the present alloy preparation since the direction of stressing strongly influences the subsequent alloy response, although a stable performance is finally observed. The alloy response after training cannot be regarded as the intrinsic characteristics of the alloy. Not the training, but the alloying technique and the appropriate heat treatment should, therefore, be the method to achieve a stable response of the alloy.

2.2. Alloying strategy to acquire stable response

According to a comprehensive investigation by MIYAZAKI *et al.* [19, 20], the critical stress for slip is highly sensitive in TiNi SMAs to both the thermomechanical treatment and the Ni content. They have clearly demonstrated that two

strategies effectively work in order to raise the critical stress for slip, and as a result, to stabilize, during cycling, the transformation temperatures of both the R-phase and martensitic transformation. Introduction of fine precipitates, actually Ti_3Ni_4 precipitates, and the introduction of dislocations. The precipitation hardening and the hardening due to a high dislocation density are the physical mechanisms behind the phenomenon.

The Ti_3Ni_4 precipitates, of the order of 40 nm in size, were found to form uniformly with an optimal state for both their size and density when the alloy specimen was aged at 673 K for 3.6 ks. However, the specimens for the multiaxial stress tests demand considerably large bar sizes, i.e., larger than 26 mm in diameter, as raw materials. It is not expected to introduce uniform plastic strain throughout the whole rod of such dimension. For this reason, the dislocation hardening mechanism was not applied for the present investigation. In order to use the precipitation hardening mechanisms, a Ni-rich Ti-51.0at% Ni polycrystalline alloys was selected for the multiaxial stress tests.

The Ti-51.0at% Ni alloy ingot was made in a carbon crucible by high-frequency vacuum induction melting. The ingot was hot forged at the temperature range between 1073 K and 1173 K to make bars of 28 mm in diameter and 150 mm in length. The bars were machined to make the outer shape and spark-cut to make the inner shape of the thin-walled turbular specimens for the multiaxial stress tests. Smaller bars of about 15 mm in diameter were extracted by spark-cutting. Rectangular tensile specimens, 1.0 mm in thickness, 2.0 mm in width, 50 mm in length and 30 mm in gauge length, were made from small bars. The specimens for both multiaxial stress tests and tensile tests were etched by acid solution after mechanical polishing. They were annealed at 673 K for 3.6 ks followed by cooling in a furnace. They were again chemically polished to remove slightly oxidized surface layers. The average grain size was about 30 μm.

The experimental results in the torsion-tension (compression) tests with this specimen are reported elsewhere [25]. A stable response of the alloy is actually demonstrated there, and the isotropy of the alloy characteristics is discussed as an important issue.

3. Fundamental alloy performance

Fundamental uniaxial alloy performance was identified for designing an effective experimental program under the multiaxial stress state.

3.1. Transformation temperatures

Transformation temperatures were determined by means of DSC (differential scanning calorimetry) tests. In Fig. 2, the upper curves were measured by

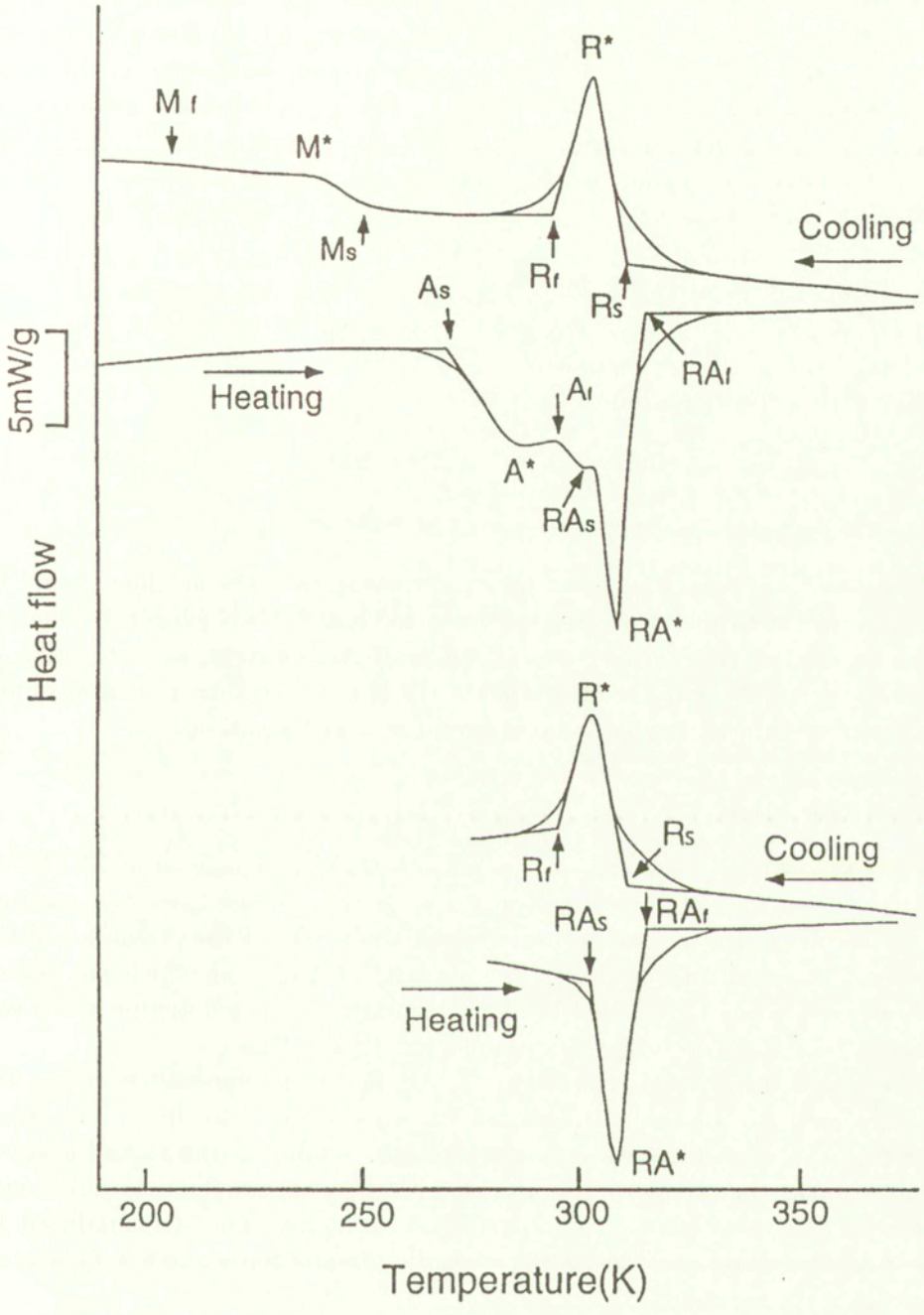

FIG. 2. DSC tests and transformation temperatures.

varying temperature between 150 K and 380 K in order to observe tqo peaks associated with the R-phase and martensitic transformations. The curve upon cooling reveals the two transformations to be well separated. However, the two peaks for the reverse transformations partially overlap each other in the curve upon heating. Therefore, a partial thermal cycling test was also conducted to observe only the R-phase transformation as shown by the lower DSC curves. The results of the transformation temperatures are summarized as follows:

R-phase transformation:

$$\text{Rs} = 306\ \text{K}, \qquad \text{Rf} = 293\ \text{K},$$

$$\text{RAs} = 305\ \text{K}, \qquad \text{RAf} = 316\ \text{K}.$$

Martensitic transformation:

$$\text{Ms} = 253\ \text{K}, \qquad \text{Mf} = 208\ \text{K},$$

$$\text{As} = 268\ \text{K}, \qquad \text{Af} = 306\ \text{K}.$$

The result indicates that the multiaxial tests in the present alloy should be carried out at the temperature range between 200 K and 375 K when investigating all the aspects of transformation and deformation behavior, as a function of temperature, including the reorientation of the R-phase and martensite variants, and the stress-induced R-phase and martensitic transformations.

3.2. Stress-strain curves

The isothermal stress-strain curves were obtained by means of a INSTRON-type testing machine at several temperatures in the proposed test temperature range. The displacement was measured from the stroke of the crosshead of the machine. The specimen was dipped in a hot bath of silicon oil, which was heated by an electric heater or cooloed by liquid nitrogen. The test temperature was controlled by ± 0.5 K in both the specimen length and time.

The results are summarized in Fig. 3. At the lower temperature range, the thermally induced R-phase variants are reoriented during loading. The reorientation of the martensite variants then follows, exhibiting the second stage of deformation on the stress-strain curves. The pseudoelasticity associated with the martensitic transformaton is observed above 300 K. The stress-induced R-phase transformation precedes the martensitic transformation in a very narrow temperature range around 336 K.

This characteristic is clearly confirmed when the critical stresses necessary to start the reorientation or transformation are plotted in Fig. 4, where σ_{M}, σ_{A} and σ_{R} stand for the martensite start stress, austenite start stress and the

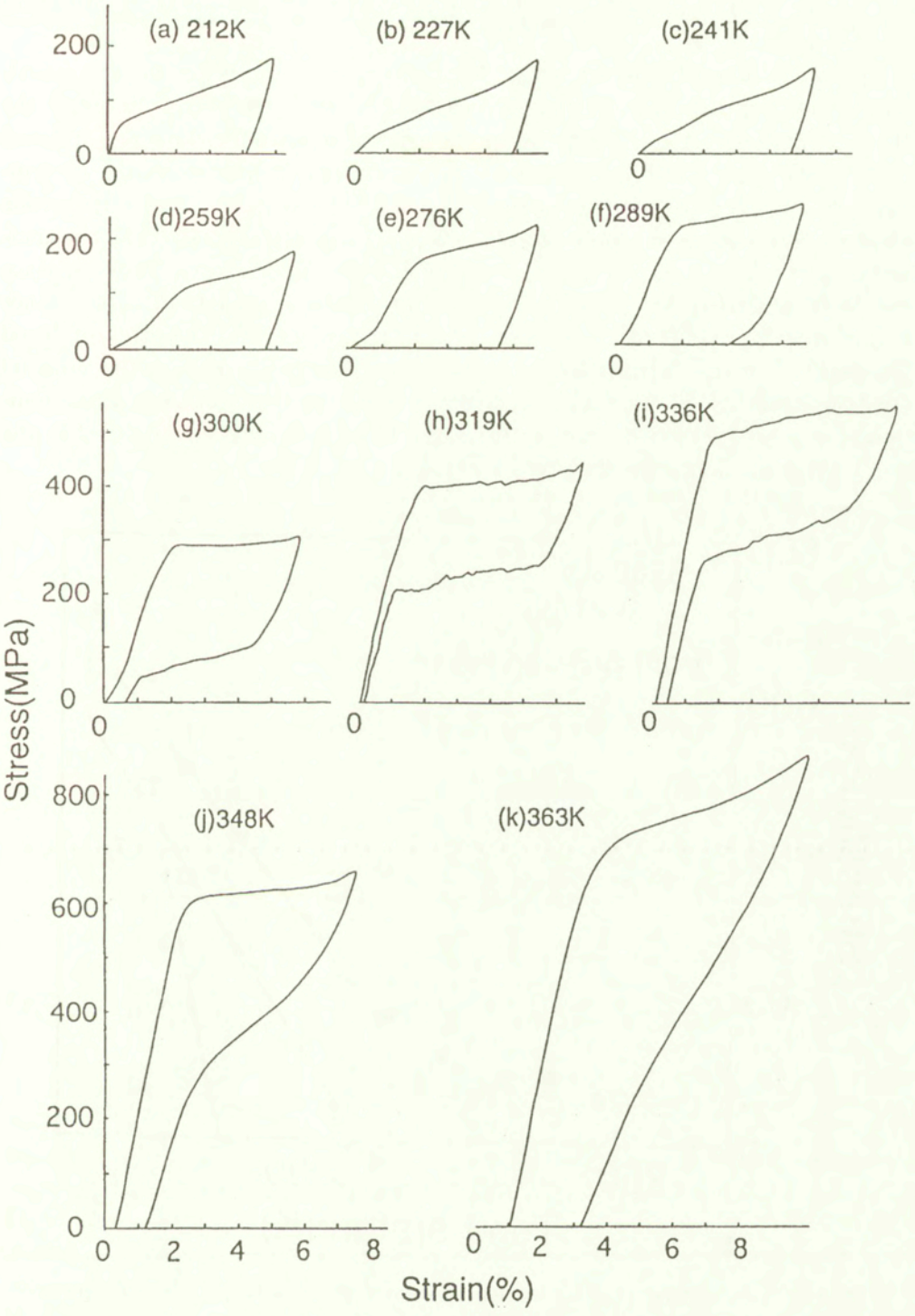

FIG. 3. Isothermal stress-strain curves.

R-phase transformation start stress, respectively (See Fig. 5 for the definition). The critical stresses need for the reorientation of the martensite variants or the R-phase variants are low compared to the critical stresses for the stress-induced transformations. The former critical stresses are nearly insensitive to the temperature. The linear temperature-dependence indicated by the lines corresponds to the Clausis-Clapeyron relation [21 – 23]. The result suggests that the multiaxial tests should start from the study of R-phase reorientation process, since the tests can safely be carried out at the lower stress level than in the other processes: the reorientation of the martensite variants, and the stress-induced R-phase and martensitic transformations. Phase diagram, not on the uniaxial stress-temperature plane like the one in Fig. 4 but, in the multiaxial stress-temperature space, should be one of the issues to be specially investigated in the study programs following the present paper.

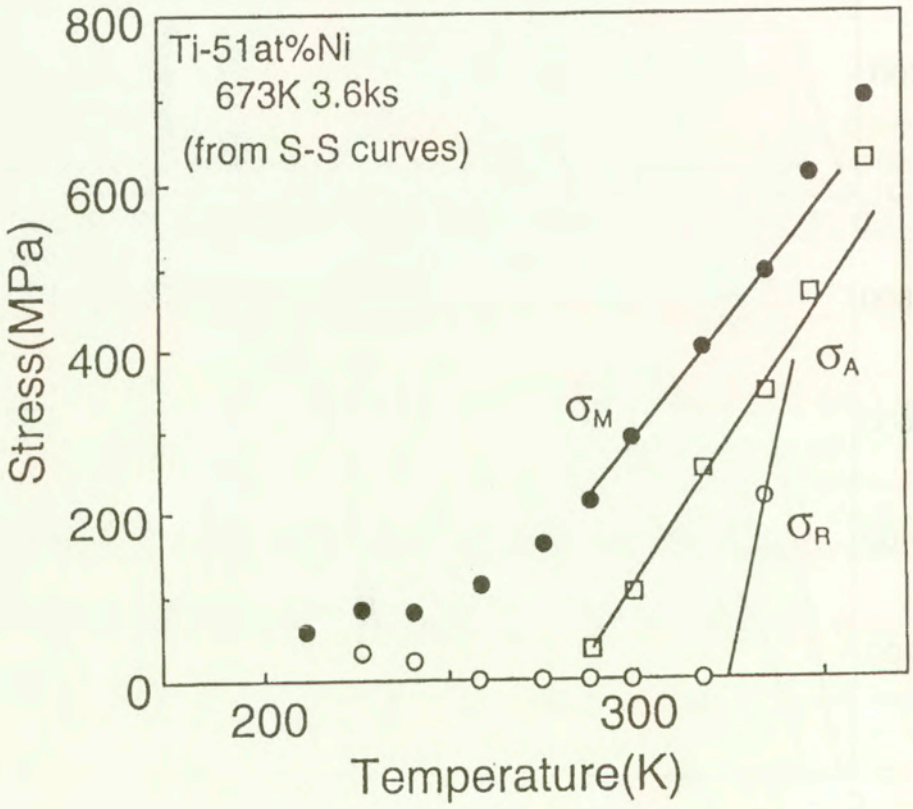

FIG. 4. Critical stress to start reorientation or transformations; Phase diagram.

Figure 5 illustrated the stress and strain characteristic parameters which identify the stress-strain curve at typical temperature ranges.

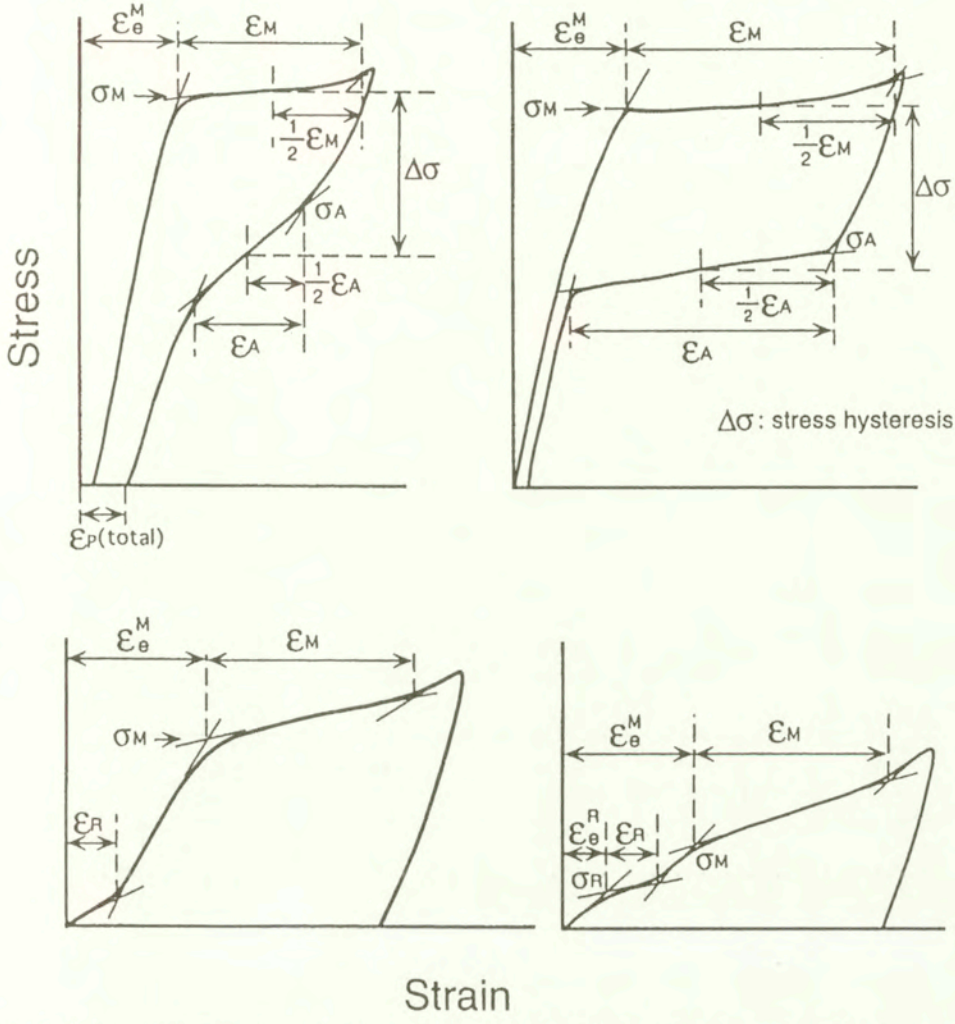

FIG. 5. Schematic diagrams of stress-strain curves, defining the characteristic stress and strain parameters.

The evolution of the strain parameters are plotted in Figs. 6 and 7. The martensitic transformation strain ε_M and the reverse transformation strain ε_A, having the values of 3 to 5%, increase with the martensite start stress σ_M, meaning they strongly depend on the temperature. As σ_M becomes larger, i.e., at higher temperature range, a full shape recovery is not expected after a full martensitic transformation. The R-phase transformation strain ε_R, which is almost temperature-independent, is much smaller in the whole temperature range than the martensitic transformation strain ε_M. It should be noted that the strain components, ε_e^R and ε_e^M, do not stand for the elastic component in a strict sense, but represent roughly the reversible part of the total strain.

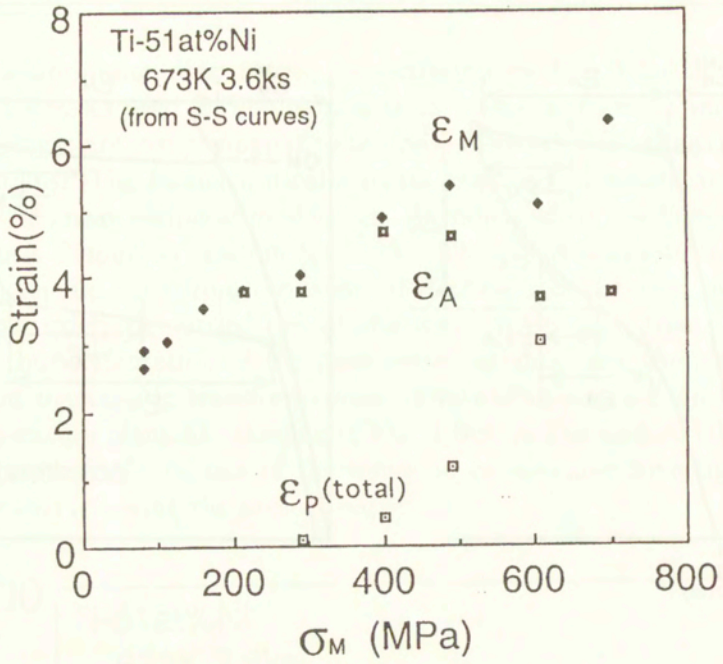

FIG. 6. Transformation strains in martensitic and reverse transformation, and evolution of irreversible strain.

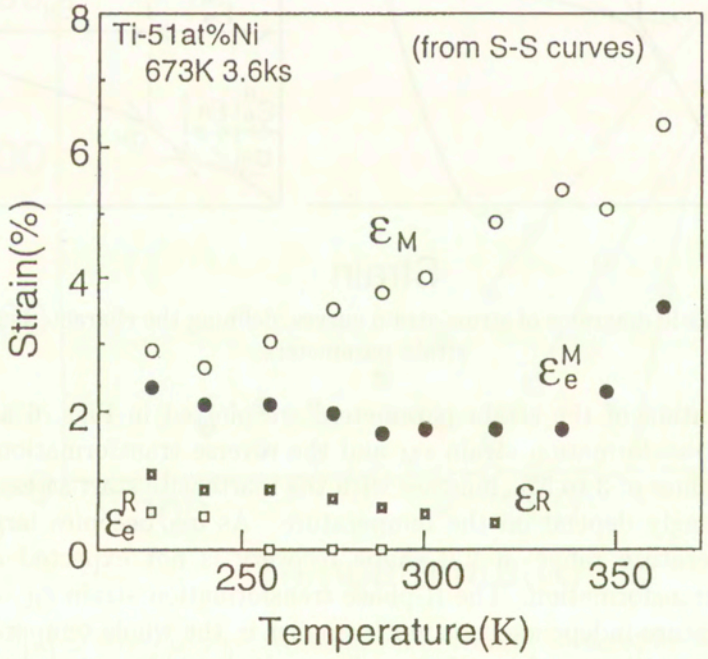

FIG. 7. Transformation strains in martensitic and R-phase transformations.

The stress hysteresis $\Delta\sigma$, which is defined in Fig. 5 and measures the size of the hysteresis loop at the pseudoelastic temperature range, depends on the temperature as plotted in Fig. 8. At the pseudoelastic temperature range around 320 K, where the full shape recovery is observed, the stress hysteresis exhibits the minimum value.

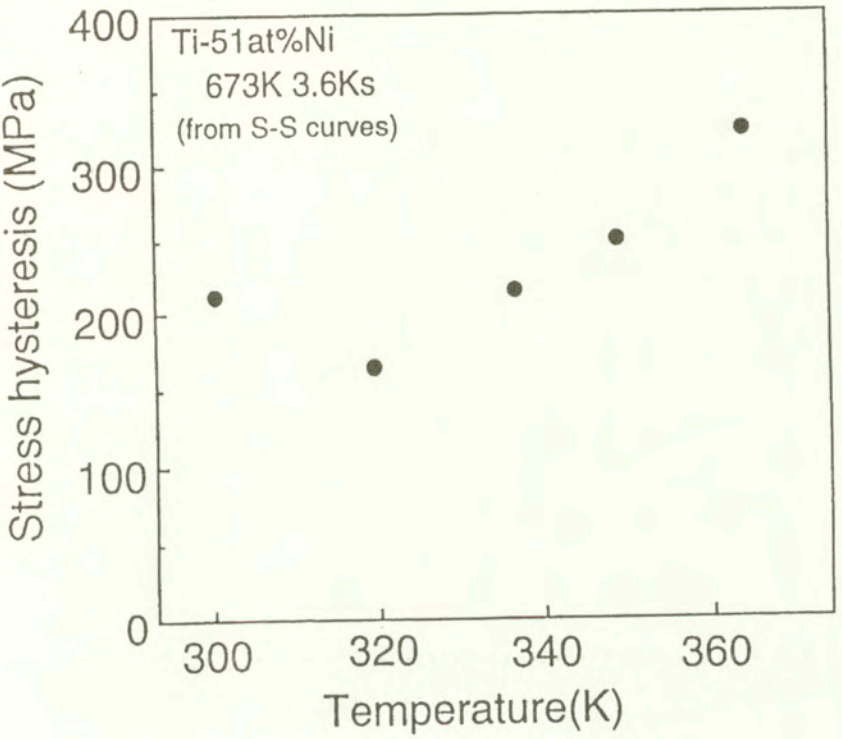

FIG. 8. Temperature-dependence of stress hysteresis.

The stress hysteresis normally decreases with increasing temperature or stress. However, it increases when considerable amount of plastic strain is induced during transformation as shown by the data at higher temperatures. This suggests that all the necessary tests associated with the martensitic transformation must be conducted at the temperature range below 320 K.

3.3. Strain-temperature curves under constant stress

Strain-temperature curves were determined under constant hold stresses with the same experimental system explained in Sec. 3.2. The cooling and heating rates were about 4 K/min in the whole tests. The result is summarized in Figs. 9 and 10. Figure 9 shows the shape memory behavior associates with both the

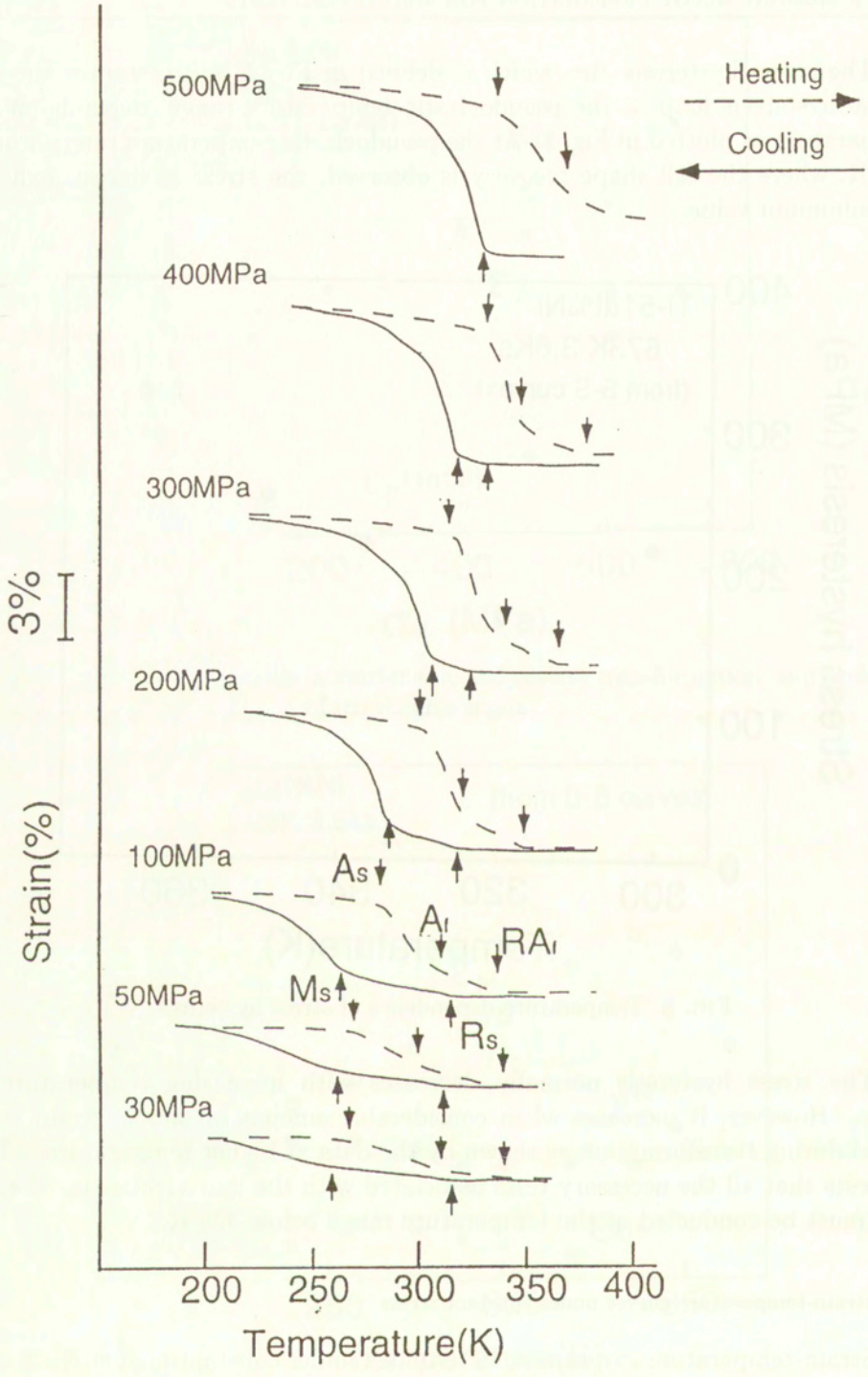

FIG. 9. Strain-temperature curves under constant hold stress.

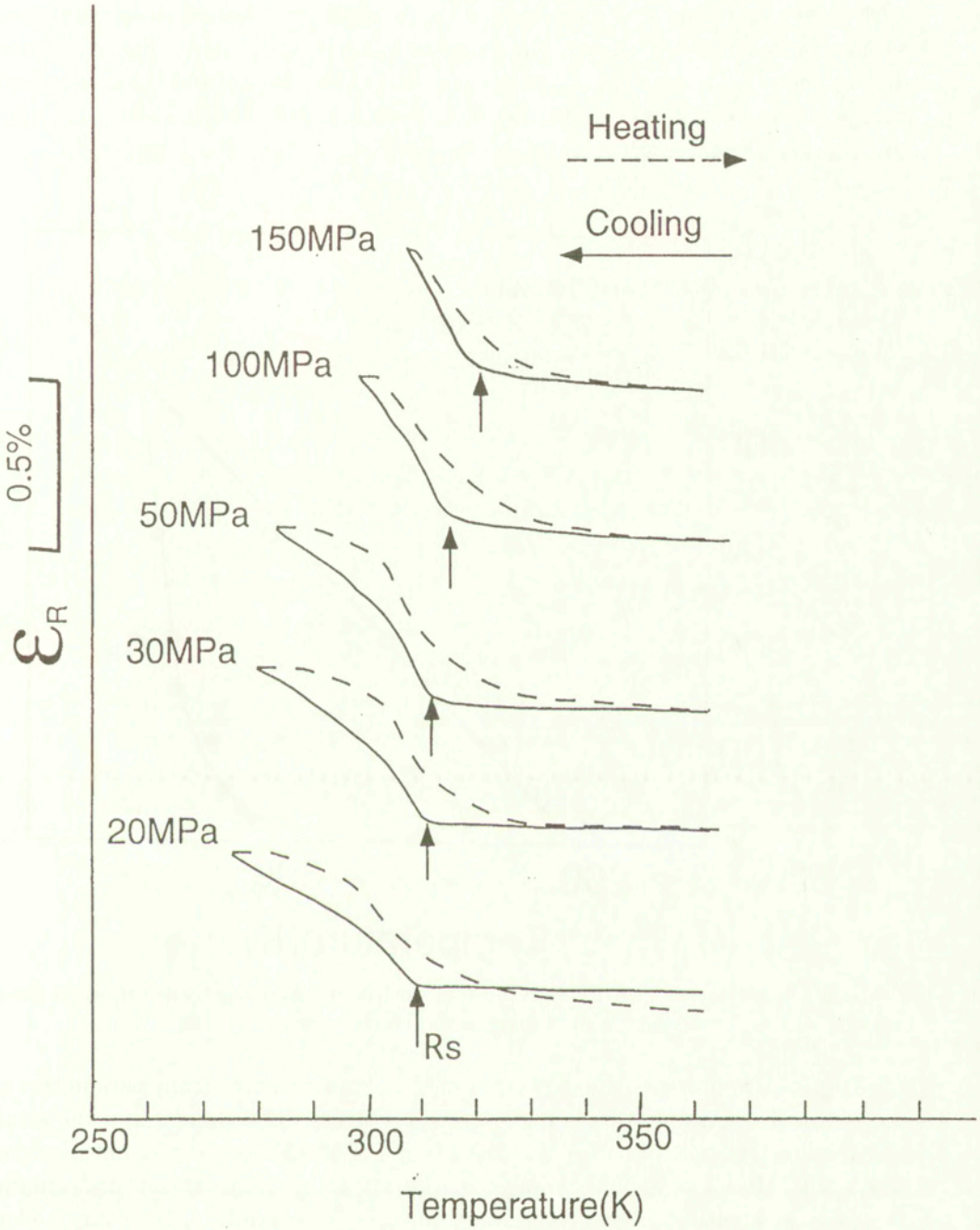

FIG. 10. Strain-temperature curves under constant hold stress; Details at lower hold stress level.

R-phase and martensitic transformations, while Fig. 10 shows that associated with only the R-phase transformation. The solid and dashed lines correspond to the shape changes upon cooling and heating, respectively. The hold-stress dependence of the transformation temperatures, Ms, As, Rs and RAf, are clearly observed. One can now construct another phase diagram shown in Fig. 11, which reveals clearer characteristics of the transformation stresses σ_M and σ_R.

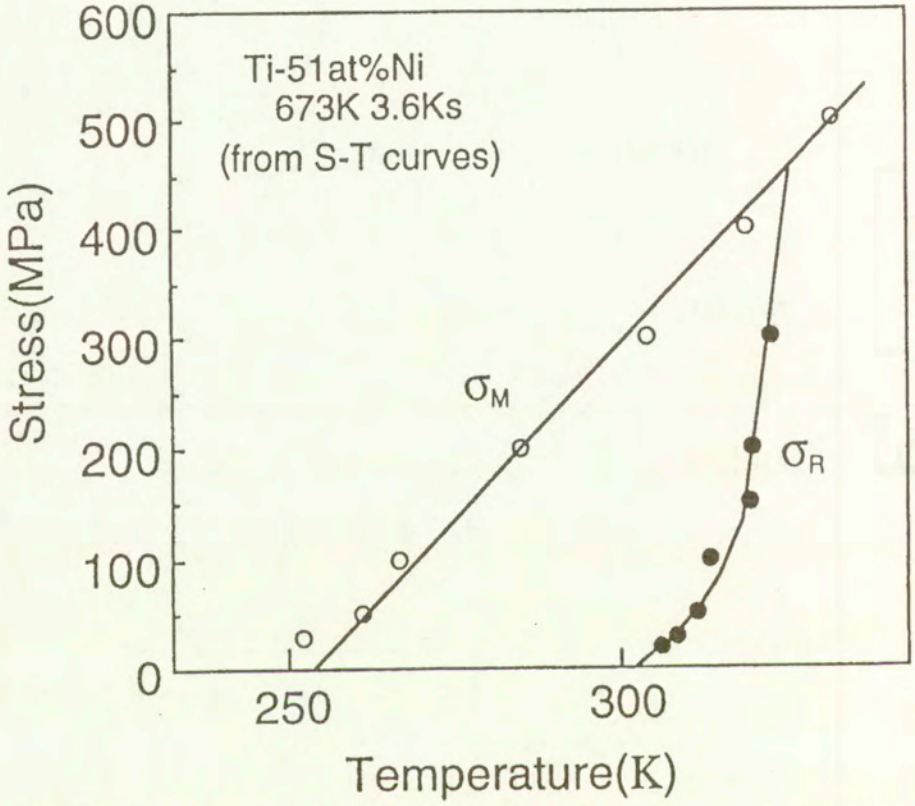

FIG. 11. Critical stress to stress-induced martensitic and R-phase transformation determined from strain-temperature curves.

Figure 12 represents the definition of the characteristic strain parameters on the strain-temperature curves under constant stress. The change in some strain parameters are shown in Figs. 13 and 14. A full shape recovery is not observed above 300 MPa. The R-phase transformation strain ε_R, is about ten times smaller than the martensitic transformation strain ε_M. It is exhibits, however, a clear sensitivity to the hold stress. This a point to be effectivelly used in practical applications.

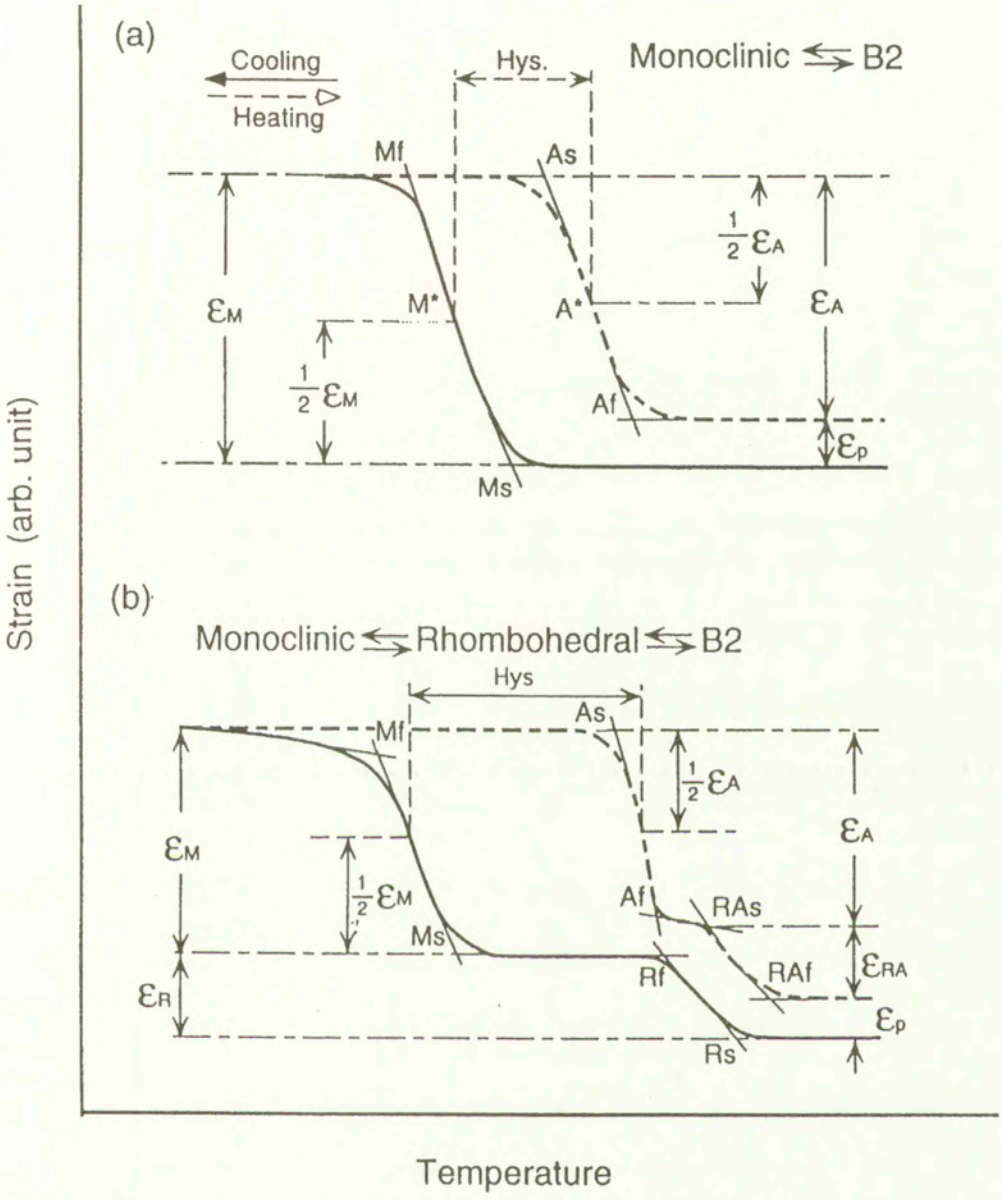

FIG. 12. Schematic diagrams of strain-temperature curves under hold stress, defining the characteristic strain parameters and transformation temperatures; (a) single stage transformation associated with the typical transformation from B2 to M(monoclinic), and (b) two-stage transformation from B2 to E(rhombohedral) to M.

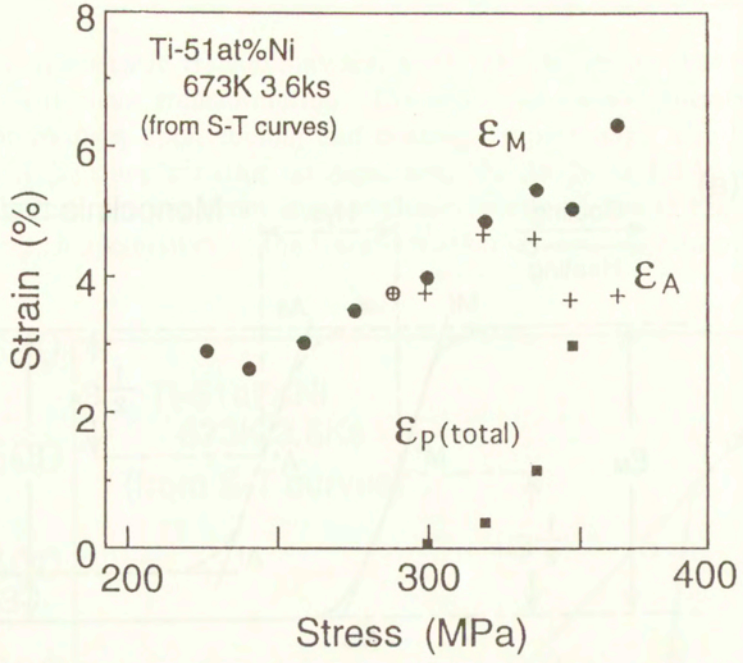

FIG. 13. Transformation strain in martensitic and reverse transformations, and evolution of irreversible strain determined from strain-temperature curves.

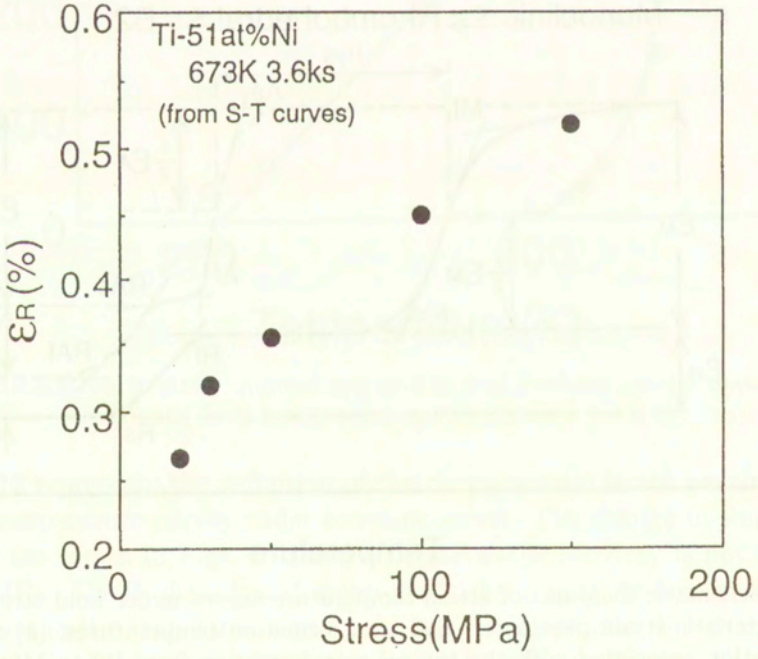

FIG. 14. Evolution of R-phase transformation strain.

The temperature hysteresis, plotted in Fig. 15, shows again that the loop is closed at the stress range around 300 MPa.

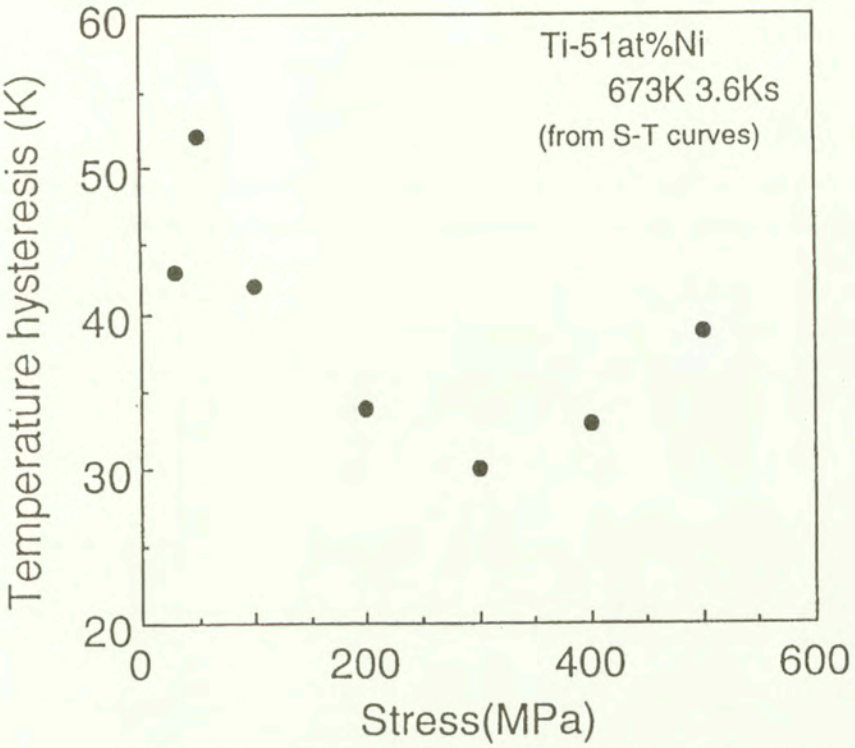

FIG. 15. Stress-dependence of temperature hysteresis.

4. Concluding remarks

A Ti-Ni shape memory alloy sample was prepared for the multiaxial tests. The training was not employed to achieve a stable response of the alloy since the method of training, more directly, the direction of stressing, strongly influences the subsequent alloy performance, thus eliminating totally the intrinsic property of the alloy.

Effective combination of the alloying technique and the heat treatment, Ti-51.0at%Ni polycrystalline shape memory alloy heat-treated by annealing at 673 K for 3.6 ks followed by cooling in a furnace, enables us to machine the thin-walled tubular specimens, 19 mm in outer diameter, 1.5 mm in wall thickness, 26 mm in maximum diameter and 122 mm in length.

Some preliminary tests were performed to identifity the fundamental alloy characteristics; the transformation temperatures, the stress-strain curves

at several temperatures and the strain-temperature curves under constant hold stresses. The data were used to design an effective experimental program.

The multiaxial tests with this test piece actually revealed that the alloy is prepared perfectly, without showing any macroscopic shape irreversibility during a series of tests [25].

Acknowledgments

The authors are grateful for supply of the alloy by Mr. T. UEKI and for preparation of the specimens by Messrs. M. TAIRA, M. KADOWAKI and H. KIKUCHI.

One of the authors (K.T.) expresses his thanks for the financial support by the Special Research Fund Tokyo Metropolitan Government. The financial aid provided by the Japan Society of Promotion of Sciences through the Japan-Europe Research Cooperative Program is also acknowledged.

References

1. E.P. GEORGE, R. GOTTHARDT, K. OTSUKA, S. TROLIER-MCKINSTRY and M. WUN-FOGLE [Eds.], *Materials for smart systems* II, Materials Research Society, Pittsburgh, 1997.
2. Z.G. WEI, R. SANDSTRÖM and S. MIYAZAKI, *Shape-memory materials and hybrid composites for smart systems, Part* I *and* II, J. Materials Sci., **33**, 3743–3762, 3763–3783, 1998.
3. T.W. DUERIG, K.M. MELTON, D. STÖCKEL and C.M. WAYMAN, *Engineering aspects of shape memory alloys*, Butterworth-Heinemann, London 1990.
4. Y. MORIYA, H. KIMURA, S. ISHIZAKI, S. HASHIZUME, S. SUZUKI, H. SUZUKI and T.SAMPEI, *Properties of* Fe-Cr-Ni-Mn-Si(-Co) *shape memory alloys*, J. Phys. IV, **1**, 4, 433–438, 1991.
5. M. TOKUDA, P. SITTNER, M. TAKAKURA and YE MEN, *Experimental study on performances in* Cu-*based shape memory alloy under multiaxial loading conditions*, Materials Sci. Research Int., **1**, 260–265, 1995.
6. P. SITTNER and M. TOKUDA, *Reorientation in combined stress-induced martensite?*, J. Phys., **8**, 5, 1003-1008, 1995.
7. P. SITTNER, Y. HARA and M. TOKUDA, *Experimental study on the thermoelastic martensitic transformation in shape memory alloy polycrystal induced by combined external forces*, Metall. Mater. Trans. A, **26A**, 2923–2935, 1995.
8. C. ROGUEDA, C. LEXCELLENT and L. BOCHER, *Experimental study of pseudoelastic behaviour of a* CuZnAl *polycrystalline shape memory alloy under tension-torsion proportional and non-proportional loading tests*, Arch. Mech., **48**, 10250–1045, 1996.
9. F. NISHIMURA, N. WATANABE, T. WATANABE and K. TANAKA, *Transformation conditions in an* Fe-*based shape memory alloy under tensile-torsional loads: Martensite start surface and austenite start/finish planes*, Materials Sci. Engng. A, **264**, 232–244, 1999.
10. F. NISHIMURA, N. WATANABE and K. TANAKA, *Evolution of martensite start condition in general thermomechanical loads of an* Fe-*based shape memory alloy*, Int. J. Mech. Sci., **42**, 347–365, 1999.

11. K. TANAKA and T. WATANABE, *Transformation conditions in an* Fe*-based shape memory alloy: an experimental study*, Arch. Mech., this issue.

12. K. JACOBUS, H. SEHITOGLU and M. BLAZER, *Effect of stress state on the stress-induced martensitic transformation in polycrystalline* Ni-Ti *alloy*, Metall. Mater. Trans. A, **27A**, 1–8, 1996.

13. K. GALL, H. SEHITOGLU, H.J. MAIER and K. JACOBUS, *Stress-induced martensitic phase transformations in polycrystalline* CuZnAl *shape memory alloys under different stress states*, Metall. Mater. Trans. A, **29A**, 763–773, 1998.

14. L. ORGEAS and D. FAVIER, *Non-symmetric tension-compression behaviour of* NiTi *alloy*, J. Phys., **8**, 5, 605–610, 1995.

15. L. ORGEAS and D. FAVIER, *Stress-induced martensitic transformation of a* NiTi *alloy in isothermal shear, tension and compression*, Acta Mater., **46**, 5579–5591, 1998.

16. E. PATOOR, A. EBERHARDT and M. BERVEILLER, *Micromechanical modelling of the shape memory behavior*, [in:] L.C. BRINSON and B. MORAN [Eds.], *Mechanics of phase transformations and shape memory alloys*, AMD **189**/PVP **292**, ASME, 23–37, 1994.

17. B. RANIECKI and CH. LEXCELLENT, *Thermodynamics of isotropic pseudoelasticity in shape memory alloys*, Eur. J. Mech. A/Solids, **17**, 185–205, 1998.

18. F.D. FISCHER, E.R. OBERAIGNER, K. TANAKA and F. NISHIMURA, *Transformation-induced plasticity revised: An update formulation*, Int. J. Solids Struct., **35**, 2209–2227, 1998.

19. S. MIYAZAKI, T. IMAI, Y. IGO and K. OTSUKA, *Effect of cyclic deformation on the pseudoelasticity characteristics of* Ti-Ni *alloys*, Metall. Trans. A, **17A**, 115–120, 1986.

20. S. MIYAZAKI, *Thermal and stress cyclic effects and fatigue properties of* Ni-Ti *alloys*, [in:] T.W. DUERIG, K.N. MELTON, D. STÖCKEL and C.M. WAYMAN [Eds.], *Engineering aspects of shape memory alloys*, Butterworth-Heinemann, 394–413, London 1990.

21. S. MIYAZAKI and K. OTSUKA, *Deformation and transition behavior associated with the* R*-phase in* Ti-Ni *alloys*, Metall. Trans. A, **17A**, 53–63, 1986.

22. S. MIYAZAKI and C.M. WAYMAN, *The* R*-phase transition and associated shape memory mechanism in* TiNi *single crystals*, Acta Metall., **36**, 181–192, 1988.

23. S. MIYAZAKI, S. KIMURA and K. OTSUKA, *Shape-memory effect and pseudoelasticity associated with the* R*-phase transition in* Ti-50.5at%Ni *single crystals*, Phil. Mag. A, **57**, 467–478, 1988.

24. K. TANAKA, F. NISHIMURA, H. KATO and S. MIYAZAKI, *Transformation thermomechanics of* R*-phase in* TiNi *shape memory alloys*, Arch. Mech., **49**, 547–572, 1997.

25. B. RANIECKI, S. MIYAZAKI, K. TANAKA, L. DIETRICH and C. LEXCELLENT, *Deformation behaviour of* TiNi *shape memory alloy undergoing* R*-phase reorientation in torsion-tension (compression) tests*, Arch. Mech., this issue.

Received April 27, 1999; new version August 30, 1999.

Arch. Mech., **51**, 6, pp. 805–832, Warszawa, 1999

Transformation conditions in an Fe-based shape memory alloy: an experimental study

K. TANAKA and T. WATANABE

Department of Aerospace Engineering
Tokyo Metropolitan Institute of Technology
J-191-0065 Hino/Tokyo, Japan
e-mail: kikitana@astan1.tmit.ac.jp

MARTENSITE AND AUSTENITE START conditions are studied experimentally in an Fe–9% Cr–5%Ni–14%Mn–6%Si polycrystalline SMA under combined tension/compression-torsion loads. The martensite start condition is represented by an oval cone in the stress-temperature space, thus being different from the von Mises theory. The third invariant of the stress deviator has a marked effect. The austenite start condition is expressed by a polygonal cone in the same stress-temperature space. Each side of the cone corresponds to the martensite variants preferably induced during mechanical loading. The direction of the austenite start plane is determined by the direction of loading whereas the amount of variants governs the position of the plane.

Keywords: Martensite start surface, Austenite start plane, Fe-based shape memory alloy, Torsion-tension (compression) tests, Stress-temperature space, Transformation conditions, non-proportional loading

1. Introduction

WHEN DESIGNING EFFECTIVE shape memory devices, one needs possibly abundant knowledge of the thermomechanical performance of the shape memory alloys (SMAs) used in the devices, under such complex situations as the cyclic thermomechanical loading, the high frequency input or the multiaxial stress states. For example, SMA composites, a sort of intelligent (smart) structures composed of a SMA component and a matrix material, should be designed by taking precisely into account of the SMA response under multiaxial stresses, although the composities themselves are subjected to a simple load [1 – 3].

Only a few papers have, however, been published on the experiments of SMAs under multiaxial stress states; SITTNER and TOKUDA [4 – 6] and ROGUEDA *et al.* [7] in Cu-based SMA, NISHIMURA *et al.* [8 – 9] in Fe-based SMA and RANIECKI *et al.* [10] in TiNi SMA. Difficulties consist in the fact that the highly computerized experimental system is required for supplying sound data. The preparation for a

large test specimen, usually a thin-walled tubular specimen, which fits the tests under multiaxial stresses and exhibits a stable response under repeated loading, is rather a difficult problem to be solved before starting the experiments [11]. The flow rule for the transformation strain and the associated normality law, the transformation start/finish conditions, the stress-strain-temperature hystereses were some of the themes investigated. Asymetry of the martensite start surface in the stress-temperature space was clearly observed in all SMA systems, thus approving the theory with the third invariant of stress tensor [10, 12], which has been suggested in the micromechanical study by PATOOR *et al.* [13, 14]. The accumulation of sound data is still urgently necessary to establish a rational theoretical framework on thermomechanical behavior of SMAs.

In this paper, following the study of the transformation conditions in an Fe-9%Cr-5%Ni-14%Mn-6%Si polycrystalline SMA by the same authors [8, 9, 15 – 20], the martensite and austenite start conditions are investigated from the experimental point of view under the combined tension/compression-torsion loads. The asymmetry of the martensite start surface in the stress-temperature space is shown to be explained by the theory proposed by RANIECKI *et al.* [10, 12]. The austenite start condition is revealed to be represented by a polygonal cone in the same stress-temperature space, the shape and position of which depend on the amount of the martensite phase and the type of martensite variants preferably induced during mechanical loading.

2. Alloy and experimental procedures

An Fe-9%Cr-5%Ni-14%Mn-6%Si polycrystalline SMA, which is the same material as that studied in the previous papers by the same authors [8, 9, 15 – 20], was tested. Its chemical composition and mechanical properties at room temperature (RT, 303 K) are tabulated in Tables 1 and 2, respectively. The thin-walled tubular specimen employed in the tests, 6 mm in outer diameter, 4 mm in inner diameter and 20 mm in gauge length, is sketched in Fig. 1.

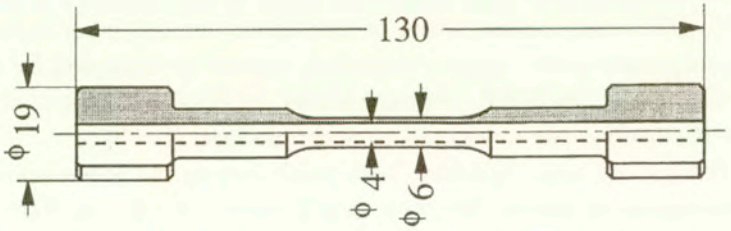

FIG. 1. Test specimen.

Table 1. Alloy composition (wt.%).

Cr	Ni	Mn	Si	C	N	Fe
9.0	5.2	14.4	6.0	0.02	0.005	Bal.

Table 2. Mechanical properties at room temperature.

0.2% proof stress	Tensile strength	Elongation	Area contraction	Elastic constants	
$\sigma_{0.2}$ MPa	σ_f MPa	ϕ %	ψ %	E GPa	G GPa
258	788	70.5	61.1	172	62

In order to obtain better shape memory performance, the following training is carried out four times successively [15, 19]: The specimen was first mechanically loaded in tension to 4% at RT, and then unloaded to the stress-free state. A thermal heating up to 873 K, holding there for 600 s and succesive cooling to RT then followed. To guarantee a stable thermomechanical response, the specimens were further subjected, prior, to the test to an additional 30 cycles of thermomechanical training: a cycle of the training is composed of an isothermal loading/unloading to 350 MPa at RT and the subsequent stress-free heating/cooling to complete the reverse transformation.

Tests were carried out by means of a servo-hydraulic testing machine (SHIMADZU, EHF–ED5/TD05–10L) equipped with a high-frequency induction heater. The tensile displacement and the angle of twist between the gauge marks were measured independently by the eddy-current sensors, while the temperature of the specimen was detected by a platinum platinum-rhodium thermocouple spot-welded at the center of the gauge length. All experimental procedures were monitored and controlled by a personal computer. The output data of the tests were stored in the PC memory for later analyses. The axial stress σ and the shear stress τ were applied simultaneously to the specimen by means of the axial force and the torque. The proportional loading path $\tau = m\sigma$ on $\sigma - \tau$ plane is identified by the path parameter m.

The stress and strain intensities are introduced to measure the progress of deformation;

$$\sigma^{\text{int}} = \sqrt{\sigma^2 + (\sqrt{3}\tau)^2}, \qquad \varepsilon^{\text{int}} = \sqrt{\varepsilon^2 + (\gamma/\sqrt{3})^2}, \tag{2.1}$$

where ε and γ stand for the axial and shear strain, respectively. Henceforth, the shear stress τ^* and the shear strain γ^* defined by

$$\tau^* = \sqrt{3}\tau, \qquad \gamma^* = 1/\sqrt{3}\gamma, \tag{2.2}$$

are often used for simplicity. The proportional loading path may be represented also by $\tau^* = m^*\sigma$ on the $\sigma - \tau^*$ plane, when a new path parameter m^* is given by $m^* = \sqrt{3}m$.

The axial transformation strain ε_{T} and the shear transformation strain γ_{T} are evaluated by the formulae

$$\varepsilon_{\mathrm{T}} = \varepsilon - \frac{\sigma}{E}, \qquad \gamma_{\mathrm{T}} = \gamma - \frac{\tau}{2G}, \tag{2.3}$$

where the Young's modulus E and the shear modulus G were determined by the experimental data, test by test. In this sense, their temperature-dependence is taken into account. The transformation strain intensity was calculated from

$$\varepsilon_{\mathrm{T}}^{\mathrm{int}} = \sqrt{\varepsilon_{\mathrm{T}}^2 + (\gamma_{\mathrm{T}}^*)^2}, \qquad \gamma_\tau^* = \gamma_{\mathrm{T}}/\sqrt{3}. \tag{2.4}$$

The specimen was loaded isothermally at RT along the proportional loading path m, over the martensite start stress σ_{Ms}^m (RT), up to the maximum stress

$$\sigma_{\max}^{\mathrm{int}} = \sqrt{(\sigma_{\max})^2 + (\tau_{\max}^*)^2}, \qquad \tau_{\max}^* = \sqrt{3}\tau_{\max}. \tag{2.5}$$

The martensite variants are induced during the loading from σ_{Ms}^m (RT) to $\sigma_{\max}^{\mathrm{int}}$.

The martensite variants formed during pre-stressing transform back to the parent phase in the subsequent heating process under constant hold stresses (σ_h, τ_h) or (σ_h, τ_h^*); $\tau_h^* = \sqrt{3}\tau_h$. The austenite start temperatures T_{As} can be determined by monitoring the $\varepsilon_T - T$, $\gamma_T - T$ or $\varepsilon_T^{\mathrm{int}} - T$ dilatation curve during heating if the transformation is assumed to start when the transformation strain ε_T, γ_T or $\varepsilon_T^{\mathrm{int}}$ reaches an offset 0.05%. For a sufficient number of tests with different values of (σ_h, τ_h^*), one can construct an austenite start surface in the axial hold stress (σ_h)-shear hold stress (τ_h^*)-temperature (T) space, the form and location of which depends strongly on the direction and amount of pre-stressing, as will be clear in the following discussion.

3. Martensite start surface under proportional loading

The martensite start stress $\sigma_{\mathrm{Ms}}^m(T_h)$ during proportional loading m (or $m^* = \sqrt{3}m$), defined of 0.05% -proof-stress, are plotted in Fig. 2 at three different test temperatures $T_h = 303$, 323 and 343 K. The result clearly shows asymmetry of the martensite start curves with respect to the shear stress axis, meaning that the compressive stress retards the martensitic transformation. The phenomenon, observed also in other SMA systems [21, 22], is investigated from the continuum-mechanical point of view by RANIECKI *et al.* [10, 12] and from the micromechanical point of view by PATOOR *et al.* [13, 14], by introducing the third invariant of the stress deviator.

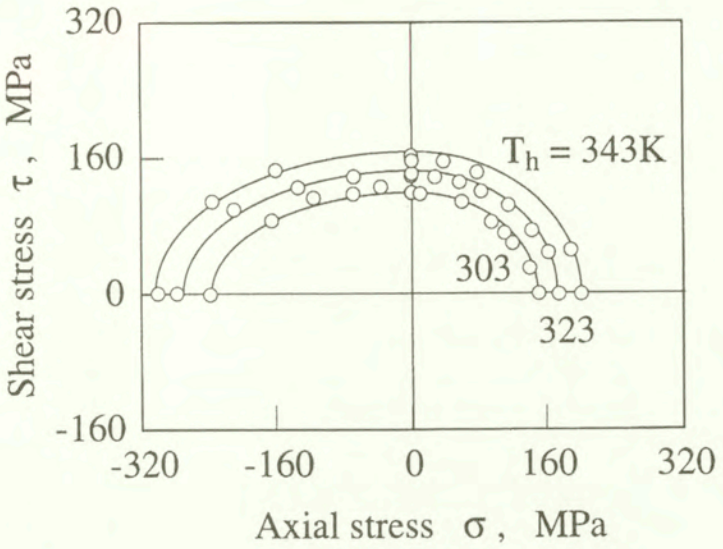

FIG. 2. Martensite start stresses during proportional loading; martensite start curves.

WERT *et al.* have clearly shown in their simulations based on metallurgy of SMAs that the martensite start condition of the stress-induced martensitic transformation is represented by a irregular polygon on the stress plane [23, 24]. Each side of the polygon corresponds to the martensite start conditions of the martensite variants which are preferably developed during loading. The martensite start curve determined in Fig. 2 is nothing else than a curve inscribed in such a polygon.

RANIECKI *et al.* [10, 12] proposed the following condition, representing the martensite start curve:

$$\sigma^{\mathrm{T}} = \frac{\sqrt{3}k(T)}{f(y,T)}, \qquad F = \sigma_{\mathrm{ef}} - \sigma^{\mathrm{T}}(y,t) = 0, \tag{3.1}$$

where another path parameter y is defined by

$$y \equiv 3\sqrt{6}\frac{J_3}{(J_2')^{3/2}};$$
$$J_2' \equiv \frac{2}{3}\sigma_{\mathrm{ef}}^2 = S_{ij}S_{ij}, \qquad J_3' \equiv \det S_{ij} = \frac{1}{3}\mathrm{tr}(\mathbf{S})^3, \tag{3.2}$$

with the second and third invariants J_2' and J_3' of the stress deviator $\mathbf{S}$. The temperature-dependent function $k(T)$ stands for the critical shear stress to start the martensitic transformation.

Note that $y = 0$ means the simple shear, whereas $y = +1$ and -1 stand for the simple tension and simple compression, respectively, and that $-1 \leq y \leq 1$.

The shape function $f(y,T)$ in Eq. (3.1), when normalized so that $f(0,T) = 1$, has the form

$$f(y,T) = \frac{\sigma^{\mathrm{T}}(0,T)}{\sigma^{\mathrm{T}}(y,T)}. \tag{3.3}$$

It should be emphasized that the condition (3.1) is reduced to the J_2-theory (von Mises theory) if $f = 1$.

When the data in Fig. 2 are evaluated by means of Eqs. (3.1) – (3.3), the values of the shape function are plotted in Fig. 3. The path-dependence of the shape function is clear, meaning that the J_3-theory proposed by RANIECKI *et al.* reasonably explains the present data. Contrary to their data in a TiNi SMA [10], the temperature-dependence is not observed in the present Fe-based SMA, at least at the temperature range investigated.

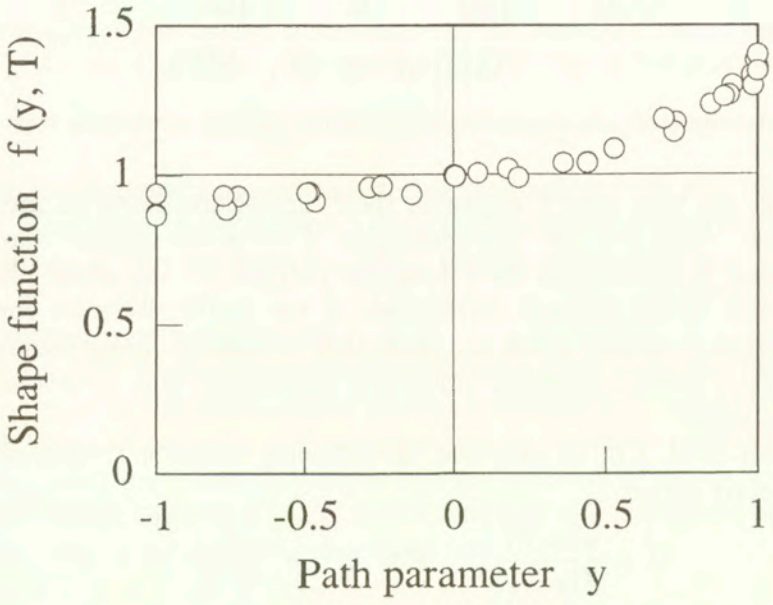

FIG. 3. Path- and temperature-dependence of shape function.

The martensite start condition of the present alloy is represented in the stress-temperature space as an oval cone illustrated schematically in Fig. 4. This surface corresponds to the initial yield surface in plasticity. When the reverse transformation progresses in the subsequent thermomechanical "unloading", the martensite start condition during thermomechanical "reloading" becomes quite different from the initial martensite start condition, as has been observed in the same Fe-based SMA by NISHIMURA *et al.* [16, 17] in the case of uniaxial loading. Generally the transformation condition depends strongly on the prior history of transformations in all SMA systems, resulting in complex stress-strain-temperature hystereses in

thermomechanical loading. The "subsequent" martensite start condition during thermomechanical loading should be an urgent theme to be investigated whether or not the condition might be a potential such as the yield condition plays the role of the plastic potential in plasticity [25].

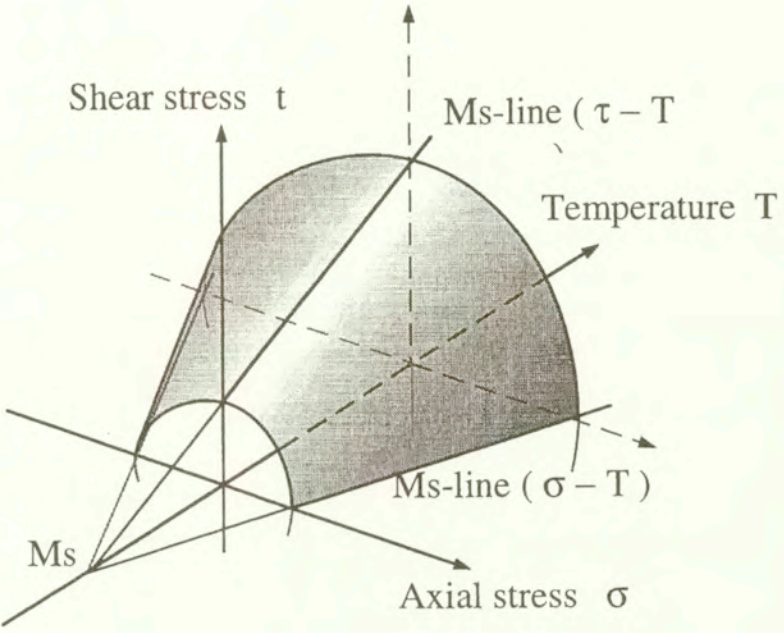

FIG. 4. Martensite start cone in stress-temperature space (Schematic).

One comment more on the martensite start cone in Fig. 4: during isothermal mechanical loading at lower temperature range, the reorientation of the temperature-induced martensite variants often progresses at low stress level [26 – 28]. The critical stress for the reorientation process is observed to be insensitive to the temperature, meaning that the condition can be represented by a cylindrical surface in the same stress-temperature space. The martensite start cone must be connected with this reorientation start cylinder at the lower temperature range. The uniaxial figure of such transformation/reorientation start condition was widely employed in the simulations of thermomechanical behavior in SMAs [29 – 33]. In the uniaxial case, the transformation/reorientation condition was shown to change its form and position on the stress-temperature plane during cyclic thermomechanical loading [34, 35]. The phenomenon should be investigated in the stress-temperature space in order to supply sound data for constructing a rational theoretical framework for transformation thermomechanics, in which the subsequent transformation condition must play a key role as a potential.

4. Austenite start plane

4.1. Austenite start line

Before going further, experimental results of uniaxial alloy response in the process of reverse transformation are summarized briefly [18]. The specimens were pre-stressed axially up to a maximum tensile stress $\sigma^{+0}_{\max}$ at RT. Here and henceforth, the superscript $+0$ means the pre-stressing along the path $m = +0$ (pure tension). The martensitic transformation starts at the martensite start stress $\sigma^{+0}_{Ms}(\mathrm{RT}) = 151$ MPa, and the amount of martensite variants M^{+0} increases in the subsequent loading process up to $\sigma^{+0}_{\max}$. Figure 5 plots the austenite start temperature $T^{+0/\varepsilon}_{As}$ versus the axial hold stress σ_h, showing clearly the linear austenite start lines, the $\mathrm{As}^{+0/\varepsilon}$-lines, with a slope $c^{+0/\sigma}_{A} = 2.1$ MPa/K. The lines correspond to the Clausius-Clapeyron relation. The superscript $+0/\varepsilon$ means that the austenite start temperature after pre-stressing along the path $m = +0$ is measured from $\varepsilon_T - T$ dilatation curves, whereas $+0/\sigma$ on c_A means that the data after pre-stressing along the path $m = +0$ are plotted on the $\sigma_h - T$ plane.

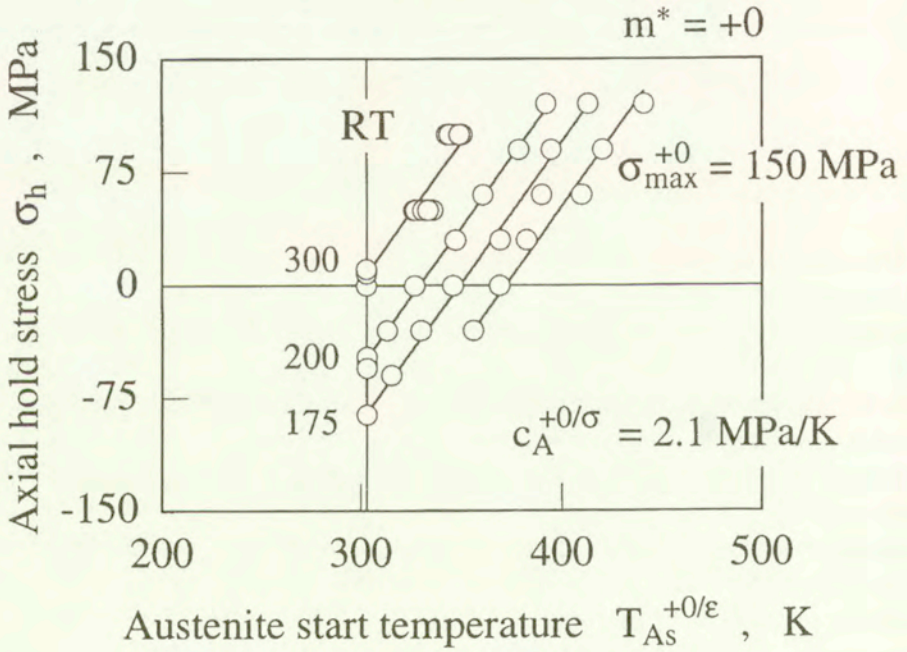

FIG. 5. Austenite start lines after tensile pre-stressing.

A different set of austenite start lines, the $\mathrm{As}^{-0/\varepsilon}$-lines, is observed as shown in Fig. 6 when the specimen is pre-stressed down to the maximum compressive stress

$\sigma^{-0}_{\max}$ at RT. The slope of the lines is $c_A^{-0/\sigma} = -2.4$ MPa/K. The transformation starts in this case at the martensite start stress $\sigma^{-0}_{Ms}(\mathrm{RT}) = -228$ MPa, and the martensite variants M^{-0} are formed from then on in the compressive loading process.

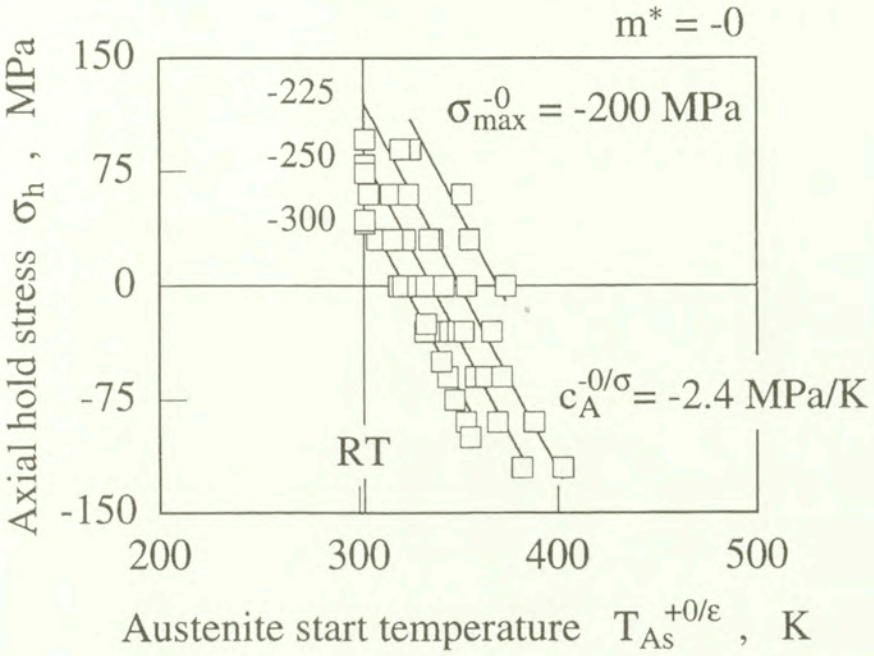

FIG. 6. Austenite start lines after compressive pre-stressing.

The following two characteristics of the austenite start lines should specially be emphasized in Figs. 5 and 6 in relation to the later discussion: Each set of austenite start lines corresponds to the martensite variants formed during prestressing. Directly speaking, the slope of the austenite start line depends on the direction of pre-stressing. Secondly, the austenite start lines translates to the lower temperature side without changing its slope when the maximum stress is larger; in other words, when the amount of martensite induced during loading is larger.

4.2. Austenite start plane after axial pre-stressing ($m = +0$)

The specimen was pre-stressed in tension up to $\sigma^{+0}_{\max} = 200$ MPa to produce the martensite variants M^{+0}. The austenite start temperatures $T^{+0/\varepsilon}_{\mathrm{As}}$ measured from $\varepsilon_T - T$ dilatation curves under hold stresses (σ_h, τ^*_h) are plotted in Fig. 7 with the shear hold stress as a parameter. The same data are re-plotted in Fig. 8

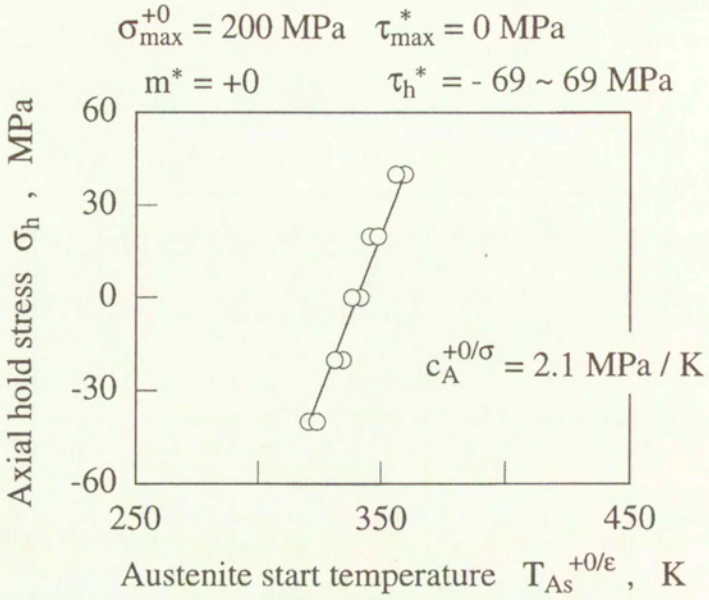

FIG. 7. Effect of axial hold stress on austenite start temperature: case of tensile pre--stressing.

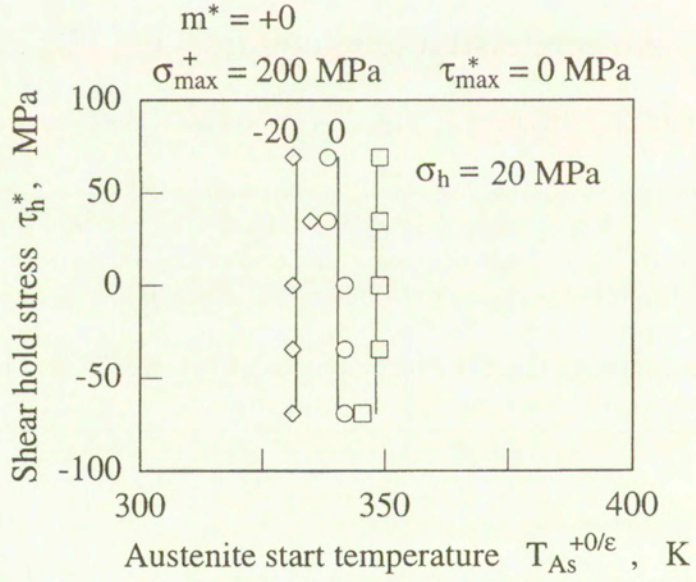

FIG. 8. Effect of shear hold stress on austenite start temperature: case of tensile pre--stressing.

with the axial hold stress as a parameter. Figures rationally conclude that the austenite start condition is represented by a plane in the axial hold stress (σ_h)-shear hold stress (τ_h^*) -temperature (T) space, as shown in Fig. 9. The austenite start plane, the $As^{+0/\varepsilon}$-plane, is perpendicular to the σ_h-T coordinate plane, and the thick solid line corresponds to the $As^{+0/\varepsilon}$ -line in Fig. 5 in the uniaxial case.

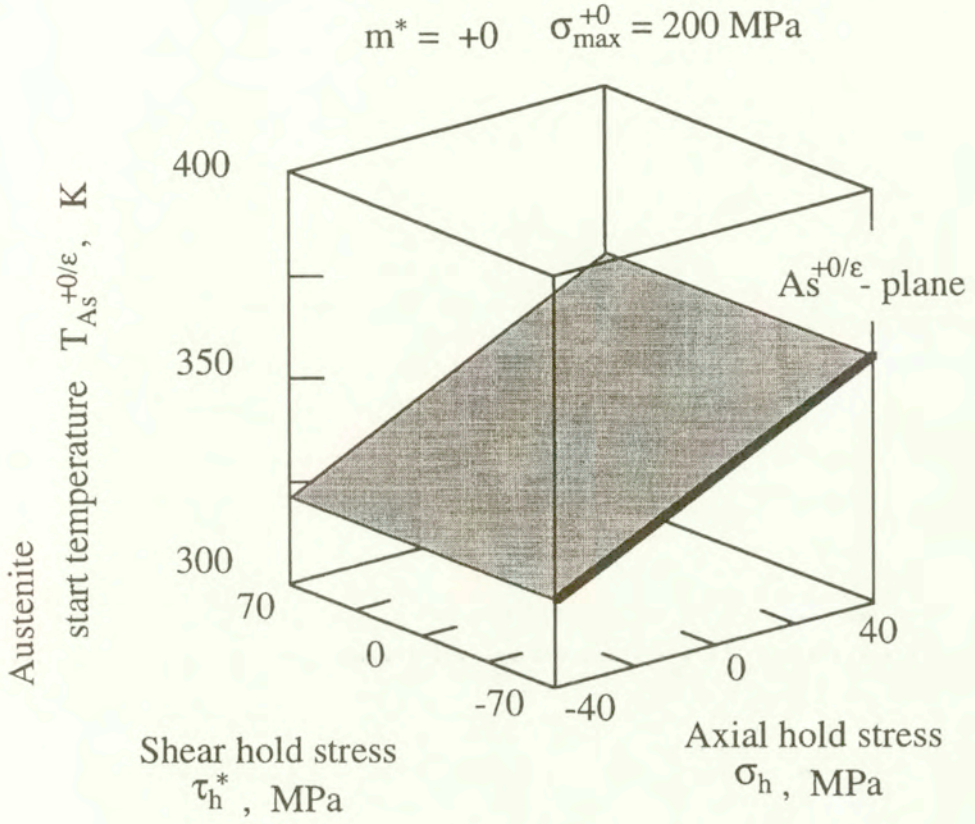

FIG. 9. Austenite start plane after tensile pre-stressing.

It is worth noting again that the $As^{+0/\varepsilon}$-plane in Fig. 9 denotes the condition to start the reverse transformation of the martensite variants M^{+0} which are induced during pre-stressing in tension.

4.3. Autensite start plane after shear pre-stressing ($m = \infty$)

The specimen was pre-stressed in torsion up to $\tau^*_{\max} = 284$ MPa ($\tau_{\max} = 164$ MPa), over the martensite start stress $\tau^*_{Ms}(\mathrm{RT}) = 217$ MPa ($\tau_{Ms} = 125$ MPa), to produce the martensite variants M^{∞} which are favorable to torsion. The austenite start temperatures $T_{\mathrm{As}}^{\infty/\gamma^*}$ measured from $\gamma^*_T - T$ dilatation curves

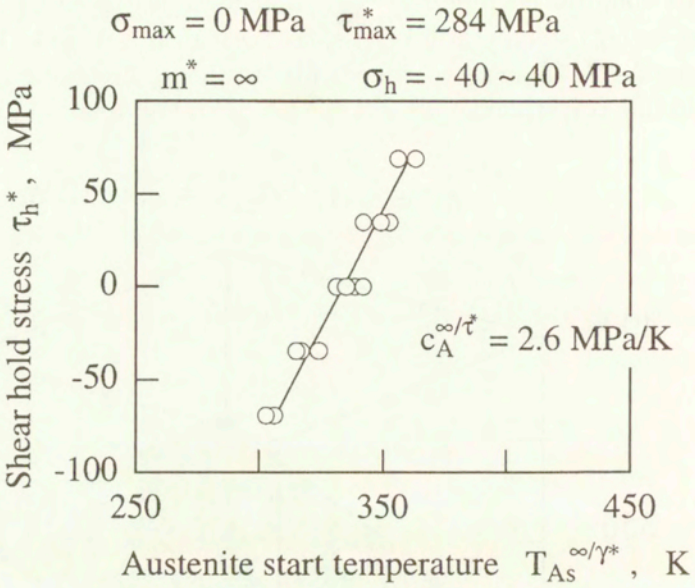

FIG. 10. Effect of shear hold stress on austenite start temperature: case of shear pre--stressing.

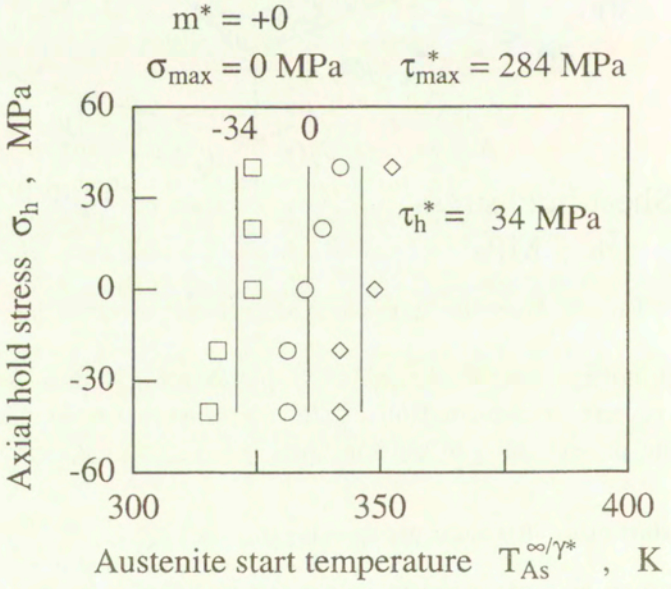

FIG. 11. Effect of axial hold stress on austenite start temperature: case of shear pre--stressing.

are plotted in Figs. 10 and 11, revealing again that the austenite start condition is represented by a plane, the $As^{\infty/\gamma*}$-plane, perpendicular to the $\tau_h^* - T$ coordinate plane (cf. Fig. 12). The intersection of the plane with the $\tau_h^* - T$ coordinate plane, denoted by the thick solid line in the figure, is nothing else than the austenite start line, the $As^{\infty/\gamma*}$-line with the slope $c_A^{\infty/\tau*} = 2.6$ MPa/K.

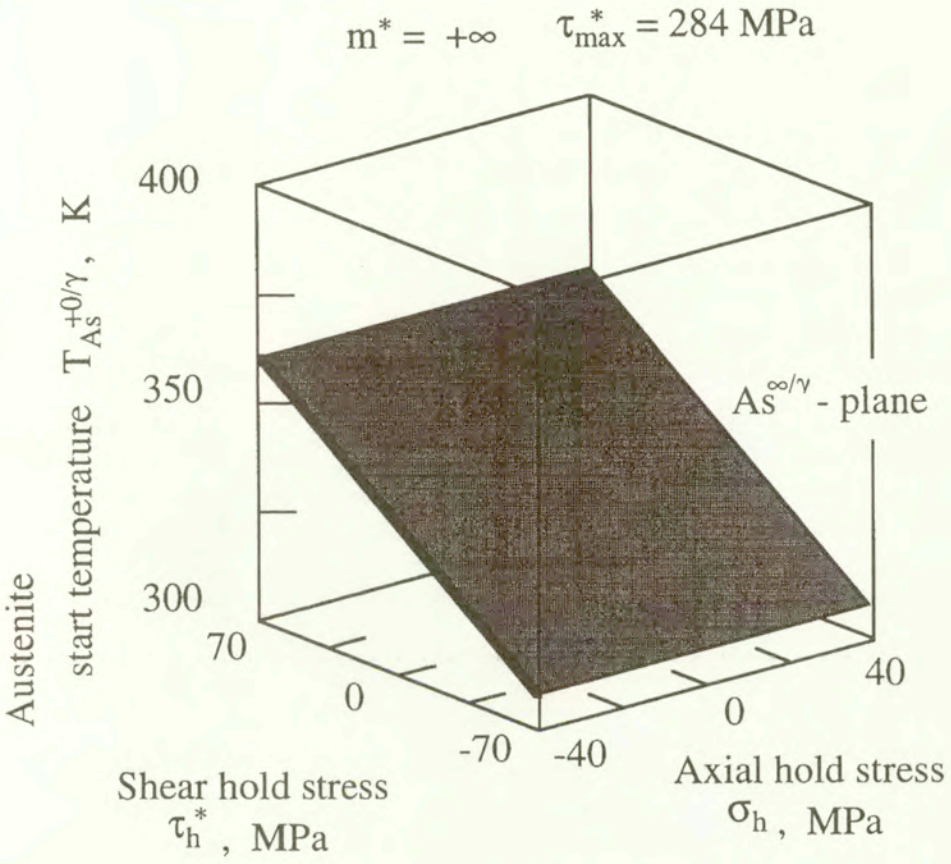

FIG. 12. Austenite start plane after shear pre-stressing.

4.4 Austenite start plane after proportional pre-stressing

Thermodynamics of martensitic transformation clearly explains the existence of not only the $As^{+0/\varepsilon}$- and $As^{\infty/\gamma*}$ -planes in Figs. 9 and 12 but also the As^{m^*}-planes which are observed after proportional pre-stressing along the path $m^*(-\infty < m^* < -0$ or $+0 < m^* < \infty)$ [8]. The following points have been proved by the present authors: When only one set of martensite variants, M^{m^*}, say, is formed during the loading along the path m^*, the iso-$T_{As}^{m^*}$ lines on the As^{m^*}-plane are, when they are projected onto the $\sigma_h - \tau_h^*$ -plane, prependicular

to the direction of pre-stressing $\tau^* = m^*\sigma$. Or equivalently, the austenite start temperature depends solely on the length of the projection of the hold stress vector (σ_h, τ_h^*) onto the direction of pre-stressing $(1, m^*)$;

$$\sigma_h^{\text{eff}} = \frac{\sigma_h + m^*\tau_h^*}{\sqrt{1+(m^*)^2}}, \tag{4.1}$$

which may be called the effective hold stress.

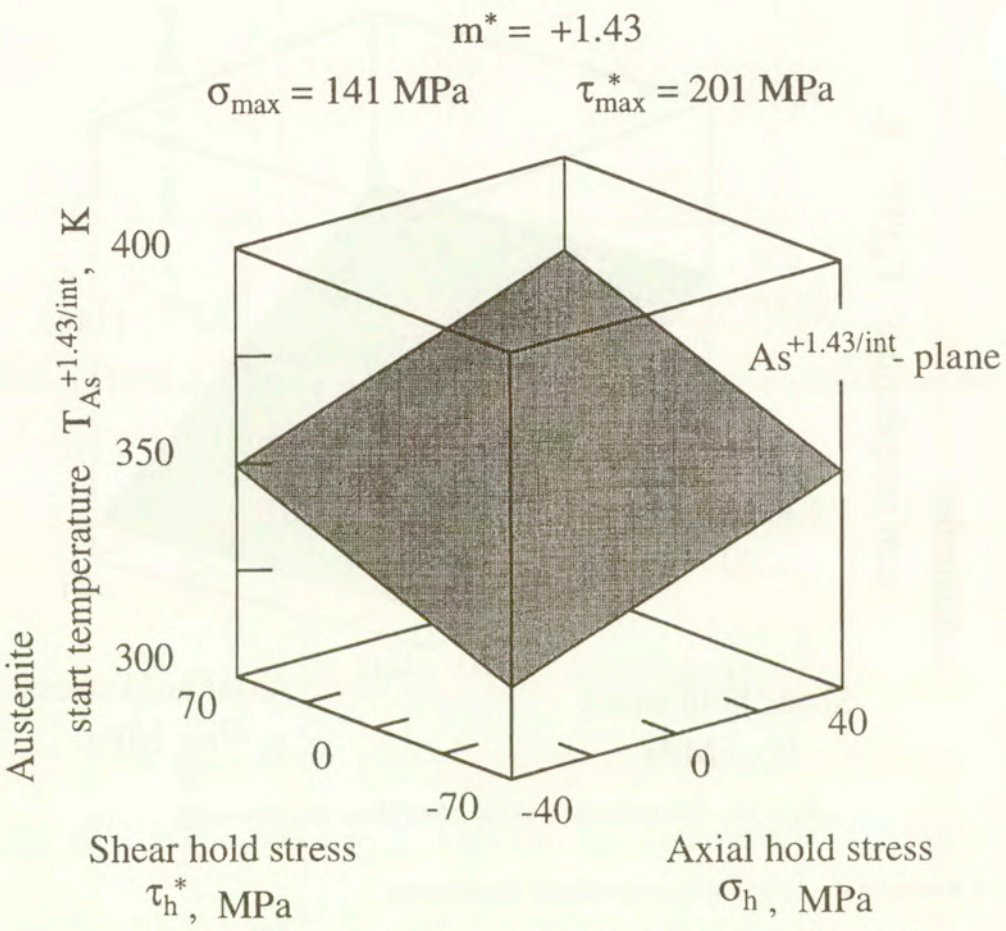

FIG. 13. Austenite start plane after proportional pre-stressing $m^* = +0.82$.

This theoretical prediction fully explains the experimental results after axial pre-stressing ($m^* = +0$) in Fig. 9 ($\sigma_h^{\text{eff}} = \sigma_h$ in this case), shear pre-stressing ($m^* = \infty$) in Fig. 12 ($\sigma_h^{\text{eff}} = \tau_h^*$ in this case), and the proportional pre-stressing along the path m^*; the case of $m^* = +1.43$ ($m = +0.83$) is given in Fig. 13. It should be noted that the austenite start temperatures necessary to construct

the plane in Fig. 13 were determined from the dilatation curves $\varepsilon_T^{\text{int}}$-T. Hence the superscript +1.43/int is used. The iso-$T_{\text{As}}^{+1.43/\text{int}}$ lines on the $\text{As}^{+1.43/\text{int}}$ -plane almost satisfy the geometrical configuration explained above. Figure 14, which contains all the data points forming the $\text{As}^{+1.43/\text{int}}$-plane in Fig. 13, well proves that the effective hold stress defined in Eq. (4.1) is an appropriate measure to determine the austenite start temperature. The slope of the line is $c_A^{+1.43/\text{eff}} = 2.1$ MPa/K.

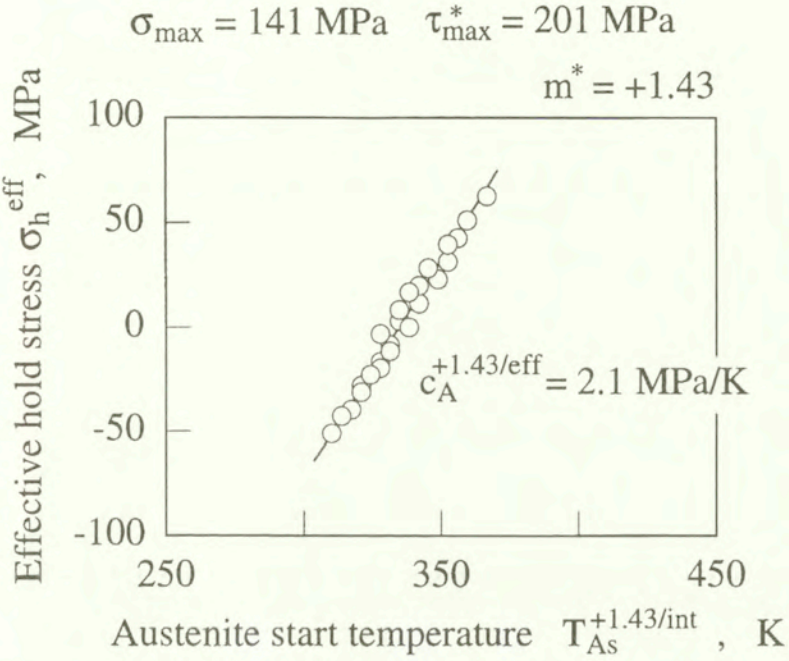

FIG. 14. Austenite start plane depending on effective hold stress: case of proportional pre-stressing $m^* = +0.82$.

4.5. Austenite start multi-planes after non-proportional pre-stressing: Shear pre-stressing followed by axial pre-stressing ($m^* = \infty \to +0$)

The austenite start plane after non-proportional pre-stressing is investigated in this subsection to show that the austenite start multi-planes are formed corresponding to martensite variants with some different orientations which are induced during pre-stressing.

The specimen was, in the first run, subjected to shear pre-stressing up to $\tau_{\text{max}}^* = 284$ MPa ($\tau_{\text{max}} = 164$ MPa) and unloaded. Tensile loading up to $\sigma_{\text{max}}^{+0} = 250$ MPa and unloading the follow in the second run. The austenite start temperatures were measured in the subsequent heating process under hold stresses (σ_h, τ_h^*).

Note that the maximum stresses $\tau^*_{\max}$ and $\sigma^{+0}_{\max}$ are higher than the martensite start stresses $\tau^*_{Ms}(\mathrm{RT}) = 217$ MPa and $\sigma^{+0}_{Ms}(\mathrm{RT}) = 151$ MPa, respectively. Therefore, the martensite variants M^{∞} which are favorable to the shear stress are induced during the first shear pre-stressing, whereas the martensite variants M^{+0} favorable to the tensile stress are expected to form during the subsequent axial pre-stressing. These two different types of variants are supposed to transform independently back in the subsequent heating process. Following the observation in Fe-based SMAs, the reorientation process $M^{\infty} \rightarrow M^{+0}$ is understood here not to progress in the second mechanical run [36].

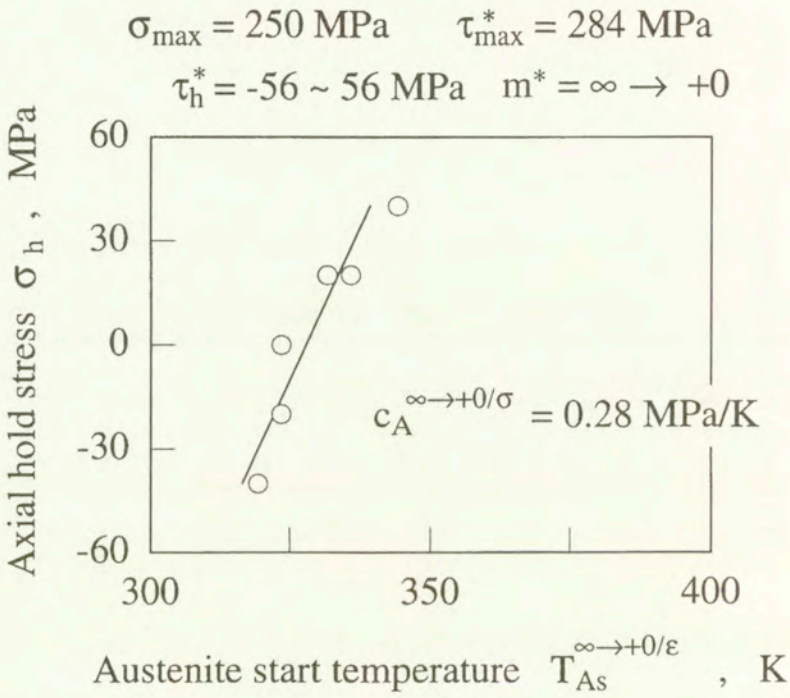

FIG. 15. Effect of axial hold stress on austenite start temperature after succesive pre-stressing $m^* = \infty$ and $m^* = +0$.

Figures 15 and 16 illustrate the austenite start temperature $T^{\infty\rightarrow+0/\varepsilon}_{\mathrm{As}}$ versus hold stresses, where the superscript $\infty \rightarrow +0/\varepsilon$ on T_{As} means that the austenite start temperatures after a successive pre-stressing $m = \infty$ and $m = +0$ are measured from $\varepsilon_T - T$ dilatation curves. The results again show that the austenite start condition is represented by a plane, the $\mathrm{As}^{\infty\rightarrow+0/\varepsilon}$ -plane, perpendicular to the $\sigma_h - T$ coordinate plane. Similar data were obtained for the austenite start temperatures $T^{\infty\rightarrow+0/\gamma^*}_{\mathrm{As}}$ measured from $\gamma^*_T - T$ dilatation curves (Figs. 17 and 18), showing that the austenite start plane, the $\mathrm{As}^{\infty\rightarrow+0/\gamma^*}$ -plane, is perpendicular to the $\tau^*_h - T$ coordinate plane.

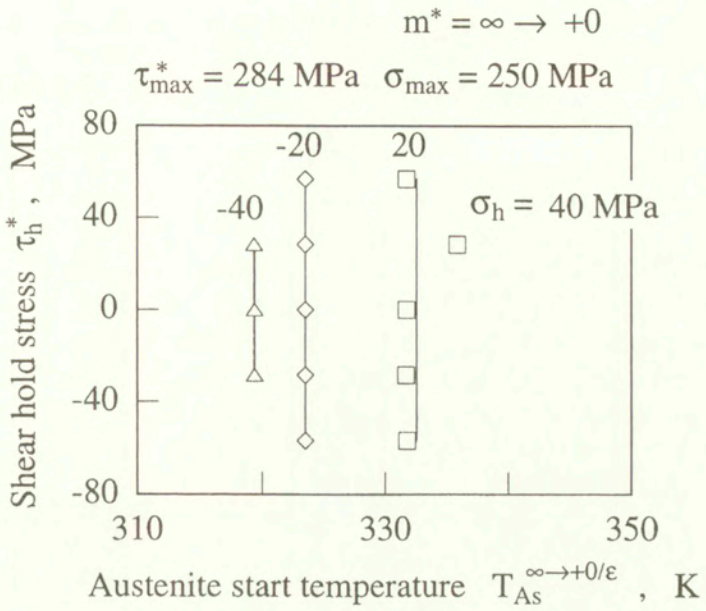

FIG. 16. Effect of shear hold stress on austenite start temperature after succesive pre-stressing $m^* = \infty$ and $m^* = +0$.

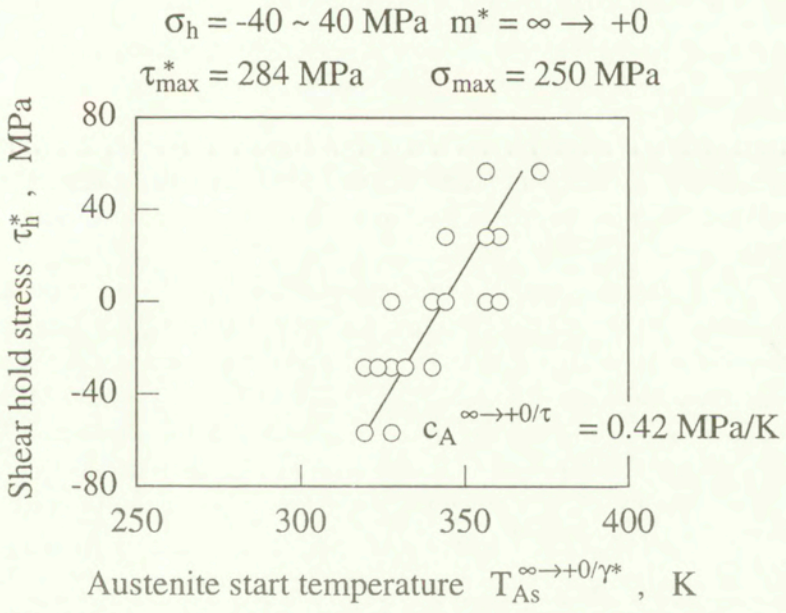

FIG. 17. Effect of shear hold stress on austenite start temperature after succesive pre-stressing $m^* = \infty$ and $m^* = +0$.

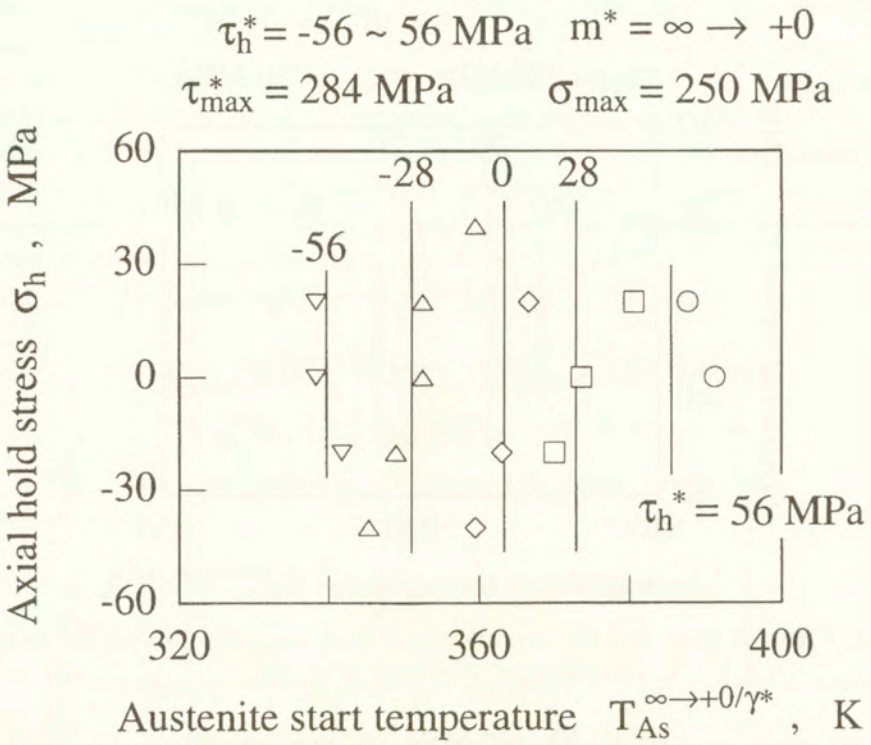

FIG. 18. Effect of axial hold stress on austenite start temperature after succesive pre--stressing $m^* = \infty$ and $m^* = +0$.

The two austenite start planes are drawn together in Fig. 19, which clearly reveals that, under all values of hold stresses tested here, the martensite variants M^{+0} transform back to the parent phase at lower temperature range than the M^{∞} variants do.

In Fig. 5 the following conclusion was drawn: the $\mathrm{As}^{+0/\varepsilon}$ -line translates to the lower temperature side without changing its slope, when $\sigma^{+0}_{\max}$ is larger. In order to show that the same is true even in the multiaxial stress state, the specimen was subjected to shear prestressing up to $\tau^*_{\max} = 329$ MPa ($\tau_{\max} = 190$ MPa) follwed by a subsequent axial pre-stressing up to $\sigma_{\max} = 250$ MPa. Note that the maximum shear stress is now larger than in the tests in Fig. 19, whereas the maximum tensile stress is the same in both tests. As before, the austenite start temperatures, $T_{\mathrm{As}}^{\infty\to+0/\varepsilon}$ and $T_{\mathrm{As}}^{\infty\to+0/\gamma^*}$, were measured independently from $\varepsilon_T - T$ and $\gamma^*_T - T$ dilatation curves, respectively. Under the condition $(\sigma_h, \tau^*_h) = (-20$ MPa, $5T$ MPa), the transformation strains ε_T and γ_T develop during heating as shown in Fig. 20. The axial transformation strain starts recovering as soon as the temperature starts to increase, whereas the shear transformation strain stays almost constant till it starts decreasing at a much ligher temperature $T_{\mathrm{As}}^{\infty\to+0/\gamma^*}$.

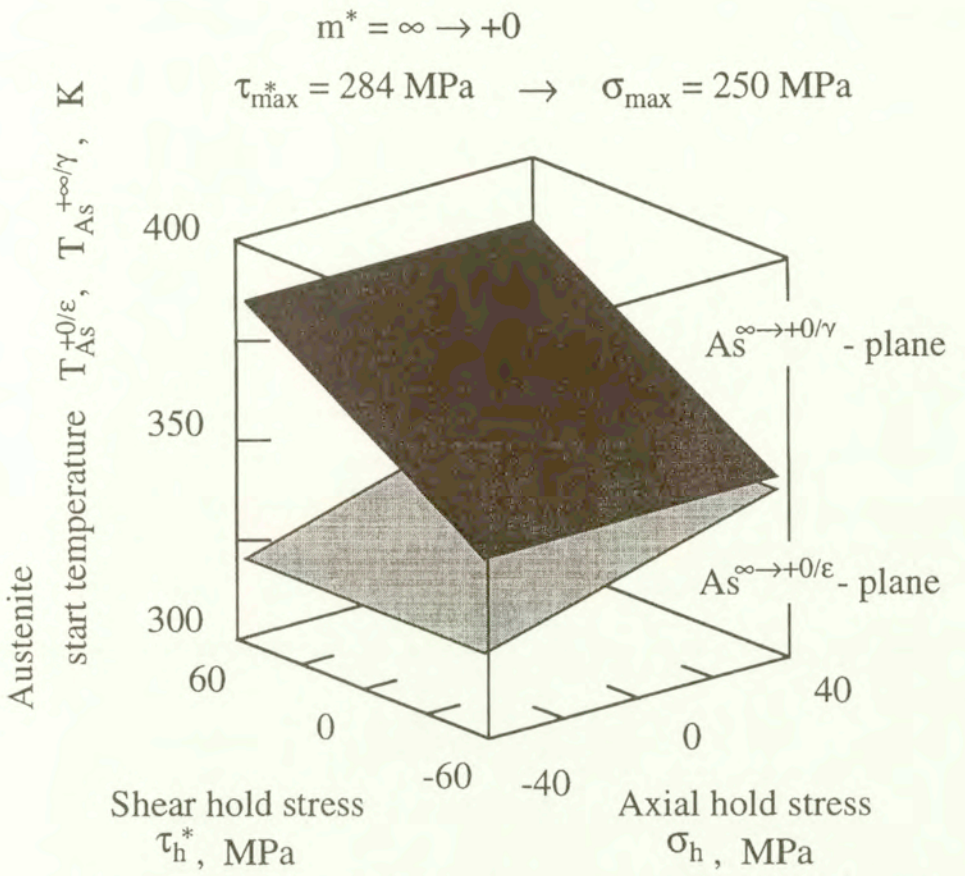

FIG. 19. Austenite start planes after succesive pre-stressing $m^* = \infty$ and $m^* = +0$: $As^{\infty\to+0/\varepsilon}$ -plane is lower in location than $As^{\infty\to+0/\gamma}$ -plane.

The result reveals that the M^{+0} variants first transforms back to the parent phase, and the M^{∞} variants follow later at higher temperature. Under the condition $(\sigma_h, \tau_h^*) = (20\ \text{MPa}, -56\ \text{MPa})$, however, the reverse is true (cf. Fig. 21).

The result on the austenite start temperatures is summarized in Fig. 22, showing that two austenite start planes now intersect. Compared to the situation in Fig. 19, the $As^{\infty\to+0/\gamma*}$-plane translates to the lower temperature side without changing the slope; in other words, the larger amount of M^{∞} variants formed during shear pre-stressing accelerates the start of reverse transformation during heating. Figure 23, which shows the data projected on the $\tau_h^* - T$ coordinate plane, confirms that the $As^{\infty\to+0/\gamma*}$-plane translates to the lower temperature side, depending on the amount of M^{∞} variants, without changing its slope. A small negative translation of the $As^{\infty\to+0/\varepsilon}$-plane, meaning the retardation of the reverse transformation, which is observed in Figs. 19 and 22, might be due partly to the "isotropic hardening" [9] in the process of shear pre-stressing.

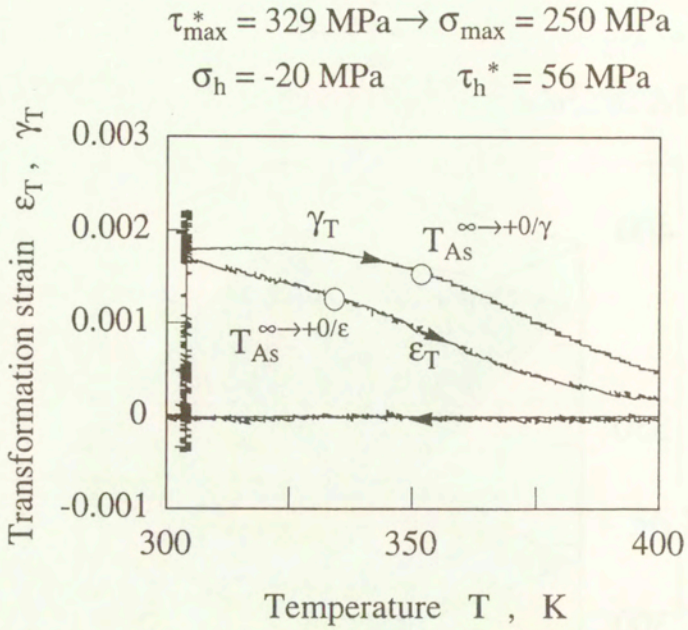

FIG. 20. Recovery of transformation strain during heating: under hold stresses far from inter-section.

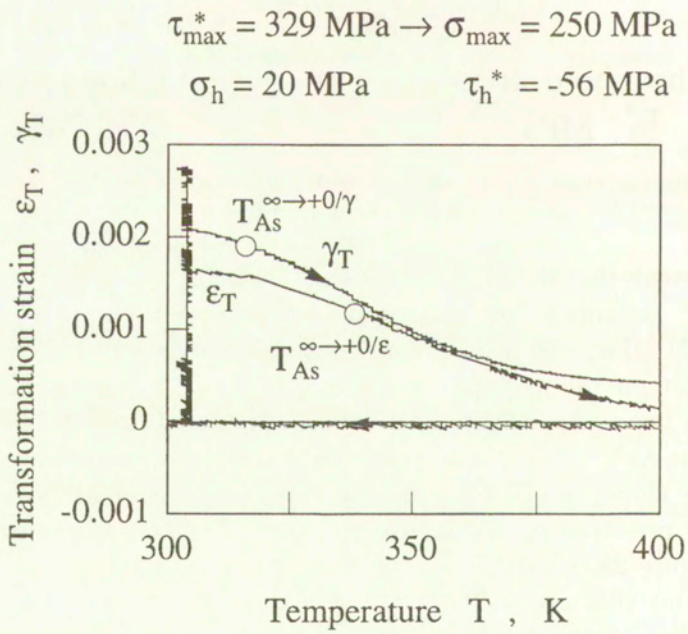

FIG. 21. Transformation strain recovery during heating: under hold stresses near inter--section.

One more important comment in Fig. 22: The reverse transformation starts when the generic point reaches the lower temperature branch of the $As^{\infty\to+0/\varepsilon}$ – and $As^{\infty\to+0/\gamma*}$ -planes. The austenite start condition is, therefore, represented by a bi-plane composed of the branches on the lower temperature side. If, not two martensite variants as discussed here but, many martensite variants are activated in the process of prestressing, the final austenite start condition must be represented by the multi-planes in the stress-temperature space.

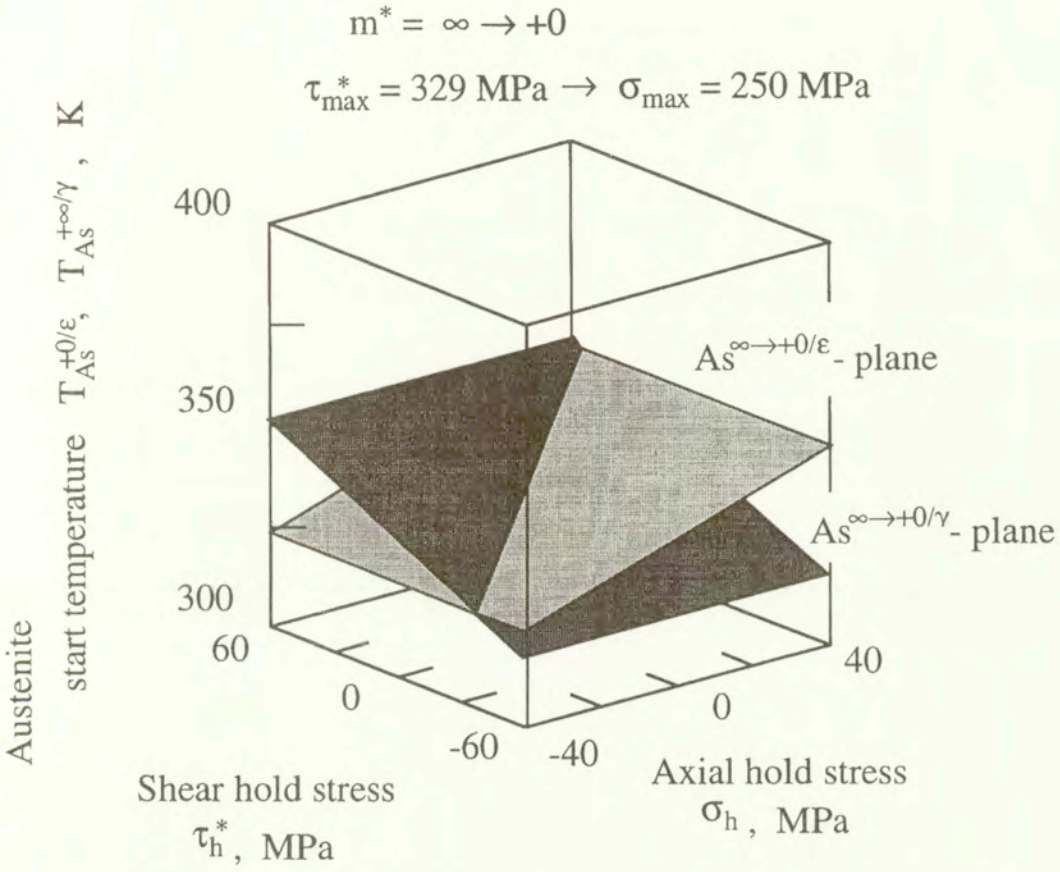

FIG. 22. Austenite start planes after succesive pre-stressing $m^* = -\infty \to m^* = +0$: $As^{\infty\to+0/\gamma}$ -plane translates down, and intersects with $As^{\infty\to+0/\varepsilon}$ -plane.

If the transformation strain intensity $\varepsilon_T^{\text{int}}$ defined in Eq. (2.4) is employed as the parameter to measure the extent of reverse transformation in the multiaxial stress states, the austenite start temperatures $T_{\text{As}}^{\infty\to+0/\text{int}}$ are obtained from $\varepsilon_T^{\text{int}} - T$ dialatation curves. The corresponding austenite start condition is nothing other than the multi-planes explained above, or rather an inscribed surface to the multi-planes. The situation is well explained in Fig. 24. The data points in

the $\sigma_h - \tau_h^* - T$ space are projected, along the intersection of $As^{\infty \to +0/\varepsilon}$ – and $As^{\infty \to +0/\gamma}$ – planes, onto the plane which is perpendicular to both the $\sigma_h - \tau_h^*$ plane and the projection of the intersection onto the $\sigma_h - \tau_h^*$ plane. The data points are actually almost on the lower temperature branches of the $As^{\infty \to +0/\varepsilon}$ – and $As^{\infty \to +0/\gamma *}$ -planes, drawn in a heavy solid line.

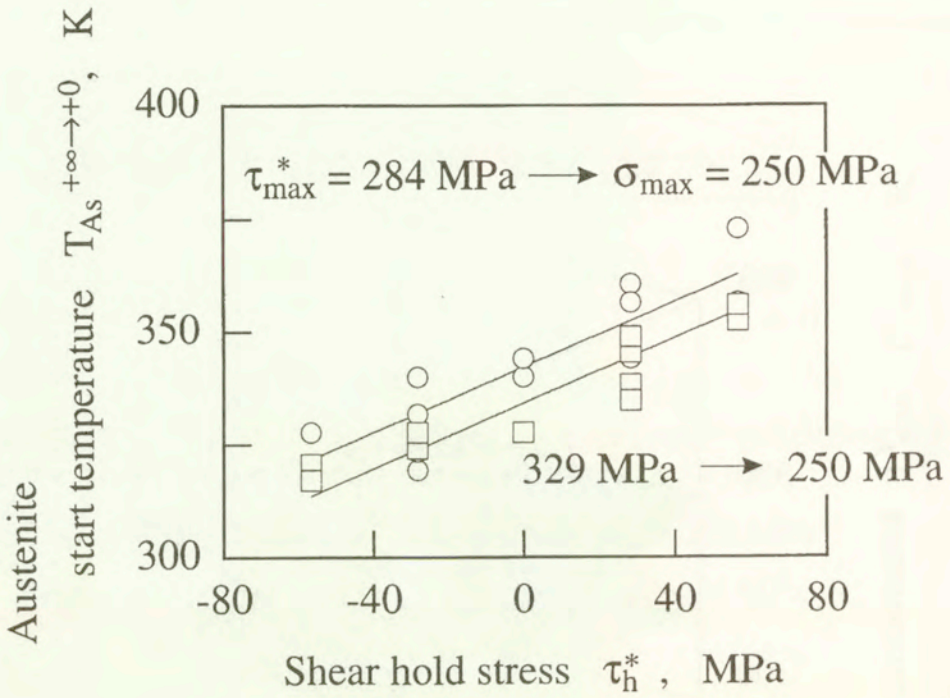

FIG. 23. Translation of austenite start plane.

4.6. Austenite start cone

A cross-section of the transformation start planes in Fig. 22 and an isotemperature plane is shown schematically in Fig. 25(a). The two straight lines, $T_{As}^{+0/\varepsilon}$ -line and $T_{As}^{\infty/\gamma *}$ -line, represent the austenite start lines on the axial hold stress (σ_h) -shear hold stress (τ_h^*) plane, which characterize that start of the reverse transformation of the martensite variants M^{+0} formed during tensile pre-stressing and of the martensite variants $M^{+\infty}$ formed during torsional pre-stressing, respectively. The thick solid line stands for the actual austenite start curve explaining the data.

If the case of compressive pre-stressing is taken into account in addition, Fig. 25(b) would be obtained as the austenite start curve on the $\sigma_h - \tau_h^*$ plane. The curve must be symmetric with respect to the σ_h-axis, but might be asymmetric

with respect to the τ_h^*-axis. If hold stress (σ_h, τ_h^*) is inside the curve, the reverse transformation does not start at this temperature, but, as will be made clear later in Fig. 26, it starts at a higher temperature.

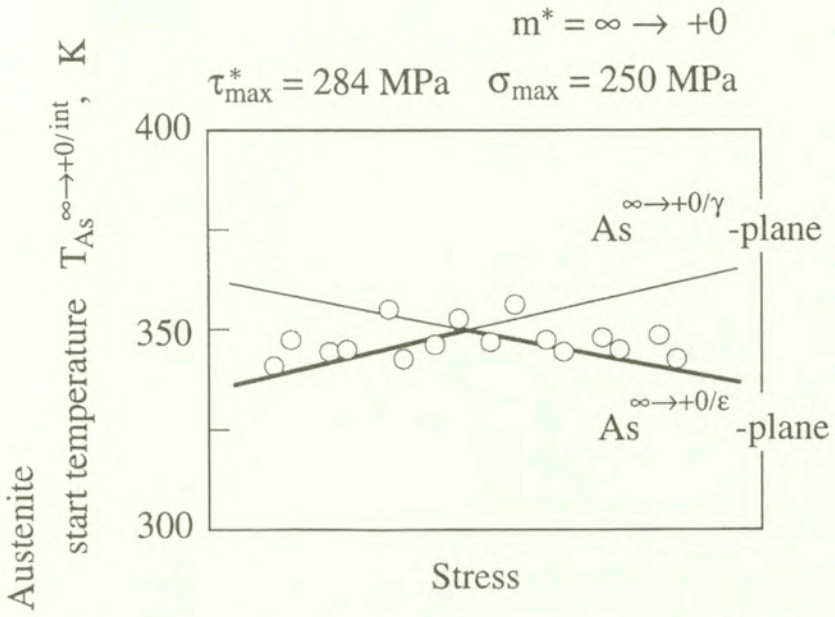

FIG. 24. Austenite start bi-plane constructed from $\varepsilon_T^{int} - T$ dilatation curves.

When the specimen is pre-stressed along a complex non-proportional load path, the austenite start polygon schematically illustrated in Fig. 25(c) would be obtained since many martensite variants with different orientations are activated during pre-stressing.

In the axial hold stress (σ_h) -shear hold stress (τ_h^*) -temperature (T) space, the situation can be sketched schematically by Fig. 26, representing a set of austenite start polygonal cones, the apex of which stands for the austenite start temperature As under stress-free state. The transformation start planes determined experimentally in Fig. 22 are drawn in the figure as the two contact planes.

Summarizing, an austenite start plane is induced in the heating process only when the corresponding martensite variants are formed during preceding martensitic transformation. Each martensite variant characterizes the slope of the plane in the stress-temperature space, whereas the extent of the martensitic transformation determines the position of the plane in the same space. In the case when the martensite variants with some different orientations are formed in the process of mechanical loading, during complex non-proportional loading, for example, the austenite start condition in the stress-temperature space is given by a polygonal cone.

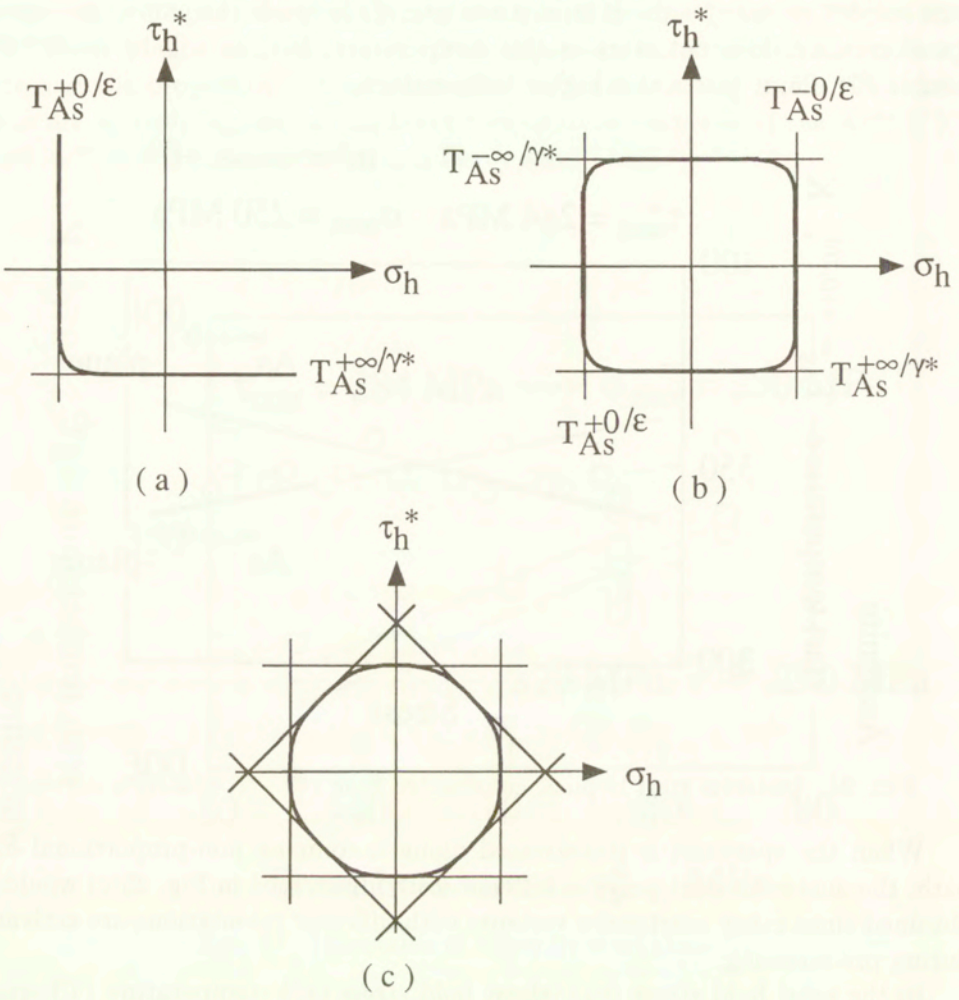

FIG. 25. Austenite start condition on stress plane.

It is worth commenting here on two points: firstly, just at the moment of the start of martensitic transformation, the alloy could exhibit the initial austenite start cone, which correspond to the initial austenite start line determined by the same authors in the uniaxial case [8]. With the progress of the martensitic transformation, the initial austenite cone degenerates into two cones, the austenite start cone and the austenite finish cone, which represent the austenite start and finish conditions, respectively. The latter condition is not discussed in the present study; see Ref. [18] for the case of uniaxial loading, and in Ref. [29] a general outlook of these two austenite start/finish cones are explained.

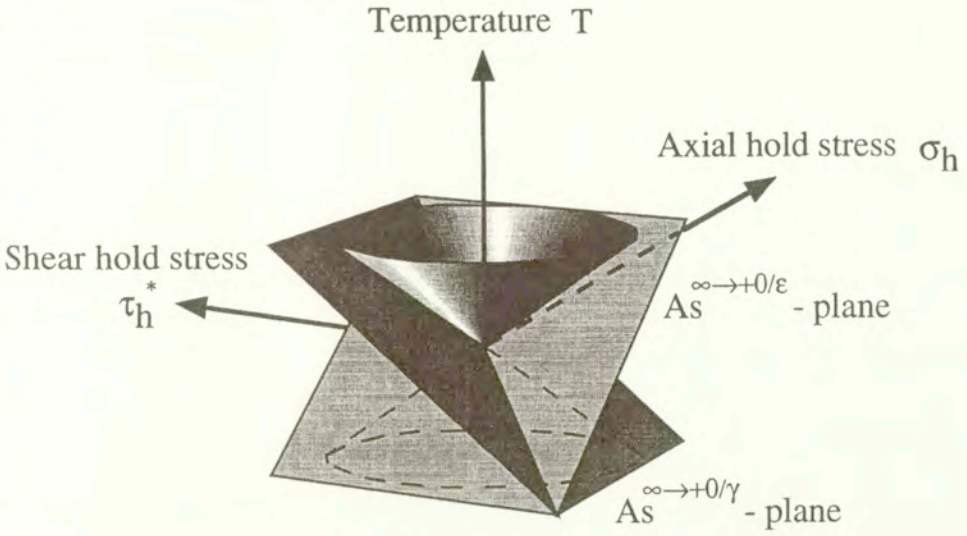

FIG. 26. Austenite start cone in stress-temperature space.

Secondly, one could construct, at each moment of reverse transformation, the subsequent austenite cone between the austenite start and finish cones. The condition is expected to play a role of the plastic potential in the unified theory of transformation/deformation in shape memory alloys [25], just like the subsequent yield condition is the plastic potential in plasticity. Its possibility is determined by checking the normality law associated with the initial martensite start curve. Comprehensive investigations are necessary in this issue.

5. Concluding remarks

The martensite and austenite start conditions are determined experimentally in an Fe-9%Cr-5%Ni-14%Mn-6%Si polycrystalline SMA under combined tension/compression-torsion loads.

The martensite start condition is represented by an oval cone in the stress-temperature space, thus being different from the von Mises theory (the J_2-theory). The asymetry of the start condition with respect to the shear stress axis, a deviation from the J_2-theory, can be well explained by introducing the third invariant of the stress deviator, approving the J_3-theory proposed by RANIECKI *et al.* [10, 12].

The austenite start condition is expressed by a polygonal cone in the same stress-temperature space. Each side of the cone corresponds to the martensite variants preferably induced during mechanical loading. Experiments clearly confirm that the direction of loading determines the direction of the austenite start plane, whereas the amount of variants governs the position of the plane.

Construction of the "subsequent" transformation condition which follows from the initial start condition during thermomechanical loading should be the next urgent topics to be attacked.

Acknowledgments

Part of this work was financially supported by the Special Research Fund/ Tokyo Metropolitan Government as well as by the Grant-in-Aid for Scientific Research (#11650095) through the Ministry of Education, Science and Culture, Japan.

References

1. V. BIRMAN, *Review of mechanics of shape memory alloy structures*, Appl. Mech. Rev., **50**, 629–645, 1997.
2. E.P. GEORGE, R. GOTTHARDT, K. OTSUKA, S. TROLIER-MCKINSTRY and M. WUN-FOGLE [Eds.] *Materials for smart systems* II, Materials Research Society, Pittsburgh 1997.
3. Z.G. WEI, R. SANDSTRÖM and S. MIYAZAKI, *Shape-memory materials and hybrid composites for smart systems, Part* I *and* II, J. Materials Sci., **33**, 3743–3762, 3763–3783, 1998.
4. M. TOKUDA, P. SITTNER, M. TAKAKURA and YE MEN, *Experimental study on performances in* Cu*-based shape memory alloy under multiaxial loading conditions*, Materials Sci. Research Int., **1**, 260–265, 1995.
5. P. SITTNER and M. TOKUDA, *Reorientation in combined stress induced martensite?*, J. Phys. IV, coll. **8**-5, 1003–1008, 1995.
6. P. SITTNER, Y. HARA and M. TOKUDA, *Experimental study on the thermoelatic martensitic transformation in shape memory alloy polycrystal induced by combined external forces*, Metall. Mater. Trans. A, **26A**, 2923–2935, 1995.
7. C. ROGUEDA, C. LEXCELLENT and L. BOCHER, *Experimental study of pseudoelastic behaviour of a* CuZnAl *polycrystalline shape memory alloy under tension-torsion proportional and non-proportional loading tests*, Arch. Mech., **48**, 1025–1045, 1996.
8. F. NISHIMURA, N. WATANABE, T. WATANABE and K. TANAKA, *Transformation conditions in an* Fe*-based shape memory alloy under tensile-torsion loads: Martensite start surface and austenite start/finish planes*, Mater. Sci. Engng. A, **264**, 232–244, 1999.
9. F. NISHIMURA, N. WATANABE and K. TANAKA, *Evolution of martensite start condition in general thermomechanical loads of an* Fe*-based shape memory alloy*, Int. J. Mech. Sci., **42**, 347–365, 1999.
10. B. RANIECKI, S. MIYAZAKI, K. TANAKA, L. DIETRICH and C. LEXCELLENT, *Deformation behaviour of TiNi shape memory alloy undergoing R-phase reorientation in torsion-tension (compression) tests*, Arch. Mech., this issue 1999.
11. K. TANAKA, K. KITAMURA and S. MIYAZAKI, *Shape memory alloy preparation for multiaxial tests and identification of fundamental alloy performance*, Arch. Mech., this issue 1999.
12. B. RANIECKI and CH. LEXCELLENT, *Thermodynamics od isotropic pseudoelasticity in shape memory alloys*, Eur. J. Mech. A/Solids, **17**, 185–205, 1998.

13. E. PATOOR A. EBERHARDT and M. BERVEILLER, *Micromechanical modelling of the shape memory behavior* [In:] L.C. BRINSON and B. MORAN [Eds.], *Mechanics of phase transformations and shape memory alloys*, AMD **189**/PVP **292**, ASME, 23–37, 1994.

14. E. PATOOR and M. BERVEILLER, *Micromechanical modelling of the thermomechanical behavior of shape memory alloys*, [In:] M. BERVEILLER and F.D. FISCHER [Eds.], *Mechanics of solids with phase changes*, 121–188, Springer-Verlag, Wien-New York 1997.

15. K. TANAKA, T. HAYASHI, F. NISHIMURA and H. TOBUSHI, *Hysteretic behavior in an* Fe-Cr-Ni-Mn-Si *polycrystalline shape memory alloy during thermomechanical cyclic loading*, J. Mater. Engng. Performance, **3**, 135–143, 1994.

16. K. TANAKA, F. NISHIMURA and H. TOBUSHI, *Effect of prior transformation on transformation start stress and temperature in an* Fe*-based shape memory alloy*, Z. Metallkde, **86**, 211–215, 1995.

17. K. TANAKA, F. NISHIMURA and H. TOBUSHI, *Transformation conditions and subloops in an* Fe*-based shape memory alloy under thermomechanical loading*, J. Phys. IV, coll.**5**-2, 477–482, 1995.

18. F. NISHIMURA, N. WATANABE and K. TANAKA, *Transformation lines in an* Fe*-based shape memory alloy under tensile and compressive stress states*, Mater. Sci Engng. A, **221**, 134–142, 1996.

19. F. NISHIMURA, N. WATANABE and K. TANAKA, *Hysteretic behavior in an* Fe*-based shape memory alloy under tensile/compressive cyclic thermomechanical loading*, Mater. Sci. Research Int., **3**, 23–30, 1997.

20. F. NISHIMURA, N. WATANABE and K. TANAKA, *Stress-strain-temperature hysteresis and martensitic transformation start line in an* Fe*-based shape memory alloy*, Mater. Sci. Engng. A, **238**, 367–376, 1997.

21. L. ORGEAS and D. FAVIER, *Non-symmetric tension-compression behaviour of NiTi alloy*, J. Phys., coll.**8**-5, 605–610, 1995.

22. L. ORGEAS and D. FAVIER, *Stress-induced martensitic transformation of a NiTi alloy in isothermal shear, tension and compression*, Acta Mater., **46**, 5579–5591, 1998.

23. T.E. BUCHHEIT, S.L. KUMPF and J.A. WERT, *Modeling the stress-induced transformation behavior of shape memory alloy single crystals*, Acta Metall. Mater., **43**, 4189–4199, 1995.

24. T.E. BUCHHEIT and J.A. WERT, *Modeling the effects of stress state and crystal orientation on the stress-induced transformation of NiTi single crystals*, Metall. Mater. Trans. A, **25A**, 2383–2389, 1994.

25. F.D. FISCHER, E.R. OBERAIGNER, K. TANAKA and F. NISHIMURA, *Transformation induced plasticity revised: an update formulation*, Int. J. Solids Struct., **35** 2209–2227, 1998.

26. S. MIYAZAKI and K. OTSUKA, *Deformation and transition behavior associated with the R-phase in Ti-Ni alloys*, Metall. Trans. A, **17A**, 53–63, 1986.

27. S. MIAZAKI and C.M. WAYMAN, *The r-phase transition and associated shape memory mechanism in TiNi single crystals*, Acta Metall., **36**, 181–192, 1988.

28. S. MIYAZAKI, S. KIMURA and K. OTSUKA, *Shape-memory effect and pseudoelasticity associated with the R-phase transition in Ti-50.5at%Ni single crystals*, Phil. Mag. A, **57**, 467–478, 1988.

29. D.J. BARRETT, *A three-dimensional phase transformation model for shape memory alloys*, J. Intelligent Material Syst. Structures, **6**, 831–839, 1995.

30. F. NISHIMURA, N. WATANABE and K. TANAKA, *Analysis of uniaxial stress-strain-temperature hysteresis in an* Fe*-based shape memory alloy under thermomechanical loading*, Computational Mater. Sci., **8**, 349–362, 1997.

31. K TANAKA, F. NISHIMURA, H. KATO and S. MIYAZAKI, *Transformation thermomechanics of R-phase in TiNi shape memory aloys*, Arch. Mech., **49**, 547–572, 1997.

32. A. BEKKER and L.C. BRINSON, *Temperature-induced phase transformation in a shape memory alloy: Phase diagram based kinetics approach*, J. Mech. Phys. Solids, **45**, 949–988, 1997.

33. A. BEKKER and L.C. BRINSON, *Phase diagram based description of the hysteresis behavior of shape memory alloys*, Acta Mater., **46**, 3649–3665, 1998.

34. K. TANAKA, F. NISHIMURA, T. HAYASHI, H. TOBUSHI and C. LEXCELLENT, *Phenomenological analysis on subloops and cyclic behavior in shape memory alloys under mechanical and/or thermal loads*, Mech. Materials, **19**, 281–292, 1995.

35. H. TOBUSHI, S. YAMADA, T. HACHISUKA, A. IKAI and K. TANAKA, *Thermomechanical properties due to martensitic and R-phase transformations of TiNi shape memory alloy subjected to cyclic loading*, Smart Mater. Struct., **5**, 788–795, 1996.

36. L. FEDERZONI and G. GUÉNIN, *Influence of the presence of pre-existing thermal ε-martensite on the formation of stress-induced ε-martensite and on the shape memory effect of a* Fe-Mn-Cr-Si-Ni *shape memory alloy*, Scripta Metall. Mater., **31**, 25–30, 1994.

Received March 24, 1999.

Arch. Mech., **51**, 6, pp. 833–845, Warszawa 1999

Fatigue properties of TiNi shape memory alloy and applications to a heat engine and an actuator

H. TOBUSHI ([1]), T. NAKAHARA ([1]), T. HASHIMOTO ([1]), Y. SHIMENO ([1]) and K. TANAKA ([2])

([1]) *Department of Mechanical Engineering*
Aichi Institute of Technology
1247 Yachigusa, Yagusa-cho, Toyota, 470–0392, Japan
E-mail: tobushi@me.aitech.ac.jp

([2]) *Department of Aerospace Engineering*
Tokyo Metropolitan Institute of Technology
Asahigaoka 6-6, Hino, Tokyo, 191–0065, Japan

THE FATIGUE PROPERTIES of a TiNi shape-memory alloy (SMA) wire in the region of the martensitic transformation and the R-phase transformation are investigated. The rotating-bending fatigue life of a wire in the region of the R-phase transformation is longer than 10^7 cycles. A tilt-disk offset SMA heat engine and an indirect-heated SMA thermal actuator are developed.

1. Introduction

THE SHAPE MEMORY EFFECT (SME) and the superelasticity (SE) appear in a shape memory alloy (SMA) [1, 2]. Using these properties, a SMA performs the two functions of a temperature sensor and a generator of working force. Furthermore, because the densities of dissipation and storage of strain energy are large, we can produce high performance elements. Thus applications of a SMA as smart materials have attracted interest. In applications to an actuator, a robot and a solid-state heat engine, a SMA is used as a working element that performs cyclic motions. Therefore, in order to evaluate the reliability of the SMA element, cyclic deformation properties of the material are important. In most SMAs, the SME and the SE appear as the result of monoclinic martensitic transformation (MT). In TiNi SMA, the SME and the SE appear also due to the rhombohedral-phase transformation (RPT) [3, 4]. In the RPT compared with the MT, strain is small but cyclic deformation properties are superior [5, 6]. In the SMA elements subjected to high-cycle deformation in a robot and a solid-state

heat engine, the fatigue life is also an important problem [7, 8]. From a viewpoint of heat transfer, thin wires are widely used as the SMA elements. Therefore, in order to evaluate the reliability of SMA elements, the fatigue properties of wires are necessary. If we use the SMA heat engines, low-grade thermal energy can be used [9, 10]. The SMA heat engines make no waste gas. From the viewpoint of energy crisis, the development of the SMA engines is expected. In the case of applications of SMA elements to vehicles, electric source is limited. If we use the SME or recovery force of SMA elements, the SMA elements are heated. In order to control movement of the SMA elements, low-level electric current is required. Therefore a new method to heat the SMA elements is necessary. In this work, the rotating-bending fatigue properties of a TiNi SMA wire in air and in water are investigated. The formulation of low cycle fatigue is investigated. A tilt-disk offset SMA heat engine and an indirect-heated SMA thermal actuator are developed.

2. Material and specimen

The material was a Ti-55.3wt%Ni SMA wire, 0.75 mm in diameter. The specimens were given shape memory of a straight line and a coiled spring through shape memory processing. The reverse-transformation completion temperature A_f was about 323 K. The wires of a straight line were used for the rotating-bending fatigue tests. The coiled springs were used for a tilt-disk offset SMA heat engine and an indirect-heated SMA thermal actuator.

3. Rotating-bending fatigue

3.1 Experimental method

The rotating-bending fatigue test machines in air and in water were used [11]. In the tests, keeping the bent form of a SMA wire constant, the wire was rotated. The maximum strain on the surface of the wire was determined by the radius of bent curvature. The strain amplitude was the maximum strain in the middle of the wire between two supports. The temperature on the surface of the wire in air was measured through a thermograph.

The rotating-bending fatigue tests under constant strain amplitude ε_a, temperature T and frequency f were carried out in air and in water, and the number of cycles to failure was measured. The tests were performed for various values of ε_a, T and f.

3.2. Fatigue in water and in air

The relationship between strain amplitude ε_a and the number of cycles to failure N_f obtained by the rotating-bending fatigue test at various test temperatures T on a constant frequency $f = 500$ cpm in water is shown in Fig. 1. In Fig. 1, experimental data are plotted by several symbols and are connected by solid lines. As seen in Fig. 1, N_f decreases with increasing both ε_a and T. In the region of small ε_a, the strain-life relationship has the knee and approaches the horizontal line. The fatigue limit is in the region of ε_a of $0.4 \sim 0.8\%$ depending on T. The inelastic part of strain ε_a in this region is connected with RPT [3, 4]. Therefore the fatigue life is very long in the region of the RPT. Compared with the MT, the RPT strain is small and the fatigue damage due to the RPT is small, resulting in long fatigue life.

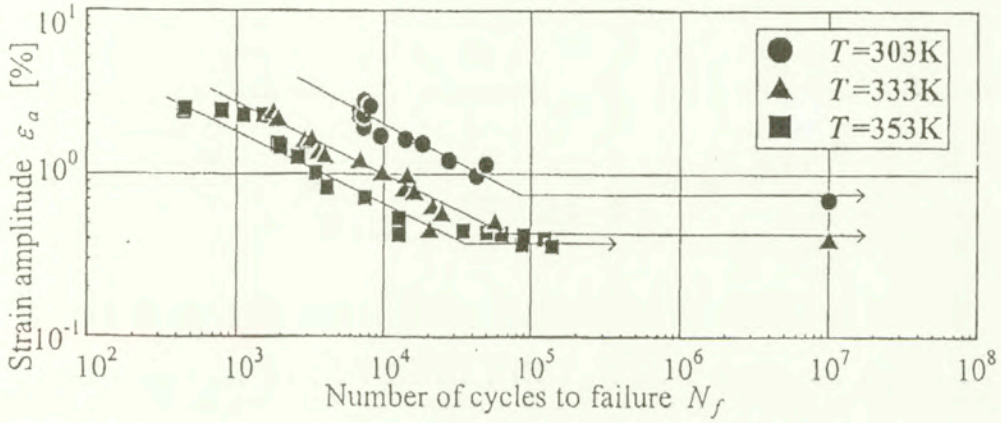

FIG. 1. Relationship between strain amplitude and number of cycles to failure at various temperatures in water on $f = 500$ cpm.

On the contrary, in the region of low-cycle fatigue for the MT strain ε_a above 1%, the strain-life relationship is expressed by the straight line having a steep slope. The slopes of the lines at various temperatures are 0.5.

The relationship between the MT stress σ_M and temperature T may be expressed by the following equation called the transformation line [12]:

$$\sigma_M = C_M(T - M_s), \tag{3.1}$$

where C_M and M_s denote a slope of the transformation line and the MT starting temperature under no stress, respectively. As found from Eq. (3.1), σ_M increases in proportion to T. Because C_M is 6 MPa/K [13], σ_M increases by 120 MPa if T increases by 20 K. Thus, if temperature is high, the MT stress increases and fatigue damage is large, resulting in short fatigue life.

The relationships between strain amplitude ε_a and the number of cycles to failure N_f for two temperatures obtained by the rotating-bending fatigue test in air and in water performed at constant frequency $f = 500$ cpm are shown in Fig. 2. In the case marked with an arrow, the specimen did not rupture.

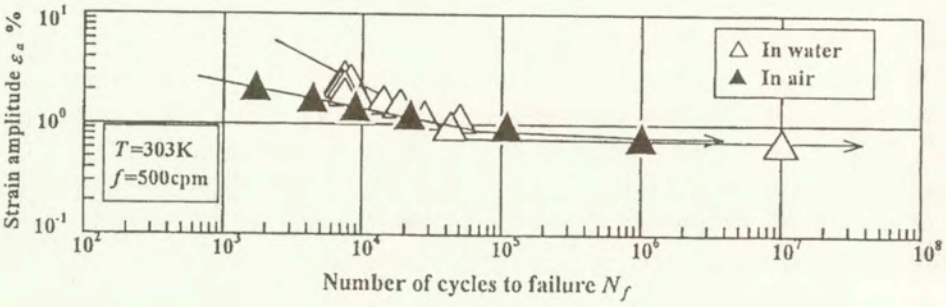

(a) T=303K

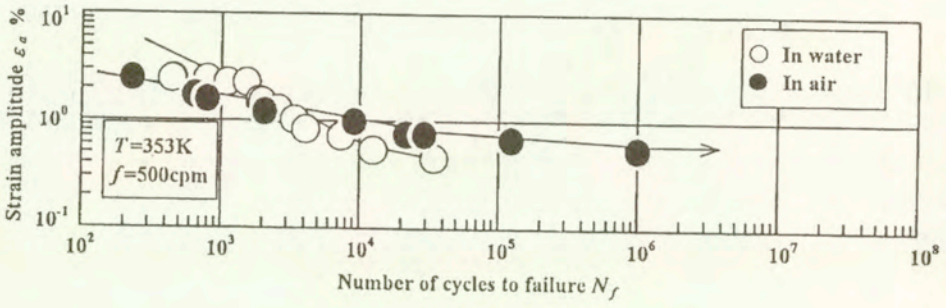

(b) T=353K

FIG. 2. Strain-life curves in air and in water on $f = 500$ cpm.

As seen in Fig. 2, the strain-life curves may be expressed by bi-linear lines. The strain-life curve has a knee in the region of $\varepsilon_a = 0.5 \sim 1\%$ and $N_f = 10^4 \sim 10^5$ cycles. In the region of ε_a larger than the knee, the slope of the lines is large. On the contrary, in the region of ε_a smaller than the knee, N_f increases markedly and the lines approach the horizontal lines. These properties are similar as those observed in Fig. 1.

The region of ε_a larger than the knee of strain-life curves is in the region after completion of the RPT and in the region of the MT. Let us discuss the slope of the lines in this region. Although the slopes of the lines are different in air and in water, both take almost the same values for each temperature. The value of slope is 0.24 in air but 0.5 in water. The value of 0.5 in water is almost the same as that for steel. The reason why the value of the slope is different for tests performed in air and in water can be explained as follows.

If ε_a is large, dissipated work during the loading and unloading processes is large, resulting in large temperature rise ΔT under cyclic deformation in air. From Eq. (3.1), it is found that if temperature increases by $\Delta T = 10$ K, σ_M increases by $\Delta\sigma_M = 60$ MPa. If stress on the surface of the wire increases, nucleation and growth of fatigue cracks are activated, resulting in small N_f. In air, if ε_a is large, ΔT is large and N_f is small, and therefore the value of slope is small. In water, because heat generated by cyclic deformation is transferred quickly to water and spread out, temperature of the specimen slightly increases. Therefore N_f is large and slope is large in water.

3.3. Formulation of low-cycle fatigue life

3.3.1. Dependence on strain amplitude. As found from the strain-life curves shown in Fig. 1, the relationship between strain amplitude ε_a and the number of cycles to failure N_f in the region of low-cycle fatigue on a logarithmic graph is practically expressed by a straight line. Therefore, similarly as in the case of Manson-Coffin relationship for steel in low-cycle fatigue, the relationship between ε_a and N_f for TiNi SMA may be expressed as follows

$$\varepsilon_a \cdot N_f^{\beta} = \alpha, \tag{3.2}$$

where α and β represent ε_a in $N_f = 1$ and the slope of the $\log\varepsilon_a - \log N_f$ curve, respectively. The value of β in water is about 0.5 at each temperature. The same value is obtained for steel.

3.3.2. Dependence on temperature. The dependence of the fatigue life on temperature will be discussed for fatigue tests performed in water, in which case temperature of the specimen increases little. The exponent β in Eq. (3.2) is about 0.5 at each temperature. The value of α decreases with increasing temperature T. As expressed by Eq. (3.1), the MT stress increases in proportion to T. If the MT stress is high, fatigue damage is large and the fatigue life is short, resulting in small α. Based on these considerations, if the relationship between α and T is plotted on a semilogarithmic graph, it is found that the relationship is expressed by a straight line. Therefore it becomes as follows

$$\alpha = \alpha_s \cdot 10^{-a(T-M_s)}, \tag{3.3}$$

where M_s is 253 K which was obtained by the DSC test. Based on the results of the fatigue test in water, the coefficients in Eq. (3.3) are determined as $\alpha_s = 8.56$ and $a = 0.012$ K^{-1}. Therefore, from Eq. (3.2), the relationship between ε_a and N_f is expressed by the following equation

$$\varepsilon_a \cdot N_f^{0.5} = 8.56 \times 10^{-0.012(T-M_s)}. \tag{3.4}$$

Thus the dependence of the fatigue life on ε_a and T is described by Eq. (3.4).

3.3.3 Evaluation of low-cycle fatigue life. The experimental results between ε_a and N_f obtained in water and the calculated results obtained by Eq. (3.4) are shown in Fig. 3. As seen in Fig. 3, the experimental results are well expressed by the calculated results. Therefore the proposed relationship is useful for evaluation of low-cycle fatigue life when we design SMA elements.

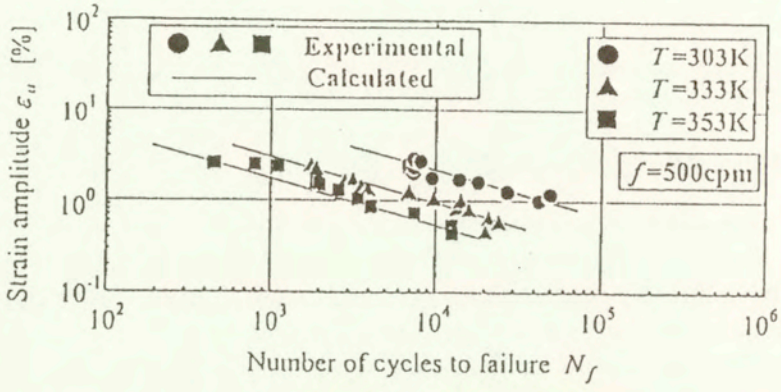

FIG. 3. Strain amplitude versus fatigue life for low-cycle fatigue region at various temperatures in water.

4. Heat engine

4.1. Tilt-disk offset SMA heat engine

The basic structure and working principle of a tilt-disk offset SMA heat engine are shown in Fig. 4.

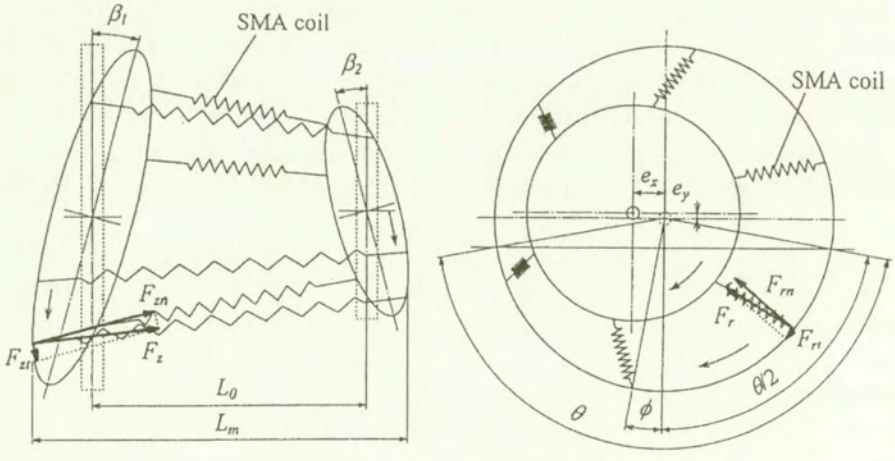

FIG. 4. Basic structure and working principle of a tilt-disk offset SMA heat engine.

The engine has two tilt disks which are facing each other. The axes of two disks are independent of each other. The center distance of two disks is L_0 in the horizontal direction. The two disks are eccentric by a distance of e_x and e_y in the horizontal and vertical directions, respectively. The disks are inclined by angles of β_1 and β_2 from the vertical direction, respectively. Each point on the circumferences of two disks is connected by a SMA helical spring. The circumference of a large disk corresponding to the heating angle θ is soaked in the hot reservoir. The center of the heating angle is inclined by the heating phase angle ϕ against the position where the SMA helical springs are most widely expanded. In the heating zone, the SMA coil contracts with radial component F_r and axial component F_z of the recovery force due to the reverse transformation. The tangential components F_{rt} and F_{zt} of the contraction force rotate the disks. The direction of rotation varies depending on e_y and ϕ.

4.2 Output power

The tilt-disk offset SMA heat engine was constructed. The output power characteristics were examined. The experimental conditions were as follows. The heating zone was in hot water and the cooling zone in air. The number of SMA coils was 12, $e_x = 5$ mm, $e_y = 0$ mm, $\beta_1 = 15°$, $\beta_2 = 0°$, $\theta = 160°$, $\phi = 40°$ and $L_0 = 110$ mm.

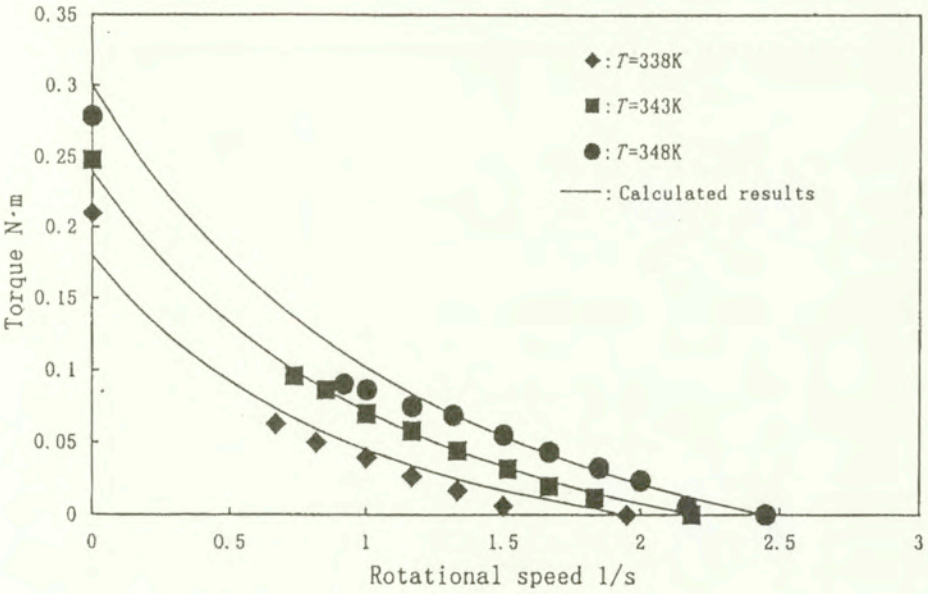

FIG. 5. Relationship between torque and rotational speed.

The relationship between torque M and rotational speed n obtained by the experiments at various temperatures T is shown in Fig. 5. As seen in Fig. 5, the torque decreases with an increase in rotational speed. The relationship between M and n can be expressed by a simple power function as follows

$$(M + M_0)(n + n_0)^b = c, \tag{4.1}$$

where n_0 denotes rotational speed under no torque and $c = M_0(2n_0)^b$. Torque at $n = 0$ is $(2^b - 1)M_0$.

The recovery stress increases in the reverse transformation region and can be approximated by a linear relationship of temperature [14, 15]. Therefore stationary torque M_0 can be expressed as function of temperature as follows:

$$M_0 = h(T - A_f) + m. \tag{4.2}$$

On the other hand, n_0 depends not only on temperature but also on viscosity of water and friction among elements of the engine. Thus n_0 is expressed by the following equation:

$$n_0 = k(T - A_f) + \nu. \tag{4.3}$$

The dependence of M_0 and n_0 on T is shown in Fig. 6. As seen in Fig. 6, the dependence of M_0 and n_0 on T is well expressed by Eqs. (4.2) and (4.3), respectively.

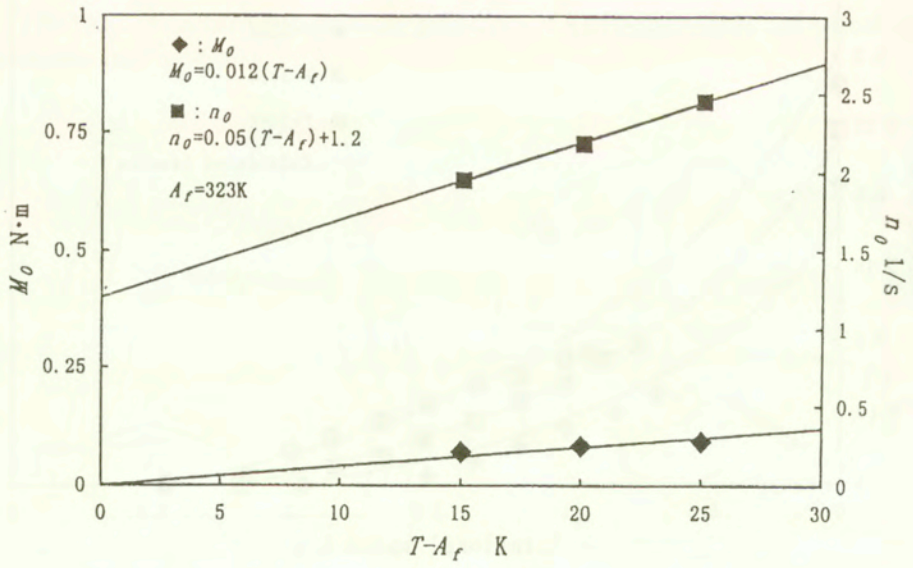

FIG. 6. M_0 and n_0 versus temperature.

Based on Eq. (4.1), the output power P can be obtained as follows:

$$P = 2\pi nM = 2\pi M_0 n \times \left\{ \left(\frac{2n_0}{n+n_0} \right)^b - 1 \right\}. \tag{4.4}$$

The relationship between P and n at various T is shown in Fig. 7. As seen in Fig. 7, the output characteristic are estimated by Eq. (4.4). Therefore Eq. (4.4) is used to obtain the optimum operating condition of SMA heat engines.

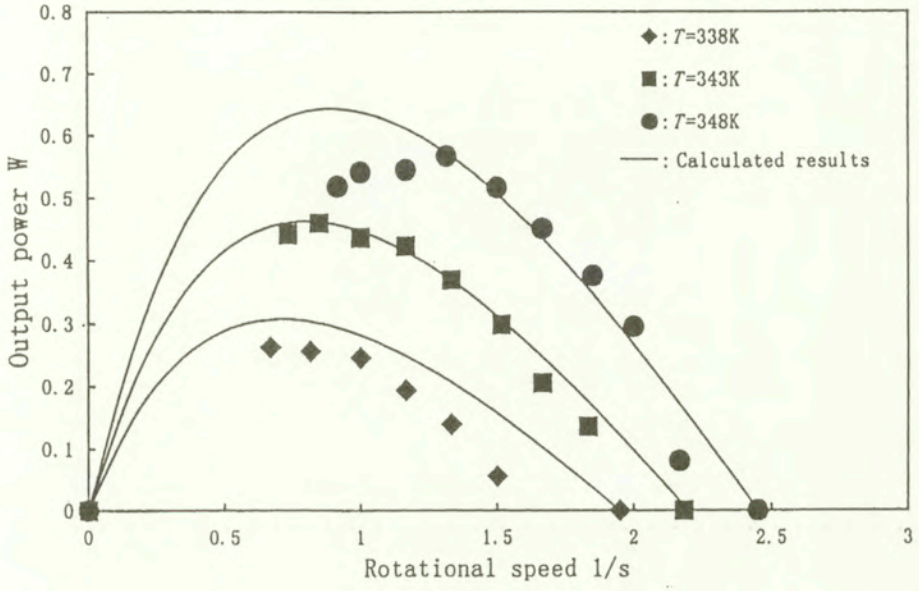

FIG. 7. Relationship between output power and rotational speed.

5. Thermal actuator

5.1. Indirect-heated SMA actuator

Thermal actuators heating with direct electric current have been investigated in various fields. Low-level electric current is required in the case of application for vehicles because of the limitation of electric source. The target of this research is focused on indirect heating of SMA using a fine wire with low level electric current. This section reports the recent activities on improving the response of an indirect-heated SMA actuator.

Enlarged view of section of a SMA wire wound by a fine wire is shown in Fig. 8(a). Air gap exists between a fine wire and a SMA wire, and thus it has

effect of decreasing heat conduction from a fine wire to a SMA wire. The material with high heat conduction coefficient is plastered between a fine wire and a SMA wire to improve heat conduction as shown in Fig. 8(b).

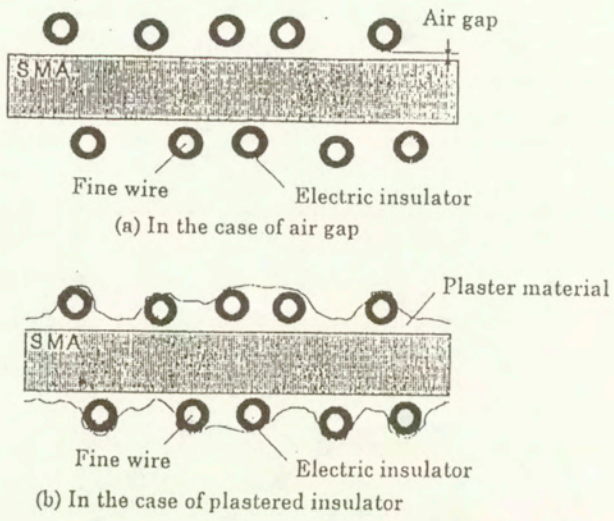

FIG. 8. Enlarged view of section.

Fig. 9 shows schematically the layout of elements in the indirectly heated SMA actuator.

Based on Fourier's law, transported heat (dq) from a fine wire at T_f to a SMA wire at T in small period $(d\tau)$ is expressed as follows:

$$dq = \frac{2\pi(T_f - T)l}{\frac{1}{\lambda_2}\log\left(\frac{r_0 + b_2}{r_0}\right) + \frac{1}{\lambda_1}\log\left(\frac{r_0 + b_2 + b_1}{r_0 + b_2}\right)} d\tau, \tag{5.1}$$

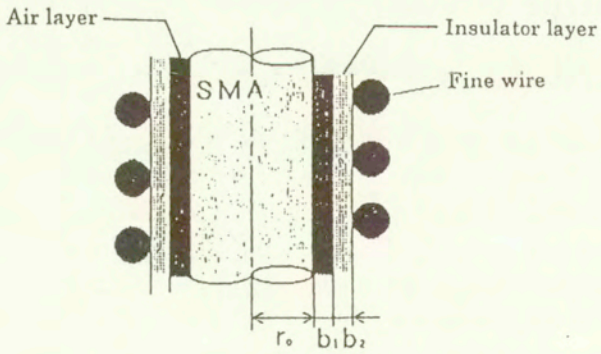

FIG. 9. Heat conduction model.

where l, T, τ and λ denote length of SMA, temperature, time and thermal conductivity, respectively. Subscripts 1 and 2 denote air and insulator, respectively. The characteristic values k_1, k_2 and k_3 of size and materials are introduced as follows:

$$k_1 = r_0^2 \gamma_0 C_0, \quad k_2 = \frac{1}{\lambda_2} \log\left(\frac{r_0 + b_2}{r_0}\right), \quad k_3 = \frac{1}{\lambda_1} \log\left(\frac{r_0 + b_2 + b_1}{r_0 + b_2}\right), \tag{5.2}$$

where γ_0 and C_0 denote density and specific heat of SMA, respectively.
The overall index K is obtained as follows:

$$K = \frac{1}{k_1(k_2 + k_3)}. \tag{5.3}$$

Non-dimensional temperature is defined by the following equation:

$$t = 1 - e^{-2K\tau}. \tag{5.4}$$

5.2. Time constant and working force

Many samples with various sizes and materials were presented in this research and response times were measured. The results are summarized in Fig. 10. As found from Fig. 10, the guideline to get high response of the SMA actuator is obtained. As found from Eqs. (5.2) and (5.3), if we use a SMA wire with diameter of a half, time constant decreases by about one fourth.

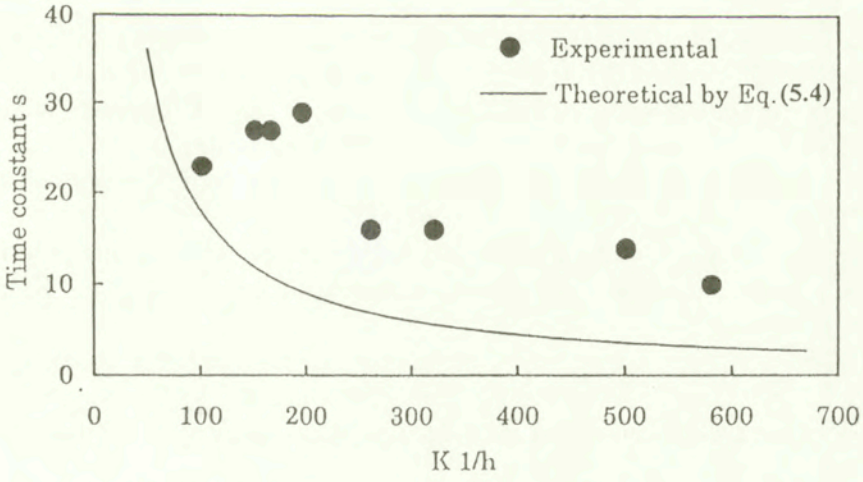

FIG. 10. Experimental and theoretical values of time constant.

Using the model which showed highest responsibility, a coiled spring actuator was manufactured. The measured response of force after electric current supply is shown in Fig. 11. The working force covers a target value. These investigations should contribute to the development of a new high-performance thermal actuator with indirect heating.

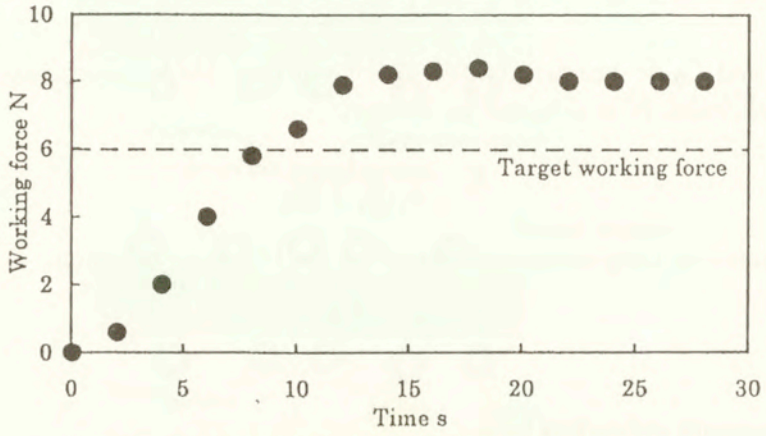

FIG. 11. Relationship between working force and time.

5. Conclusions

The fatigue properties of the TiNi SMA wire subjected to rotating bending have been investigated experimentally. A tilt-disk offset SMA heat engine and an indirect-heated SMA thermal actuator are developed. The main results obtained are summarized as follows.

1. If the strain amplitude is found in the RPT region, the fatigue life is longer than 10^7 cycles. If the strain amplitude is found in the MT region, the fatigue life is shorter than 10^5 cycles. The dependence of low-cycle fatigue life on temperature is expressed by the proposed fatigue equation.

2. The working properties of the tilt-disk SMA heat engine depend on various parameters.

The dependence of output power characteristics on temperature is estimated by the proposed equation. The optimum operating condition of the SMA heat engine is evaluated.

3. The heat conduction model of the indirect-heated SMA actuator is proposed. The time constant and working force are evaluated by the proposed model. The condition to develop the indirect-heated SMA actuator is clarified.

Acknowledgements

The authors wish to express their gratitude to Polish Academy of Sciences, Japan Society for the Promotion of Science and the Nitto Foundations for financial supports.

References

1. J. PERKINS [Ed.], *Shape memory effects in alloys*, Plenum Press, New York 1975.
2. H. FUNAKUBO [Ed.], *Shape memory alloys*, Gordon and Breach Science Pub., New York 1987.
3. K. OTSUKA, *Introduction to the R-phase transition*, 36–45 [in:] Engineering aspects of shape memory alloys, T. W. Duerig, K. N. Melton, D. Stockel, C. M. Wayman, [Eds.], Butterworth-Heinemann, London 1990.
4. S. MIYAZAKI and K. OTSUKA, *Deformation and transition behavior associated with the R-phase in Ti-Ni alloys*, Metall. Trans. A, **17A**, 53–63, 1986.
5. H. TOBUSHI, S. YAMADA, T. HACHISUKA, A. Ikai and K. TANAKA, *Thermomechanical properties due to martensitic and R-phase transformations of TiNi shape memory alloy subjected to cyclic loadings*, Smart Mater. Struct., **5**, 788–795, 1996.
6. H. TOBUSHI, T. HACHISUKA, T. HASHIMOTO and S. YAMADA, *Cyclic deformation and fatigue of a TiNi shape-memory alloy wire subjected to rotating bending*, Trans. ASME, J. Eng. Mater. Tech, **120**, 64–70, 1998.
7. K.N. MELTON and O. MERCIER, *Fatigue of NiTi thermoelastic martensites*, Acta Metall., **27**, 137–144, 1979.
8. S. MIYAZAKI, *Development and characterization of shape memory alloys*, 69–147 [in:] Shape memory alloy, M. Fremond and S. Miyazaki, Springer Wien, New York 1996.
9. W.S. GINELL, J.L. MCNICHOLS, Jr. and J.S. CORY, *Nitinol heat engines for low-grade thermal energy conversion*, Mech. Eng., **101**, 5, 28–33, 1979.
10. H. TOBUSHI, K. KIMURA, H. IWANAGA and J.R. CAHOON, *Basic research on shape memory alloy heat engine (Output power characteristics and problems in development)*, JSME Inter. J., Ser. I, **33**, 2, 263–268, 1990.
11. H. TOBUSHI, T. HACHISUKA. S. YAMADA and P.H. LIN, *rotating -bending fatigue of aTiNi shape-memory alloy wire*, Mech. Mater., **26**, 35–42, 1997.
12. K. TANAKA, S. KOBAYASHI and Y. SATO, *Thermomechanics of transformation pseudoelasticity and shape memory effect in alloys*, Inter. J. Plasticity, **2**, 59–72, 1986.
13. H. TOBUSHI, P.H. LIN, K.TANAKA, C. LEXCELLENT and A. IKAI, *Deformation properties of TiNi shape memory alloy*, J. de Phys. IV, C2, **5**, 409–413, 1995.
14. K. TANAKA, T. HAYASHI, Y. ITOH and H. TOBUSHI, *Analysis thermomechanical behavior of shape memory alloys*, Mech. Mater., **13**, 207–215, 1992.
15. P.H. LIN, H. TOBUSHI, K. TANAKA, C. LEXCELLENT and A. IKAI, *Recovery Stress of TiNi shape memory alloy under constant strain*, Arch. Mech., **47**, 2, 281–293, 1995.

Received January 13, 1999; new version April 19, 1999.

Arch. Mech., **51**, 6, pp. 847–864, Warszawa, 1999

Three-dimensional constitutive equations of polycrystalline shape memory alloy

M. TOKUDA ([1]), M. YE ([1]), B. BUNDARA ([2]) and P. SITTNER ([3])

([1]) *Department of Mechanical Engineering, Mie University, Kamihama, Tsu 514-8507, Japan*

([2]) *JSPS-Post Doctral Fellow from Slovenia*

([3]) *Institute of Physics, Czech Academy of Sciences, Na Slovance 2, 180-40 Prague 8, Czech Republic*

QUITE UNIQUE and interesting behavior of shape memory alloy (SMA) under complex loading conditions, including the complicated path-dependence, have been observed in systematic experiments by applying some combined loads of axial force and torque to the thin-walled tubular specimen of Cu-based polycrystalline shape memory alloy. A set of constitutive equations is proposed, which can describe the complicated behavior observed in the experiments. The mesoscopic approach is employed in the formulation because the complicated behavior is closely related to the microstructural changes of the material, and the obtained equations show a reasonable agreement with the exprimental results. In the first paper, the process of modelling and the details of the formulated constitutive equations are described, and the comparison between the experimental results and the results evaluated by using the proposed constitutive equations will be shown in the second report.

1. Introduction

SHAPE MEMORY ALLOYS (SMA) were expected to become very important for the engineering applications because of their unique thermo-mechanical properties [1]. Therefore, quite active research and development has been continued in the recent years [2 – 4]. In order to support the engineering applications, the basic and fundamental research work has also been vital; for example, the material development of SMA of better qualities (e.g., the thin-film of SMA [5 – 9]), the development of less expensive SMA and the improvement of their functions and properties (e.g., Fe-based SMA [10, 11]), the experimental research works [12, 13] to investigate the mechanisms of thermo-mechanical properties and their modeling and formulation [14 – 23] appropriate for the prediction of the material

behavior and the design of devices constructed from SMA elements. This paper is concentrated on modeling and formulation of the thermo-mechanical properties of SMA.

The research on the modeling and formulations in the last decades were mostly limited to simple loading conditions (particularly, uniaxial tensile loading), and thus the applications have been considered on the basis of these works. On the other hand, when we take into account the fact that the basic deformation mechanism of SMA is a combination of (1) the temperature (T)-induced martensite phase transformation, and (2) the stress ($\sigma_{ij} : i, j = 1, 2, 3$)-induced martensite phase transformation, various and unknown unique behaviors of SMA are possible. Actually, new engineering applications of SMA can be developed for the multi-axial/complex loading conditions. As an example, the positioning devices or actuators which perform complicated three-dimensional motions themselves by controlling several stress components can be designed. Also, further investigation and clear understanding of new features of SMA will be helpful in the design of future intelligent material systems [24 – 26]. In the literature, however, there are only few reports on the basic research focused on the behavior of SMA under complex loading conditions, experimentally and theoretically as well. From the above mentioned point of view, the authors have continued a series of systematic experiments on the thermo-mechanical behavior of polycrystalline SMA under complex loading conditions, by applying the combined loads of axial force and torque to the thin-walled tubular specimen of Cu-based polycrystalline SMA [27 – 32]. In the experimental part of the research, unique behavior have been obtained. Some phenomena can not be observed by the simple loading experiments. For example,

1. In the proportional deformation tests using the combined loads of axial force and torque, the corresponding deformation is also proportional. That is, the thin-walled tube exhibits the simultaneous torsional and axial (elongation/contraction) deformations under this stress condition[29, 30].

2. Strong and unique path dependence was confirmed. That is, the obtained strain states are different when the stress paths are different, though the current stress states are the same. One special exception is that the zero-stress state corresponds to the zero-strain state, regardless of their paths. That is, the original shape of the specimen is memorized [29, 30].

3. When only the axial force is changed after the combined load of axial force and torque is applied to the thin-walled tube, the tube shows torsional deformation too without any change of torsional loading. The same kind of deformation can be observed under no change of axial force. That is, the axial deformation of a tube can be obtained by changing the torsional loading without any change of axial force. This is also one of the interesting features of SMA under complex loading conditions [29, 30].

4. When a tubular specimen subjected to the torsional loading is heated up to a certain temperature, the torsional deformation induced by the martensite phase transformation decreases monotonically and finally disappears. On the other hand, when the specimen subjected to the reverse torsional load following the forward torsional loading is heated up, the change of torsional deformation was observed to be non-monotonic, that is, the direction of torsional deformation changes during the heating process [32]. The same phenomenon can be expected in the case of tension-compression loading. That is, the specimen will be longer at first and shorter in the next stage during the monotonic heating process.

The experimental results under complex loading conditions including the above exposed interesting phenomena could be understood clearly by considering the microscopic behavior of martensite variants. In the present paper, a set of constitutive equations of SMA under the complex (general) thermo-mechanical loading conditions is proposed, which can reproduce the special behavior obtained in the experiments. In the formulation of constitutive equations, the meso-mechanical modeling approach [33] proposed by one of the authors is employed, which can incorporate the multi-layered microstructure of the polycrystalline materials. This meso-mechanical modeling approach was employed for the formulation of inelastic (or plastic) constitutive equations of polycrystalline metallic materials whose main deformation mechanism is slipping (by dislocations) inside the grains, especially under complex/general loading conditions, where the complicated metallurgical dislocation mechanisms controlling the slip deformation are taken account into by using the so-called slip system idea, and the mechanical model of a grain can be obtained as the collection of several slip systems. The interactions among slip systems are assumed in the grain component. The polycrystal model is composed of a large number of crystal grain components and the interactions among grains are determined by using a micromechanical approach. In the present case of polycrystalline SMA, the mechanism of phase transformation is employed instead of the slip mechanism.

In the present report, the derivation of a set of constitutive equations of SMA under complex loading conditions is described. In the following second report, the accuracy/reliability, and applicability of these constitutive equations are discussed by comparing the calculated results with the corresponding experimental ones.

2. Thermo-mechanical model of phase- transformation

The basic phase transformation mechanisms of SMA are the temperature-induced and stress-induced martensite phase transformation. The deformation induced by these martensite phase transformations is considered to be the twin-

type (shear) deformation with a negligibly small change of volume, and controlled by the temperature and the stress tensor [1, 34]. This twin-type (shear) deformation occurs only in the crystallographically determined (easy twin) directions on the crystallographically determined (easy twin) planes. This twin (shear) deformation system with a specific direction and a specific plane is hereafter named the phase transformation system and corresponds to the technical term "slip system" used in the crystal plasticity.

When SMA is subjected to the thermal loading (the change of temperature) only, the martensite phase transformation with the (twin-type) shear strain occurs. However, in this case, no macroscopically significant deformation of crystal grain (as well as the polycrystal composed of these grain components) can be observed. This phenomenon can be explained as follows: in the case of temperature change without any applied external or internal stress, the phase transformation is possible to occur simultaneously in every transformation systems with different orientations, and thus the induced shear (twin) strains cancel each other in the average. On the other hand, in the case of stress-induced phase transformation, the phase transformation occurs in the phase transformation systems with the preferable orientations to the stress state. Thus, only the shear strains with specific directions are summed-up and consequently, the significant macroscopic inelastic deformation can be observed in the crystal components (as well as in the polycrystal).

Our engineering interests are the macroscopic inelastic deformations, the force produced when the deformation is constrained, and their combination. Therefore, only the case when the material is subjected to some stresses is considered in the present paper. The effect of temperature is incorporated as the temperature effect on the shear stress which is necessary for the phase transformation, i.e., on the critical (resolved) shear stress. The typical feature of temperature effect is that the lower is the temperature, the easier the martensite phase transformation will occur (the smaller will be the critical shear stress). That is, the deformation of SMA needs larger stress at higher temperature. This feature of SMA is quite different from that of usual metallic materials with the slip or diffusion mechanism controlled by thermo-activation.

The above-mentioned phase transformation mechanism is determined by using the "shear stress τ – phase transformation) shear strain γ^{PT} – temperature T" relation of the phase transformation system. When the material is of the austenite structure (the parent phase), the mechanical characteristic of this transformation system can be expressed by the loading curve OABC and the unloading curve CDEO shown in Fig. 1, where $\tau_{\mathrm{MS}}(T)$, $\tau_{\mathrm{AS}}(T)$, and $\tau_{\mathrm{AF}}(T)$ are the martensite phase transformation start and finish shear stresses, and the austenite (reverse) phase transformation start and finish shear stresses at the temperature T, respectively. The γ^{PT} is the phase transformation shear strain and $\gamma^{\mathrm{PT}}_{\mathrm{max}}$ is the

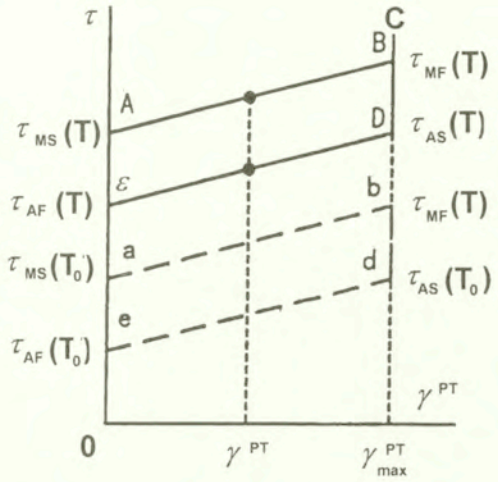

FIG. 1. Typical stress-strain relation of phase transformation system (I).

maximum value of γ^{PT}. In this figure, at the temperature T, the martensite phase transformation in the phase transformation system begins at point A, and the martensite strain γ^{PT} increases with the increase of shear stress τ along the line AB. The increase of γ^{PT} stops at point B at which the martensite phase transformation is completed, and then γ^{PT} does not increase though the shear stress increases (B$\rightarrow$ C). In the next step, when the stress is unloaded from the point C, the reverse transformation starts at the point D where the stress is smaller than the stress at B, and this reverse transformation is completed at the point E. The dashed curve in Fig. 1 shows the relation between the shear stress τ and the phase transformation strain γ^{PT} at a different temperature $T_0 (< T)$. The dashed loop abde at the temperature T_0 can be obtained by shifting the loop ABDE at the temperature T without any change of its shape. The sub-loading process can be incorporated as follows: As shown in Fig. 2, when the material is unloaded ($d\tau < 0$) at the point P during the martensite phase transformation, the phase transformation strain γ^{PT} does not change and the shear stress reaches the point Q on the reverse transformation line DE. If the unloading ($d\tau < 0$) is continued, the reverse phase transformation begins at the point Q and the shear phase transformation strain γ^{PT} decreases Q$\rightarrow$ R$\rightarrow$ E). When the material is loaded ($d\tau > 0$) at the point R on the reverse transformation line, the reverse transformation stops and the transformation shear strain γ^{PT} does not change till the stress arrives at the point S on the phase transformation line AB. The detail of sub-loop (or internal loop) PQRS depends on the material and has been still discussed in [35 – 41]. In the present paper, the simplest form has been selected.

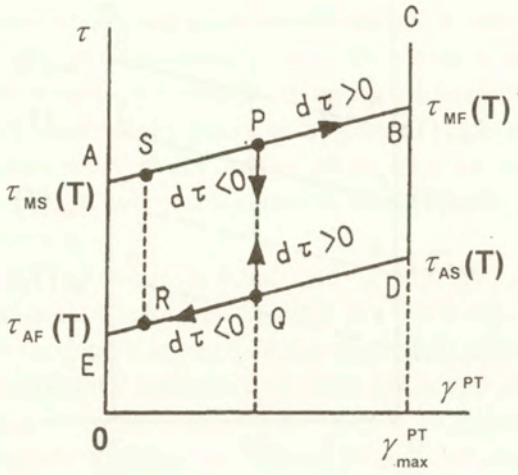

FIG. 2. Typical stress-strain relation of phase transformation system (II).

The relation between shear stress τ and (phase transformation) shear strain γ^{PT}-temperature T mentioned above can be formulated in the following form.

First, when the linear strain hardening rule shown in Figs. 1 and 2 is assumed for simplicity, the critical shear stress for martensite phase transformation $\tau_{\mathrm{M}}(\gamma^{\mathrm{PT}}, T)$ at the phase transformation shear strain γ^{PT} and the temperature T is expressed as follows:

$$\tau_{\mathrm{M}}(\gamma^{\mathrm{PT}}, T) = \tau_{\mathrm{MS}}(T) + H\gamma^{\mathrm{PT}}, \tag{2.1}$$

where H is the hardening coefficient (the material constant). The martensite start stress $\tau_{\mathrm{MS}}(T)$ is assumed to depend on the temperature T linearly, what has been confirmed both experimentally as well as theoretically (Clausius-Clapeyron equation [1, 34]), and thus,

$$\tau_{\mathrm{MS}}(T) = \tau_{\mathrm{OMS}} + \beta(T - T_0), \tag{2.2}$$

where β is the material constant, and τ_{OMS} is the martensite phase transformation (critical) shear stress at the reference temperature T_0 (for example, the room temperature). By using (2.1) and (2.2), $\tau_{\mathrm{M}}(\gamma^{\mathrm{PT}}, T)$ can be expressed in the following form:

$$\tau_{\mathrm{M}}(\gamma^{\mathrm{PT}}, T) = \tau_{\mathrm{OMS}} + \beta(T - T_0) + H\gamma^{\mathrm{PT}}. \tag{2.3}$$

Following (2.3), the martensite phase transformation start function (M-type yield function) F_{M} is obtained in the following form:

$$F_{\mathrm{M}} = \tau - \left[\tau_{\mathrm{OMS}} + H\gamma^{\mathrm{PT}} + \beta(T - T_0)\right], \tag{2.4}_1$$

where τ is the shear stress resolved on the considered phase transformation system. When the shear stress τ satisfies the equation

$$F_{\mathrm{M}} = 0, \tag{2.4}_2$$

the deformation is as follows:

1. Under the loading condition, that is, for $dF_{\mathrm{M}} = d\tau - \beta dT > 0$, the martensite phase transformation takes place and thus, $d\gamma^{\mathrm{PT}} > 0$. In this situation, considering that $d\tau - H d\gamma^{\mathrm{PT}} - \beta dT = 0$, from $(2.4)_1$ and $(2.4)_2$

$$d\gamma^{\mathrm{PT}} = (d\tau - \beta dT)/H, \tag{2.5}$$

2. Under the neutral loading $dF_{\mathrm{M}} = 0$, or for the unloading $dF_{\mathrm{M}} < 0$, i.e., under the condition $dF_{\mathrm{M}} = d\tau - \beta dT \leq 0$, the martensite phase transformation does not occur and the deformation is elastic. Therefore, the increment of phase transformation induced shear strain $d\gamma^{\mathrm{PT}}$ is expressed as follows:

$$d\gamma^{\mathrm{PT}} = 0. \tag{2.6}$$

The relation between the stress increment $d\tau$ and the strain increment $d\gamma^{\mathrm{PT}}$ can be summarized in the following form:

$$d\gamma^{\mathrm{PT}} = \langle dF_{\mathrm{M}} \rangle \langle \gamma^{\mathrm{PT}}_{\max} - \gamma^{\mathrm{PT}} \rangle (d\tau - \beta dT)/H, \tag{2.7}$$

where

$$\langle X \rangle = 1 \quad \text{for} \quad X > 0, \quad \langle X \rangle = 0 \quad \text{for} \quad X \leq 0, \tag{2.8}$$

and $\gamma^{\mathrm{PT}}_{\max}$ is the material constant (the maximum phase transformation shear strain); the γ^{PT} can not increase after the phase transformation is completed in the phase transformation system, and $\langle \gamma^{\mathrm{PT}}_{\max} - \gamma^{\mathrm{PT}} \rangle$ in (2.7) is used for this mechanism. As found from (2.3), the $\gamma^{\mathrm{PT}}_{\max}$ and the martensite phase transformation finish shear stress $\tau_{\mathrm{MF}}(T)$ are related in the following form:

$$\tau_{\mathrm{MF}}(T) = \tau_{\mathrm{OMS}} + \beta(T - T_0) + H\gamma^{\mathrm{PT}}_{\max}. \tag{2.9}$$

In what follows, the formulation of the reverse (austenite) phase transformation is considered in the similar way as that mentioned in the case of the martensite phase transformation. According to Fig. 1, the reverse (austenite) phase transformation critical shear stress τ_{A} is expressed in the linear strain-hardening form:

$$\tau_{\mathrm{A}}(\gamma^{\mathrm{PT}}, T) = \tau_{\mathrm{OAF}} + H\gamma^{\mathrm{PT}} + \beta(T - T_0), \tag{2.10}$$

where τ_{0AF} is the reverse phase transformation (critical) shear stress at the reference temperature T_0. Therefore, the austenite (reverse) phase transformation function (A-type yield function) F_A is

$$-F_A = \tau - \left[\tau_{OAF} + H\gamma^{PT} + \beta(T - T_0)\right], \tag{2.11}_1$$

where τ is the (resolved) shear stress on the considered phase transformation system. When the stress state τ satisfies the following equation:

$$F_A = 0, \tag{2.11}_2$$

the deformation can be classified as follows.

1. Under the loading condition; $dF_A = -d\tau + \beta dT > 0$, the austenite (reverse) phase transformation occurs, and thus, $d\gamma^{PT} < 0$. From $(2.11)_1$ and $(2.11)_2$, $d\tau - Hd\gamma^{PT} - \beta dT = 0$, and then,

$$d\gamma^{PT} = (d\tau - \beta dT)/H. \tag{2.12}$$

2. Under the neutral loading $dF_A = 0$, or under the unloading condition $dF_A < 0$, that is, in the case of $dF_A = -d\tau + \beta dT \leq 0$, the austenite (reverse) phase transformation does not proceed, and thus, the phase transformation (shear) strain increment $d\gamma^{PT}$ is as follows;

$$d\gamma^{PT} = 0. \tag{2.13}$$

The stress-strain relation explained above can be summarized in the following form;

$$d\gamma^{PT} =< dF_A >< \gamma^{PT} > (d\tau - \beta dT)/H, \tag{2.14}$$

where $< \gamma^{PT} >$ is used to take into account that the reverse transformation stops when the existing phase transformation strain γ^{PT} is included completely by the reverse transformation.

3. Thermo-mechanical model of crystal grain component

The deformation property (stress-strain-temperature relation) of crystal grain component with the phase transformation systems described in the previous section can be formulated in the following manner.

The number of phase transformation systems in the crystal grain is assumed to be M (for example, $M = 24$ for the martensite phase transformation of Cu-based SMA used in authors' experiments). When the single crystal grain is in uniform stress state $\sigma_{ij}(i, j = 1, 2, 3)$, the shear stress $\tau(m)$ resolved on the m-th

$(m = 1, 2, .., M)$ phase transformation system can be obtained by the following equation:

$$\tau(m) = \sum_{i,j=1}^{3} \alpha_{(m)ij}\sigma_{ij}. \tag{3.1}$$

The coefficient $\alpha_{(m)ij}$ in (3.1) is the so-called generalized Schmid factor defined as follows:

$$\alpha_{(m)ij} = \left[s_{(m)i}n_{(m)j} + s_{(m)j}n_{(m)i}\right]/2, \tag{3.2}$$

where $s_{(m)i}$ and $n_{(m)i}(i = 1, 2, 3)$ are the unit vector along the shear direction and the unit vector normal to the transformation plane of the m-th phase transformation system, respectively. By using the obtained resolved shear stress $\tau_{(m)}$, the shear strain increment $d\gamma^{\mathrm{PT}}_{(m)}$ of the m-th phase transformation system can be estimated by (2.7) and (2.14) when only the m-th system becomes active. When some systems become active simultaneously in the crystal grain component, the corrections are necessary in order to incorporate the interactions among the phase transformation systems as described below.

2. The critical shear stresses $\tau_{\mathrm{M}(m)}$ and $\tau_{\mathrm{A}(m)}$ for the m-th phase transformation system are affected by a different active transformation system: interactions among the phase transformation systems in a grain. If the isotropic hardening rule is employed for simplicity, the $\tau_{\mathrm{M}(m)}$ and $\tau_{\mathrm{A}(m)}$ are modified as follows:

$$\tau_{\mathrm{M}(m)}(\gamma^{\mathrm{PT}}, T) = \tau_{\mathrm{OMS}} + \beta(T - T_0) + H\sum_{p=1}^{\mathrm{M}} \gamma^{\mathrm{PT}}(p), \tag{3.3}$$

$$\tau_{\mathrm{A}(m)}(\gamma^{\mathrm{PT}}, T) = \tau_{\mathrm{OAF}} + \beta(T - T_0) + H\sum_{p=1}^{\mathrm{M}} \gamma^{\mathrm{PT}}(p). \tag{3.4}$$

2. The phase transformation can not proceed any more after the phase transformation covers the whole area of the grain component. That is, the following equation in the volume fraction $\xi_{(m)}$ of the m-th $(m = 1.2, .., M)$ phase transformation system has to be considered:

$$\sum_{m=1}^{\mathrm{M}} \xi_{(m)} \leq 1. \tag{3.5}$$

By considering the relation $\xi_{(m)} = \gamma^{\mathrm{PT}}_{(m)}/\gamma^{\mathrm{PT}}_{\max}$, the phase transformation stops when the following equation is satisfied:

$$\sum_{m=1}^{\mathrm{M}} \gamma^{\mathrm{PT}}_{(m)} = \gamma^{\mathrm{PT}}_{\max}. \tag{3.6}$$

By incorporating the above two corrections, the relation between the increment of resolved shear stress $d\tau_{(m)}$ and the increment of phase transformation shear strain $d\gamma^{\mathrm{PT}}_{(m)}$ can be obtained as follows:

$$d\gamma^{\mathrm{PT}}_{(m)} = \left\langle dF_{X(m)} \right\rangle \left\langle \gamma^{\mathrm{PT}}_{\max} - \sum_{p=1}^{\mathrm{M}} \gamma^{\mathrm{PT}}_{(p)} \right\rangle G\left(\gamma^{\mathrm{PT}}_{(m)}\right) \cdot \left(d\tau_{(m)} - \beta dT\right) \Big/ H. \tag{3.7}$$

In this equation,

$$F_{X(m)} = F_{\mathrm{M}(m)}, \quad G\left(\gamma^{\mathrm{PT}}_{(m)}\right) = 1, \quad \text{when } F_{\mathrm{M}(m)} = 0, \tag{3.8}_1$$

$$F_{X(m)} = F\mathrm{A}(m), \quad G\left(\gamma^{\mathrm{PT}}_{(m)}\right) = \left\langle \gamma^{\mathrm{PT}}_{(m)} \right\rangle, \quad \text{when } F_{\mathrm{A}(m)} = 0, \tag{3.8}_2$$

$$F_{X(m)} = 0, \quad G\left(\gamma^{\mathrm{PT}}_{(m)}\right) = 1, \quad \text{when } F_{\mathrm{M}(m)} \neq 0, \quad F_{\mathrm{A}(m)} \neq 0, \tag{3.8}_3$$

where

$$F_{\mathrm{M}(m)} = \tau_{(m)} - \left[\tau_{0\mathrm{MS}} + H \sum_{p=1}^{\mathrm{M}} \gamma^{\mathrm{PT}}_{(p)} + \beta(T - T_0) \right], \tag{3.8}_4$$

$$-F_{\mathrm{A}(m)} = \tau_{(m)} - \left[\tau_{0\mathrm{AF}} + H \sum_{p=1}^{\mathrm{M}} \gamma^{\mathrm{PT}}_{(p)} + \beta(T - T_0) \right]. \tag{3.8}_5$$

On the other hand, the phase transformation (deviatoric) strain increment de^{PT}_{ij} of the crystal grain component can be obtained as follows:

$$de^{\mathrm{PT}}_{ij} = \sum_{m=1}^{\mathrm{M}} \alpha_{(m)ij} d\gamma^{\mathrm{PT}}_{(m)}. \tag{3.9}$$

Therefore, if (3.7) is employed in (3.9),

$$de^{\mathrm{PT}}_{ij} = \sum_{m=1}^{\mathrm{M}} \alpha_{(m)ij} \left\langle dF_{X(m)} \right\rangle \left\langle \gamma^{\mathrm{PT}}_{\max} - \sum_{p=1}^{\mathrm{M}} \gamma^{\mathrm{PT}}_{(p)} \right\rangle \cdot G\left(\gamma^{\mathrm{PT}}_{(m)}\right) \left(d\tau_{(m)} - \beta dT\right) \Big/ H. \tag{3.10}$$

By considering the incremental form of (3.1),

$$d\tau_{(m)} = \sum_{i,j=1}^{3} \alpha_{(m)ij} d\sigma_{ij}, \tag{3.11}$$

the relations among the increment of phase transformation strain de_{ij}^{PT}, the increment of stress $d\sigma_{ij}$, and the increment of temperature dT for the crystal grain component can be obtained in the following form.

$$(3.12)_1 \qquad de_{ij}^{\mathrm{PT}} = \sum_{m=1}^{\mathrm{M}} \alpha_{(m)ij} \left\langle dF_{X(m)} \right\rangle \left\langle \gamma_{\max}^{\mathrm{PT}} - \sum_{p=1}^{\mathrm{M}} \gamma_{(p)}^{\mathrm{PT}} \right\rangle \cdot G\left(\gamma_{(m)}^{\mathrm{PT}}\right) \sum_{k,l}^{3} \alpha_{(m)kl} d\sigma_{kl} - \beta dT \Big) \Big/ H,$$

$$(3.12)_2 \qquad d\gamma_{(m)}^{\mathrm{PT}} = \left\langle dF_{X(m)} \right\rangle \left\langle \gamma_{\max}^{\mathrm{PT}} - \sum_{p=1}^{\mathrm{M}} \gamma_{(p)}^{\mathrm{PT}} \right\rangle G\left(\gamma_{(m)}^{\mathrm{PT}}\right) \cdot \left(\sum_{i,j=1}^{3} \alpha_{(m)ij} d\sigma_{ij} - \beta dT \right) \Big/ H,$$

with the conditions:

$$(3.12)_3 \qquad F_{X(m)} = F_{\mathrm{M}(m)},\ G\left(\gamma_{(m)}^{\mathrm{PT}}\right) = 1, \quad \text{when } F_{\mathrm{M}(m)} = 0,$$

$$(3.12)_4 \qquad F_{X(m)} = F_{\mathrm{A}(m)},\ G\left(\gamma_{(m)}^{\mathrm{PT}}\right) = \left\langle \gamma_{(m)}^{\mathrm{PT}} \right\rangle, \quad \text{when } F_{\mathrm{A}(m)} = 0,$$

$$(3.12)_5 \qquad F_{X(m)} = 0,\ G\left(\gamma_{(m)}^{\mathrm{PT}}\right) = 1, \quad \text{when } F_{\mathrm{M}(m)} \neq 0,\ F_{\mathrm{A}(m)} \neq 0,$$

where

$$(3.12)_6 \qquad F_{\mathrm{M}(m)} = \tau_{(m)} - \left[\tau_{\mathrm{OM}} + H \sum_{p=1}^{\mathrm{M}} \gamma_{(p)}^{\mathrm{PT}} + \beta(T - T_0) \right],$$

$$(3.12)_7 \qquad -F_{\mathrm{A}(m)} = \tau_{(m)} - \left[\tau_{\mathrm{OM}} + H \sum_{p=1}^{\mathrm{M}} \gamma_{(p)}^{\mathrm{PT}} + \beta(T - T_0) \right],$$

$$(3.12)_8 \qquad \tau_{(m)} = \sum_{i,j=1}^{3} \alpha_{(m)ij} \sigma_{ij}.$$

As it can be found from the set of Eq. $(3.12)_{1-7}$, the obtained stress-strain-temperature relations are of a form of the theory whose internal variables are

the phase transformation strain $\gamma_{(m)}^{\mathrm{PT}}(m = 1, 2..., M)$. When we recall $M = 24$ for the martensite phase transformation and the corresponding reverse phase transformation, the deformation of a single crystal grain component is found to be controlled by 24 internal variables.

The increment of total strain $d\varepsilon_{ij}$ of the crystal grain component is as follows:

$$d\varepsilon_{ij} = d\varepsilon_{ij}^{e} + d\varepsilon_{ij}^{\mathrm{PT}} + d\varepsilon_{ij}^{\mathrm{T}}, \tag{3.13}$$

where $d\varepsilon_{ij}^{e}$, $d\varepsilon_{ij}^{\mathrm{PT}}$ and $d\varepsilon_{ij}^{\mathrm{T}}$ are the elastic part, phase transformation part, and thermal part of (total) strain increment $d\varepsilon_{ij}$, respectively. The elastic and thermal parts can be described as follows, when the material is assumed to be elastically and thermally isotropic,

$$d\varepsilon_{ij}^{e} = ds_{ij}/2G + \delta_{ij}\sigma/3K, \tag{3.14}$$

$$d\varepsilon_{ij}^{\tau} = \beta\delta_{ij}dT, \tag{3.15}$$

where δ_{ij} is the Kronecker delta, s_{ij} and σ are the deviatoric and volumetric parts of stress tensor σ_{ij}, respectively, G is the shear modulus, K is the bulk modulus, β is the coefficient of thermal expansion.

The conclusion of this section is that the stress-temperature relation of the grain component is given by a set of Eqs. $(3.12)_{1-7}$, (3.13) – (3.15) whose form is of the internal variable type.

4. Thermo-mechanical model of the polycrystal

When the stress-strain-temperature relation of a polycrystal is derived on the basis of stress-strain-temperature relation of its crystal grain component, the interactions among grain components have to be reconsidered. That is, each grain component has its own stress and strain depending on its own orientation in the polycrystal because each grain has the anisotropy related with the phase transformation system: thus the complicated interactions among grains appear in order to satisfy the compatibility condition of strain as well as the equilibrium condition of stress in the polycrystal. Thus the non-uniform stress and strain distributions appear even if the applied load is quite simple, for example, the uniaxial tension of a solid bar. The effect of non-uniform strain and stress distributions on the mechanical properties of polycrystalline materials are very important, especially when the strain or stress path is complex (e.g., non-proportional stress/strain history including the arbitrary change of temperature). This kind of interaction effect would be even more significant in the case of SMA than the polycrystalline metallic materials whose deformation mechanism is the dislocation slip. For example, as described in Sec. 2, the phase transformation can occur by the change

of temperature without any stress, but the significant deformation can not be observed in this case, because the produced phase transformation shear strain cancel each other. On the other hand, if the material is in some state of stress, only the preferable phase transformation system becomes active, and significant phase transformation strain can be observed even if the stress is rather small (due to the temperature effect). That is, the produced internal (residual) stress may have a significant effect on the macro-deformation of polycrystalline materials. This effect of internal or residual stress is quite interesting for the design of two-way shape memory properties of SMA, and thus the effect of residual stress or internal stress are quite interesting from the engineering application as well as the micromechanic points of view. Also, the internal stress may have an important role on the path dependent behavior when the polycrystalline material is subjected to a complex loading path. This is one of the main reasons why the meso-mechanical technique [33] was employed for the derivation of constitutive equations in this research work.

The above mentioned interaction among grain can be taken into account by using the well-developed mechanics of inhomogeneous solids. The typical models proposed on the basis of inhomogeneous solid mechanics are the KBM model [43, 44] (self-consistent model) and eigen-strain model [45, 46]. Both of them are based on the inclusion theory developed by ESHELBY [42]. According to the inclusion theory, the stress and strain distributions in the inclusions are uniform and have a quite simple linear relation with the applied load, when the spherical or ellipsoidal anisotropic inclusion is embedded in an isotropic elastic matrix. Therefore, the stress and strain distributions are uniform in the inclusions, and thus, the complicated stress and strain distributions around the grain boundaries in the case of a polycrystal can not be incorporated directly. There exists no convenient (simple) model which can incorporate the distributions of stress and strain in each grain component. This kind of effect has been investigated by using the finite element analyses. However, it is very difficult to incorporate this effect in the compact constitutive equations. Moreover, this grain boundary effect has been investigated by using the electron microscopy as well as the computer analysis (e.g., FEM analysis, molecular dynamic analysis, etc.). However, so many unknown problems are still left for futher consideration.

Among two convenient and simple theories of inhomogeneous solid mechanics metioned above, the eigen-strain theory is rather effective, e.g., in the deformation course of materials reinforced by dispersed particles, and on the other hand, the KBW model is effective in the case of, for example, the polycrystal composed of many grain components where the characteristics of grain component are as follows:

1. the grain component has its orientation described by the generalized Schmid factor,

2. the grain component has a limit of transformability described by Eq. (3.5), and thus the size, shape and location of the grain in the polycrystal are not considered in the model, though the volume fraction is taken into account. In this case, the following equation can be obtained for SMA with the phase transformation mechanism.

$$s_{ij}^{(k)} - S_{ij} = \alpha G \left(e_{ij}^{\mathrm{PT}(k)} - E_{ij}^{\mathrm{PT}} \right), \tag{4.1}$$

where $s_{ij}^{(k)}$ is the deviatoric stress component of the k-th grain component embeded in the polycrystal, S_{ij} is the averaged (macroscopic) deviatoric stress $\left[S_{ij} = \text{average} \left(s_{ij}^{(k)} \right) \right]$, $e_{ij}^{\mathrm{PT}(k)}$ is the (deviatoric) phase transformation strain components of the k-th grain, E_{ij}^{PT} is the averaged (macroscopic) phase transformation $\left[E_{ij}^{\mathrm{PT}} = \text{average} \left(e_{ij}^{(k)} \right) \right]$, G is the averaged shear modulus of polycrystal. The coefficient α in (4.1) is still being discussed in the case of inelastic matrix and it is not the material constant, in general. However, the coefficient α is assumed to be constant in the engineering applications, for simplicity. The proposed values are as follows:

$\alpha = 0$ (for stress constant model, the so-called Maxwell model),
$\alpha = 0.2$ (for modified KBW model by Berveiller-Zaoui [47]),
$\alpha = 1.0$ (for KBW original model [43]),
$\alpha = 2.0$ (for strain constant model, the so-called Voigt model),
$\alpha = \infty$ (for inelastic strain constant model; Taylor model),

In the final stage of this paper, one simple example of consitutive equations of SMA incorporating the interaction among grains in the polycrystal is demonstrated in a closed form. Here the stress constant model ($\alpha = 0$) is selected as an example. That is,

$$\sigma_{ij}^{(k)} = \Sigma_{ij} = S_{ij} + \delta_{ij}\Sigma. \tag{4.2}$$

where S_{ij} and Σ are the deviatoric and volumetric parts of stress Σ_{ij}, respectively, and δ_{ij} is the Kroncker delta. In this case, the total strain increment $d\varepsilon_{ij}^{(k)}$ of the k-th grain component in the polycrystal model can be described as follows:

$$\begin{aligned} d\varepsilon_{ij}^{(k)} &= d\varepsilon_{ij}^{e(k)} + d\varepsilon_{ij}^{\mathrm{PT}(k)} + d\varepsilon_{ij}^{\mathrm{T}(k)} \\ &= ds_{ij}^{(k)}/2G + \delta_{ij} d\sigma^{(k)}/3K + \beta \delta_{ij} dT + d\varepsilon_{ij}^{\mathrm{PT}(k)} \\ &= dS_{ij}/2G + \delta_{ij} d\Sigma/3K + \beta \delta_{ij} dT + \sum_{m=1}^{\mathrm{M}} \left[\alpha_{(m)ij}^{(k)} \left\langle dF_{X(m)}^{(k)} \right\rangle \right. \end{aligned} \tag{4.3}$$

$$\cdot \left\langle \gamma_{\max}^{\mathrm{PT}} - \sum_{p=1}^{\mathrm{M}} \gamma_{(p)}^{\mathrm{PT}(k)} \right\rangle G^{(k)} \left(\gamma_{(m)}^{\mathrm{PT}}\right) \cdot \left(\sum_{k,l=1}^{3} \alpha_{(m)kl}^{(k)} dS_{kl} - \beta dT \right) \Big/ H \Bigg] \tag{4.3}$$

[cont.]

The strain increment dE_{ij} of the polycrystal model can be expressed by the following equation:

$$dE_{ij} = \sum_{k=1}^{\mathrm{K}} V^{(k)} \Bigg\{ dS_{ij}/2G + \delta_{ij} d\sum /3K + \beta \delta_{ij} dT + \sum_{m=1}^{\mathrm{M}} \Bigg[\alpha_{(m)ij}^{(k)} \left\langle dF_{X(m)}^{(k)} \right\rangle \cdot \left\langle \gamma_{\max}^{\mathrm{PT}} - \sum_{p=1}^{\mathrm{M}} \gamma_{(p)}^{\mathrm{PT}(k)} \right\rangle G^{(k)} \left(\gamma_{(m)}^{\mathrm{PT}}\right) \cdot \left(\sum_{k,l=1}^{3} \alpha_{(m)kl}^{(k)} dS_{kl} - \beta dT \right) \Big/ H \Bigg] \Bigg\} \tag{4.4}$$

where $V^{(k)}$ is the volume fraction of the k-th grain component. Therefore,

$$dE_{ij} = \sum_{k=1}^{\mathrm{K}} V^{(k)} \Bigg\{ \sum_{m=1}^{\mathrm{M}} \Bigg[\alpha_{(m)ij}^{(k)} \left\langle dF_{X(m)}^{(k)} \right\rangle \cdot \left\langle \gamma_{\max}^{\mathrm{PT}} - \sum_{p=1}^{\mathrm{M}} \gamma_{(p)}^{\mathrm{PT}(k)} \right\rangle G^{(k)} \left(\gamma_{(m)}^{\mathrm{PT}}\right) \cdot \left(\sum_{k,l=1}^{3} \alpha_{(m)kl}^{(k)} dS_{kl} - \beta dT \right) \Big/ H \Bigg] \Bigg\} + dS_{ij}/2G + \delta_{ij} d\sum /3K + \beta \delta_{ij} dT, \tag{4.5}$$

where

$$\gamma_{(p)}^{\mathrm{PT}(k)} = \int d\gamma_{(p)}^{\mathrm{PT}(k)}, \tag{4.6}$$

and

$$\begin{aligned} F_{X(m)}^{(k)} &= F_{\mathrm{M}(m)}^{(k)}, \quad \text{if } F_{\mathrm{M}(m)}^{(k)} = 0, \\ F_{X(m)}^{(k)} &= F_{\mathrm{A}(m)}^{(k)} = 0, \quad \text{if } F_{\mathrm{A}(m)}^{(k)} = 0, \end{aligned} \tag{4.7}$$

where

$$\begin{aligned} F_{\mathrm{M}(m)}^{(k)} &= \tau_{(m)}^{(k)} - [\tau_{\mathrm{OM}} + H\gamma_{(m)}^{\mathrm{PT}(k)} + \beta(T - T_0)], \\ -F_{\mathrm{A}(m)}^{(k)} &= \tau_{(m)}^{(k)} - [\tau_{\mathrm{OA}} + H\gamma_{(m)}^{\mathrm{PT}(k)} + \beta(T - T_0)]. \end{aligned} \tag{4.8}$$

A set of Eqs. (4.4) – (4.8) is an example of a set of constitutive equations constructed on the basis of a mesoscopic approach. In this approach, the simplest models are selected for each structural levels. It is possible to use more complicated but elegant and more accurate models for all structures and interactions between them. When we select the model of a structure, it is very important to consider the balance of reliability/accuracy among the selected models as well as the computer capacity according to the engineering needs.

Finally, it should be noted that the proposed constitutive equations can be described symbolically in a form of internal variable theory, where internal variables are $\gamma_{(m)}^{\mathrm{PT}(k)}$, in a following manner.

$$
\begin{aligned}
dE_{ij} &= \sum_{k,l=1}^{3} F_{ijkl}\left(S_{pq}, \Sigma, T : \gamma_{(m)}^{\mathrm{PT}(n)}\right) dS_{kl} \\
&\quad + F_{ij}\left(S_{ij}, \Sigma, T : \gamma_{(m)}^{\mathrm{PT}(n)}\right) d\Sigma + F_{ij}^{\mathrm{T}}(S_{pq}, \Sigma, T : \gamma_{(m)}^{\mathrm{PT}(k)}) dT, \\
d\gamma_{(m)}^{\mathrm{PT}(k)} &= \sum_{p,q=1}^{3} H_{(m)pq}^{(k)}(S_{ij}, \Sigma, T : \gamma_{(m)}^{\mathrm{PT}(k)}) dS_{pq} \\
&\quad + H_{(m)}{}^{(k)}\left(S_{ij}, \Sigma, T : \gamma_{(m)}^{\mathrm{PT}\,(k)}\right) d\Sigma + H_{(m)}^{\mathrm{T}}{}^{(k)}\left(S_{ij}, \Sigma, T : \gamma_{(m)}^{\mathrm{PT}\,(k)}\right) dT.
\end{aligned}
\tag{4.9}
$$

5. Concluding remarks

The thermo-mechanical models selected for each structural level are quite simple and can be treated without any computer. For example, the inhomogeneous solid mechanical model was developed long ago, and these models were capable of solving so many important engineering problems without the aid of computer.

In our opinion, even if the macroscopic behavior is quite complex depending on the history of thermo-mechanical loading, this complicated behavior can be reproduced by a combination of some simple mechanisms corresponding to each structural level. That is, if the materials are considered to be a kind of thermo-mechanical system composed of simple mechanical components (materials), the complicated behavior can be reproduced.

References

1. FUNAKUBO, *Shape memory alloy* (in Japanese), Sangyo-tosho, 1984.
2. K. TANAKA, H. TOBUSHI, S. MIYZAKI, Kikai-no-kenkyu (in Japanese), **46**, 3, 1–7, 1994.

3. H. TOBUSHI, Transaction of Japan Society Plastic Forming (in Japanese), **34**, 403, 910–916, 1994.
4. H. HORIKAWA, K. OHTSUKA, New Materials (in Japanese), **5**, 7, 68–73, 1994.
5. S. MIYAZAKI *et all.*, Proc. of Int. Symp. on Microsystem, Intelligent Materials and Robots, (in Japanese), Sendai, 235–238, 1995.
6. K. OHTSUKA, Materia (Transaction of Japan Society of Metals) (in Japanese), **37**, 2, 125–132, 1998.
7. S. MIYAZAKI, Materia (Transaction of Japan Society of Metals) (in Japanese), **35**, 2, 179–184, 1996.
8. M. MATSUMOTO *et. al.*, Proc. of Japan-France Seminar on Intelligent Materials and Structure, 247–250, Sendai 1997.
9. S. TAKABAYASH *et. al.*, Materials Science Research International, **2**, 3, 148–152, 1994.
10. F. NISHIMURA *et. al.*, Materials Sciences Research International, **3**, 1, 23–30, 1997.
11. F. NISHIMURA, N. WATANABE and K. TANAKA, Transactions of JSMS, **46**, 8, 900–905, 1997.
12. P.H. LIN *et al.*, Transaction of ISME (series A), **60**, 596, 126–133, 1994.
13. P.H. LIN *et al.*, Arch. Mech., **42**, 2, 281–293, 1995.
14. K. TANAKA, Res Mechanica, **18**, 251–263, 1986.
15. K. TANAKA *et al.*, Materials Sciences Research International, **1**, 1, 23–30, 1995.
16. B. RANIECKI and C. LEXCELLENT, Eur. J. Mech. A/Solids, **13**, 1, 21–50, 1994.
17. B. RANIECKI and O. BRUHNS, Arch. Mech., **43**, 1, 3, 343–376, 1991.
18. M. BERVEILLER, E. PATOOR, M. BUISSON, Journal de Physique IV, colloque C4, suplement au Journal de Physique III, **1**, C4/383–C4/396, 1991.
19. D. ENTEMEYER, E. PATOOR, A. EBERHARDT and M. BERVEILLER, Journal de Physique IV, Colloque C8, Suplement at Journal de Physique III, **5**, C8/233–C8/238, 1995.
20. E. PATOOR, D. ENTEMEYER, A. EBERHARDT and M. BERVEILLER, Program and Abstract of IUTAM Symposium: Microstructural Aspect of Thermoplasticity, 70–71, Ruhr Univ., Bochum, Germany 1997.
21. W-Y. YIN, Q-P. SUN and K-C. HWANG, Proc. of AEPA'97, 9–14, Hiroshima, Japan 1997.
22. C. LEXCELLENT and G. BOURBON, Proc. of AEPA'97, 653–658, Hiroshima, Japan 1997.
23. Z. LIU and G.J. WENG, Proceedings of Plasticity'97 [Ed.] A.S. Khan, 165–166, Jeanu, Alaska 1997.
24. M. TAYA *et al.*, Proc. of the Japan-France Seminar on Intelligent Materials and Structures, 199–222, Sendai, Japan 1997.
25. M. KAWAI *et al.*, Proc. of the Japan-France Seminar on Intelligent Materials and Structures, 223–246, Sendai, Japan 1997.
26. Y. FURUYA and M. TAYA, Transaction of JSM, (in Japanese), **60**, 12, 1163–1172, 1996.
27. M. TOKUDA and P. SITTNER, Kikai-no-kenkyu (in Japanese) **49**, 4, 9–13, 1997.
28. P. SITTNER and M. TOKUDA, Transaction of JSMS, (in Japanese), **44**, 5, 597–601, 1995.
29. M. TOKUDA and P. SITTNER, Transaction of JSMS (in Japanese), **45**, 5, 527–536, 1996.
30. M. TOKUDA, P. SITTNER, M. TAKAKURA and YE MEN, Material Science Research International, **1**, 4, 260–265, 1995.

31. P. SITTNER, Y. HARA, M. TOKUDA, Metallurgical and Materials Transaction, **26A**, 2932–2935, 1995.

32. M. TOKUDA and P. SITTNER, Kikai-no-kenkiyu (in Japanese), **49**, 9, 29–34, 1997.

33. M. TOKUDA, Ouyou-suuri (in Japanese), **5**, 4, 60–72, 1995.

34. K. TANAKA, H. TOBUSHI and S. MIYAZAKI, *Mechanical properties of shape memory alloy*, Youkendo 1993.

35. I. MÜLLER and H. XU, Acta Metallurgica et Materialia, **39**, 3, 263–271, 1991.

36. I. MÜLLER and G. ZAK, Journal de Physique IV, Colloque C8, supplement au Journal de Physique III, **5**, C8/197–C8/201, 1995.

37. I. MÜLLER, Continuum Mech. Thermodyn., **1**, 125–142, 1989.

38. B. BUNDARA, Materials Science Research International, **4**, 4, 275–280, 1998.

39. B. BUNDARA, Proceedings of IMMM'97, 373–380, Mie University Press 1997.

40. B. BUNDARA, M. TOKUDA and M. YE, Research Reports of the Faculty of Engineering, Mie University, **23**, 13–22, 1998.

41. K. TANAKA, F. NISHIMURA and H. TOBUSHI, Journal of Intelligent Material System and Structure, **5**, 487–493, 1994.

42. J.D. ESHELBY, Proc. R. Soc. Lond., Ser. A **241**, 376, 1957.

43. E. KRONER, Acta Metall., **9**, 155, (1961.

44. J.W. HUCHINSON, J. Mech. Phys. Solids, **12**, 11, 1964.

45. T. MURA, *Micromechanics of defects in solids*, Martinus Nijhoff Publishers, 1982.

46. M. TAYA, Materia (Transaction of Japan Society of Metal) (in Japanese), **33**, 3, 279–289, 1994.

47. M. BERVEILLER and A. ZAOUI, J. Mech. Phys. Solids, **26**, 325, 1979.

Received May 4, 1999; revised version October 8, 1999.

Arch. Mech., **51**, 6, pp. 865–884, Warszawa, 1999

Estimation and prediction of local strain-induced martensitic transformation

Y. TOMITA ([1]) and Y. SHIBUTANI ([2])

([1]) *Graduate School of Science and Technology, Kobe University, Kobe, Japan*

([2]) *Graduate School of Engineering, Osaka University, Osaka, Japan*

UNIAXIAL TENSION TESTS were performed under constant strain rate and different environmental temperatures from 77 K to 373 K to identify the concrete form of the constitutive equation for TRIP steels. Subsequently, a new experimental procedure based on microhardness testing which provides local information regarding the transformation has been proposed. To elucidate the dependence of the martensitic transformation on the nonuniform deformation and consequently, to validate the proposed constitutive equation, the volume fraction of the martensite phase is predicted and measured by using computational simulation and experimental procedures, respectively, for the uniaxial tension of the bars with a ringed notch. Good correspondence between the local volume fraction of the martensite phase around the notch obtained by both methods verifies the validity of the proposed constitutive equation for the nonuniform deformation behavior. It has been further clarified that the development of the martensitic phase may relieve the strain localization around the notch tip and subsequently, will increase the energy absorption which is accompanied by an improvement in the toughness.

1. Introduction

MARTENSITIC TRANSFORMATION of transformation-induced plasticity (TRIP) steel is observed during large deformation in the low-temperature range [1]. Owing to the duplex phase of austenite and martensite, the TRIP steel functionally improves the ductility and fracture toughness. However, strain and temperature dependence on the deformation behavior and microscopic transformation mechanism are quite complicated and it may be very difficult to determine a method for the improvement of the mechanical properties merely by experiments. To date, the constitutive equation accounting for the temperature and strain effect on the martensitic transformation [2] and its generalization to account for the stress state [3], strain rate sensitivity [4], and the stress state for stacking fault energy [5] have

been proposed and computational simulations have been conducted to exemplify the transformation behavior and the mechanisms for improving the mechanical properties through the forming processes. For the transformation behavior which is very sensitive to the orientation of the crystalline direction, however, the validity and limitation of the applicability of the constitutive equation should be examined.

With regard to the experimental estimation of the volume fraction of martensitc phase, different methods have been employed so far. Among them are X-ray diffraction [6], magnetic [7], density [8] and electrical resistivity [9] methods which are mainly concerned with the estimation of the average volume fraction of the martensite phase over a relatively large area or volume. As indicated by OLSON and COHEN [2], the strain induced transformation is closely related to the local nonuniform deformation; therefore, development of the experimental procedure for the estimation of the local distribution of the martensite phase is indispensable.

In this study, SUS304 steel which is a typical TRIP steel, is employed as the material for the experiments. Through the precise tension tests conducted under the environmental temperature of 77 K to 373 K, the effect of transformation on macroscopic stress-strain relation is clarified. Then, using the magnetic method, the volume fraction of martensite is measured for the specimens at various strain levels, and the relation between the volume fraction of the martensitic phase and strain is established. With these results and the microhardness test, the master curve for volume fraction of martensite vs. microhardness is established for the measurement of the local distribution of martensitic phase. Subsequently, the master curve is used to estimate the local distribution of the martensite phase over the cross-section of the bar with ringed notch under tension with an environmental temperature of 77 K. The results are compared with those obtained by computational simulation and the validity and limitations of the computational simulation are discussed.

2. Uniaxial tension test

Figure 1 shows the equivalent stress-plastic strain relations of the SUS304 stainless steel specimen shown in the inset with chemical composition indicated in Table 1, deformed under average strain rate of 5×10^{-4}/s and environmental temperatures of 373 K, 303 K, 293 K, 273 K, 253 K, 233 K, 213 K, 193 K, 153 K, 113 K and 77 K. Water, ethanol cooled by liquid nitrogen and liquid nitrogen are respectively used as cooling media for the environmental temperatures of 373 K to 273 K, 253 K to 153 K and 77 K. Whereas, liquid nitrogen vapor was used to realize the environmental temperature of 113 K; therefore, the heat conduc-

tion conditions for the case of 113 K could be different from those of the other cases. The black circles in the figure indicate the load maximum points where the instability, in Considere's sense, takes place. After the load maximum point, the nonuniform deformation, i.e., necking, starts with a substantial decrease of the nominal stress. The stress-strain relation for 373 K which is higher than the Md temperature, indicates the stress-strain relation for austenite since the martensitic transformation may not occur. Due to the strengthening mechanism caused by the martensitic transformation, the onset of maximum load is remarkably delayed and as a result, substantial extendibility is realized. Although the temperature of the Ms point for the material is lower than that of liquid nitrogen, very rapid stiffening at the plastic straining is observed due to plastic strain-induced martensitic transformation.

Table 1. Chemical composition of type 304 austenitic stainless

	Stainless Steel (SUS304)									
Element	C	Si	Mn	P	S	Ni	Cr	Mo	N	Nb
wt %	0.076	0.45	1.18	0.028	0.023	8.19	18.22	0.06	0.0786	> 0.01

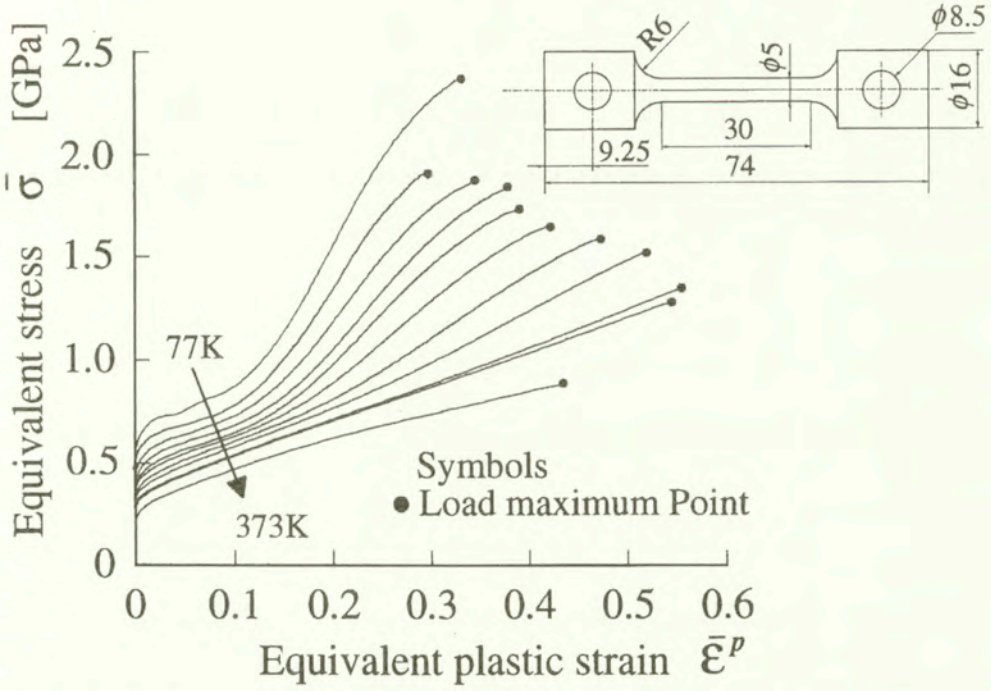

FIG. 1. Equivalent stress $\bar{\sigma}$-plastic strain $\bar{\varepsilon}^p$ relations for SUS304 stainless steel deformed with strain rate 5.0×10^{-4}/s under different environmental temperatures 77–373 K.

The mechanisms for the improvement of ductility can be clarified by investigating Considere's condition for the onset of instability [4]. Due to the strengthening effect of the martensitic transformation, the rate of work-hardening $d\sigma/d\varepsilon$ first increases to a maximum, then decreases due to the saturation of the martensitic transformation, and finally, the front of the curve joins the stress-strain curve. Although, in the low-temperature range, the increase in the work-hardening rate is considerable; the rapid saturation causes a high rate of decrease in work-hardening and a rise in the stress strain curve, which causes the onset of instability in the early stage of deformation. Consequently, to improve the ductility of the material due to martensitic transformation is not simply the increase of the final value of the volume fraction of martensitic phase but the process of martensitic transformation including the effects of strain rate and temperature, which should be accounted for in the design of forming processes. Further discussion on this topic was presented in a separate paper [10]. The slightly different feature observed in the stress-strain relation for 113 K could be attributed to the above mentioned different cooling condition with respect to the other cases.

3. Estimation of volume fraction of martensitic phase by means of microhardness test

The microhardness testing device employed for the present investigation is a dynamic ultramicrohardness testing device (Shimazu DUH-201). A specially designed automatic positioning device and Shimazu DUH-201 consist of an automatic multipoint measuring system which enables the estimation of the hardness distribution over the desired area. The experimental conditions such as holding time, indentation load and surface conditions have been investigated in an earlier work [11].

In order to establish the master curve for the volume fraction of martensitic phase f^m vs. vs microhardness H, circular chips with 0.5 mm thickness made from the uniformly deformed specimen with different plastic strains under liquid nitrogen are prepared. In this investigation, the magnetic permeability method was employed to estimate the magnetization-magnetic field relation [11]. Figure 2 shows the obtained magnetic permeability μ vs. equivalent plastic strain $\bar{\varepsilon}^p$ relation. The volume fraction of the martensite phase should be calculated based on the magnetic permeability for the specimen with 100% volume fraction of martensitic phase. However, since it is very difficult to obtain the specimen with 100% volume fraction of martensitic phase, saturation magnetization method [8] was utilized to estimate the true volume fraction of the martensite phase for the circular chips with 30% plastic strain. The saturation value of magnetization of the martensitic phase can be expressed by $\sigma^m = 214.5 - 3.12(C_r + 0.5N_i)$; C_r, N_i

indicate the weight percentage of individual chemical elements. The corresponding saturation value is $\sigma^m = 144.9$ [emu/g]. Therefore, with estimation value of 30% plastic strain by means of the magnetic permeability method $\sigma^{0.3} = 120$ [emu/g], we can estimate the volume fraction of martensitic phase at 30% plastic strain as $f^m_{0.3} = \sigma^{0.3}/\sigma^m = 0.828$, which will be used to estimate the volume fraction of martensitic phase versus equivalent plastic strain.

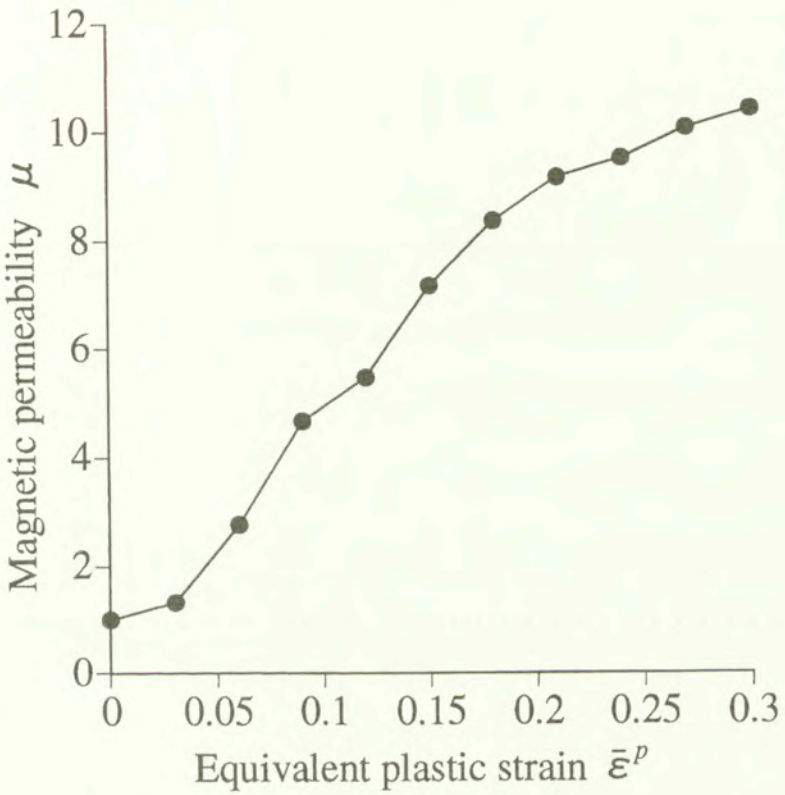

FIG. 2. Magnetic permeability μ vs. equivalent plastic strain $\bar{\varepsilon}^p$.

Thus, the obtained volume fraction of the martensitic phase-equivalent plastic strain is shown in Fig. 3, which exhibits the typical s-shaped curve seen in the volume fraction of martensitic phase vs. plastic strain. The same specimens employed for the above experiment are used to obtain the microhardness vs. equivalent plastic strain relation as shown in Fig. 4. In the figure, microhardness was estimated using three different indentation loads, 196, 490 and 1960 mN. Depending on the relative size of the indent with respect to microstructure of the material, the microhardness changes with the indentation loads. Therefore, in this investigation, depending on the employed indentation load, the corresponding relation will be used for the estimation of the local distribution of the volume

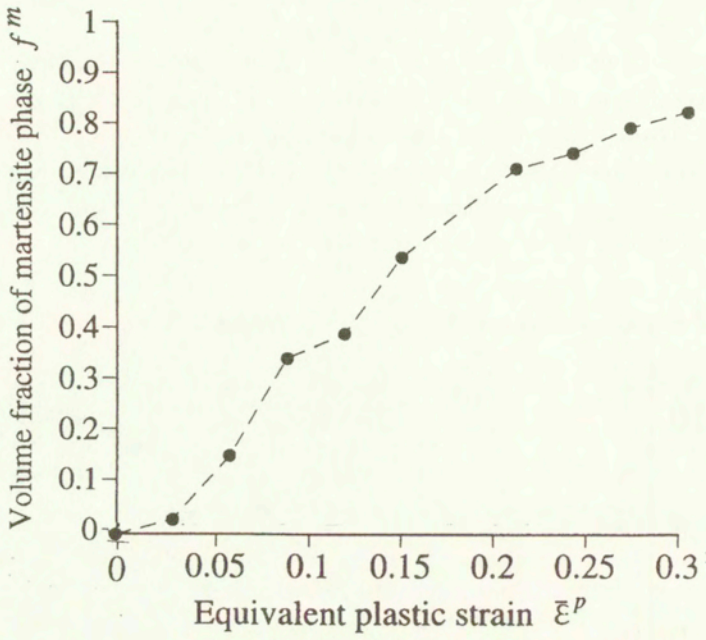

FIG. 3. Volume fraction of martensite phase f^m vs. equivalent plastic strain $\bar{\varepsilon}^p$ relations.

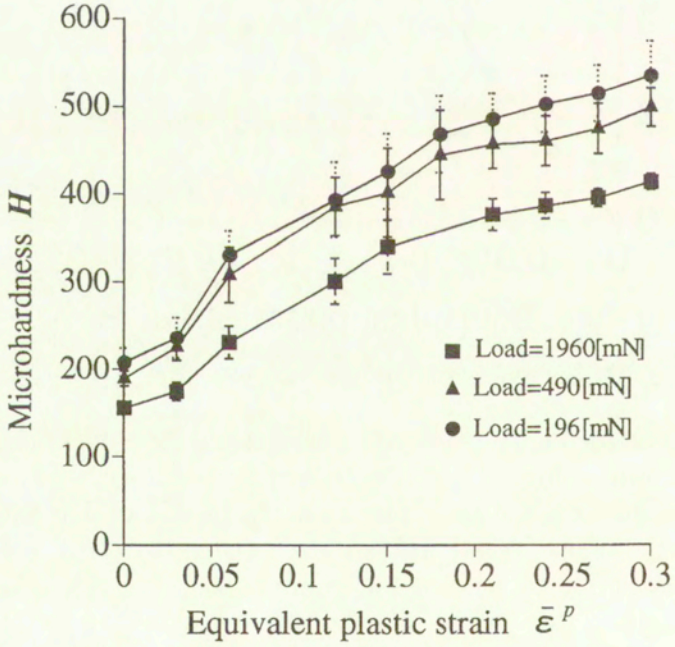

FIG. 4. Microhardness H vs. equivalent plastic strain $\bar{\varepsilon}^p$ relations for three different indentation loads.

fraction of martensitic phase. The master curves for volume fraction of martensitic phase vs. microhardness shown in Fig. 5 can be established by using the relations in Figs. 3 and 4. The corresponding master curve is finally expressed as

$$
\begin{aligned}
(3.1) \qquad f^m &= C_1 H^2 + C_2 H + C_3, \\
P &= 196 \text{ mN} : C_1 = 4.25 \times 10^{-6}, C_2 = 3.82 \times 10^{-4}, \; C_3 = 1.20 \times 10^{-1}, \\
P &= 490 \text{ mN} : C_1 = 5.83 \times 10^{-6}, C_2 = 1.09 \times 10^{-3}, \; C_3 = 1.90 \times 10^{-2}, \\
P &= 1960 \text{ mN} : C_1 = 5.62 \times 10^{-6}, C_2 = 1.47 \times 10^{-4}, \; C_3 = 1.59 \times 10^{-1}.
\end{aligned}
$$

Equation (3.1) will be fully employed for the estimation of local distribution of volume fraction of the martensitic phase.

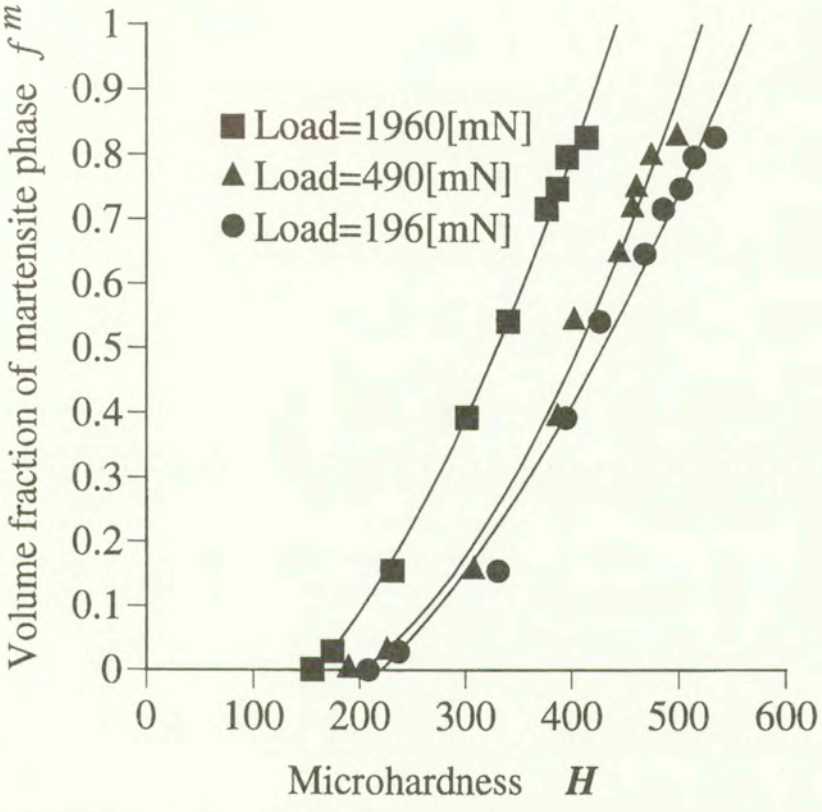

FIG. 5. Volume fraction of martensite phase f^m vs. microhardness H relation for three different indentation loads.

4. Constitutive equation of TRIP steels

For the self-completeness of the paper, a brief explanation of the constitutive equation utilized in this investigation is given. OLSON and COHEN [2] established

a fundamental model for strain-induced martensitic transformation kinetics which can express the temperature dependence of the transformation phenomena. This phenomenological model was constructed under the assumption that the transformation occurred at the intersection of the shear band in the austenite mother phase with a prescribed possibility. STRINGFELLOW *et al.* [3] generalized the Olson and Cohen model so as to include the stress state and the contribution of the martensite phase to the strength. TOMITA and IWAMOTO [4] modified the two models to include the experimental finding that the mode of the deformation behavior is controlled by the shear band mode as the strain rate increases [12]. The rate of increase of the volume fraction of the martensitic phase, $\dot{f}^m$, is given by

$$
\begin{aligned}
\dot{f}^m &= A(1-f^m)\dot{\bar{\varepsilon}}_a^{\,\mathrm{pslip}}, \\
A &= \alpha\beta n(f^{sb})^{n-1}(1-f^{sb}), \\
\dot{f}^{sb} &= \alpha(1-f^{sb})\dot{\bar{\varepsilon}}_a^{\,\mathrm{pslip}}, \\
\beta &= \frac{\eta}{\sqrt{2\pi}\sigma_g}\int_{-\infty}^{g}\exp\left\{-\frac{(g'-g_0)^2}{2\sigma_g^2}\right\}dg', \\
g &= -T+g_1\Sigma,
\end{aligned}
\tag{4.1}
$$

where $\dot{\bar{\varepsilon}}_a^{\,\mathrm{pslip}}$ is the equivalent strain rate of slip deformation in austenite, f^{sb} is the volume fraction of the shear band, β is the probability that an intersection forms a martensitic embryo [3, 4] and n and η are geometric constants. g is the driving force of transformation, g_0 is the mean value of g, g_1 is a constant and σ_g is the standard deviation. α is a parameter related to the stacking fault energy and is a function of temperature T [3], strain rate $\dot{\bar{\varepsilon}}_a^{\,\mathrm{pslip}}$ [4] and the stress triaxiality parameter $\Sigma = \sigma_{ii}/(3\bar{\sigma})$ [5] as

$$
\alpha = \left(\alpha_1 T^2 + \alpha_2 T + \alpha_3 - \alpha_4\Sigma\right)\left(\frac{\dot{\bar{\varepsilon}}_a^{\,\mathrm{pslip}}}{\dot{\varepsilon}_r}\right)^M, \tag{4.2}
$$

where M is the strain rate sensitivity exponent, $\alpha_1 - \alpha_4$ are material parameters and $\dot{\varepsilon}_r$ is the reference strain rate. Next, the plastic strain rate $\dot{\varepsilon}_{ij}^{p}$ is assumed to be the sum of the plastic strain rate $\dot{\varepsilon}_{ij}^{\,\mathrm{pslip}}$ induced by the slip deformation in austenite and martensite, and $\dot{\varepsilon}_{ij}^{\,\mathrm{ptrans}}$ induced by the transformation. Furthermore, the transformation plastic strain rate is split into a deviatoric part, $\dot{\varepsilon}_{ij}^{\,\mathrm{pshape}}$, related to the shape change, and a dilatational part, $\dot{\varepsilon}_{ij}^{\,\mathrm{pdilat}}$, expressing the volume change. Under the assumptions that the strain rate $\dot{\varepsilon}_{ij}^{\,\mathrm{pshape}}$ is considered to

be coaxial with deviatoric stress [4] and that $\dot{\varepsilon}_{ij}^{p\text{dilat}}$ can be expressed in terms of the volume change $\Delta\nu$, which has the value of $0.02 - 0.05$ for austenite steel, the plastic strain rate $\dot{\varepsilon}_{ij}^{p}$ can be expressed as

$$
\begin{aligned}
\dot{\varepsilon}_{ij}^{p} &= p_{ij}\dot{\bar{\varepsilon}}^{p} + s_{ij}\Delta\nu\dot{f}^{m}, \\
p_{ij} &= \frac{3\sigma'_{ij}}{2\overline{\sigma}}, \\
s_{ij} &= -p_{ij}\Sigma + \frac{\delta_{ij}}{3}, \\
\dot{\bar{\varepsilon}}^{p} &= \dot{\bar{\varepsilon}}^{p\text{slip}} + R\dot{f}^{m} + \Sigma\Delta\dot{f}^{m}, \\
R &= R_0 + R_1\left(\frac{\overline{\sigma}}{\sigma_a}\right),
\end{aligned}
\tag{4.3}
$$

where $\dot{\bar{\varepsilon}}^{p}$ is the work equivalent measure of the equivalent plastic strain-rate with respect to Mises-type equivalent stress $\overline{\sigma}$, and R is the parameter accounting for the magnitude of shape changes and depends on the stress. σ_a is the initial yield stress of austenite and R_0 and R_1 are constants. The constitutive equation for the stress rate can be established by introducing the plastic strain rate in Eq. (4.3) into the thermoelastic constitutive equation, as discussed by TOMITA and IWAMOTO [4].

Since strain-induced transformation is quite sensitive to temperature, the mechanical characteristics of the material induced by transformation are strongly affected by the temperature change caused by the irreversible work. Consequently, thermocoupled analysis [13] is unavoidable for the prediction of the deformation behavior of TRIP steel. The constitutive equation of a two-phase composite material of austenite including the volume fraction of martensitic phase f^m is established in a manner similar to that described by STRINGFELLOW *et al.* [3], applying Eshelby's theory [14]. The forward gradient method is introduced to improve the computational efficiency. The identification of the material parameters has been done based on the procedure described by STRINGFELLOW *et al.* [3], SHIMIZU [15] and IWAMOTO *et al.* [5]. The material and computational parameters employed in this investigation are shown in Appendix.

5. Estimation of distribution of volume fraction of martensitic phase

The proposed method is applied for the estimation of the distribution of the volume fraction of the martensite phase over the cross-section of the ringed-notched specimen subjected to uniaxial tension under an environmental tempe-

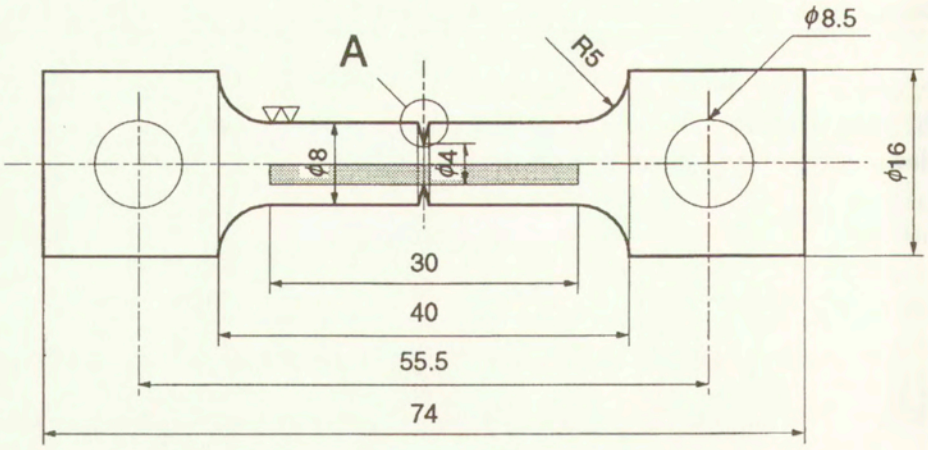

Specimen

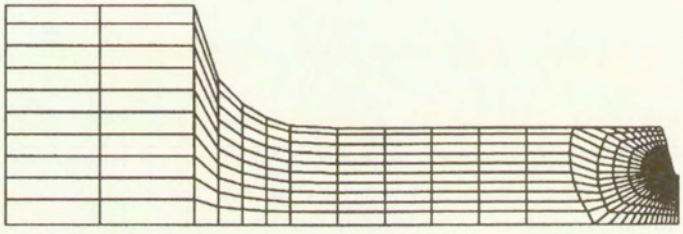

Computational Model

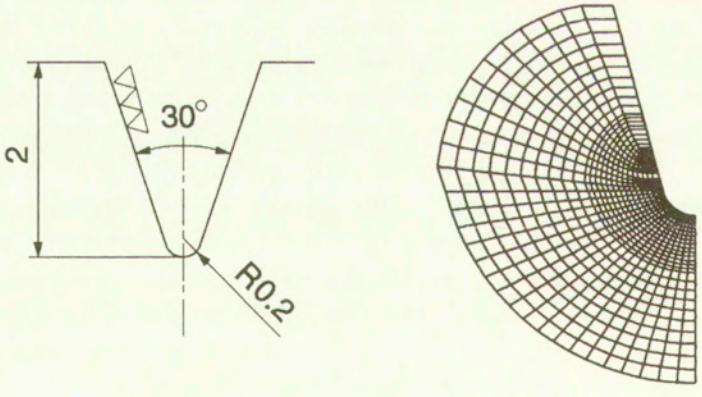

Magnification of A

FIG. 6. Specimen profile and computational model for finite element simulation.

rature of 77 K. The specimen profile and the dimensions are shown in Fig. 6. The average strain rate was set to be 5×10^{-5}/s and the loading was stopped when the end displacement reached 0.32 mm and 0.5 mm. After unloading, the specimens for the measurement of microhardness were prepared by wire cutting and electropolishing with sufficient care to avoid the formation of the surface layer. The automatic estimation of martensitic distribution over the cross-section near the notch tip has been done with three different indentation loads of 1960 mN, 490 mN and 196 mN. Figure 7 indicates the distribution of the volume fraction of the martensitic phase f^m along the radial direction x. The fluctuation of the volume fraction of the martensitic phase due to the nonuniform distribution of the martensite phase is observed. Its amplitude increases as the indentation load decreases which can be attributed to the averaging effect of the martensitic phase. Decrease of the indentation load which causes the decrease of the size of the indent may pick up the more localized distribution of the martensite phase.

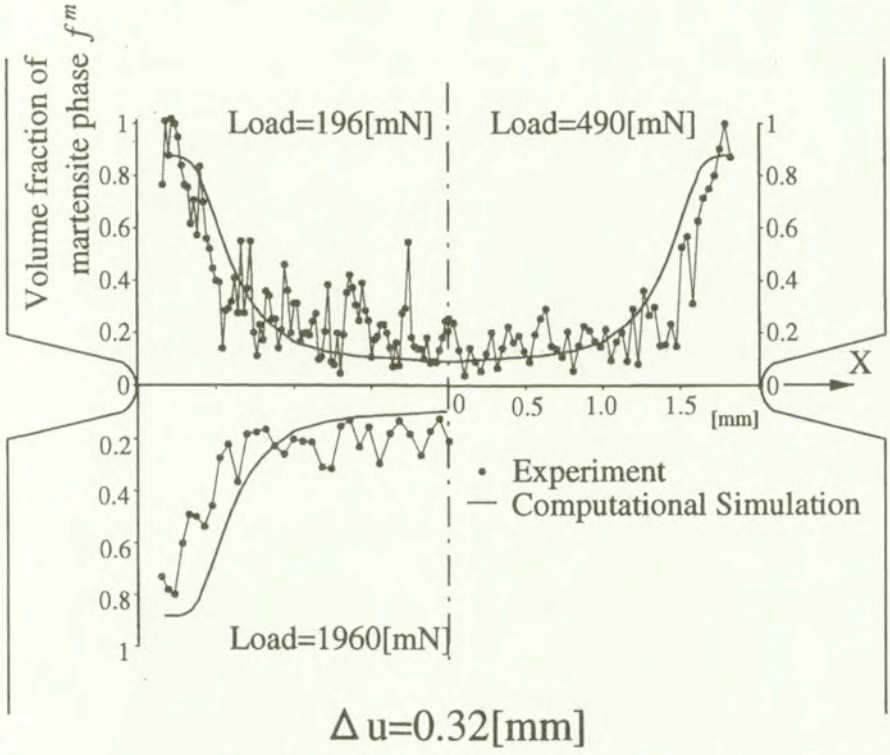

FIG. 7. Distribution of volume fraction of martensitic phase f^m along radial direction estimated using three different indentation loads and that estimated by computational simulation.

Figure 8 indicates the distribution of the volume fraction of the martensite phase f^m over the cross-section near the notch tip. Approximately 2000, 4000 and

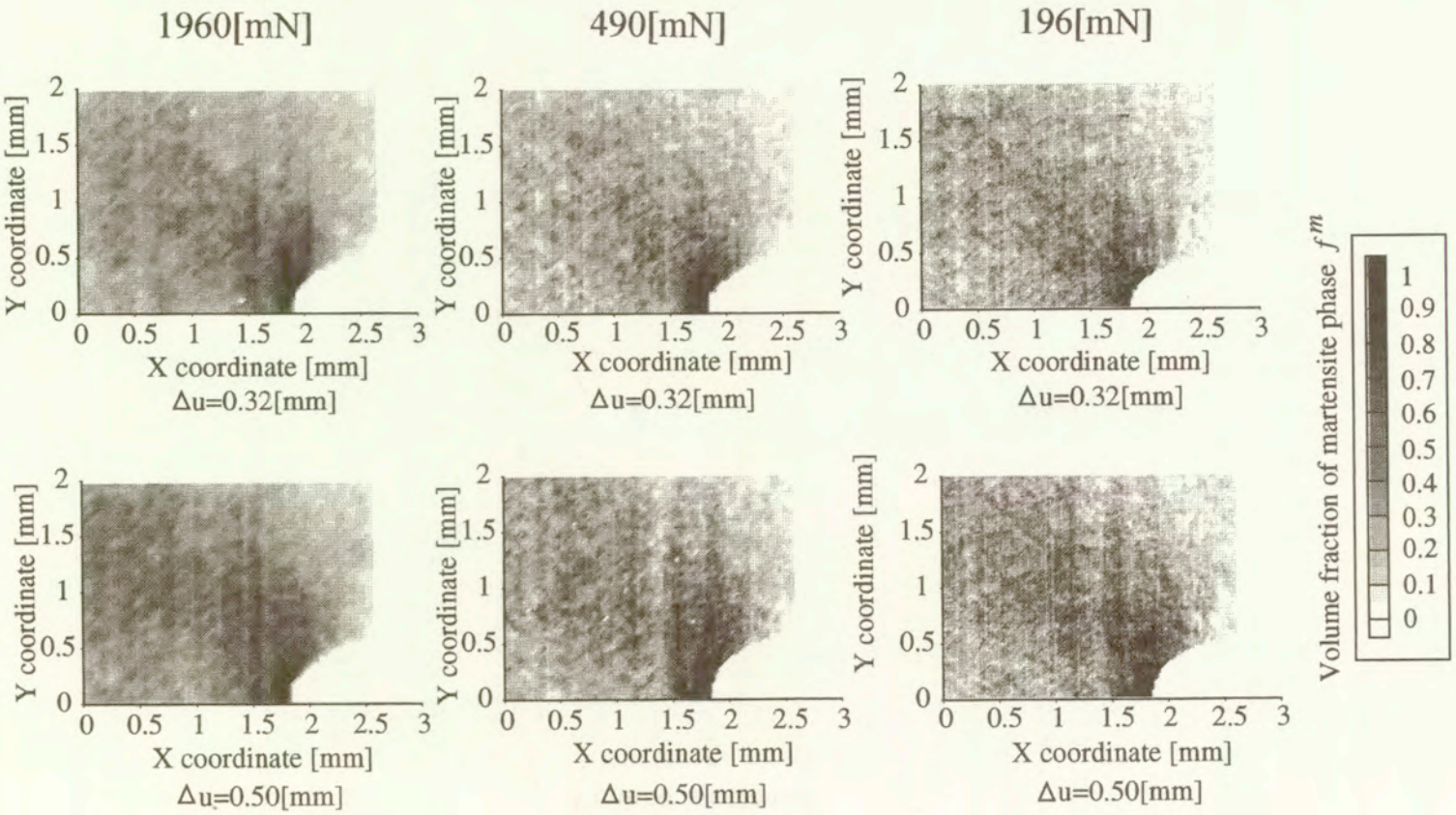

FIG. 8. Distribution of volume fraction of martensitic phase f^m near the notch tip estimated using three different indentation loads.

12000 points have been measured for 1960 mN, 490 mN and 196 mN indentation loads, respectively. In accordance with the local deformation of the notch, the region with high volume fraction of the martensitic phase emanating from the notch tip, spread in approximately 45° direction to the tension axes, which indicates that the martensitic transformation substantially depends on the slip deformation of the crystals [16]. By increasing the number of indentation points and decreasing the indentation load, the clearer distribution of the martensitic phase can be revealed. Due to the strain localization around the notch tip, the region with low martensitic transformation can be observed along the ligament direction of the notch root. Furthermore, the results extract the nonuniform transformation behavior depending on the crystalline direction in the multicrystal with average grain size, 100 μm. Thus, by increasing the number of indentation points, the clearer local information on the transformation can be obtained.

To examine the applicability of the constitutive equation for the prediction of the transformation behavior of TRIP steels, computational simulation has been performed for the specimen modeled by the finite element discretization shown in Fig. 6. Figures 7 and 9 indicate the distribution of volume fraction of martensitic phase f^m predicted by computational simulation and estimated by an experimental method. Apart from the fluctuation of the distribution of the volume fraction of the martensitic phase, a very clear correspondence is seen for both results, which implies the applicability of the constitutive equation for the estimation of the volume fraction of the martensite phase created by the highly nonuniform deformation. However, the results also indicate the limitation of the computational simulation with the constitutive equation developed, based on the volume fraction of the martensitic phase for problems with highly-localized deformation behavior. Therefore, a different type of transformation model which enables the estimation of the local martensite phase should be incorporated; this will be our future work.

Thus, the proposed method of estimation of local distribution of the volume fraction of the martensitic phase clarifies the validity of the prediction of the average martensitic phase distribution based on the phenomenologically developed constitutive equation to some extent, so that we will further discuss the deformation behavior of ringed notched bars. Figure 10 shows the evolution of the volume fraction of martensitic phase with the deformation under the environmental temperatures of 77 K and 293 K. A high volume fraction of the martensite phase is observed during the earlier stage of deformation at 77 K as compared with the case at 293 K, which can be explained by the following distribution of equivalent plastic strain $\bar{\varepsilon}^p$ and triaxiality factor Σ for the respective temperatures, which are shown in Fig. 11. In both cases, the magnitude of plastic equivalent strain is insensitive to the environmental temperature, so that it is recognized that the strong dependence of the probability that an intersection forms a martensitic

FIG. 9. Comparison between distribution of volume fraction of martensite phase estimated experimentally (upper) and by computational simulation (lower).

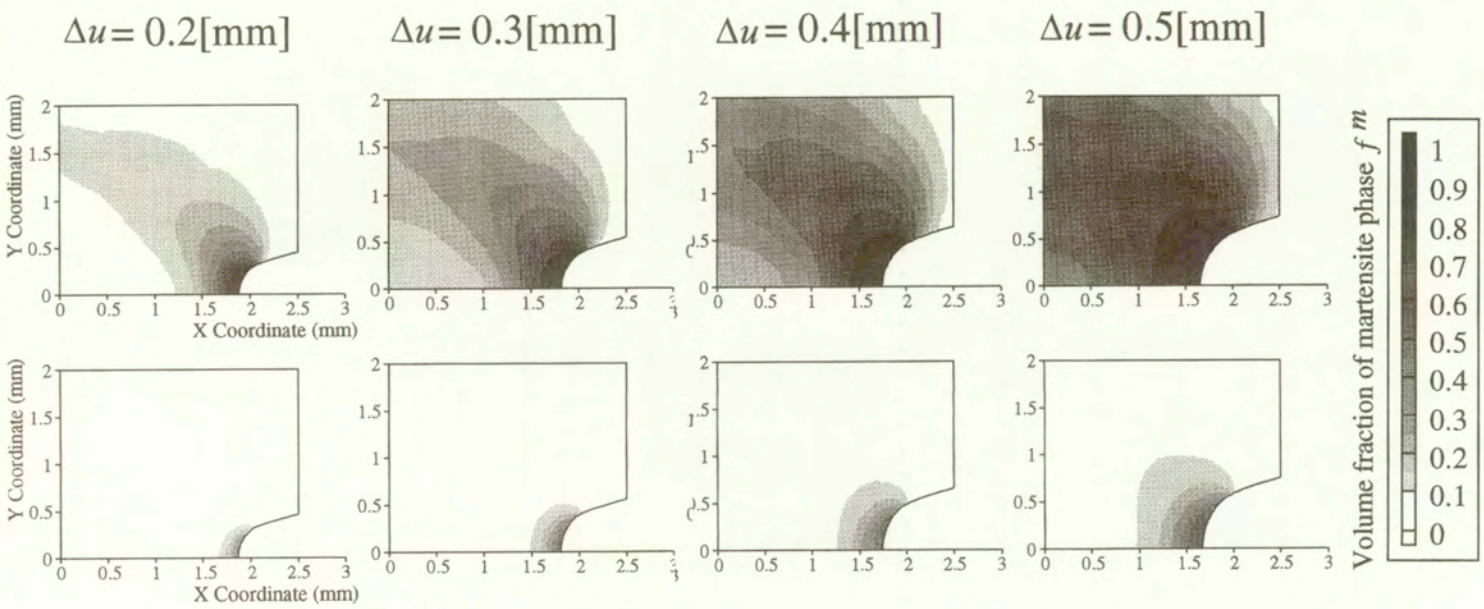

FIG. 10. Distribution of volume fraction of martensite phase f^m for environmental temperatures of 77 K and 293 K estimated by computational simulation.

FIG. 11. Distribution of equivalent strain $\bar{\varepsilon}^p$, triaxiality parameter Σ and volume fraction of martensite phase f^m.

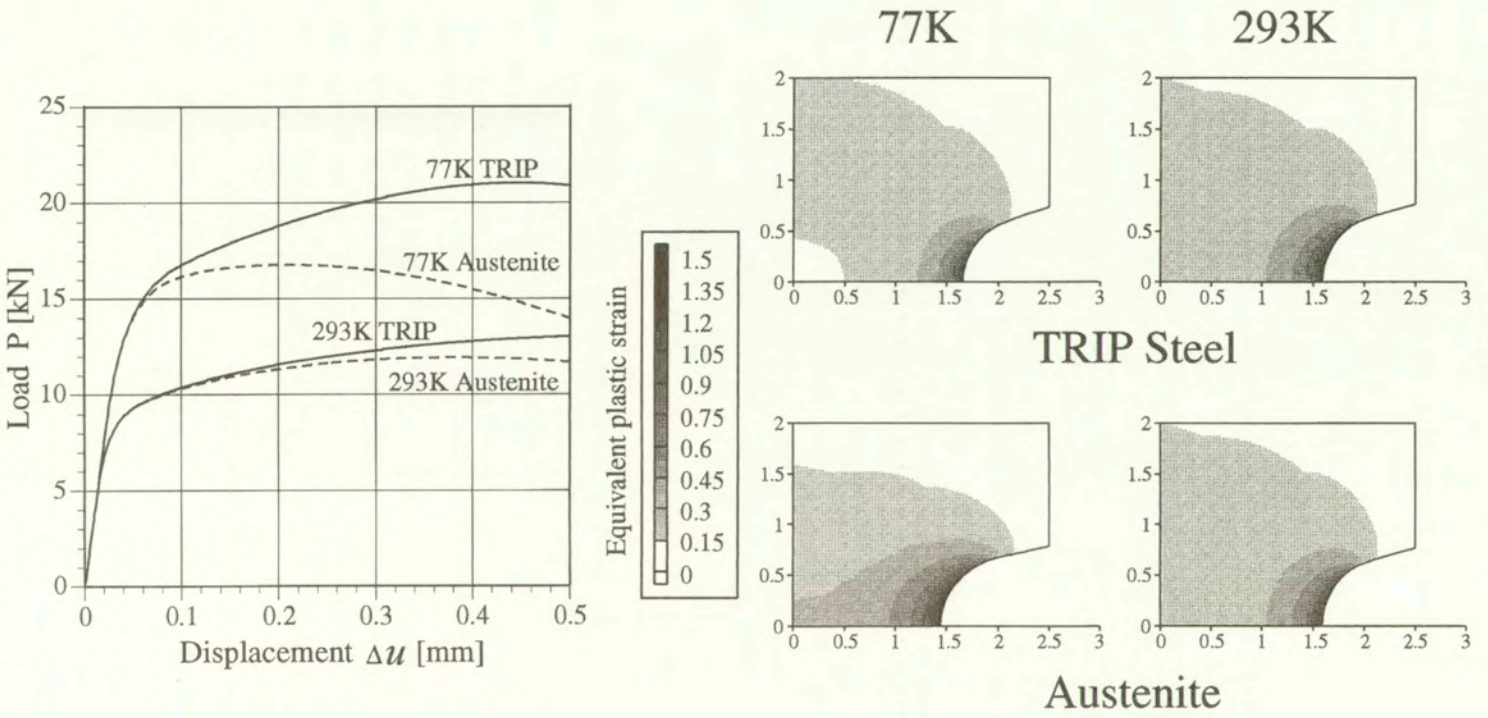

FIG. 12. (a) Load vs. displacement Δu relation and (b) equivalent plastic strain $\bar{\varepsilon}^p$ distribution for environmental temperatures of 77 K and 293 K. For the sake of comparison, the results for the nontransforming case, austenite, are also indicated.

embryo, in other words, the driving force to transformation, on the temperature, substantially affects the transformation.

Figure 12 indicates the load P and displacement Δu relations for the uniaxial tension of the notched specimens deformed under different environmental temperatures. For the purpose of comparison, the nontransforming case, austenite, is also shown. For the low- temperature case, there is a remarkable increase of force due to transformation so that the work required for the deformation increases, which is attributable to the distributing effect by the strengthening caused by martensitic transformation near the notch tip, which is indicated in the plastic equivalent strain distribution. Thus, martensitic transformation may contribute toward the increase in energy absorption from the outside, which yields the improvement of toughness.

6. Conclusion

In this study, through the precise tension tests conducted under the environmental temperatures of 77 K to 373 K, the effect of transformation on the macroscopic stress-strain relation and the improvement mechanism of ductility have been clarified. Then, with the volume fraction of martensite phase estimated using the magnetic method and microhardness measured by employing ultramicrohardness tester, the master curves for volume fraction of martensite phase vs. microhardness for various indentation loads have been established for the measurement of local distribution of volume fraction of the martensitic phase. Subsequently, the established master curves were employed for the estimation of the local distribution of the martensite phase over the cross-section of a ring-notched bar under tension. The results were compared with those obtained by computational simulation with a phenomenologically developed constitutive equation, and the validity and the limitation of the computational simulation have been clarified. By the computational simulation of different environmental temperatures, it has been clarified that the improvement of energy absorption due to the distributing effect of a highly deformed region by the martensitic transformation contributes toward the improvement of ductility. Furthermore, it is expected that the experimental method with low indentation load will enable the estimation of the highly localized distribution of the volume fraction of the martensitic phase.

Acknowledgments

Financial support from the Ministry of Education of Japan is gratefully acknowledged. I wish to thank Mr. T. IWAMOTO, Research Associate of Hiroshima University, for valuable discussions and graduate students Messrs. T. OGAWA,

A. TANIYAMA, M. SHIMIZU and H. SAKAUE, Kobe University, for assistance with the calculations and experiments.

Appendix

Material parameters at temperature employed in the present investigation are summarized. The discussion concerning the identification of material parameters can be found in [3 – 5] and [15].

Stress-strain relation for austenite and martensite phases are

$$\overline{\sigma} = \sigma_y + c_1 \{1.0 - \exp(-c_2 \overline{\varepsilon})\}^{c_3}, \qquad \sigma_y = c_4 \exp(-c_5 T),$$

where $c_1 = 1861.0$, $c_2 = 0.628$, $c_3 = 0.748$, $c_4 = 660.0$, $c_5 = 0.0027$ with elastic modulus $E_a = 215.7 - 0.0692T$ (GPa) and Poisson's ratio $\nu = 0.3$ for austenite phase and $c_1 = 1191.0$, $c_2 = 1.33$, $c_3 = 0.540$, $c_4 = 1056.0$, $c_5 = 0.0013$ with elastic modulus $E_m = 237.3 - 0.0692T$ (GPa) and Poisson's ratio for martensite phase.

Evolution of volume fraction of martensitic phase is indicated as Eqs. (4.1) and (4.2) with material parameters $\eta = 4.5$, $M = 0.013$, $\dot{\varepsilon}_r = 5.0 \times 10^{-4}$/s, $\alpha_1 = 0.0$, $\alpha_2 = -7.92 \times 10^{-2}$, $\alpha_3 = 27.1$, $\alpha_4 = 10.23$ for $T \geq 273$ K. The standard deviation σ_g, mean value g_0 and constant g_1 are 17.0, -276.0 and 28.7, respectively [3 –5].

Constitutive equation for plastic strain rate is expressed as in Eq. (4.3) with $R_0 = 0.02$, $R_1 = 0.02$ and $\Delta\nu = 0.02$.

Additional parameters are density $\rho = 0.78 \times 10^4$ (Kg/m^3), specific heat $c = 0.46 \times 10^3$ (J/kg· K), thermal conductivity $\kappa = 16.3$ (W/m· K), heat transfer coefficient with air $h = 25.0$ (W/m^2· K), thermal expansion $\alpha = 17.3 \times 10^{-6}$/K and latent heat $l_r = -1.50 \times 10^4$ (J/kg).

References

1. Y. TAMURA, *TRIP Steels* (in Japanese), Steel and Iron, 56–3, 429–445, 1979.
2. G.B. OLSON and M. COHEN, *Kinematics of strain-induced martensitic nucleation*, Metall Trans. **A**, 6, 791–795, 1975.
3. R.G. STRINGFELLOW, D.M. PARKS and G.B. OLSON, *A constitutive model for transformation plasticity accompanying strain-induced martensitic transformation in metastable austenitic steels*, Acta Metall, **40**, 1703–1716, 1992.
4. Y. TOMITA and T. IWAMOTO, *Constitutive modeling of TRIP steel and its application to the improvement of mechanical properties*, Int. J. Mech. Sci., **37**, 1295–1305, 1995.
5. T. IWAMOTO, T. TSUTA and Y. TOMITA, *Investigation on deformation mode dependence of strain-induced martensitic transformation in TRIP steels and modeling of transformation kinetics*, Int. J. Mech. Sci., **40**, 173–182, 1998.

6. J. DURNIN and K.A. RIDAL, *Determination of retained austenite in steel by X-ray diffraction*, J. Iron & Steel Institute, **206**, 60–67, 1968.

7. G.C. CURTIS and J. SHERWIN, *Magnetic method for the estimation of ferrite in stainless steel welds*, British J. Applied Physics, **12**, 344–345, 1961.

8. T TANAKA and K. HOSHINO, *Measurement of strain-induced martensitic phase* (in Japanese), Nisshin Seiko Technical Report **52**, 36–47, 1985.

9. A. TAKIMOTO, T. INOUE and S. SHOUDA, *Relationship between the electrical resisitivity and the volume fraction of martensite induced by quenching and deformation* (in Japanese), J. Japan Inst. Metals. **49**, 5, 313–319, 1985.

10. Y. TOMITA and T. IWAMOTO, *Computational simulation of enhancement of ductility in TRIP steels due to environmental temperature control during deformation processes*, Proc. Plasticity'95, 331–334, 1995, Gordon and Breach.

11. Y. SHIBUTANI, A. TANIYAMA, Y. TOMITA and T. ADACHI, *Measurement of local strain-induced martensitic phase transformation by microhardness*, JSMS Japan, **46**, 893–899, 1997.

12. S.S. HECKER, M.G. STOUT, K.P. STAUDHAMMER and J.L. SMITH, *Effect of strain state and strain rate on deformation induced transformation in 304 stainless steel: Part I. Magnetic measurements and mechanical behavior*, Metall Trans **A**, 13, 619–626, 1982.

13. Y. TOMITA, A. SHINDO and S. SASAYAMA, *Plane strain tension of thermo-elasto-viscoplastic blocks*, Int. J. Mech. Sci. **32**, 613–622, 1990.

14. J.D. ESHELBY, *The determination of the elastic field of an ellipsoidal inclusion, and related problems*, Proc. Roy. Soc. Lond., **A241**, 376–396, 1957.

15. M. SHIMIZU, *Evaluation of strain-induced martensitic phase transformation behavior by microhardness and its application to constitutive modeling of TRIP steel* (in Japanese), Solid Mechanics Research Laboratory Report, No. 9802, 1–63, 1998.

16. J.A. VENABLES, *The martensitic transformation in stainless steel*, Phil. Mag., **7**, 35–43, 1964.

Received January 13, 1999.

Arch. Mech., **51**, 6, pp. 885–911, Warszawa 1999

On the macroscopic free energy potential for Shape Memory Alloys treated as a two-phase continuum

A. ZIÓŁKOWSKI, and B. RANIECKI

Polish Academy of Sciences
Institute of Fundamental Technological Research,
Świętokrzyska 21, 00–0949 Warsaw, Poland

IN THE PRESENT PAPER, a macroscopic free energy potential for shape memory alloys in the pseudoelastic range of their behavior is derived. It is assumed that the macro-element made of Shape Memory Alloy (SMA) is composed of austenitic and martensitic phase. It is stipulated that on the mezo-scale level, the micro-constituents obey generalized thermoelastic Hooke's law, in which eigenstrains connected with martensitic phase transformation are present. The primary target of the paper is not determination of the specific form of the macro free energy but revealing its structure resulting from the micro-macro transition. This structure is of a fundamental significance for subsequent development of macroscopic constitutive relations for Shape Memory Alloys. Micro-macro transition procedure allows for identifying the correspondence between the actual micro-phenomena and individual terms appearing in the free energy macro-potential. The performed calculations throw a new light on the so-called accommodation energy, a part of which is the interaction (coherence) energy appearing in contemporary literature. On the application side, it was possible to explain a certain paradox appearing in the attempts made to describe the behavior of some TiNiX ternary alloys (TiNi alloy) undergoing R-phase transformation.

1. Introduction

RECENTLY MUCH ATTENTION in research and industry has been focused on materials, which exhibit properties unusual in comparison to "standard" materials. These materials can further be used for construction of smart structures (see e.g. [22]). Shape memory alloys such as NiTi, TiNiCo, TiNiAl, CuZnAl, CuAlNi are prime candidates here. They are already used in construction of connectors, release mechanisms, control devices, medical tools and many other engineering mechanisms (see [14]). What makes the shape memory alloys special is that they can fully recover from relatively large strains (on the level of $4\% - 8\%$ in practical applications) upon appropriate stress and/or temperature histories. Metallurgical studies showed that this special effect of SMA materials originates from the thermoelastic martensitic transformation (see e.g. [12]). During this transforma-

tion, a high temperature and high symmetry austenitic phase of SMA transforms into a low temperature and lower symmetry martensitic phase. The transformation may be induced either by lowering temperature or applying stress. The microstructures appearing as a result of this transformation were extensively investigated in metallurgical literature during the last forty years and are at present quite well known. For an extensive review of the thermoelastic martensitic transformation and microstructure properties arising from the metallurgical point of view we shall send the reader to the book by CHRISTIAN [3] and his very recent paper [2]. The theoretical works aiming at the description of shape memory alloys behavior lagged behind the experimental ones until late 80-ties and beginning of the 90-ties when a number of models of SMA materials mechanical behavior appeared. Apparently, FALK [4] has proposed the first macroscopic thermodynamic constitutive model of SMA materials. He postulated the free energy potential in the form of a 6^{th} degree polynomial. He managed to obtain a good qualitative description of SMA materials in pseudoelstic range of their behavior, without introducing any internal variables in his model. The coherence energy Φ^{AM} proportional to the product of martensitic phase and austenitic phase fraction made a big step in modeling of Shape Memory Alloys. This term introduced heuristically into the free energy potential allowed for a good quantitative description of the hysteresis loop formation on the grounds of non-equilibrium thermodynamics.

Many researchers have adopted this approach, e.g. Müller and his collaborators managed to model successfully the macroscopic behavior of shape memory alloys subjected to one-dimensional mechanical loading ([10], [6]). RANIECKI, LEXCELLENT and TANAKA [18], [17] developed the so-called R_L incremental macroscopic model. The model is three-dimensional and allows for arbitrary thermo-mechanical loading. The typical behavior of CuZnAl mono-crystalline sample during isothermal uniaxial tension is sketched in Fig. 1. The σ_1^{AM} denotes the critical stress of forward transformation, σ_1^{MA} denotes the critical stress of reverse transformation, γ is the amplitude of pseudoelastioc flow at simple tension. This behavior may be easily reproduced with the aid of the R_L model. The dashed line shows the states of full thermodynamic equilibrium predicted by this model. It may be shown that the equilibrium is unstable when $\Phi^{AM} > 0$ and this explains, on a theoretical ground, the formation of the hysteresis loop as discussed in [18]. It was also shown in [18] that $\Phi^{AM} > 0$ when $\sigma_1^{AM} > \sigma_1^{MA}$.

The R_L model has been adopted in [7] for description of the R-phase transformation. However, in this case $\sigma_1^{AM} < \sigma_1^{MA}$, what is shown schematically in Fig. 2. Identification of the macroscopic constitutive model material parameters leads to negative values of the term Φ^{AM}. The negative value of interaction energy Φ^{AM} constitutes a paradox and deserves further investigation. The dashed line in Fig. 2 shows the states of full thermodynamic equilibrium predicted by the model. Deviation of the real paths from the paths of full thermodynamic equi-

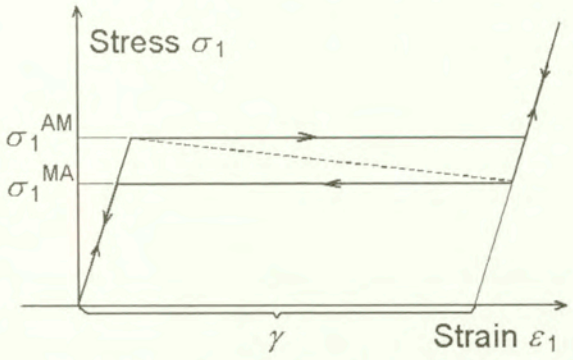

FIG. 1. Typical behavior of CuZnAl alloy.

librium can not be explained anymore by its instability. LIM and MCDOWELL performed experimental works on NiTi samples and presented the discussion devoted to the interaction energy Φ^{AM} in [8]. At the end of their paper they propose that the interaction energy should be a function of temperature, internal variables and phase fractions, but not necessarily proportional to their product. They do not lead to any specific explicit expression for the interaction energy.

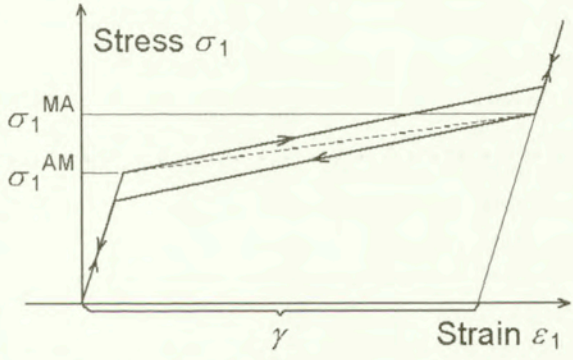

FIG. 2. Typical behavior of TiNi alloy undergoing R-phase transformation.

The present paper is an attempt to analyze the fundamental problem of the general structure of macroscopic free energy potential enabling the description of SMA materials. We are not trying at the same time to construct here a new or revised micro-mechanical or macroscopic constitutive model of SMA materials. The procedure applied to construct such a model when the free energy potential is already known is clearly indicated in papers [17] and [18]. We will start our investigation from the so-called mezo-scale of observation. All our starting mezo-scale assumptions will be supported by metallurgical observations on this scale. We will postulate elastic behavior of both phases on this scale of observation. It

is worth noticing that even when the particular micro-constituents of the macro-element behave elastically, the overall response of the material may be non-elastic and possibly dissipative. The reason for that is the evolving microstructure in the RVE (phase transformation or reorientation of martensitic variants) and usually the accompanying it phenomenon of energy dissipation.

We will not investigate these issues in the present paper, sending interested readers to the papers by ABEYARATNE and KNOWLES [1] or RANIECKI and TANAKA [19]. We are studying an arbitrary but fixed instant of the phase transformation progress. The macro-element is assumed to be in the thermodynamic equilibrium with respect to the external thermodynamic variables (macroscopic strain $\boldsymbol{\varepsilon}^{(z)}$ and temperature T). Constrained thermodynamic equilibrium is postulated with respect to the parameters describing the microstructure of macro-element **H**. One of the simplest parameters of this kind is the mass fraction of martensitic phase z. Hence, all the theorems of the theory of elasticity will be valid in our considerations.

Later, taking into account the changing microstructure of the RVE or phase fraction z will result in changing the eigenstrains of the phase transformation, but will not result in a change of the general structure of free energy macro-potential. As a result of our mezo-macro transition procedure, we will obtain free energy expressed in terms of macro-state variables understood as relevant averaged values of the corresponding mezo-variables. We will not solve the mezo-mechanical problem explicitly, as this would require prescribing a fixed RVE microstructure. The microstructures observed in real samples are pretty complex and finding analytical solutions for them might be extremely difficult. Nevertheless, we will obtain the sought structure of the free energy macro-potential. The particular terms appearing there may be interpreted in terms of the underlying mezo-scale phenomena and mezo-scale variables. The wealth of alloys exhibiting shape memory effects indicate that some terms appearing in the free energy macro-potential derived from mezo-mechanical assumptions may be neglected for some alloys but not for the others. Also the observation of macroscopic behavior of certain SMA materials allows drawing the conclusion that some microscopic phenomena do not take place there. For example, ideal pseudoelastic flow will indicate the formation of martensitic plates without complex internal microstructure (composed e.g. of one martensitic variant). Strong work-hardening observed during the R-phase transformation indicates the formation of many martensitic plates with internal substructure. Several authors tried to derive constitutive relations for the SMA materials starting from micro-mechanical considerations; see, e.g. papers by PATOOR *et. al.* [13] or SUN *et. al.* [20]. The authors mentioned above concentrated on deriving the "working" constitutive models of SMA materials. They were not concentrating to a large extent on the macroscopic free energy macro-potential itself.

2. Thermoelastic martensitic transformation experimental evidence in mezo-scale of observation

The most important information from metallurgical literature concerning thermoelastic martensitic transformation is shortly recalled in the present section. The information specified below is necessary for a proper choice of mezo-scale variables (and their properties) appearing in the mezo-scale mechanical problem posed in the subsequent sections. Various patterns of martensitic structure appearing on subsequent levels of observation are illustrated schematically in Figs. 3 to 6. In the materials science literature devoted to martensitic transformations, e.g. CHRISTIAN [3], OLSON and OWEN [12] or WARLIMONT, DELAEY [21], the following properties characteristic for martensitic transformations could be found:

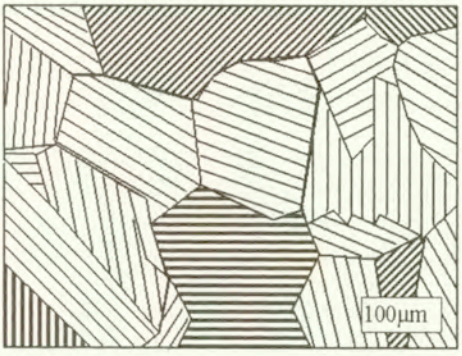

FIG. 3. Schematic view of polycrystalline martensitic microstructure in Cu-Al. Observe different orientation of martensitic plates in different grains (after WARLIMONT and DELAEY [21]).

a) Martensitic phase transformation is athermal, i.e. it does not depend on the time and the rate of change of parameters inducing it.

b) Martensitic transformation is coherent and is also called generalized plane strain transformation since during this transformation the planes are formed, which remain invariant (not deformed and not rotated). They are called habit planes, and constitute a border between the parent and product phases. The atoms, which actually take part in transformation, move in the same direction by a distance proportional to the distance from the habit plane.

c) Martensitic transformation is diffusionless, i.e. chemical composition of the parent and martensitic phase is the same.

d) Thermoelastic martensitic transformation is shear strain dominant displacive transformation progressing by nucleation and growth, where shear strains can reach about a dozen percent while the bulk strain is very limited (max. up to 0.5%) [12].

e) Typical generic element of thermoelastic martensite structure is a thin plate or a thin lens (see Fig. 4). The martensitic plate has usually an internal microstructure itself composed of twin martensitic variants (see Fig. 5)).

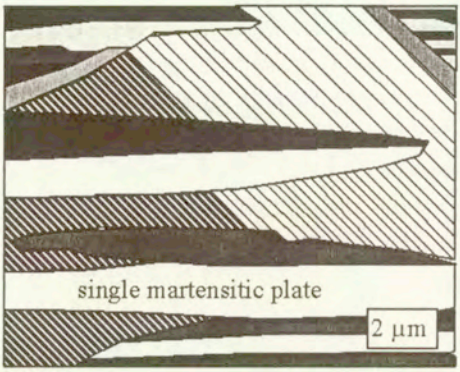

FIG. 4. Schematic view of formation of groups of martensitic plates (after WARLIMONT and DELAEY [21]).

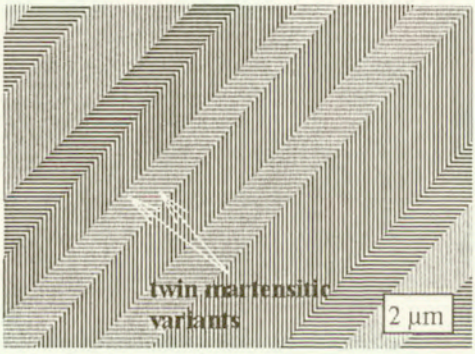

FIG. 5. Schematic view of internal microstructure of martensitic plates (after WARLIMONT and DELAEY [21]).

f) Thermoelastic martensite may be induced thermally or mechanically.

g) The martensitic phase usually has an internal hierarchical microstructure. On the higher level it consists of many martensitic plates. They in turn may consist of several martensitic variants. For example, the martensite induced thermally has usually the microstructure with groups of four self-accommodating martensitic variants. On the other hand, the martensite induced by or at the presence of stress has the microstructure with martensitic variants of preferred orientation with respect to the applied stress direction (see, e.g. PUTAUX and CHEVALIER [16]). This last feature allows proposing a macroscopic constitutive relation between the external stress tensor $\sigma^{(z)}$ and the phase transformation eigenstrain tensors.

The above experimental evidence known from the metallurgical literature will be analyzed in the next section from the point of view of continuum thermo-mechanics. The issue of phase transformation kinetics is not touched in the present paper. The reason for that is that the macro-element of the Shape Memory Alloy is investigated in the present paper at a fixed point of the phase transformation progress. This means that the investigations in the present work are limited to a generalized problem of elasticity. The approach is quite similar to that applied in the problems of homogenization of composites, when the primary task is the determination of the effective moduli.

3. Continuum mechanics approach to thermo-elastic martensitic transformation

In the present section we are studying thermo-elastic martensitic transformation properties from the point of view of continuum thermo-mechanics. This will enable us to adopt suitable mezo-scale variables with properties adequate for the description of the shape memory alloys behavior. The properties of mezo-scale variables identified hereby on the basis of experimental evidence will translate to macro-variables through the averaging procedure. In our investigation we will use the postulate of local state, saying that the behavior of the material in a material point is predetermined by its closest neighborhood, the so-called Representative Volume Element - RVE (see Fig. 6). On the level of RVE, the mezo-scale variables depend on spatial coordinate x. The averaging procedure carried out over the volume of RVE will result in the value of macroscopic variable in the material point.

The property a) of the previous section on the mezo- and macro- scale of observation must result in the rate-independence of the constructed constitutive model of shape memory alloy. This is the assumption made in the present paper, which finds its reflection in the independence of the phase mezo-scopic potentials adopted in the next section from the rates of state parameters. They depend only on the state parameters themselves. It also suggests construction of rate-independent phase transformation kinetic equations, which are not discussed here.

In the property b) it is said that the martensitic transformation is coherent. This means that the field of displacements appearing in the continuum mechanics problem must be continuous, but not the strains field, which may be discontinuous on the phase boundaries. The second part of property b) allows us to draw a conclusion that the gradient of deformation $\mathbf{F}_2$ in a single martensitic plate can be expressed as $\mathbf{F}_2 = \mathbf{1} + \boldsymbol{\lambda} \otimes \mathbf{n}$. Where the austenitic phase has been adopted as the reference state ($\mathbf{F}_1 = \mathbf{1}$), λ is a vector of martensitic phase distorsion,

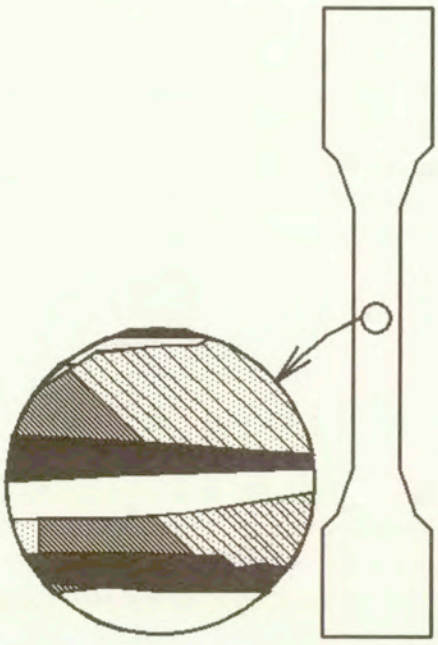

FIG. 6. Representative volume element of SMA.

while $\mathbf{n}$ is a vector normal to the austenite-martensite interface. The volume strain in thermoelastic martensitic transformation does not exceed 0.5%. Hence, it is justified to adopt the approximation that volume and weight fractions of the austenite and thermo-elastic martensite are identical $\rho_1 = \rho_2$. The relation $\det(\mathbf{F}_2)/\det(\mathbf{F}_1) = \rho_1/\rho_2 = 1 + \boldsymbol{\lambda} \cdot \mathbf{n}$ shows how the volumetric strain can be estimated from the measurement of microscopic parameters $\boldsymbol{\lambda}$ and $\mathbf{n}$.

Also from d) we know that the shear strains observed in SMA materials are limited to a dozen percent or so. In practical applications they usually do not exceed 8%. Hence, it is justified to conduct the present investigations within the framework of the small strains theory. The form of deformation gradient $\mathbf{F}_2$ specified above is valid, with good reliability, for a single martensitic plate. Metallographic micrographs of martensitic structures indicate (see e.g. [21]) that this simple form of deformation gradient cannot be adopted even on the mezo-scale of observation, unless the evolution of a single martensitic plate or even of a single martensitic variant is studied.

In the present paper it is assumed that the phase transformation eigenstrain tensors are functions of the position in the RVE volume and are not constant. This last assumption is natural in view of the complicated martensitic microstructures resulting from thermoelastic martensitic transformation (see, e.g. Fig. 6). When only single martensitic plate will appear composed of single martenstic

variant, then the transformation eigenstrain is constant. In the case, when one martensitc plate composed of twin alternating martensitic variants then the eigenstrain may be assumed to be constant but with the vector $\boldsymbol{\lambda}$ different from the previous case. In general, on the meso-scale of observation supposition on non-homogeneous phase transformation eigenstrain is well justified. The non-homogeneity results from formation of many martensitic plates with internal substructure as observations e) and g) indicate.

In the present investigation another important simplifying assumption is made, stating that the tensors of elastic stiffness and elastic compliance of austenitic and martensitic phase $\mathbf{L}_\alpha$ and $\mathbf{M}_\alpha \equiv (\mathbf{L}_\alpha)^{-1}$ $(\alpha = 1, 2)$ are material constants independent of the thermodynamic state. The thermal expansion coefficients α, and specific heats c, are material constants and are assumed to be the same for both phases.

The property f) calls for development of the SMA materials theory within the thermodynamical framework. This is actually done in the present paper. It should also find its reflection in the forward and reverse phase transformation criteria as well as in the phase transformation kinetic relations.

4. Formulation of mezo-mechanical boundary value problem of two phase continuum for RVE

In this section we explicitly formulate the problem of mezo-mechanics for representative volume element of shape memory alloy. The problem is posed in meso-scale state variables. When a solution of the problem is known, the explicit form of stress macro-potential may be obtained by "simple" averaging of meso-scale variables over the RVE volume. We already remarked that the martensitic structures appearing in RVE are usually very complex. This practically excludes the possibility to find an analytical solution of the posed problem. The solution derived in the present paper is to a large extent formal one. Nevertheless, it gives useful information on the form of the free energy potential allowable from the point of view of micro-mechanics. It also allows to predict, which macroscopic terms may be neglected in this potential for some microstructures and not for the others.

We will assume that thermoelastic properties of individual phases are described on meso-scale by free energy micro-potentials identical with those adopted in the linear theory of thermo-elasticity. This means that the phases on meso-scale obey generalized Hook's laws,

$$\rho\phi_{(\alpha)}(\hat{\tilde{\boldsymbol{\varepsilon}}}_\alpha(\mathbf{x},T),T) = 0.5(\hat{\tilde{\boldsymbol{\varepsilon}}}_\alpha(\mathbf{x},T) - \hat{\boldsymbol{\Gamma}}_\alpha(\mathbf{x},T)) \cdot \mathbf{L}_\alpha(\dot{\tilde{\boldsymbol{\varepsilon}}}_\alpha(\mathbf{x},T) - \hat{\boldsymbol{\Gamma}}_\alpha(\mathbf{x},T)) + \rho\phi^0_{(\alpha)}(T), \tag{4.1}$$

(4.1) [cont.]
$$\rho\phi^0_{(\alpha)}(T) = c[T - T_0 - T\ln(T/T_0)] + \left(u_0^{*(\alpha)} - T_{s_0}^{*(\alpha)}\right),$$
$$\hat{\Gamma}_\alpha(\mathbf{x}, T) = \hat{\Gamma}^0_\alpha(\mathbf{x}, T) + \boldsymbol{\alpha}(T - T_0).$$

The $u_0^{*(\alpha)}$, $s_0^{*(\alpha)}$ are internal energies and entropies of the phases, while $\rho = \rho^0_{(\alpha)}$ $(\alpha = 1, 2)$ is the density at reference temperature T_0 and at stress-free state $\boldsymbol{\sigma} = 0$ (assumed to be the same for both phases). The $\hat{\hat{\boldsymbol{\varepsilon}}}_\alpha(\mathbf{x}, T)$ are the fields of total strain in the respective phases. The eigenstrains $\hat{\Gamma}_\alpha(\mathbf{x}, T)$ of the phases with respect to the reference configuration $(\boldsymbol{\sigma} = 0, T = T_0)$ might, in general, be of various physical origin. In the present paper we explicitly take into account the strains originating from thermal expansion of the material and eigenstrains originating from thermoelastic phase transformation $(\hat{\Gamma}^0_\alpha(\mathbf{x}, T))$. Please note that we have made an assumption that phase transformation eigenstrains does depend on temperature. This assumption is well justified for the case of the so-called R-phase transformation [7]. In the case of monoclinic martensitic transformation in the pseudoelastic range of SMA materials behavior, the $\hat{\Gamma}^0_\alpha$ may be adopted to be independent of temperature. The dependence of $\hat{\Gamma}^0_\alpha$ on location in the RVE results from the assumption that RVE domain will usually embrace the austentic phase and many martensitic variants. In our present investigations, the microstructure of the RVE domain is assumed to be known and fixed, being otherwise totally arbitrary. We neglect at the moment any eigenstrains originating from, e.g. the plastic deformations induced as a result of the SMA training procedure. The training procedure of SMA materials is a standard step in obtaining so-called two-way shape memory effect.

In the sequel $\pi^f_0(T)$ denotes the difference of free energy micro-potentials of the phases at the stress-free state $(\boldsymbol{\sigma} = 0)$,

(4.2)
$$\pi^f_0(T) = \phi^0_{(1)} - \phi^0_{(2)} = \Delta u^* - T\Delta s^*, \quad \Delta u^* = u_0^{*(1)} - u_0^{*(2)},$$
$$\Delta s^* = s_0^{*(1)} s_0^{*(2)}.$$

The mean free energy macro-potential of RVE (per unit of volume) may be expressed with the aid of the meso-scale state variables as follows,

(4.3)
$$\rho\Phi = <\rho\phi>_{\mathrm{v}_0} = \rho\Phi_0 + \rho\Phi_m,$$
$$\rho\Phi_0 = \rho(z_1\phi^0_{(1)}(T) + z_2\phi^0_{(2)}(T)) = c[T - T_0 - T\ln(T/T_0)]$$
$$+u_0^{*(1)} - Ts_0^{*(1)} - z_2\pi^f_0(T),$$

(4.3) [cont.]
$$\rho\Phi_m = 0.5\left[z_1\left\langle \hat{\hat{\boldsymbol{\sigma}}}(\mathbf{x},T)\cdot\mathbf{M}_1\hat{\hat{\boldsymbol{\sigma}}}_\alpha(\mathbf{x},T)\right\rangle_{\mathrm{v}_1} + z_2\left\langle \hat{\hat{\boldsymbol{\sigma}}}(\mathbf{x},T)\cdot\mathbf{M}_2\hat{\hat{\boldsymbol{\sigma}}}(\mathbf{x},T)\right\rangle_{\mathrm{v}_2}\right],$$

$$\hat{\hat{\boldsymbol{\varepsilon}}}(\mathbf{x},T)\equiv\hat{\hat{\boldsymbol{\varepsilon}}}_\alpha(\mathbf{x},T),\quad \hat{\hat{\boldsymbol{\sigma}}}(\mathbf{x},T)\equiv\hat{\hat{\boldsymbol{\sigma}}}_\alpha(\mathbf{x},T),\quad \text{for } \mathbf{x}\in V_\alpha,$$

$$V_0\equiv V_1+V_2,$$

$$z_\alpha\equiv V_\alpha/V_0,\quad z_1+z_2\equiv 1,\quad \langle(\cdot)\rangle_\alpha\equiv\frac{1}{V_\alpha}\int\limits_{V_\alpha}(\cdot)dV.$$

where Φ_0 is an average free energy of mixture of phases at a stress-free state, Φ_m is an average elastic energy stored in macro-element as a result of the conditions applied on its boundary. The $\hat{\hat{\boldsymbol{\sigma}}}_\alpha(\mathbf{x},T)$ are the stress fields in the volumes of respective phases V_α, $\alpha=1,2$. The symbol V_0 denotes total volume of a macro-element. The definitions $(4.3)_4$ are only used to shorten the notation. In the case of shape memory alloys, due to a slight difference in density of austenitic and martensitic phases, the mass fractions z_α and volume fractions v_α of the respective phases can be identified.

The elastic energy Φ_m is here of special interest. It can be determined with the aid of solution to the following boundary value problem of micro-mechanics. Let us suppose that RVE with volume v_0 is a composite structure of two coherent elastic phases with volumes v_α ($\alpha=1,2$), and with an arbitrary but fixed microgeometry. We assume the RVE to be statistically representative. An RVE is regarded as statistically representative of macro-response of the continuum material neighborhood, if and only if an arbitrary constant macro-stress Σ produces, through solution of the relevant boundary value problem with traction boundary condition ($\mathbf{t}^0(\mathbf{x})=\mathbf{n}\cdot\boldsymbol{\Sigma}$ on ∂V), a macrostrain ($\mathbf{E}^\Sigma=<\boldsymbol{\varepsilon}(\mathbf{x},\boldsymbol{\Sigma})>_{\mathrm{v}}$) such that when the displacement boundary conditions ($\mathbf{u}^0(\mathbf{x})=\mathbf{x}\cdot\mathbf{E}^\Sigma$ on ∂V) are imposed instead, then the macrostress ($<\boldsymbol{\sigma}(\mathbf{x},\boldsymbol{\Sigma})>_{\mathrm{v}}=\boldsymbol{\Sigma}^\Sigma\cong\boldsymbol{\Sigma}$) is obtained, where the equality holds to a given degree of accuracy (see also NEMAT-NASSER and HORI [11]). The direct consequence of statistical representativeness of RVE is that the macrostrain potential $\Psi^\Sigma(\boldsymbol{\Sigma})\equiv<\psi^\Sigma>_{\mathrm{v}}$ and the macrostress potential $\Phi^E(\mathbf{E})\equiv\langle\phi^E\rangle_{\mathrm{v}}$ correspond to each other in the sense that $\partial(\Psi^\Sigma(\boldsymbol{\Sigma}))/\partial(\boldsymbol{\Sigma})\cong\mathbf{E}$ while $\partial(\Phi^E(\mathbf{E}))/\partial(\mathbf{E})\cong\boldsymbol{\Sigma}$, and in accordance with the Legendre transformation $\Psi^\Sigma(\boldsymbol{\Sigma})+\Phi^E(\mathbf{E})\cong\boldsymbol{\Sigma}\cdot\mathbf{E}$. This in turn enables us to impose either the traction or the displacement boundary conditions when posing the problem of micro-mechanics aiming at derivation of the particular Helmholz or Gibbs macro-potential.

In accordance with the thermodynamic formalism, simple derivation of (4.1) with respect to $\hat{\hat{\boldsymbol{\varepsilon}}}(\mathbf{x},T)$ gives us generalized Hook's laws, which must be obeyed by the phases,

$$\hat{\hat{\boldsymbol{\varepsilon}}}(\mathbf{x},T)=\mathbf{M}_\alpha\hat{\hat{\boldsymbol{\sigma}}}_\alpha(\mathbf{x},T)+\hat{\boldsymbol{\Gamma}}_\alpha(\mathbf{x},T),\qquad \hat{\boldsymbol{\Gamma}}_\alpha(\mathbf{x},T)=\hat{\boldsymbol{\Gamma}}_\alpha(T)+\hat{\boldsymbol{\Gamma}}^d_\alpha(\mathbf{x},T),\tag{4.4}$$

$$\mathbf{x}\in V_\alpha\ \alpha=1,2,$$

$$\hat{\hat{\boldsymbol{\varepsilon}}}_\alpha(\mathbf{x},T)=\frac{1}{2}\left(\nabla\hat{\hat{\mathbf{u}}}_\alpha+{}^T\nabla\hat{\hat{\mathbf{u}}}_\alpha\right),\qquad \boldsymbol{\Gamma}_\alpha(T)=\left\langle\hat{\boldsymbol{\Gamma}}_\alpha(\mathbf{x},T)\right\rangle_\alpha,$$

$$\left\langle\hat{\boldsymbol{\Gamma}}^d_\alpha(\mathbf{x},T)\right\rangle_\alpha\equiv 0.$$

where $\boldsymbol{\Gamma}_\alpha(T)$ is the volume average of the local eigenstrain field $\hat{\boldsymbol{\Gamma}}_\alpha(\mathbf{x},T)$ over the domain of the phase α, while $\hat{\boldsymbol{\Gamma}}^d_\alpha(\mathbf{x},T)$ is the field of deviations of the eigenstrain field from the respective mean value $\boldsymbol{\Gamma}_\alpha(T)$. The fields $\hat{\hat{\boldsymbol{\sigma}}}(\mathbf{x},T)$ and $\hat{\hat{\boldsymbol{\varepsilon}}}(\mathbf{x},t)$ can be discontinuous on the phase boundaries.

We are searching for the displacement field $\hat{\hat{\mathbf{u}}}(\mathbf{x},T)$ continuous in the whole domain of RVE, which at a fixed microgeometry, prescribed fields of eigenstrain $\hat{\boldsymbol{\Gamma}}_\alpha(\mathbf{x},T)$ and prescribed uniform boundary condition on the surface ∂V of the macro-element,

$$\mathbf{n}\cdot\hat{\hat{\boldsymbol{\sigma}}}(\mathbf{x},T)\Big|_{\partial V}=\mathbf{n}\cdot\boldsymbol{\sigma}^{(z)}.\tag{4.5}$$

(where $\boldsymbol{\sigma}^{(z)}=\text{const}$ denotes the prescribed uniform stress. Naturally, it is equal to the average stress in the RVE. It denotes also macroscopic stress in the investigated macroscopic material point), gives after substitution into (4.4), the stress fields $\hat{\hat{\boldsymbol{\sigma}}}_\alpha(\mathbf{x},T)$, which identically satisfy the mechanical equilibrium equations,

$$\operatorname{div}(\hat{\hat{\boldsymbol{\sigma}}}(\mathbf{x},T))=0.\tag{4.6}$$

Boundary condition (4.5) is commonly accepted in all those derivation where the postulate of local state is assumed to be valid. The postulate asserts that the state of the body in a material point is determined by the arbitrarily small neighborhood around that point (RVE). In that perspective, the postulate of local state tells us that the variations of the local field far from the investigated material point are irrelevant in evaluating its macroscopic state. Hence we may adopt a constant boundary condition on the RVE boundary and neglect any deviations from the mean value on the RVE boundary. Precise formulation of Representative Volume Element Problem requires its infinite dimensions. In actual calculations, the size of the RVE is chosen to be sufficiently large to comprise the

characteristic features of the investigated microstructure and at the same time, sufficiently small to make the postulate of local state valid within acceptable accuracy. The prescribed uniform boundary condition on the RVE boundary in fact predetermines in a natural way the unknown macroscopic state in a material point.

In further part of the present investigation we will keep the temperature T fixed until the very last section. Hence we will not write it explicitly in the further formula believing that it does not produce any misunderstandings. This means at the same time that we will investigate the isothermal problem of elasticity in the next sections. We will return to the full explicit notation with temperature T where necessary.

In general, the problem of elasticity (4.4) – (4.6) posed for actual martensitic microstructures is very difficult. However, when the solution is known, it is very easy to evaluate the elastic energy Φ_m by a simple substitution of the known solution. After the averaging procedure we may obtain an expression for the macroscopic free energy potential (4.3). It will be a function of state parameters measurable on the macro-scale (e.g. phase fractions, averaged eigenstrains, elastic properties of individual phases) as well as some parameters characterizing the RVE microstructure (e.g. the number and direction of martensitic plate layers, etc.).

In the next sections we will try to find a symbolical solution of the micro-mechanical problem posed above, convenient for obtaining a clear structure of the function Φ_m. For that purpose it will be advantageous to divide the solution of the original problem of micro-mechanics into auxiliary problems. This will be done in the next section.

5. Auxiliary boundary value problems of mezo-mechanics

The elastic energy Φ_m strongly depends on actual configuration of the phases emerging during phase transformation, i.e. microstructure of the RVE. The two idealized situations can be distinguished leading to the lower and upper estimates of elastic energy Φ_m, so-called REUSS and VOIGT estimates, respectively (see, e.g. HILL ([5]). In the case of VOIGT estimate it is assumed that average strains in individual phases are equal, what corresponds to a mechanical model of the RVE consisting of a set of springs connected in parallel under load. Alternatively we may imagine that this situation corresponds to the macro-element microstructure composed of flat martensitic and possibly austenitic plates oriented in parallel to the applied stress vector. Then the obtained value of energy constitutes the upper estimate of the real value of RVE elastic energy. In the case of Reuss estimate it is assumed that the average stresses in an individual phases are equal.

This supposition corresponds to a mechanical model of the RVE consisting of a set of springs connected in series under loading force or a microstructure composed of martensitic plates and possibly austenitic plates oriented perpendicularly to the applied stress vector. The Reuss model gives a lower estimate of the actual elastic energy of the RVE. Usually none of these microstructures appears in reality and the actual elastic energy of RVE lies somewhere between the REUSS and VOIGT estimate.

The fields of stresses, strains and displacements of original problem (4.4) – (4.6) is now decomposed in a special way,

$$\hat{\mathbf{u}}(\mathbf{x}) = \breve{\mathbf{u}}(\mathbf{x}) + \boldsymbol{\varepsilon}^{(z)}\mathbf{x}, \quad \hat{\hat{\boldsymbol{\varepsilon}}}(\mathbf{x}) = \breve{\boldsymbol{\varepsilon}}(\mathbf{x}) + \boldsymbol{\varepsilon}^{(z)}, \quad \hat{\hat{\boldsymbol{\sigma}}}(\mathbf{x}) = \breve{\boldsymbol{\sigma}}(\mathbf{x}) + \boldsymbol{\sigma}^{(z)},$$

(5.1)

$$\boldsymbol{\varepsilon}^{(z)} \equiv \mathbf{M}^V \cdot \boldsymbol{\sigma}^{(z)} + \boldsymbol{\Gamma}^V, \quad \mathbf{M}^V \equiv z_1\mathbf{M}_1 + z_2\mathbf{M}_2.$$

From (4.5) and $(5.1)_3$ it results that the following condition must be fulfilled,

$$\mathbf{n} \cdot \breve{\boldsymbol{\sigma}}(\mathbf{x})\,|_{\partial V} = 0. \tag{5.2}$$

Thus, the average stress over the total volume of RVE (V0) from the field $\breve{\boldsymbol{\sigma}}(\mathbf{x})$ is equal to zero.

There is an infinite number of additive decompositions in the linear problem of elasticity (4.4) – (4.6). Separation of certain uniform fields of stresses and strains from the solution of the original problem of mezo-mechanics has a twofold application. On the one hand, we want to isolate in the macroscopic free energy potential the terms connected with boundary condition (4.5). On the other hand, we want to obtain the additive decomposition of the total elastic energy of macro-element Φ_m . We will show below that the energy Φ_m may be decomposed into additive form (5.3) linked with additive decomposition expressed by (5.1). The additive decomposition will consist of two parts, the first of which is the lower (Reuss) estimate while the second, in accordance with the result obtained by HILL [5], is always non-negative,

$$\rho\Phi_m = \frac{1}{2}\left(\boldsymbol{\varepsilon} - \boldsymbol{\Gamma}^V\right) \cdot \mathbf{L}^R \left(\boldsymbol{\varepsilon} - \boldsymbol{\Gamma}^V\right) + W^*, \tag{5.3}$$

where $\boldsymbol{\Gamma}^V \equiv \langle \hat{\boldsymbol{\Gamma}}(\mathbf{x}) \rangle_0 = z_1\boldsymbol{\Gamma}_1 + z_2\boldsymbol{\Gamma}_2$ is the average (over the whole RVE volume) phase transformation eigenstrain, while $\mathbf{L}^R$ is the Reuss estimate of the effective tensor of elastic moduli, $\mathbf{L}^R = (\mathbf{M}^V)^{-1}$.

Substituting (5.1) and $(4.4)_2$ into $(4.4)_1$ we have,

$$\boldsymbol{\varepsilon}^{(z)} + \breve{\boldsymbol{\varepsilon}}_\alpha(\mathbf{x}) = \mathbf{M}^V(\breve{\boldsymbol{\sigma}}_\alpha(\mathbf{x}) + \boldsymbol{\sigma}^{(z)}) + j_\alpha(\mathbf{M}_2 - \mathbf{M}_1)(\breve{\boldsymbol{\sigma}}_\alpha(\mathbf{x}) + \boldsymbol{\sigma}^{(z)}) \tag{5.4}$$

$$+\boldsymbol{\Gamma}^V + j_\alpha(\boldsymbol{\Gamma}_2 - \boldsymbol{\Gamma}_1) + \hat{\boldsymbol{\Gamma}}^d_\alpha(\mathbf{x})$$

and subsequently,

$$\breve{\varepsilon}_\alpha(\mathbf{x}) = \mathbf{M}_\alpha \breve{\sigma}_\alpha(\mathbf{x}) + j_\alpha \boldsymbol{\Delta}^f + \hat{\Gamma}^d_\alpha(\mathbf{x}),$$

(5.5)

$$\boldsymbol{\Delta}^f \equiv (\boldsymbol{\Gamma}_2 - \boldsymbol{\Gamma}_1) + (\mathbf{M}_2 - \mathbf{M}_1)\boldsymbol{\sigma}^{(z)},$$

where the following identities were used,

$$\mathbf{M}_\alpha = \mathbf{M}^V + j_\alpha(\mathbf{M}_2 - \mathbf{M}_1), \quad \boldsymbol{\Gamma}_\alpha = \boldsymbol{\Gamma}^V + j_\alpha(\boldsymbol{\Gamma}_2 - \boldsymbol{\Gamma}_1), \tag{5.6}$$

$$j_1 = -z_2, j_2 = z_1.$$

The expression for $\boldsymbol{\Delta}^f$ can also be expressed in terms of $\boldsymbol{\varepsilon}^{(z)}$ using the identities shown below,

$$(\boldsymbol{\Gamma}_2 - \boldsymbol{\Gamma}_1) \equiv (\mathbf{L}^{\mathrm{U}})^{-1}(\mathbf{L}_2\boldsymbol{\Gamma}_2 - \mathbf{L}_1\boldsymbol{\Gamma}_1 + (\mathbf{L}_1 - \mathbf{L}_2)\boldsymbol{\Gamma}^V),$$

(5.7)

$$(\mathbf{M}_2 - \mathbf{M}_1)\left(\mathbf{M}^{\mathrm{V}}\right)^{-1} \equiv (\mathbf{L}^{\mathrm{U}})^{-1}(\mathbf{L}_1 - \mathbf{L}_2) \quad \text{where} \quad \mathbf{L}^U = z_2\mathbf{L}_1 + z_1\mathbf{L}_2.$$

Combining (5.7) with $(5.1)_2$ we obtain,

$$\boldsymbol{\Delta}^f = (\mathbf{L}^{\mathrm{U}})^{-1}\boldsymbol{\Sigma}^f, \quad \boldsymbol{\Sigma}^f \equiv \boldsymbol{\Sigma}^\Gamma + \mathbf{L}^d\boldsymbol{\varepsilon}^{(z)}, \quad \boldsymbol{\Sigma}^\Gamma \equiv \mathbf{L}_2\boldsymbol{\Gamma}_2 - \mathbf{L}_1\boldsymbol{\Gamma}_1, \tag{5.8}$$

$$\mathbf{L}^d \equiv (\mathbf{L}_1 - \mathbf{L}_2).$$

In view of $(5.5)_1$, (5.2) and (4.6), the primary problem of micro-mechanics has been reduced to the following problem,

$$\breve{\varepsilon}_\alpha(\mathbf{x}) = \mathbf{M}_\alpha \breve{\sigma}_\alpha(\mathbf{x}) + \hat{\Gamma}^*_\alpha(\mathbf{x}), \quad \operatorname{div}(\breve{\boldsymbol{\sigma}}) = 0, \quad \breve{\mathbf{t}}(\mathbf{x})\,|_{\partial V} = 0,$$

(5.9)

$$\hat{\Gamma}^*_\alpha(\mathbf{x}) \equiv j_\alpha \boldsymbol{\Delta}^f + \hat{\Gamma}^d_\alpha(\mathbf{x}).$$

When the solution of problem (5.9) is known, then the solution of primary problem (4.4) – (4.6) can be immediately found with the aid of (5.1). The decomposition (5.1) leads to the following division of macro-element elastic energy,

$$\rho\Phi_m = \frac{1}{2}\left[z_1\left\langle\left(\breve{\boldsymbol{\sigma}}(\mathbf{x}) + \boldsymbol{\sigma}^{(z)}\right)\cdot\mathbf{M}_1\left(\breve{\boldsymbol{\sigma}}(\mathbf{x}) + \boldsymbol{\sigma}^{(z)}\right)\right\rangle_1 + z_2\left\langle\left(\breve{\boldsymbol{\sigma}}(\mathbf{x}) + \boldsymbol{\sigma}^{(z)}\right)\cdot\mathbf{M}_2\left(\breve{\boldsymbol{\sigma}}(\mathbf{x}) + \boldsymbol{\sigma}^{(z)}\right)\right\rangle_2\right] \tag{5.10}$$

$$= \frac{1}{2}\left[z_1\left\langle\breve{\boldsymbol{\sigma}}(\mathbf{x})\cdot\mathbf{M}_1\breve{\boldsymbol{\sigma}}(\mathbf{x})\right\rangle_1 + z_2\left\langle\breve{\boldsymbol{\sigma}}(\mathbf{x})\cdot\mathbf{M}_2\breve{\boldsymbol{\sigma}}(\mathbf{x})\right\rangle_2 + \boldsymbol{\sigma}^{(z)}\cdot\mathbf{M}^V\boldsymbol{\sigma}^{(z)}\right],$$

since

$$2\left(z_1\langle\breve{\boldsymbol{\sigma}}(\mathbf{x})\rangle_1\cdot\mathbf{M}_1\boldsymbol{\sigma}^{(z)}+z_2\langle\breve{\boldsymbol{\sigma}}(\mathbf{x})\rangle_2\cdot\mathbf{M}_2\boldsymbol{\sigma}^{(z)}\right)$$

$$=2(-z_1z_2+z_1z_2)(\Delta\boldsymbol{\varepsilon}-\boldsymbol{\Delta}^f)\cdot\boldsymbol{\sigma}^{(z)}=0,$$

where in the above formulae the following relations were used (see (5.9)),

$$\langle\breve{\boldsymbol{\sigma}}(\mathbf{x})\rangle_1=-z_2\mathbf{L}_1(\Delta\boldsymbol{\varepsilon}-\boldsymbol{\Delta}^f),\quad \langle\breve{\boldsymbol{\sigma}}(\mathbf{x})\rangle_2=z_1\mathbf{L}_2(\Delta\boldsymbol{\varepsilon}-\boldsymbol{\Delta}^f),\tag{5.11}$$

$$<\breve{\boldsymbol{\varepsilon}}(\mathbf{x})>_\alpha=<\breve{\boldsymbol{\varepsilon}}(\mathbf{x})>_0+j_\alpha\Delta\boldsymbol{\varepsilon},\quad \Delta\boldsymbol{\varepsilon}=<\breve{\boldsymbol{\varepsilon}}(\mathbf{x})>_2-<\breve{\boldsymbol{\varepsilon}}(\mathbf{x})>_1,$$

$$<\breve{\boldsymbol{\sigma}}(\mathbf{x})>_0=0,\quad <\hat{\boldsymbol{\Gamma}}^d_\alpha(\mathbf{x})>_\alpha=0.$$

After substituting $(5.1)_2$ into $(5.10)_2$, the explicit form of energy W^* appearing in (5.3) is obtained,

$$W^*=\frac{1}{2}\left[z_1\langle\breve{\boldsymbol{\sigma}}(\mathbf{x})\cdot\mathbf{M}_1\breve{\boldsymbol{\sigma}}(\mathbf{x})\rangle_1+z_2\langle\breve{\boldsymbol{\sigma}}(\mathbf{x})\cdot\mathbf{M}_2\breve{\boldsymbol{\sigma}}(\mathbf{x})\rangle_2\right]\geq 0.\tag{5.12}$$

Hereby, we have proved that with the additive decomposition (5.1), additive decomposition of elastic energy (5.3) is linked. It is worth noting that decomposition (5.3) is quite arbitrary. At the moment it has the drawback that energy W^* depends explicitly on $\boldsymbol{\varepsilon}^{(z)}$. We will correct this deficiency later by introducing the energy W^{**}.

As it can be seen from (5.9) and (5.12), the energy W^* can be interpreted as an elastic energy of specific comparative macro-element with no force loads on external walls, and stored in the effect of operation of the "Ersatz" eigenstrains $\hat{\boldsymbol{\Gamma}}^*_\alpha(\mathbf{x})$ defined by $(5.9)_2$. The comparative macro-element has the same microstructure and material properties as the actual macro-element.

Let us return to the problem (5.9). The solution of this problem may also be expressed as a sum of two auxiliary solutions in a manner similar to that applied in the case of the original problem,

$$\begin{aligned}
\breve{\mathbf{u}} &= \breve{\mathbf{u}}'(\mathbf{x})+\breve{\mathbf{u}}''(\mathbf{x}),\quad \breve{\boldsymbol{\varepsilon}}(\mathbf{x})=\breve{\boldsymbol{\varepsilon}}'(\mathbf{x})+\breve{\boldsymbol{\varepsilon}}''(\mathbf{x}),\\
\breve{\boldsymbol{\sigma}}(\mathbf{x}) &= \breve{\boldsymbol{\sigma}}'(\mathbf{x})+\breve{\boldsymbol{\sigma}}''(\mathbf{x}),\\
\breve{\boldsymbol{\varepsilon}}'_\alpha(\mathbf{x}) &= \mathbf{M}_\alpha\breve{\boldsymbol{\sigma}}'_\alpha(\mathbf{x})+j_\alpha\boldsymbol{\Delta}^f,\quad \breve{\boldsymbol{\varepsilon}}''_\alpha(\mathbf{x})=\mathbf{M}_\alpha\breve{\boldsymbol{\sigma}}''_\alpha(\mathbf{x})+\hat{\boldsymbol{\Gamma}}^d_\alpha(\mathbf{x}),\\
\breve{\mathbf{t}}'(\mathbf{x})\,|_{\partial V} &= \breve{\mathbf{t}}''(\mathbf{x})\big|_{\partial\mathrm{v}}=0.
\end{aligned}\tag{5.13}$$

The physical reason for appearance of non-vanishing fields $\breve{\boldsymbol{\sigma}}''_\alpha(\mathbf{x})$, $\breve{\boldsymbol{\varepsilon}}''_\alpha(\mathbf{x})$, can be the formation (during phase transformation) of variously oriented mismatching variants of martensitic plates, e.g. due to kinematic constraints. These fields do

not depend on the average values $\boldsymbol{\Gamma}_\alpha$ of eigenstrains of particular phases, nor on the average total stress $\boldsymbol{\sigma}^{(z)}$ prescribed by the boundary condition.

The following relations are valid due to the boundary conditions of auxiliary problems (5.13) (see also NEMAT-NASSER and HORI [11]),

$$\begin{aligned}\langle \breve{\boldsymbol{\sigma}}'(\mathbf{x}) \cdot \breve{\boldsymbol{\varepsilon}}'(\mathbf{x})\rangle_0 &= \langle \breve{\boldsymbol{\sigma}}''(\mathbf{x}) \cdot \breve{\boldsymbol{\varepsilon}}'(\mathbf{x})\rangle_0 = \langle \breve{\boldsymbol{\sigma}}'(\mathbf{x}) \cdot \breve{\boldsymbol{\varepsilon}}''(\mathbf{x})\rangle_0 \\ &= \langle \breve{\boldsymbol{\sigma}}''(\mathbf{x}) \cdot \breve{\boldsymbol{\varepsilon}}''(\mathbf{x})\rangle_0 = 0, \\ \langle \boldsymbol{\sigma}(\mathbf{x}) \cdot \boldsymbol{\varepsilon}(\mathbf{x})\rangle_0 &\equiv \frac{1}{V_0}\int\limits_{V_0} \boldsymbol{\sigma}(\mathbf{x}) \cdot \boldsymbol{\varepsilon}(\mathbf{x}) dV.\end{aligned} \tag{5.14}$$

This means that the average work of stresses on the corresponding strains calculated over the total volume of the macro-element is always equal to zero. The above relations result directly from application of the Gauss theorem, the mechanical equilibrium conditions and boundary conditions of the auxiliary problems. In the sequel, the following notation is used,

$$\begin{aligned}&\boldsymbol{\varepsilon}'_\alpha = \langle \breve{\boldsymbol{\varepsilon}}'_\alpha(\mathbf{x})\rangle_\alpha, \quad \boldsymbol{\varepsilon}''_\alpha = \langle \breve{\boldsymbol{\varepsilon}}''_\alpha(\mathbf{x})\rangle_\alpha, \quad \Delta\boldsymbol{\varepsilon}' = \boldsymbol{\varepsilon}'_2 - \boldsymbol{\varepsilon}'_1, \\ &\qquad\qquad\qquad\qquad\qquad\qquad\qquad\qquad \Delta\boldsymbol{\varepsilon}'' = \boldsymbol{\varepsilon}''_2 - \boldsymbol{\varepsilon}''_1, \\ &\boldsymbol{\sigma}'_\alpha = \langle \breve{\boldsymbol{\sigma}}'_\alpha(\mathbf{x})\rangle_\alpha, \quad \boldsymbol{\sigma}''_\alpha = \langle \breve{\boldsymbol{\sigma}}''_\alpha(\mathbf{x})\rangle_\alpha, \quad \Delta\boldsymbol{\sigma}' = \boldsymbol{\sigma}'_2 - \boldsymbol{\sigma}'_1, \\ &\qquad\qquad\qquad\qquad\qquad\qquad\qquad\qquad \Delta\boldsymbol{\sigma}'' = \boldsymbol{\sigma}''_2 - \boldsymbol{\sigma}''_1.\end{aligned} \tag{5.15}$$

Averaging $(5.13)_2$ over the total volume of RVE and using $(5.13)_1$ and $(5.11)_2$ yields,

$$\begin{aligned}&\Delta\boldsymbol{\sigma}' = \mathbf{L}^U(\Delta\boldsymbol{\varepsilon}' - \boldsymbol{\Delta}^f), \quad \Delta\boldsymbol{\sigma}'' = \mathbf{L}^U\Delta\boldsymbol{\varepsilon}'', \\ &\Delta\boldsymbol{\sigma} = \Delta\boldsymbol{\sigma}' + \Delta\boldsymbol{\sigma}'', \quad \Delta\boldsymbol{\varepsilon} = \Delta\boldsymbol{\varepsilon}' + \Delta\boldsymbol{\varepsilon}'', \quad \Delta\boldsymbol{\sigma} = \mathbf{L}^U(\Delta\boldsymbol{\varepsilon} - \boldsymbol{\Delta}^f).\end{aligned} \tag{5.16}$$

The above relations will be used in the next section.

6. The accommodation energy $\mathbf{W}^{**}$

The decomposition of energy W^* (5.12) can be performed in the same way as in the case of energy Φ_m (formula (5.10)),

$$\begin{aligned}W^* = \frac{1}{2}\Big[&z_1\Big\langle (\breve{\boldsymbol{\sigma}}' + \breve{\boldsymbol{\sigma}}'') \cdot \mathbf{M}_1(\breve{\boldsymbol{\sigma}}' + \breve{\boldsymbol{\sigma}}'')\Big\rangle_1 \\ &+ z_2\Big\langle (\breve{\boldsymbol{\sigma}}' + \breve{\boldsymbol{\sigma}}'') \cdot \mathbf{M}_2(\breve{\boldsymbol{\sigma}}' + \breve{\boldsymbol{\sigma}}'')\Big\rangle_2\Big].\end{aligned} \tag{6.1}$$

Then using the relations $(5.13)_2$ for $\mathbf{M}_\alpha \breve{\boldsymbol{\sigma}}_\alpha(\mathbf{x})$ and simplifying the obtained formula by means of relations (5.14), we have,

$$W^* = \frac{1}{2}\Big[z_1 z_2 \Big\langle \breve{\boldsymbol{\sigma}}_1'(\mathbf{x}) \Big\rangle_1 \cdot \boldsymbol{\Delta}^f - z_1 z_2 \Big\langle \breve{\boldsymbol{\sigma}}_2'(\mathbf{x}) \Big\rangle \cdot \boldsymbol{\Delta}^f - z_1 \Big\langle \breve{\boldsymbol{\sigma}}_1''(\mathbf{x}) \cdot \hat{\boldsymbol{\Gamma}}_1^d(\mathbf{x}) \Big\rangle_1 - z_2 \Big\langle \breve{\boldsymbol{\sigma}}_2''(\mathbf{x}) \cdot \hat{\boldsymbol{\Gamma}}_2^d(\mathbf{x}) \Big\rangle_2 + 2z_1 \Big\langle \breve{\boldsymbol{\sigma}}_1'' \Big(\mathbf{x}\Big) \cdot \big(\breve{\boldsymbol{\varepsilon}}_1'(\mathbf{x}) + z_2 \boldsymbol{\Delta}^f\big) \Big\rangle_1 + 2z_2 \Big\langle \breve{\boldsymbol{\sigma}}_2''(\mathbf{x}) \cdot \Big(\breve{\boldsymbol{\varepsilon}}_2'(\mathbf{x}) - z_1 \boldsymbol{\Delta}^f\Big) \Big\rangle_2 \Big]. \tag{6.2}$$

Next, using $(5.8)_1$, (5.15) and taking advantage of the properties (5.16), we obtain,

$$2W^* = -z_1 z_2 \boldsymbol{\Sigma}^f \cdot \Big(\Delta\boldsymbol{\varepsilon}' + 2\Delta\boldsymbol{\varepsilon}'' - \boldsymbol{\Delta}^f\Big) - z_1 \Big\langle \breve{\boldsymbol{\sigma}}_1''(\mathbf{x}) \cdot \hat{\boldsymbol{\Gamma}}_1^d(\mathbf{x}) \Big\rangle_1 - z_2 \Big\langle \breve{\boldsymbol{\sigma}}_2''(\mathbf{x}) \cdot \hat{\boldsymbol{\Gamma}}_2^d(\mathbf{x}) \Big\rangle_2. \tag{6.3}$$

The solution of the problem marked by the "prime" symbol can be written in the following symbolic form (see also HILL [5]),

$$\breve{\boldsymbol{\varepsilon}}_\alpha'(\mathbf{x}) = \boldsymbol{\mathcal{M}}_\alpha(\mathbf{x})\boldsymbol{\Sigma}^f, \qquad \Delta\boldsymbol{\varepsilon}' = \boldsymbol{\mathcal{M}}\boldsymbol{\Sigma}^f, \quad \boldsymbol{\mathcal{M}} = \langle \boldsymbol{\mathcal{M}}_2(\mathbf{x}) \rangle_2 - \langle \boldsymbol{\mathcal{M}}_1(\mathbf{x}) \rangle_1, \tag{6.4}$$

where concentration tensors $\boldsymbol{\mathcal{M}}_\alpha$ depend in general on the parameters representing microstructure, phase fractions and elastic moduli, etc..

The average partial strains (second-order strains) constituting the solution of the problem (4.4) – (4.6) can be now expressed as follows,

$$\hat{\bar{\boldsymbol{\varepsilon}}}_\alpha = \boldsymbol{\varepsilon}^{(z)} + j_\alpha(\boldsymbol{\mathcal{M}}\boldsymbol{\Sigma}^f + \Delta\boldsymbol{\varepsilon}''). \tag{6.5}$$

There exists a direct relation between the tensor $\boldsymbol{\mathcal{M}}$ and the classical Hill's concentration tensors. The general averaged solution of the original problem investigated can be presented in the form,

$$\hat{\bar{\boldsymbol{\varepsilon}}}_\alpha = \langle \hat{\bar{\boldsymbol{\varepsilon}}}_\alpha(\mathbf{x}) \rangle_\alpha = \mathbf{A}_\alpha \boldsymbol{\varepsilon}^{(z)} + \mathbf{D}_{\alpha 1}\boldsymbol{\Gamma}_1 + \mathbf{D}_{\alpha 2}\boldsymbol{\Gamma}_2. \tag{6.6}$$

Using (5.8) and assuming $\hat{\boldsymbol{\Gamma}}_\alpha^d(\mathbf{x}) \equiv 0$ $(\Delta\boldsymbol{\varepsilon}'' \equiv 0)$, it can be easily observed by comparison of (6.5) and (6.6), that the following relations are valid,

$$\mathbf{A}_\alpha = \mathbf{I} + j_\alpha \boldsymbol{\mathcal{M}}(\mathbf{L}_1 - \mathbf{L}_2), \qquad \mathbf{D}_{\alpha 1} = -j_\alpha \boldsymbol{\mathcal{M}}\mathbf{L}_1, \quad \mathbf{D}_{\alpha 2} = j_\alpha \boldsymbol{\mathcal{M}}\mathbf{L}_2. \tag{6.7}$$

Because the Hill's concentration tensors $\mathbf{A}_\alpha, \mathbf{D}_{\alpha 1}, \mathbf{D}_{\alpha 2}$ depend on the single fourth order tensor $\mathfrak{M}$, then whenever one of them is known, then the other one can be immediately determined, in view of the relations (6.7).

The relations (6.4) yield,

$$W^* = \frac{1}{2} z_1 z_2 \boldsymbol{\Sigma}_f \cdot \left((\mathbf{L}^{\mathrm{U}})^{-1} - \mathfrak{M} \right) \boldsymbol{\Sigma}^f + [z_1 W_1 + z_2 W_2] - z_1 z_2 \boldsymbol{\Sigma}^f \cdot \mathcal{N},$$

(6.8)

$$\mathcal{N} \equiv \Delta\boldsymbol{\varepsilon}'', \quad W_1 \equiv -\frac{1}{2} < \breve{\boldsymbol{\sigma}}_1''(\mathbf{x}) \cdot \hat{\boldsymbol{\Gamma}}_1^d(\mathbf{x}) >_1,$$

$$W_2 \equiv -\frac{1}{2} < \breve{\boldsymbol{\sigma}}_2''(\mathbf{x}) \cdot \hat{\boldsymbol{\Gamma}}_2^d(\mathbf{x}) >_2 .$$

When deviations from the average values of the eigenstrains in the phases $\hat{\boldsymbol{\Gamma}}_\alpha^d(\mathbf{x}) \equiv 0$, then the terms $\mathbf{W}_\alpha$ and $\mathcal{N}$ are also identically equal to zero and the first term appearing on the right hand side of $(6.8)_1$ is the only non-zero term. It should be observed that tensors $\mathfrak{M}$, $\mathcal{N}$ and energies $\mathbf{W}_\alpha$ do not depend on $\boldsymbol{\sigma}^{(z)}$ and on $\boldsymbol{\Gamma}_\alpha$, they are however functions of the macro-element micro-geometry, elastic moduli $\mathbf{L}_\alpha$ and phase fractions z_α.

The terms W_α $(6.8)_2$ can be expressed in the form where parts linearly proportional to the phase mass fractions z_α are explicitly separated,

$$W_\alpha = W_\alpha^* + j_\alpha W_\alpha^0, \tag{6.9}$$

where the terms $W_\alpha^* \geq 0$ do not depend linearly on z_α.

Then the expression for energy W^* takes the form,

$$W^* = z_1 z_2 \rho\Phi_{it} + z_1 W_1^* + z_2 W_2^* \geq 0$$

$$\rho\Phi_{it} \equiv \frac{1}{2} \boldsymbol{\Sigma}^f \cdot \left((\mathbf{L}^{\mathrm{U}})^{-1} - \mathfrak{M} \right) \boldsymbol{\Sigma}^f - \boldsymbol{\Sigma}^f \cdot \mathcal{N} + \Delta W^0, \quad \Delta W^0 = W_2^0 - W_1^0. \tag{6.10}$$

Using (4.3), (5.3) and (6.10), the macroscopic free energy potential of SMA macro-element may be expressed as follows,

$$\rho\Phi = \frac{1}{2} (\boldsymbol{\varepsilon}^{(z)} - \boldsymbol{\Gamma}^V) \cdot \mathbf{L}^R (\boldsymbol{\varepsilon}^{(z)} - \boldsymbol{\Gamma}^V) + z_1 z_2 \rho\Phi_{it} + z_1 W_1^* + z_2 W_2^* + \rho\Phi_0(T). \tag{6.11}$$

By direct differentiation of the free energy function Φ with respect to $\boldsymbol{\varepsilon}^{(z)}$, we can obtain the thermo-mechanical constitutive relations for the SMA macro-element. They are valid when the conditions for elastic behavior of the material

are fulfilled (no phase transformation or dissipative change of microstructure). They take the following form,

$$\boldsymbol{\sigma}^{(z)} \equiv \partial(\rho\Phi)/\partial\boldsymbol{\varepsilon}^{(z)} = \mathbf{L}^{ef}\boldsymbol{\varepsilon}^{(z)} + \boldsymbol{\varepsilon}^{pe},$$

$$\mathbf{L}^{ef} \equiv \mathbf{L}^{R} + z_1 z_2 \mathbf{L}^{d}\left((\mathbf{L}^{\mathrm{U}})^{-1} - \mathcal{M}\right)\mathbf{L}^{d}, \tag{6.12}$$

$$\boldsymbol{\varepsilon}^{pe} \equiv \left(\mathbf{L}^{ef}\right)^{-1}\left[\mathbf{L}^{R}\boldsymbol{\Gamma}^{V} - z_1 z_2\left(\mathbf{L}^{d}\cdot\left((\mathbf{L}^{\mathrm{U}})^{-1} - \mathcal{M}\right)\boldsymbol{\Sigma}^{\Gamma} - \mathbf{L}^{d}\mathcal{N}\right)\right].$$

Neither the effective elastic tensor $\mathbf{L}^{ef}$ nor the effective (macroscopic) phase transformation eigenstrain tensor $\boldsymbol{\varepsilon}^{pe}$ does depend on $\boldsymbol{\varepsilon}^{(z)}$. In the case when $\mathbf{L}_1 = \mathbf{L}_2$, the above expressions can be considerably simplified to give,

$$\mathbf{L}^{ef} \equiv \mathbf{L}, \qquad \boldsymbol{\varepsilon}^{pe} \equiv \boldsymbol{\Gamma}^{V}, \qquad \boldsymbol{\sigma}^{(z)} \equiv \mathbf{L}\left(\boldsymbol{\varepsilon}^{(z)} - \boldsymbol{\Gamma}^{V}\right). \tag{6.13}$$

A more detailed discussion of some special cases will be presented in the next section. We may now rewrite the expression for the free energy of the SMA macro-element in the most convenient form,

$$\rho\Phi = \frac{1}{2}(\boldsymbol{\varepsilon}^{(z)} - \boldsymbol{\varepsilon}^{pe})\cdot\mathbf{L}^{ef}(\boldsymbol{\varepsilon}^{(z)} - \boldsymbol{\varepsilon}^{pe}) + W^{**} + \rho\Phi_0(T). \tag{6.14}$$

The formula (6.14) constitutes the central result of the present paper.

Comparing (6.11) and (6.14) and using inequality (5.12) it is easy to show that the following inequality holds,

$$W^{**} \equiv z_1 z_2 \rho\Phi^{*}_{it} + z_1 W^{*}_{1} + z_2 W^{*}_{2} \geq 0, \tag{6.15}$$

while

$$\rho\Phi^{*}_{it} \equiv \frac{1}{2}\boldsymbol{\varepsilon}^{pe}\mathbf{L}^{d}\left((\mathbf{L}^{\mathrm{U}})^{-1} - \mathcal{M}\right)\mathbf{L}^{d}\boldsymbol{\Gamma}^{V} + \frac{1}{2}\left(\boldsymbol{\Gamma}^{V} + \boldsymbol{\varepsilon}^{pe}\right)\left(\mathbf{L}^{d}\left((\mathbf{L}^{\mathrm{U}})^{-1} - \mathcal{M}\right)\boldsymbol{\Sigma}^{\Gamma} - \mathbf{L}^{d}\mathcal{N}\right) + \frac{1}{2}\boldsymbol{\Sigma}^{\Gamma}\left((\mathbf{L}^{\mathrm{U}})^{-1} - \mathcal{M}\right)\boldsymbol{\Sigma}^{\Gamma} - \boldsymbol{\Sigma}^{\Gamma}\mathcal{N} + \Delta W^{0}. \tag{6.16}$$

Please note that the energy Φ^{*}_{it} defined by (6.16) does not depend on $\boldsymbol{\varepsilon}^{(z)}$.

The general form of function Φ (formula (6.14)) derived in this paper is valid for an arbitrary microstructure. The weak point is here the fact that the functional dependence of the objects $\mathcal{M}$, $\mathcal{N}$ and W_α on particular micro-structural geometry is not known, neither is their evolution with applied external thermo-mechanical loads (e.g. $\boldsymbol{\varepsilon}$ and T). In general, the dependence of average phase transformation eigenstrains $\boldsymbol{\Gamma}_\alpha$ on the temperature or mechanical load is also

not known. Hence the expression for free energy potential (6.14) is in fact quite formal.

It would be interesting for the reader to see how this result may be used to obtain the explicit free energy potential applicable for construction of the SMA materials incremental constitutive model. Such a model has been already constructed. It is the so-called R_L model of SMA pseudoelastic behavior proposed by RANIECKI, LEXCELLENT and TANAKA in [18] and later extended by RANIECKI and LEXCELLENT in [17]. We will specify below the simplifications that had to be introduced into the formula (6.14) in order to obtain the form of free energy function used in the R_L model of the SMA materials behavior,

i) It was assumed that both the phases constitute isotropic elastic solids with the same elastic moduli, the same thermal expansion coefficient α and the same specific heats c. Then the Reuss and Voigt estimates, as well as the tensors $\mathbf{L}^{ef}$, $\mathbf{L}^R$, $\mathbf{L}^U$, reduce to the one isotropic tensor of elastic moduli $\mathbf{L}$ ($\mathbf{L}^d \equiv 0$).

ii) The eigenstrains were proposed in the form,

$$\boldsymbol{\Gamma}_1 = \alpha_0(T - T_0)\mathbf{1}; \qquad \boldsymbol{\Gamma}_2 = \alpha_0(T - T_0)\mathbf{1} + \mathbf{k}, \tag{6.17}$$

where $\mathbf{1}$ denotes the second order unit tensor, and $\mathbf{k}$ constitutes an approximation of the overall average strain connected with thermoelastic phase transformation. This assumption leads to the following estimation of the tensor: $\boldsymbol{\varepsilon}^{pe} = \boldsymbol{\Gamma}^V = \alpha_0(T - T_0)\mathbf{1} + z_2\mathbf{k}$. Moreover, the authors of the R_L model have accepted that the trace of the phase distortion tensor $\mathbf{k}$ is always zero, and that it is always collinear with the total strain deviator in accordance with the following formula,

$$\mathbf{k} = \eta\overline{\boldsymbol{\varepsilon}}/\varepsilon, \qquad \varepsilon = (\overline{\boldsymbol{\varepsilon}} \cdot \overline{\boldsymbol{\varepsilon}})^{1/2}, \qquad \mathrm{tr}(\mathbf{k}) = 0, \tag{6.18}$$

where η is an amplitude of pseudoelastic flow in simple tension.

iii) The energy of internal interactions between the phases $z_1 z_2 \rho \Phi^*_{it}$ (see (6.16)) was proposed in the form of a linear function of temperature,

$$\Phi^*_{it}(T) = \overline{u}_0 - T\overline{s}_0, \tag{6.19}$$

where $\overline{u}_0, \overline{s}_0$ are material constants, which are to be identified on the basis of the existing experimental data. Hence, as a first guess in the R_L model, the influence of changing microstructure and mass fractions on the tensors $\left((\mathbf{L}^{\mathrm{U}})^{-1} - \mathcal{M}\right)$, $\mathcal{N}$ and scalar ΔW^0 has been neglected. Note that when $\mathbf{L}^d \equiv 0$ then in formula (6.16) only the last three terms are non-zero.

iv) It was additionally assumed that the term W_1^* is negligible, while $W_2^* = \overline{u}_0^{*(1)} - T\overline{s}_0^{*(1)}$ is a linear function of temperature, this assumption allows us to include subsequently the terms connected with W_2^* i.e. $\overline{u}_0^{*(2)}$, $\overline{s}_0^{*(2)}$ into the terms $u_0^{*(2)}$, $s_0^{*(2)}$ representing the internal energy and entropy of the martensitic phase

formation in the reference state ($\boldsymbol{\sigma} = 0, T = T_0$). The last operation allows us to use negative interaction energy $z_1 z_2 \rho \Phi^*_{it}$ during modeling of the R-phase transformation. We will present a more detailed discussion on that subject in the next section.

After substitution of the simplifying assumptions from **i**) to **iv**) into the formula (6.14) we obtain the form of free energy function proposed in paper [18],

$$\Phi_c = (\boldsymbol{\varepsilon} - \boldsymbol{\varepsilon}^{pe}) \cdot \mathbf{L}(\boldsymbol{\varepsilon} - \boldsymbol{\varepsilon}^{pe})/2 - (T - T_0)\boldsymbol{\alpha}_0 \cdot \mathbf{L}(\boldsymbol{\varepsilon} - \boldsymbol{\varepsilon}^{pe}) + \phi^*(T, z),$$

$$\phi^*(T, z) \equiv c(T - T_0) - cT \ln(T/T_0) + u_0^{*(1)} - T s_0^{*(1)} - z\pi_0^f(T) + \phi_{it}(T)(1 - z)z, \tag{6.20}$$

$$\boldsymbol{\varepsilon}^{pe}(z, \mathbf{k}) = \eta z \overline{\boldsymbol{\varepsilon}}/\varepsilon.$$

We will omit here the discussion on how to construct the SMA constitutive model using Φ_c, and its validation with the macroscopic experimental evidence obtained for SMA materials, sending the interested readers to the papers [17, 18, 7].

7. Discussion and conclusions

In the previous section we have obtained the expression for macroscopic free energy function assumed to be valid for shape memory alloys in their pseudoelastic range of behavior (6.14). The first term appearing on the right hand side of formula (6.14) is "classical". It is quite well known from, e.g. the theory of plasticity. It represents a response of the system loaded mechanically in the form of elastic energy storage, which is fully recoverable under unloading. The strains $\boldsymbol{\varepsilon}^{pe}$ represent in general the inelastic strains and may be of various origins (phase transformation, reorientation, plasticity, and other non-mechanical fields, e.g. magnetic or thermal).

The last term on the right hand side of formula (6.14) is also quite classical. It can be used to describe the thermal phenomena – taking place in the material, such as e.g. heat capacity or entropy change of the SMA macro-element during the loading or unloading processes.

The most interesting term appearing in the formula (6.14) is the term W^{**} that we called the accommodation energy. It is defined by the formula (6.15) and is always non-negative. The thermo-elastic martensitic transformation takes place in a SMA macro-element upon reaching certain critical conditions. The austenite-martensite microstructure starts to appear adapting to the external

load. By adaptation we mean minimization of free energy of the macro-element "as much as possible". We will explain what we mean by that thereafter. The thermo-elastic martensitic transformation is coherent. This constraint must be fulfilled at all times. For some special austenite-martensite microstructures it is possible without using any force. In such cases the microstructure is like a set of perfectly matching "puzzle" pieces. We may say that "ideal accommodation of microstructure to the applied loading" takes place. This expression can be often found in the literature devoted to physical foundations of metallurgy. We may express this special situation in precise mathematical terms of the problem of mezo-mechanics investigated in the present paper.

Let us assume that the tensor $\boldsymbol{\Delta}^f$ ($(5.5)_2$ or (5.8)) takes the form of a symmetric diadic of two vectors. Let us also assume that the fields $\hat{\boldsymbol{\Gamma}}^d_\alpha(\mathbf{x})$ $(4.4)_2$ fulfill the compatibility conditions in the regions of individual phases and geometrical consistency conditions on the inter-phase boundaries. Then the pairs of fields,

$$(7.1) \qquad \breve{\boldsymbol{\varepsilon}}'_\alpha(\mathbf{x}) = j_\alpha \boldsymbol{\Delta}^f, \qquad \breve{\boldsymbol{\sigma}}'_\alpha(\mathbf{x}) = 0 \quad \text{and} \quad \breve{\boldsymbol{\varepsilon}}''_\alpha(\mathbf{x}) = \hat{\boldsymbol{\Gamma}}^d_\alpha(\mathbf{x}), \quad \breve{\boldsymbol{\sigma}}''_\alpha(\mathbf{x}) = 0,$$

make the actual solution of the problem (5.9) (as they identically satisfy the required equilibrium and boundary conditions). Comparing $(6.21)_1$ with $(6.4)_1$ we obtain $\mathcal{M} = (\mathbf{L}^{\mathrm{U}})^{-1}$. Substituting $(6.21)_4$ into $(6.8)_2$ we obtain $\mathcal{N} = 0$, $W_\alpha = 0$. Taking advantage of (6.9) we have $\Delta W^0 = 0$, $W^*_\alpha = 0$ for $\alpha = 1, 2$. Using the previous equalities in (6.12) and (6.16) it appears that $\mathbf{L}^{ef} = \mathbf{L}^R$, $\boldsymbol{\varepsilon}^{pe} = \boldsymbol{\Gamma}^V$, $\rho\Phi^*_{it} = 0$. Finally, from (6.15) we obtain $W^{**} = 0$ and the free energy potential (6.14) takes the value of lower (Reuss) estimate $\rho\Phi = \frac{1}{2}(\boldsymbol{\varepsilon}^{(z)} - \boldsymbol{\Gamma}^V) \cdot \mathbf{L}^R(\boldsymbol{\varepsilon}^{(z)} - \boldsymbol{\Gamma}^V) + \rho\Phi_0(T)$ for the considered ideally accommodated microstructure. For the illustrative purposes we may imagine this ideally accommodated "microstructure" as four mono-crystalline martensitic plates composed of one martensitic variant each (no lower level internal martensitic substructure), embedded in mono-crystalline austenite. Such a self-accommodated group of martensitic plates quite often appears for thermally induced thermo-elastic martensite. In the case of self-accommodating group, instead of condition $(6.21)_3$, a more stringent condition $\breve{\boldsymbol{\varepsilon}}''_\alpha(\mathbf{x}) = \hat{\boldsymbol{\Gamma}}^d_\alpha(\mathbf{x}) \equiv 0$ is fulfilled. We may say that when thermally induced groups of self-accommodating martensitic plates are formed then ideal strain accommodation takes place. In such a case not only the energy W^{**} but also the macroscopic total strain of the sample is zero. When "only" $W^{**} = 0$, we may speak about ideal energetic accommodation of the microstructure to the applied load.

In general, it is impossible for the macro-element microstructure to "adapt ideally" to the external load $\boldsymbol{\sigma}^{(z)}$. This means that the conditions (6.21) are not fulfilled in general. In such a case, the compatibility conditions in the regions

of individual phases and the coherency conditions on the inter- and intra- phase boundaries must be enforced by self-equilibrating internal stresses of the second kind. On the macroscopic scale it means that energy $W^{**} > 0$. The energy W^{**} can be termed the energy of unaccommodation of the macro-element microstructure to the prescribed external loading or the coherency energy (MÜLLER and XU [10]). Alternatively it may be termed, as we do it, the accommodation energy since it is this energy, which assures the satisfaction of the compatibility conditions for the actual strain fields and coherence conditions for the displacement fields.

In Section 1 we indicated the paradox in the attempts to describe SMA materials behavior during the R-phase transformation. Identification of the model material parameters led in the case of NiTi alloy undergoing the R-phase transformation to negative values of an interaction energy Φ^{AM}, which seemed somehow impossible on physical grounds. Now we may explain this paradox as follows. The formula (6.15) defines the accommodation energy W^{**}, which as it has been shown above, is always non-negative. The interaction energy $\Phi^{AM} = z_1 z_2 \rho \Phi^*_{it}$ is only a part of the accommodation energy W^{**}. The energy Φ^{AM} may be negative for some special microstructures when at the same time, the terms W_1^* and/or W_2^* are non-negative and $z_1 W_1^* + z_2 W_2^* \geq z_1 z_2 \rho \Phi^*_{it}$. Such a situation occurs when the fields of deviations $\hat{\Gamma}^d_\alpha(\mathbf{x})$ from the mean values of phase eigenstrains are "highly" incompatible (incommensurate). The macroscopic stress-strain curves obtained for NiTi samples undergoing the R-phase transformation (see e.g. Fig. 2), and the investigations presented in the present paper allow to draw conclusion that the reach incommensurate microstructure is forming in the sample undergoing R-phase transformation. In order to coerce the coherence kinematic constraints of the transformation, relatively high energy W_2^* is necessary (in this particular case we may safely assume for not trained NiTi specimens that W_1^* is negligible). The experimental works by MIYAZAKI, WAYMAN [9] confirm this supposition, as they report the formation of incommensurate microstructures in the NiTi samples undergoing R-phase transformation.

The energies $W^*_\alpha (\alpha = 1, 2)$ may be completely neglected, e.g. in the case of a CuZnAl mono-crystalline alloy undergoing monoclinic martensitic transformation. This case studied by MÜLLER and XU [10] gave a false impression that the coherency energy $z_1 z_2 \rho \Phi^*_{it}$ introduced by them heuristically constitutes all of the accommodation energy W^{**}.

Although we have managed to explain why and when the interaction energy might be negative, a new open scientific problem has appeared why the actual paths for R-phase transformation deviate from the paths of full thermodynamic equilibrium. In the case of monoclinic martensitic transformation when the interaction energy is positive, it could be explained by instability of full ther-

modynamic equilibrium path. When the interaction energy is negative, the full equilibrium path is stable (see e.g. [18]).

We will discuss one more potential field of application of our research. It is connected with the two-way shape memory effect. At present, a number of different training techniques are applied in order to induce a two-way shape memory effect:

– Deform a sample in fully martensitic state above the plastic yield limit of martensite.

– Deform the sample in austenitic (martensitic) state by application of force, then reduce (increase) the temperature below M_f (above A_f) in the presence of the applied stress.

– Deform the sample in the austenitic state after formation of minute precipitates due to the aging procedure.

The M_f denotes here the martensite finish temperature, while A_f austenite finish temperature. Stabilization and "saturation" of the acquired effect is obtained by application of cyclic mechanical loading at constant temperature, or by cyclic thermal loading at constant (stress, strain), or by application of mixed techniques.

On the micro-scale of observation, all the techniques listed above target at generation of localized centers of internal stresses (possibly uniformly distributed) in the high temperature parent phase. These localized centers of internal stresses are permanent crystallographic lattice defects such as dislocations induced by deformation (techniques one and two mentioned above), stress-induced retained martensite (technique two), precipitates (technique three).

On the macro-scale, the primary target of these procedures is to create self-equilibrated initial stress field within the SMA element in order to enforce particular geometrical path of the forward and reverse phase transformations. The typical apparent macroscopic results of the two-way effect training procedure, consisting in cyclic thermo-mechanical treatment are,

- Existence of the permanent strain at zero stress.
- Shifting of forward critical transformation temperature σ^{AM} towards lower values.
- Serious increase of hardening slope.
- Change in shape and decrease in size of the hysteresis loop.

The evolution resulting from the two-way training procedure of shape memory alloy can be well grasped by comparing the stress-strain curve of Fig. 1 for not trained SMA, and that in Fig. 2 in the paper [15] (which is schematically very similar to the Fig. 2 of the present paper). From the similarity of the stress-strain curves for "R-phase transformation" and "two-way shape memory effect" we can guess that energetically similar phenomena take place in the both cases. We have already revealed in the present section that proper description of the R-phase

transformation requires fulfillment of the inequality $z_1 W_1^* + z_2 W_2^* \geq z_1 z_2 \rho \Phi_{it}^*$. In the case of R-phase transformation it appeared that it was sufficient to assume W_2^* was strictly positive. This term arises from the incompatible eigenstrain fields resulting from the R-phase transformation. In the case of two-way shape memory effect both terms $W_\alpha^* (\alpha = 1, 2)$ most probably will have to be assumed to be strictly positive in order to obtain proper modeling description of this effect. On microscopic grounds this statement can be justified by the existence of incompatible strain fields resulting from the training procedure in both phases. They will result from plastic strains, the retained martensite eigenstrains or strains resulting from precipitates in the parent phase, and from incompatible phase transformation eigenstrains in the product phase.

The successful constitutive model of the two-way shape memory effect will require the assumption of the proper form of the terms W_α^* and their evolution. Even when at the beginning they will be zero for a "virgin" SMA sample material ($W_\alpha^* = 0$), after several or several dozens of training cycles, a certain amount of energy will be stored in the modified microstructure of the shape memory macroelement. The self-equilibrated micro-stresses will appear, which do not vanish even when one of the phases completely disappears.

Acknowledgment

The Polish State Committee for Research has financially supported the part of the present work (KBN) under Project No 3P40403507.

References

1. R. ABEYARATNE, J.K. KNOWLES, *On the driving traction acting on a surface of strain discontinuity in a continuum*, J. Mech. Phys. Solids, **38**, 345, 1990.
2. J.W. CHRISTIAN, *Crystallographic theories, interface structures, and transformation mechanisms*, Metallurgical and Materials Transactions A, **25A**, 1821–1839, 1994.
3. J.W. CHRISTIAN, *Theory of transformations in metals and alloys*, Pergamon Press 1965.
4. F. FALK, *One-dimensional model of shape memory alloys*, Arch. Mech., **35**, 1, 63–84, 1983.
5. R. HILL, *Elastic properties of reinforced solids: Some theoretical principles*, J.Mech. Phys. Solids, **11**, 357–372, 1963.
6. Y. HUO, I. MÜLLER, *Nonequilibrium thermodynamics of pseudo-elasticity*, Continuum Mech. Thermodyn, **5**, 3, 163, 1993.
7. C. LEXCELLENT, H. TOBUSHI, A. ZIÓŁKOWSKI, K. TANAKA, *Thermodynamical model of reversible R-phase transformation in TiNi shape memory alloy*, Int. J. Pres. Ves. Piping, **58**, 51–57,1994.
8. T.J. LIM, D.L. MCDOWELL, *Path dependence of shape memory alloys during cyclic loading*, Journal of Intelligent Material Systems and Structures, **6**, November, 1995.

9. S. MIYAZAKI, C.M. WAYMAN, *The R-phase transformation and associated shape memory mechanism in TiNi single crystals*, Acta Metallur. Mat., **36**, 181, 1988.

10. I. MÜLLER, H. XU, *On the pseudoelastic hysteresis*, Acta Metallur. Mat., **39**, 263–271, 1991.

11. S. NEMAT-NASER, M. HORI, *Micromechanics: Overall properties of heterogeneous materials*, North Holland 1993.

12. G.B. OLSON, W.S. OWEN [Eds.], *Martensite, A Tribute to Morris Cohen*, ASM International, 1992.

13. E. PATOOR, A. EBERHARDT, M. BERVEILLER, *Micomechanical modeling of superelasticity in shape memory alloys*, Journal de Physique, **IV**, 6, C1-277–292, 1996.

14. A.R. PELTON, D. HODGSON, T. DUERIG [Eds.], *Proceedings of The First International Conference on Shape Memory and Superelastic Technologies SMST-94*, Pacific Grove, CA, March 7-10, 1994.

15. C. PICORNELL, M. SADE, E. CESARI, *Characteristics of the martensitic transformation and the induced two-way shape memory effect after training by compressive pseudoelastic cycling in Cu-Zn-Al single crystals*, Metallurgical and Materials Transactions A, **25A**, 687–695, 1994.

16. J.L. PUTAUX, J.P. CHEVALIER, *HREM Study of self-accommodated thermal ε-martensite in and Fe-Mn-Si-Cr-Ni Shape Memory Alloy*, Acta Mater., **44**, 4, 1701–1716, 1996.

17. B. RANIECKI, C. LEXCELLENT, *R_L – models of pseudoelasticity and their specifications for some shape memory alloys*, Europ. J. of Mechanics Solids, **13**, 1, 1–30, 1994.

18. B. RANIECKI, C. LEXCELLENT, K. TANAKA, *Thermodynamic models of pseudoelastic behavior of shape memory alloys*, Arch. Mech. **44**, 3, 261–284, 1992.

19. B. RANIECKI, K. TANAKA, *On the thermodynamic driving force for coherent phase transformations*, Int. J. Engng. Sci., **32**, 12, 1845–1858, 1994.

20. Q.P. SUN, K.C. HWANG, S.W. YU, *A micromechanics constitutive model of transformation plasticity with shear and dilatation effect*, J. Mech. Phys. Solids, **39**, 4, 507–524, 1991.

21. H. WARLIMONT, L. DELAEY, *Martensitic transformations in copper-silver- and gold-based alloys*, Pergamon Press, 1974.

22. *A Workshop Report for the National Science Foundation: Rebuilding and Enhancing the Nation's Infrastructure: A Role for Intelligent Material Systems and Structures*, Journal of Intelligent Material Systems and Structures, **6**, 1, 1995.

Received December 16, 1998; revised version November 22, 1999.

DIRECTIONS FOR THE AUTHORS

The journal *ARCHIVES OF MECHANICS (ARCHIWUM MECHANIKI STOSOWANEJ)* deals with the printing of original papers which should not appear in other periodicals.

As a rule, the volume of a paper should not exceed 40 000 typographic signs, that is about 20 type-written pages, format: 210×297 mm, leaded. The papers should be submitted in two copies. They must be set in accordance with the norms established by the Editorial Office. Special importance is attached to the following directions:

1. The title of the paper should be as short as possible.

2. The text should be preceded by a brief introduction; it is also desirable that a list of notations used in the paper should be given.

3. The formula number consists of two figures: the first represents the section number and the other the formula number in that section. Thus the division into subsections does not influence the numbering of formulae. Only such formulae should be numbered to which the author refers throughout the paper, and also the resulting formulae. The formula number should be written on the left-hand side of the formula; round brackets are necessary to avoid any misunderstanding. For instance, if the author refers to the third formula of the set (2.1), a subscript should be added to denote the formula, viz. $(2.1)_3$.

4. All the notations should be written very distinctly. Special care must be taken to write small and capital letters as precisely as possible. Semi-bold type should be underlined in black pencil. Explanations should be given on the margin of the manuscript in case of special type face.

5. It has been established to denote vectors by semi-bold type. Trigonometric functions are denoted by sin, cos, tg and ctg, inverse functions – by arc sin, arc cos, arc tg and arc ctg; hyperbolic functions are denoted by sh, ch, th and cth, inverse functions – by Arsh, Arch, Arth and Arcth.

6. Figures in square brackets denote reference titles. Items appearing in the reference list should include the initials of the first name of the author and his surname, also the full title of the paper (in the language of the original paper); moreover;

a) In the case of books, the publisher's name, the place and year of publication should be given, e.g.,

5. S. Ziemba, *Vibration analysis*, PWN, Warszawa 1970;

b) In the case of a periodical, the full title of the periodical, consecutive volume number, current issue number, pp. from ... to ..., year of publication should be mentioned; the annual volume number must be marked in black pencil so as to distinguish it from the current issue number, e.g.,

6. M. Sokołowski, *A thermoelastic problem for a strip with discontinuous boundary conditions*, Arch. Mech., **13**, 3, 337–354, 1961.

7. The authors should enclose a summary of the paper. The volume of the summary is to be about 100 words.

8. The authors are kindly requested to enclose the figures prepared on diskettes (format PCX, BitMap or PostScript).

Upon receipt of the paper, the Editorial Office forwards it to the reviewer. His opinion is the basis for the Editorial Committee to determine whether the paper can be accepted for publication or not.

The printing of the paper completed, the author receives 25 copies of reprints free of charge. The authors wishing to get more copies should advise the Editorial Office accordingly, not later than the date of obtaining the galley proofs.

The papers submitted for publication in the journal should be written in English. No royalty is paid to the authors.

Please send us, in addition to the typescript, the same text prepared on a diskette (flopy disk) 3 1/2″ as an ASCII file, preferably in the TEX or LATEX format in Dos or Unix format.

EDITORIAL COMMITTEE
ARCHIVES OF MECHANICS
(ARCHIWUM MECHANIKI STOSOWANEJ)

Archives of Mechanics

Contents of issue 6 vol. 51

Arch. Mech., T. **51**, nr 6, str. 645–912, Warszawa 1999